



UNIVERSITAT  
POLITÈCNICA  
DE VALÈNCIA

Departamento de Ingeniería Electrónica

Improved characterization systems for quartz crystal microbalance sensors: parallel capacitance compensation for variable damping conditions and integrated platform for high frequency sensors in high resolution applications

By: José Vicente García Narbón

Supervised by: Dra. Yolanda Jiménez Jiménez

Valencia, January 2016



*AM<sup>a</sup> Carmen*



*A mi madre*

*A mis abuelos, María y Vicente*



Los agradecimientos son la parte más difícil de escribir de una tesis. Es muy complicado condensar en unos pocos párrafos el apoyo recibido a lo largo de tantos años de esfuerzo y sinsabores (y alguna que otra pequeña victoria).

En primer lugar, quiero agradecer a Antonio la oportunidad que me dio de unirme al laboratorio hace ya más de una década y su dirección en los primeros tiempos. A Yolanda, mi directora en los últimos tiempos, agradecerle el empujón que me hacía falta para poder cumplir los plazos impuestos cuando se nos comió el tiempo.

Tantos años en el laboratorio dan para tener la fortuna de compartir trabajo con muchas personas. Agradezco a mis compañeros todos esos ratos de apoyo, de tirarnos de los pelos cuando todo va bien, los cafés, incluso alguna cerveza. Yeison, Maribel, Román, Pablo, Carmen, Juan Antonio, Ángel, y a algún otro que seguro me dejaré por el camino, gracias.

A los compañeros de AWSensors, por sufrir (me/connmigo) durante la escritura. Muy especialmente a los que repiten nominación. A vosotros os toca doble.

Por supuesto, dar infinitas gracias a mi familia, especialmente a mi madre, María Luisa, que ha sido siempre y seguirá siendo un ejemplo a seguir. A mis tíos Rafa y Julia, y a mis primos, David y Martín, por su cariño (y por los embutidos del pueblo).

A mis amigos, Felipe, Gus, Toni, Amparo, Jose Luis, Vicky, Toni, Rocío, Amparo, etc... sólo puedo decirles: muchas gracias por insistir. Y a mis “sobrinos”, por alegrar el peor de los días con un abrazo.

Y por supuesto a M<sup>a</sup> Carmen, por estar media vida a mi lado. Y por preparar el desayuno...



## Resumen

Durante las dos últimas décadas se han propuesto diferentes interfaces electrónicos para medir los parámetros más importantes de caracterización de los cristales de microbalanza de cuarzo (QCM). La medida de los parámetros adecuados del sensor para una aplicación específica es muy importante, ya que un error en la medida de dichos parámetros puede resultar en un error en la interpretación de los resultados. Los requerimientos del sistema de caracterización dependen de la aplicación. En esta tesis se proponen dos sistemas de caracterización para dos ámbitos de aplicación que comprenden la mayoría de las aplicaciones con sensores QCM: 1) Caracterización de materiales bajo condiciones de amortiguamiento variable y 2) detección de sustancias con alta resolución de medida. Los sistemas propuestos tratan de resolver la problemática detectada en los ya existentes.

Para aplicaciones en las que el amortiguamiento del sensor varía durante el experimento, se propone un sistema basado en una nueva configuración de la técnica de compensación automática de capacidad (ACC). La nueva configuración proporciona la medida de la frecuencia de resonancia serie, la resistencia dinámica y la capacidad paralelo del sensor. Además, permite una fácil calibración del sistema que mejora la precisión en la medida. Se presentan resultados experimentales para cristales de 9 y 10MHz en medios fluidos, con diferentes capacidades en paralelo, demostrando la efectividad de la compensación de capacidad. El sistema presenta alguna desviación en frecuencia con respecto a la frecuencia resonancia serie, medida con un analizador de impedancias. Estas desviaciones son explicadas convenientemente, debidas al comportamiento no ideal específico de algunos componentes del circuito. Una nueva propuesta de circuito se presenta como posible solución a este problema.

Para aplicaciones de alta resolución se propone una plataforma integrada para caracterizar sensores acústicos de alta frecuencia. El sistema propuesto se basa en un nuevo concepto en el que el sensor es interrogado, mediante una fuente externa muy estable y de muy bajo ruido, a una frecuencia constante mientras se monitorizan los cambios producidos por la carga en la fase del sensor. El uso de sensores de alta frecuencia aumenta la sensibilidad de la medida, por otro lado, el sistema de caracterización diseñado reduce el ruido en la misma. El resultado es una mejora del límite de detección (LOD). Se consigue con ello uno de los retos pendientes en los dispositivos acústicos de alta frecuencia. La validación de la plataforma desarrollada se realiza con una aplicación de un inmunosensor basado en cristales QCM de alta frecuencia fundamental (HFF-QCM) para la detección de dos pesticidas: carbaryl y tiabendazol. Los resultados obtenidos para el Carbaryl se comparan con los obtenidos con otra tecnología acústica de alta frecuencia basada en sensores Love, con la técnica óptica basada resonancia superficial de plasmones (SPR) y con la técnica de referencia Enzyme Linked Immuno Assay (ELISA). El LOD obtenido con los sensores acústicos HFFQCM y Love es similar al obtenido con las técnicas ELISA y mejora en un orden de magnitud al obtenido con SPR.

La sencillez conceptual del sistema propuesto junto con su bajo coste, así como la capacidad de miniaturización del resonador de cuarzo hace posible la caracterización de múltiples sensores integrados en una configuración en array, esto permitirá en un futuro alcanzar el reto de la detección multianalito para aplicaciones High-Throughput Screening (HTS).

## Resum

Durant les dues últimes dècades s'han proposat diferents interfases electrònics per a mesurar els paràmetres més importants de caracterització dels cristalls de microbalança de quars (QCM). La mesura dels paràmetres adequats del sensor per a una aplicació específica és molt important, perquè un error en la interpretació dels resultats pot resultar en un error en la interpretació dels resultats. Els requeriments del sistema de caracterització depenen de l'aplicació. En aquesta tesi, es proposen dos sistemes de caracterització per a dos àmbits d'aplicació que comprenen la majoria de les aplicacions amb sensors QCM: 1) Caracterització de materials sota condicions d'amortiment variable i 2) detecció de substàncies amb alta resolució de mesura. Els sistemes proposats tracten de resoldre la problemàtica detectada en els ja existents.

Per a aplicacions en les quals l'amortiment del sensor varia durant l'experiment, es proposa un sistema basat en una nova configuració de la tècnica de compensació automàtica de capacitat (ACC). La nova configuració proporciona la mesura de la freqüència de ressonància sèrie, la resistència dinàmica i la capacitat paral·lel del sensor. A més, permet un calibratge fàcil del sistema que millora la precisió de la mesura. Es presenten els resultats experimentals per a cristalls de 9 i 10 MHz en mitjans fluids, amb diferents capacitats en paral·lel, demostrant l'efectivitat de la compensació de capacitat. El sistema presenta alguna desviació en freqüència respecte a la freqüència de ressonància sèrie, mesurada amb un analitzador d'impedàncies. Aquestes desviacions són explicades convenientment, degudes al comportament no ideal específic d'alguns components del circuit. Una nova proposta de circuit es presenta com a possible solució a aquest problema.

Per a aplicacions d'alta resolució es proposa una plataforma integrada per a caracteritzar sensors acústics d'alta freqüència. El sistema proposat es basa en un nou concepte en el qual el sensor és interrogat mitjançant una font externa

molt estable i de molt baix soroll, a una freqüència constant mentre es monitoritzen els canvis produïts per la càrrega en la fase del sensor. L'ús de sensors d'alta freqüència augmenta la sensibilitat de la mesura, per altra banda, el sistema de caracterització dissenyat redueix el soroll en la mateixa. El resultat és una millora en el límit de detecció (LOD). S'aconsegueix amb això un dels reptes pendents en els dispositius acústics d'alta freqüència. La validació de la plataforma desenvolupada es realitza amb una aplicació d'un immunosensor basat en cristalls QCM d'alta freqüència fonamental (HFF-QCM) per a la detecció de dos pesticides: carbaryl i tiabendazol. Els resultats obtinguts per al carbaryl es comparen amb els obtinguts amb altra tecnologia acústica d'alta freqüència basada en sensors Love, amb la tècnica òptica basada en ressonància superficial de plasmons (SPR) i amb la tècnica de referència Enzyme Linked Immuno Assay (ELISA). El LOD obtingut amb els sensors acústics HFF-QCM i Love és similar al obtingut amb les tècniques ELISA i millora en un ordre de magnitud el obtingut amb SPR.

La senzillesa conceptual del sistema proposat junt amb el seu baix cost, així com la capacitat de miniaturització del ressonador de quars fa possible la caracterització de múltiples sensors integrats en una configuració en array, el que permetrà en un futur assolir el repte de la detecció multianalític per a aplicacions High-Throughput Screening (HTS).

## **Abstract**

Different electronic interfaces have been proposed to measure major parameters for the characterization of quartz crystal microbalance (QCM) during the last two decades. The measurement of the adequate parameters of the sensor for a specific application is very important, since an error in this measure can lead to an error in the interpretation of the results. The requirements of the system of characterization depend on the application. In this thesis we propose two characterization systems for two types of applications that involve the majority of sensor applications: 1) Characterization of materials under variable damping conditions and 2) Detection of substances with high measurement resolution. The proposed systems seek to solve the problems detected in the systems currently in use.

For applications in which the sensor damping varies during the experiment, we propose a system based on a new configuration of the technique of automatic capacitance compensation (ACC). This new configuration provides the measure of the series resonance frequency, the motional resistance and the parallel capacitance of the sensor. Moreover, it allows an easy calibration of the system that improves the precision in the measurement. We show the experimental results for 9 and 10 MHz crystals in fluid media, with different capacitances in parallel, showing the effectiveness in the capacitance compensation. The system presents some deviation in frequency with respect to the series resonance frequency, as measured with an impedance analyser. These deviations are due to the non-ideal, specific behaviour of some of the components of the circuit. A new circuit is proposed as a possible solution to this problem.

For high-resolution applications we propose an integrated platform to characterize high-frequency acoustic sensors. The proposed system is based on a new concept in which the sensor is interrogated by means of a very stable,

low-noise external source at a constant frequency, while the changes provoked by the change in the phase of the sensor are monitored. The use of high-frequency sensors enhances the sensitivity of the measure, whereas the design characterization system reduces the noise in the measurement. The result is an improvement in the limit of detection (LOD). This way, we achieve one of the challenges in the acoustic high-frequency devices. The validation of the platform is performed by means of an immunosensor based in high fundamental frequency QCM crystals (HFF-QCM) for the detection of two pesticides: carbaryl and thiabendazole. The results obtained for carbaryl are compared to the results obtained by another high-frequency acoustic technology based in Love sensors, with the optical technique based in surface plasmonic resonance and with the gold standard technique Enzyme Linked Immunoassay (ELISA). The LOD obtained with the acoustic sensors HFF-QCM and Love is similar to the one obtained with ELISA and improves by one order of magnitude the LOD obtained with SPR. The conceptual ease of the proposed system, its low cost and the possibility of miniaturization of the quartz resonator, allows the characterization of multiple sensors integrated in an array configuration, which will allow in the future to achieve the challenge of multianalyte detection for applications of High-Throughput Screening (HTS).

# Contents

---

<b>FOREWORD .....</b>	<b>I</b>
<b>1 INTRODUCTION .....</b>	<b>1</b>
1.1 MOTIVATION.....	1
1.2 OVERVIEW OF ACOUSTIC WAVE SENSORS.....	4
1.2.1 QCM devices .....	6
1.2.2 FBAR devices .....	8
1.2.3 LM-SAW devices .....	9
1.3 MODELS FOR QCM SENSORS.....	12
1.4 INTERFACE ELECTRONIC SYSTEMS FOR AT-CUT QUARTZ SENSORS.....	21
<b>2 OBJECTIVES .....</b>	<b>31</b>
<b>3 RESULTS .....</b>	<b>35</b>
3.1 IMPROVED ELECTRONIC INTERFACES FOR AT-CUT QUARTZ CRYSTAL MICROBALANCE SENSORS UNDER VARIABLE DAMPING AND PARALLEL CAPACITANCE CONDITIONS .....	37
3.2 A DIFFERENT POINT OF VIEW ON THE SENSITIVITY OF QUARTZ CRYSTAL MICROBALANCE SENSORS.....	81
3.3 HIGH-FREQUENCY PHASE SHIFT MEASUREMENT GREATLY ENHANCES THE SENSITIVITY OF QCM IMMUNOSENSORS .....	115
3.4 LOVE MODE SURFACE ACOUSTIC WAVE AND HIGH FUNDAMENTAL FREQUENCY QUARTZ CRYSTAL MICROBALANCE IMMUNOSENSORS FOR THE DETECTION OF CARBARYL PESTICIDE.....	145
<b>4 CONCLUDING REMARKS .....</b>	<b>153</b>
<b>APPENDIX I. DESIGN AND IMPLEMENTATION OF A QCM CHARACTERIZATION SYSTEM WITH AUTOMATIC PARALLEL CAPACITANCE CANCELLATION .....</b>	<b>157</b>

I.1.	AUTOMATIC CAPACITANCE COMPENSATION (ACC) SYSTEM.....	159
I.1.i.	Design schematics.....	160
I.1.ii.	Printed circuit board design.....	170
I.2.	FPGA BASED COMMUNICATIONS AND DATA ACQUISITION SYSTEM.....	177
I.2.i.	FPGA based logic.....	180
I.2.i.a.	Reciprocal frequency counter core .....	181
I.2.i.b.	AD7864 ADC driver interface core .....	190
I.2.i.c.	PowerPC firmware .....	198
I.2.ii.	Design schematics.....	207
I.2.iii.	Printed circuit board design .....	216
I.3.	SYMMETRICAL POWER SUPPLY.....	223
I.3.i.	Design schematics.....	224
I.3.ii.	Printed circuit board design.....	226
I.4.	INSTRUMENT’S ENCLOSURE. AWS ACC-QCM-09 .....	228

**APPENDIX II. DESIGN AND IMPLEMENTATION OF AN INTEGRATED PLATFORM FOR HIGH FREQUENCY QCM SENSORS IN HIGH-RESOLUTION APPLICATIONS ..... 231**

II.1.	ELECTRONIC CHARACTERIZATION SYSTEM .....	234
II.1.i.	Electronic Characterization System Implementation.....	238
II.1.i.a.	Signal Generator .....	238
II.1.i.b.	Quadrature Coupler Circuit .....	240
II.1.i.c.	Sensor Circuit .....	242
II.1.i.d.	Bus Adapter Circuit.....	250
II.1.i.e.	Control and Communications System .....	254
II.2.	HFF-QCM SENSORS AND FLOW CELL.....	261
II.3.	FLOW INJECTION ANALYSIS SYSTEM.....	263
II.4.	INSTRUMENT’S ENCLOSURE. AWS A10 RP.....	264

**REFERENCES ..... 267**

**CONTEXT OF RESEARCH ..... 279**

**PUBLICATIONS ..... 283**





## Foreword

---

This Thesis is divided into the following chapters:

In chapter 1, the necessity of developing alternative characterization systems that overcome the problems detected in the ones currently used in two application areas is established. Those mentioned areas are: 1) fluids and material characterization under variable damping conditions, and 2) detection of substances with high resolution. With this aim, a brief review of the different electronic interfaces currently used is introduced in section 1.4. For each electronic interface, the electronic parameters of the sensor provided by the system together with its advantages and drawbacks are described. Previously, in section 1.3, the main electronic parameters of the sensor to be monitored by the electronic interface are introduced. These parameters are defined starting from the main models used to characterize the compound resonator formed by the quartz in contact with the load.

Once the necessity of proposing alternative characterization systems is justified, the objectives of the Thesis are defined in chapter 2.

---

Chapter 3 contains the four contributions made with this Thesis work. These contributions are presented in a format of compendium of peer-reviewed publications (format accepted by the Universitat Politècnica de València).

Chapter 3.1 entitled “Improved Electronic Interfaces for AT-Cut Quartz Crystal Microbalance Sensors under Variable Damping and Parallel Capacitance Conditions” was published in *Review of Scientific Instruments*, Vol. 79, 075110, (2008). In this contribution, a new configuration of an automatic capacitance compensation technique based on a double PLL is introduced. The new electronic interface proposed permits working with variable damping loads. The contribution includes as experimental results comparative measurements with an impedance analyzer as reference instrument. Details about the hardware, firmware and software developed to obtain a real prototype are included in appendix I.

Chapter 3.2, entitled “A Different Point of View of the Sensitivity in QCM Sensors” was published in *Measurement Science and Technology*, Volume 20, Number 12. In this contribution, a new concept of electronic interface that interrogates the sensor at a fixed frequency and measures the device phase changes is proposed. This new concept allows improving the Limit of Detection (LOD) of the acoustic technique. The phase response provided by the interface is related with mass changes with a simple equation, also derived in the contribution, which provides quantitative information of the process monitored. The proposed interface circuit together with the developed equation are valid only for small changes in the load, that is, for high resolution detection. Details about the hardware, firmware and software developed to obtain a real prototype are included in appendix II.

Chapter 3.3, entitled “High-Frequency phase shift measurement greatly enhances the sensitivity of QCM immunosensors” was published in *Biosensors*

and *Bioelectronics*, Volume 65, 15 March 2015, Pages 1-8. This article contains the experimental validation of the measurement concept proposed in chapter 3.2 for High Fundamental Frequency Quartz Crystal Microbalance (HFF-QCM) sensors. In this paper an immunosensor for the detection of Carbaryl and Thiabendazole pesticides is presented. The results are compared with other immunoassays for the same pesticide: conventional QCM, ELISA and SPR techniques.

Chapter 3.4, entitled “Love Mode Surface Acoustic Wave and High Fundamental Frequency Quartz Crystal Microbalance immunosensors for the detection of carbaryl pesticide” was published in *Procedia Engineering*, Volume 87, 2014, Pages 759-762, ISSN 1877-7058. In this contribution the prototype developed in chapter 3.2 is used to compare the LOD of carbaryl detection for two high frequency acoustic device technologies: Love Wave sensors and HFF-QCM sensors. One of the advantages of the prototype proposed in chapter 3.2 is the ability to characterize acoustic wave sensors of different technologies using the same electronic setup. This allows comparing the results provided by both technologies under the same conditions.

Chapter 4 includes the Thesis conclusions together with the future research lines open with this work.

The manuscript ends with a brief description of the context of research in which the Thesis has been developed, and a list of the scientific communications derived from the work presented in this Thesis.



# 1 Introduction

---

## 1.1 Motivation

From the first applications of AT-cut quartz crystals as sensors in solutions more than 20 years ago, the so-called Quartz Crystal Microbalance (QCM) sensor is becoming into a good alternative or complementary analytical method in a great deal of applications in the fields of analytical and physical chemistry, medical diagnostics and biotechnology. This technique has extensively been employed in the literature just for the monitoring of many substance absorption. The capability of QCM to operate in liquid has extended the number of applications including fluids and polymer characterization, pathogen and microorganism detection, peptides (Furtado et al., 1999), study of cell and bacterial adhesion at specific interfaces (Richert et al., 2002), bacteriophages (Hengerer et al., 1999), adsorption and hybridization of oligonucleotides (Höök et al., 2001), pollutants detection, such as organic pollutants in food and the environment (March et al., 2009), characterization of adsorbed proteins (Ben-Dov et al., 1997), DNA & RNA interactions with

---

complementary strands, genetically modified organisms (GMOs) (Stobiecka et al., 2007) and detection of bacteria (Fung and Wong, 2001) and viruses (Zhou et al., 2002), among others

The appropriate evaluation of this analytical tool requires recognizing the different steps involved and to be conscious of their importance and limitations:

1. Measurement of the appropriate sensor parameters in relation to the specific application. This includes a suitable electronics and cell interfaces;
2. Extraction of the effective physical parameters related to the model selected for the specific application, starting from the measurements in the previous step. This is one of the most complicated steps, including mathematical models combined with appropriate measurements in step 1; and
3. Interpretation of the physical, chemical or biological phenomena, which enable to explain the extracted parameters of the selected model. This is the last step and the final role of the analytical method.

Step 1 is very important because an erroneous sensor parameter measurement can lead to a misinterpretation of the phenomena involved during the experiment. In this sense, the selection of the electronic interface for a specific application is a key factor, and its limitations must be known to be conscious of its suitability.

During the last fifteen years, the main research lines in the group in which this work has been developed have been focused in the development of electronic interfaces for QCM sensor characterization. In particular, the efforts have been concentrated in developing interface QCM circuits in two application areas (which in turn include a great deal of QCM applications): 1) fluids and material characterization under variable damping conditions, and 2) detection of substances with high resolution. In each application area, the

classical interface systems have been studied and their shortcomings have been analyzed. Finally, alternative systems that overcome those mentioned shortcomings have been proposed.

For those applications under variable damping conditions some deviations in the measurements have been detected when working with classical oscillators. In particular, different oscillators' configurations have provided different measurements in apparently the same resonator conditions. Since the sensor plays an active role in the system, this shortcoming is attributed to the influence of the external circuitry to the sensor. In this sense, impedance analyzers are more appropriate techniques, since the sensor is characterized in isolation; however, its high cost and large dimensions prevent its use for applications out of the laboratory. Therefore, there is a real need to develop an electronic QCM interface that passively interrogates the sensor and fulfills the requirements of small size and low cost.

On the other hand, there are other applications in which the acoustic damping does not change along the experiment, and where main requirements are to achieve a low Limit of Detection (LOD) and multianalyte detection for High-Throughput Screening (HTS). Low values of LOD are achieved both by using High Fundamental Frequency QCM (HFF-QCM) resonators and by limiting the noise contribution of the experimental set-up. Regarding multianalyte feature, a fast interface system is required to achieve this functionality. Although impedance analyzers allow for characterizing HFF-QCM sensors, they are not suitable for fast measurements. On the contrary, although oscillators allow for a fast characterization, frequency instabilities when working for sensor characterization at higher frequencies prevent their use for high resolution applications. Thus, in these applications, there is a need to develop a low noise and fast electronic interface able to characterize HFF-

---

QCM sensors with the ability to characterize simultaneously several sensors in real time.

It can be concluded that there is a need to propose new characterization systems to overcome the shortcomings of current QCM interfaces, contributing in this way to the first step: “*Measurement of the appropriate sensor parameters in relation to the specific application*”. With this aim, this Thesis is presented.

## 1.2 Overview of Acoustic Wave Sensors

Sensors based on acoustic wave devices act as electro-piezo-mechanical transducers whose electrical properties reflect their mechanical properties. When the acoustic wave generated by the transducer penetrates in a medium with mechanical properties different from those of the device, the wave velocity and amplitude are modified. Due to the transducer electromechanical coupling, changes in the mechanical properties of the material through which the wave propagates are translated in changes in the electrical properties of the device. These electrical changes can be measured in terms of electrical impedance spectrum changes.

Different types of acoustic sensing elements exist, varying in wave propagation and deflection type, and in the way they are excited (Ferrari and Lucklum, 2008). They can be classified into two main categories: *Bulk Acoustic Waves* (BAW) and *Surface-Generated Acoustic Waves* (SGAW). In BAW devices the acoustic wave propagates unguided through the volume of the substrate. These devices are mostly excited through the piezoelectric or capacitive effects by using electrodes on which an alternative voltage is applied. In SGAW devices the acoustic waves are generated and detected in the surface of the piezoelectric substrate by means of Interdigital Transducers (IDTs). Moreover, acoustic devices may work with longitudinal waves (with the deflection in the direction of propagation) or shear waves (with the deflection perpendicular to the

direction of propagation). Longitudinal waves generated by the device radiate compressional waves into a liquid in contact with it. This causes severe attenuation. The number of biochemical applications is extended for in-liquid applications; in these cases, it is necessary to minimize the acoustic radiation into the medium of interest and the shear wave is mostly used.

The three important BAW devices are Quartz Crystal Microbalances (QCM), Film Bulk Acoustic Resonators (FBAR) and cantilevers. Figure 1 shows their basic structure and typical dimensions. The vibrating mode of cantilevers is not suited for operation in liquids due to the high damping. The classical Quartz Crystal Microbalance (QCM) is the most used acoustic device for sensor applications. The QCM transduction mechanism has been studied in detail for many years, and it is currently a mature and affordable technology (Andle and Vetelino, 1994; Janshoff et al., 2000). Other acoustic devices also operate properly in contact with liquid media, for example *Film bulk Acoustic Resonators* (FBAR) or *Love Mode-Surface Acoustic Wave* (LM-SAW), among others. Although this Thesis is focused on QCM technology, a brief review of the different technologies used in the implementation of acoustic sensors could be very useful because the new aspects presented in this Thesis, in relation to the new sensor characterization interfaces, can be considered for the other devices as well; this is the case of LM-SAW. Next, a brief description of QCM, FBAR and LM-SAW devices is included.

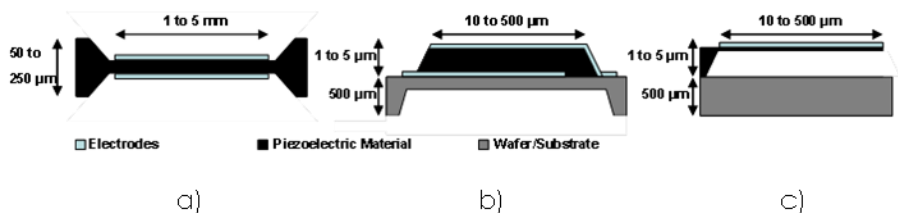


Figure 1. Bulk acoustic devices: a) QCM, b) FBAR and c) Cantilevers. Reprinted from (Montagut et al., 2011a).

---

### 1.2.1 QCM devices

The classical QCM is formed by a thin slice of AT-cut quartz crystal sandwiched between a two-electrode structure. A shear strain is induced in an AT-cut quartz crystal when an alternating-current (AC) voltage is applied across it through opposite electrodes deposited on its surfaces. The result is the generation of a transversal acoustic traveling wave, combined with a confinement structure, to produce a standing wave whose frequency is determined jointly by the velocity of the traveling wave and the dimensions of the structure (Eq.(1)). Shear waves are generated, which makes the operation in liquids suitable (Kanazawa and Gordon II, 1985).

$$f = \frac{N}{h_q} n \quad \text{with } n = 1,3,5, \dots \quad (1)$$

In Eq.(1)  $N=1664 \text{ kHz}\cdot\text{mm}$  for an AT-cut quartz,  $h_q$  is the crystal thickness and  $n$  is the harmonic number.

QCM has been the most used acoustic device for sensor applications since 1959, when Sauerbrey established the relation between the shift in the resonance frequency and the change in the surface mass density deposited on the sensor face. The linear relationship between the frequency variation and the mass surface density change provides the theoretical absolute mass sensitivity, which is proportional to the square of the selected harmonic resonant frequency,  $f_n$ , according to the following expression (Sauerbrey, 1959):

$$S_a = \frac{\Delta f}{\Delta m} = -\frac{2}{\rho v} \frac{f_n^2}{n} \quad (\text{Hz cm}^2 \text{ng}^{-1}) \quad (2)$$

where  $\Delta f$  is the frequency shift,  $\Delta m$  is the surface mass density change on the active sensor's surface,  $\rho$  is the quartz density,  $v$  the propagation velocity of the wave in the AT cut crystal,  $f_n$  is the frequency of the selected harmonic

resonant mode and  $n$  is the harmonic number ( $n=1$  for the fundamental mode). According to Eq.(2), the higher the fundamental frequency of the crystal the higher the theoretical mass sensitivity; working with higher harmonics increases the sensitivity as well, but not as much as in the previous case, because the harmonic number appears dividing.

For AT-cut quartz crystals, the limit of detection (LOD) or surface mass resolution for a minimum detectable frequency shift  $\Delta f_{min}$  will be given by:

$$\Delta m_{min} = \frac{\Delta f_{min}}{S_a} \quad (3)$$

Despite the extensive use of QCM technology, some challenges such as the improvement of the sensitivity and the limit of detection in High Fundamental Frequency-QCM (HFF-QCM), remain unsolved. Absolute sensitivities of a 30 MHz QCM reach  $2 \text{ Hz cm}^2 \text{ ng}^{-1}$ , with typical mass resolutions around  $10 \text{ ng cm}^{-2}$  (Lin et al., 1993). An electrodeless QCM biosensor for 170MHz fundamental frequency, with a sensitivity of  $67 \text{ Hz cm}^{-2} \text{ ng}^{-1}$ , has been reported (Ogi et al., 2009). This shows that the HFF-QCM technique still remains a promising technique. Increasing the sensitivity through an increase of the fundamental resonant frequency of the crystal is not a simple task, mainly due to fragility of HFF-QCM sensors. Traditional QCM sensors work at resonance frequencies between 5 and 10 MHz, which correspond to crystal thicknesses between  $332,8 \text{ }\mu\text{m}$  and  $166,4 \text{ }\mu\text{m}$  (Eq.(1)). These thicknesses are reduced to around  $11 \text{ }\mu\text{m}$  for fundamental frequencies around 150 MHz. HFF-QCM are developed by using Inverted Mesa technology (Fig. 2), with this technology those extremely thin thicknesses are reached only in the central area of the quartz wafer allowing a thicker frame around it.

---

Theoretical mass sensitivity obtained through Sauerbrey's equation, is right only on conditions where only inertial mass effects contribute on the resonant frequency shift of the QCM sensor, in a perturbative approximation and assuming that the adlayer exhibits properties close to those of quartz (Arnau et al., 2006; Jiménez et al., 2008; Kankare, 2002; Voinova et al., 2002). However, QCM sensors are more than a microbalance and other effects, such as the viscoelasticity, can contribute on the electrical response of the sensor. This broadens the applications fields, but introduces new challenges: 1) development of more comprehensive models which appropriately relate the physical properties of the deposited layers with the electrical response of the sensor, 2) definition of new strategies to extract multiple physical properties from the electrical impedance of the sensor and 3) development of new electronic interfaces able to provide the suitable electronic parameters needed to a reliable physical parameter extraction.

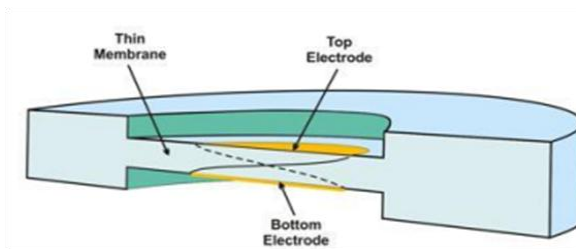


Figure. 2. Inverted Mesa Technology.

### 1.2.2 FBAR devices

A typical Film Bulk Acoustic Resonator (FBAR) consists of a piezoelectric thin film (such as ZnO or AlN) sandwiched between two metal layers (Figure 1b). As happened with other types of acoustic sensors, FBARs have been used for filter applications in RF devices (Lakin, 2005; Vale et al., 1990). In 2003, FBARs were used for the first time for gravimetric bio-chemical sensing applications (Gabl et al., 2003). They basically function like QCMs, but

with thicknesses for the piezoelectric thin film significantly smaller (between 100 nm and a few  $\mu\text{m}$ ), allowing FBARs to resonate in the GHz range. An important feature of FBAR technology is its integration compatibility with CMOS technologies, which would permit the sensor to be integrated with the electronics. However, the miniaturization of sensor devices should go in parallel with the miniaturization of the microfluidic system which is an important challenge not solved yet. On the other hand, although higher sensitivities than for QCMs could be reached due to its higher resonance frequency, the noise level is higher as well, thus moderating the gain in resolution (Gabl et al., 2004; Wingqvist et al., 2008, 2007). The higher frequency and the smaller size of the resonator result in a stronger effect of the boundary conditions on the FBAR performance than on the QCM response. The first shear mode FBAR biosensor system working in liquid environment was reported in 2006 (Weber et al., 2006). The device had a mass sensitivity of  $585 \text{ Hz cm}^2 \text{ ng}^{-1}$  and a limit of detection of  $2.3 \text{ ng cm}^{-2}$ , already better than that obtained with QCM ( $5.2 \text{ ng cm}^{-2}$ ) for the same antigen/antibody recognition measurements. However, these results have been compared with typical 10 MHz QCM sensors; therefore HFF-QCM sensors working, for instance, at 150 MHz could have much higher resolution than the reported FBAR sensors. In 2009 a FBAR for the label-free biosensing of DNA attached on functionalized gold surfaces was reported (Nirschl et al., 2009). The sensor operated at about 800 MHz, had a mass sensitivity of about  $2000 \text{ Hz cm}^2 \text{ ng}^{-1}$  and a minimum detectable mass of about  $1 \text{ ng cm}^{-2}$ .

### 1.2.3 LM-SAW devices

Love Mode Surface Acoustic Wave devices (LM-SAW), have recently been reported as more sensitive than the classical QCM-based devices (Rocha-Gaso et al., 2014, 2009). The LM-SAW sensor is a layered structure formed, basically, by a piezoelectric substrate and a guiding layer (Figure 3). The input

port of a LM-SAW sensor is comprised of metal interdigital electrodes (IDTs), with alternative electrical polarity, deposited over the piezoelectric substrate. Applying a RF signal, a mechanical acoustic wave is launched into the piezoelectric material due to the inverse piezoelectric phenomenon. The generated acoustic wave propagates through the guiding layer arriving at an output IDT. The separation between the IDTs defines the sensing area where biochemical interactions at the sensor surface cause changes in the properties of the acoustic wave (wave propagation velocity and amplitude) (Ballantine et al., 1996). Thus, at the output IDT the electrical signal can be monitored after a delay. The piezoelectric substrate of a LM-SAW device primarily excites a shear horizontal surface acoustic wave (SH-SAW) or a surface skimming bulk wave (SSBW) depending on the material and excitation mode of the substrate. Both waves have shear horizontal particle displacements, which makes this device suitable for in-liquid applications.

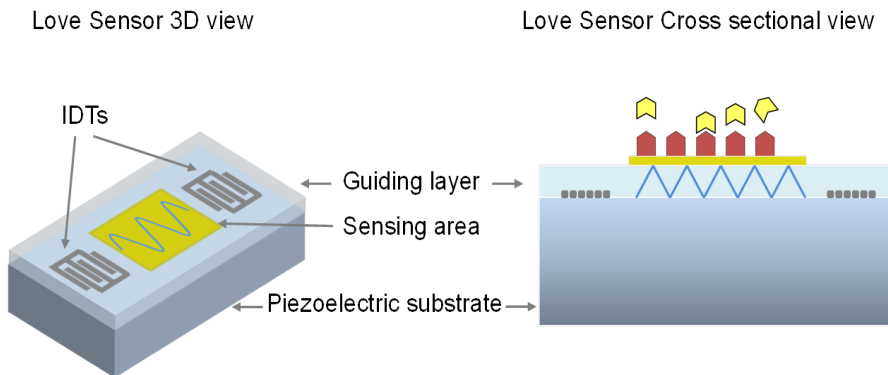


Figure 3. Basic structure of a LW sensor.

In most cases, LM-SAW devices operate in the SH wave mode with the acoustic energy confined within the thin guiding layer (typically submicrometer); thus LM-SAW devices are able to operate, without compromising the fragility of the device, at higher frequencies than QCMs. This enhances the detection sensitivity (Francis, 2006; Fu et al., 2010;

Gronewold, 2007; Länge et al., 2008). Kalantar and coworkers reported a sensitivity of  $95 \text{ Hz cm}^2\text{ng}^{-1}$  for a 100MHz Love mode sensor, which is much better than the values reported for classical QCM technology (Kalantar-Zadeh et al., 2003); however, until now any comparison has been made with HFF-QCM devices. Moreover, Moll and coworkers reported a LOD for a Love sensor of  $400 \text{ ng cm}^{-2}$ , this reveals once again that an increase in the sensitivity does not mean, necessarily, an increase in the LOD (Moll et al., 2007).

LM-SAW is not a mature technology so as QCM. Parameter extraction, as well as the interpretation of the results is more complex than QCM. Moreover, in order to avoid the capacitive coupling between the IDTs through the liquid deposited over the device while allowing the contact of the central area between the IDTs with the liquid medium, it is necessary to design special flow cells which generate a minimum distortion (Rocha-Gaso et al., 2014) in the path of the acoustic wave.

QCM devices are the most common devices used as acoustic wave based sensors. The main reason is that the simple geometry of the device and the predominant thickness-shear mode of the propagating wave are propitious conditions for a comprehensive derivation of the acoustic-electrical behavior of quartz crystal devices. FBAR and LM-SAW acoustic microsensors introduced in this section have more complicated wave propagation pattern. Different models which relate the physical properties of the media deposited over the sensor with its electrical response have been proposed along the history. The knowledge of this models permits to define the parameters to be measured for an appropriate evaluation of the sensor response, which is essential to outline the requirements of the suitable electronic interfaces. Moreover, an electrical model appropriately representing its impedance would be very useful to treat the QCM sensor as a component included in those mentioned electronic interfaces, this will permit to analyze its performance in relation to the circuitry

that surround it and to discuss the problem associated with the different electronic systems used to characterize the sensor.

### 1.3 Models for QCM Sensors

AT-cut Quartz Crystal Resonators (QCRs) are typically used for the characterization of processes involving sensitive interfaces realized with a coating which, in turn, contacts to a second medium. This second medium can be considered as “semi-infinite” when its thickness is greater than the wave’s penetration length. In general, both the coating and the contacting media are viscoelastic as indicated in Figure 4.

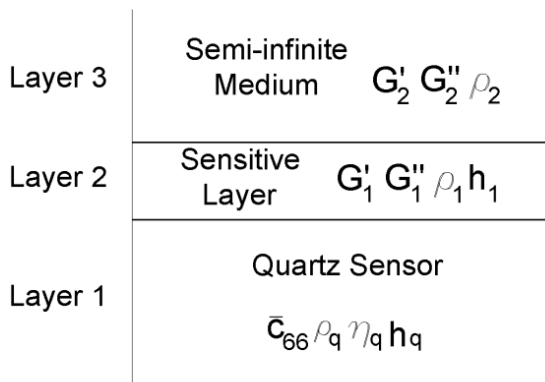


Figure 4. Cross-section of a thickness shear mode resonator loaded by a two-layer viscoelastic medium.

The coated quartz crystal can be considered as a composite resonator. Analyte sorption in the sensitive layer results in a measurable change of properties of this layer. For gaseous fluids contacting second media the Q-factor of a quartz crystal is high, thus the resonant frequency is very stable and can be measured with high resolution. Exposure of the resonator to a liquid results in energy loss caused by viscous damping and therefore a decrease of the Q-factor. However, as the decay length of shear waves at typical frequencies for QCRs is so small the acoustic energy is dissipated only in a very thin liquid layer

adjacent to the driving surface, thus making the Q-factor still remarkable high to ensure a significant resonance.

The most comprehensive one-dimensional model to characterize the compound resonator in Figure 5 is the Transmission Line Model (TLM). This model provides the electrical admittance  $Y$ , and its real and imaginary parts,  $G$  and  $B$ , respectively, as a function of the geometrical and physical parameters of the three layers as follows:

$$Y = G + jB = j\omega C_0^* + \frac{1}{Z_m} \quad (4)$$

where  $C_0^* = C_0 + C_p$  being  $C_0$  the so-called static capacitance, which arises from electrodes located on opposite sides of the dielectric quartz resonator, and  $C_p$  an added external parallel capacitance accounting for packaging, connection, etc.  $Z_m$  is the impedance of the so-called motional branch which arises from electrically excited mechanical motion in the piezoelectric crystal and it is given by:

$$Z_m = \frac{1}{j\omega C_0} \frac{1 - j \frac{Z_L}{Z_q} \cot \alpha_q}{\frac{K^2}{\alpha_q} \left[ 2 \tan\left(\frac{\alpha_q}{2}\right) \right] - j \frac{Z_L}{Z_q}} \quad (5)$$

where  $K$  is the complex electromechanical coupling factor for a lossy quartz,  $\alpha_q$  is the complex acoustic wave phase across the lossy quartz,  $Z_q$  is the quartz characteristic impedance, and  $Z_L$  is the surface acoustic load impedance. The parameters  $C_0$ ,  $K$ ,  $\alpha_q$  and  $Z_q$  in (4) and (5) depend on intrinsic properties

---

of quartz and on the crystal thickness  $h_q$ , the effective electrode area  $A_q$  and the quartz crystal losses  $\eta_q$ ; the effective values of the crystal thickness, the electrode area and the quartz crystal losses must be obtained by sensor calibration (Jiménez et al., 2008).

On the other hand, the physical and geometrical properties of the layers deposited on the crystal are included in the surface acoustic load impedance  $Z_L$ :

$$Z_L = Z_1^c \frac{Z_2 + Z_1^c \tanh(\gamma_1 h_1)}{Z_1^c + Z_2 \tanh(\gamma_1 h_1)} \quad (6)$$

where  $Z_1^c = (\rho_1 G_1)^{1/2}$  is the characteristic impedance of the coating, being  $G_1 = G'_1 + jG''_1$  the complex shear modulus and  $\rho_1$  the density;  $\gamma_1 = j\omega\rho_1/Z_1^c$  is the complex wave propagation factor in the coating,  $h_1$  is the coating thickness, and  $Z_2$  is the acoustic load impedance at the coating surface, which corresponds to the characteristic impedance of the semi-infinite medium, it is to say  $Z_2 = (\rho_2 G_2)^{1/2}$ , where  $\rho_2$  and  $G_2$  are the density and the complex shear modulus of the second medium, respectively.

$Z_m$  can be appropriately modelled by the series lumped element model in Fig.6a,  $L_m^q, C_m^q, R_m^q, Z_m^L$ , where  $L_m^q, C_m^q, R_m^q$  refer to the unperturbed sensor and  $Z_m^L$  is a complex impedance representing the contribution of the load, this equivalent circuit model is called Lumped Element Model (LEM). For our purposes, it is not necessary to know the expressions relating  $L_m^q, C_m^q, R_m^q, C_0^*$  (unperturbed quartz resonator) to the physical and geometrical properties of the quartz and they can be found elsewhere (Arnau et al., 2001; Lucklum et al., 2008; Martin et al., 1991). Near the resonance and under the “small surface

condition”, the electrical impedance  $Z_m^L$  is proportional to the surface acoustic load impedance  $Z_L$ :(Arnau et al., 2001).

$$Z_m^L = \frac{\pi}{4K^2 \omega_s C_0 Z_{cq}} Z_L \quad (7)$$

In the previous equation  $\omega_s$  is the Motional Series Resonant Frequency (MSRF) in the unperturbed state and  $K$  is the lossless electromechanical coupling factor.

Moreover,  $Z_m^L$  can be split, under certain conditions, into the lumped elements  $L_m^L$ ,  $C_m^L$  and  $R_m^L$  as described in Figure 5b giving rise to the Extended-Butterworth Van-Dyke (EBVD) model (Arnau et al., 2001).

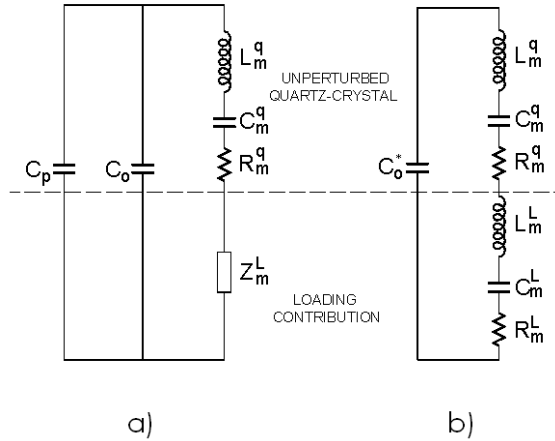


Figure 5. Equivalent circuit models for loaded QCR: (a) lumped element model (LEM), and (b) extended-Butterworth Van-Dyke (BVD) model.

The base that makes QCM useful as sensor is the relationship between the electrical complex admittance  $Y$  and the physical parameters of the load, which come into Eq.(4) through the acoustic impedance  $Z_L$  (Eq.(6)). Thus, by appropriate characterization of the electrical parameters of the sensor, it is

---

possible to extract the physical parameters of the coating. Eqs.(4) to (6) indicate that, for an accurate evaluation of  $Z_L$  in the most general case, it is necessary to obtain: 1) the effective values of  $h_q$ ,  $C_0$  and  $\eta_q$ , 2) the parasitic capacitance  $C_p$  and 3) electrical admittance (or impedance) of the sensor.

1) Effective values of  $h_q$ ,  $C_0$  and  $\eta_q$

These parameters are obtained from the reference state of the sensor. In some applications the unperturbed state of the quartz (quartz+air) is the reference state like, for instance, in liquid property characterization. However, in most applications the reference state is not the unperturbed state, and because these parameters can change with the load (Jiménez et al., 2006; Lucklum and Hauptmann, 1997), it is better to take as reference the sensor parameters just before the beginning of the process to be monitored. For example, in electrochemical applications the sensor is in contact with an electrolytic solution, it is to say with a Newtonian liquid of known characteristic impedance and, therefore, this is the state to take as reference. Nevertheless, whatever the reference state was the extraction of the effective values of  $h_q$ ,  $C_0$  and  $\eta_q$  is done by measuring the electrical response of the resonator loaded with media of known properties over a range of frequencies near resonance, and fitting the measured response to the electrical parameters of a selected equivalent-circuit model (Jiménez et al., 2006).

2) Parasitic parallel capacitance external to the resonator,  $C_p$

This parameter can be obtained from  $C_0^*$  and  $C_0$  through:

$$C_p = C_0^* - C_0 \quad (8)$$

The determination of  $C_0^*$  can be made at a frequency as high as the double of the resonant frequency (Cady, 1964).

$C_p$  value is useful in applications where the influence of the dielectric properties of the load have to be accounted for (Barnes, 1991). Sometimes special electrode configuration (Zhang and Vetelino, 2001) or different excitation principles (Ferrari and Lucklum, 2008; Zhang and Vetelino, 2001) are used to enhance relevant physical properties of the material under investigation, namely the electrical parameters permittivity and conductivity. In these configurations both the static and parasitic capacitances change and their magnitudes strongly depend on the electrical properties of the material under investigation.

### 3) Electrical admittance or impedance of the sensor

The electrical parameters of the sensor to be measured in order to perform the physical parameters extraction of the media deposited over its surface depend on the specific application and on the electronic interface used. When several physical properties must be extracted, a complete characterization of the sensor is normally required. In this case appropriate electronic interfaces must be available, for instance, impedance or network analyzers. Fortunately, there is a great deal of applications where a complete characterization of the sensor is not necessary, since the number of physical properties to be extracted is limited. In these cases, only “key” parameters of the sensor need to be monitored in order to obtain the desired information. Many of these applications fall in the area of QCM applications in solutions, such as in some piezoelectric biosensors experiments, or for liquids characterization.

Instead of using  $G$  and  $B$  for obtaining  $Z_L$  and, in turn, the physical properties of the layers, many researches usually employ the resonant frequency ( $\Delta f$ ) and the motional resistance shifts ( $\Delta R_m$ ), the reasons will be explained next.

Starting from Eq.(7), the acoustic load impedance can be approximated to:

---


$$Z_L = Z_{cq} \frac{4K^2 \omega_s C_o}{\pi} Z_m^L = \frac{\pi Z_{cq}}{2\omega_s L_m^q} \Delta Z_m \quad (9)$$

In the former equation the notation  $Z_m^L$  has been changed by  $\Delta Z_m$ ; in fact,  $Z_m^L$  represents the increment in  $Z_m$  with respect to the unperturbed sensor. Separating Eq.(9) into real and imaginary parts, the following equations result:

$$R_L = \frac{\pi Z_{cq}}{2\omega_o L_q} \Delta R_m \quad (10)$$

$$X_L = \frac{\pi Z_{cq}}{2\omega_o L_q} \Delta X_m \quad (11)$$

where  $R_L$  and  $X_L$  are the real and imaginary parts of the acoustic load impedance,  $Z_L$ , and  $\Delta R_m$  and  $\Delta X_m$  are the real and imaginary parts of the motional impedance shift with respect to the unperturbed state.

In Eq. (10), the motional resistance shift is directly related to the real part of the acoustic load impedance; on the other hand  $\Delta X_m$ , in Eq. (11) can be associated with the motional frequency shift through the acoustic load concept if one assumes that the modified BVD circuit is appropriate for characterizing the loaded resonator (this is the main approximation which is not completely fulfilled in general, but is an optimal approach in a great deal of applications). Effectively, unchanged motional capacitance of the BVD circuit allows relating the loading contribution with the increase of the motional inductance  $L_m^L$  (this condition is not coherently fulfilled, for instance, near the film resonance). Under these conditions, the shift in the imaginary part of the motional

impedance is  $\Delta X_m = L_m^L \omega$ , which can be related to the motional frequency shift as follows (Arnau et al., 2001):

$$\Delta f_s \approx -\frac{f_o}{2} \frac{L_L}{L_q} = -\frac{f_o}{2} \frac{L_L \omega_o}{L_q \omega_o} \rightarrow \Delta X_m \approx -2 L_q \omega_o \frac{\Delta f_s}{f_o} \quad (12)$$

Thus, Eq. (11) results in the following:

$$X_L = -\frac{\pi Z_{cq}}{f_o} \Delta f_s \quad (13)$$

Therefore, direct explicit relationships between the real and imaginary parts of the acoustic load impedance,  $Z_L$ , and the two typical measurable values, the frequency shift,  $\Delta f_s$ , and the change in the motional resistance,  $\Delta R_m$ , in the BVD equivalent circuit can be obtained, simplifying the characterization interfaces and the subsequent calculations. This is one of the reasons why many researchers employ the resonant frequency and the motional resistance shifts.

In addition, it is important to state that the majority of the simpler models derived from the most comprehensive TLM, such as LEM or the EBVD model, assume that the resonator operates around the MSRF. Furthermore, it is important to mention that most of simpler equations used to relate frequency and resistance shifts to the properties of the load have been derived assuming that the resonator is oscillating at its true MSRF. Thus, measurements of loading-induced frequency changes made with the resonator operating at a frequency different from the true MSRF could not agree with the models derived for QCM sensors. This discrepancy is especially pronounced when the resonator is loaded with heavy damping media. Another characteristic which makes the MSRF more interesting than other frequencies is that its value is independent of parallel capacitance changes. For all that mentioned, the

---

MSRF and the motional resistance are parameters of the loaded resonator to be measured.

On the other hand, it is important to notice that only these two parameters are not always enough for a complete determination of physical parameters of interest of the load under study. In general, more than two unknowns are present in quartz sensor applications; in these cases a complete characterization of the admittance spectrum of the sensor (Jiménez et al., 2006), or the measurement at several harmonics the MSRF and the motional resistance, can be useful.

TLM, LEM and EBVD are the most popular physical models used by researchers for applications which involve two viscoelastic layers (Fig.4). On the other hand, there are some applications in which, due to the nature of the load, the physical model can be simplified. For instance, for a single acoustically thin or rigid coating, the surface acoustic load impedance has only an imaginary component, which is proportional to the surface mass density of the coating see Eq.(13) (Jiménez et al., 2008; Lucklum et al., 2008):

$$Z_L = j\omega\rho_1 h_1 \quad (14)$$

Eq.(13) applied to this simple case gives rise to Sauerbrey equation. For a semi-infinite viscoelastic fluid medium in contact with the sensor, the surface acoustic load impedance has both real and imaginary components described by Eq.(14):

$$Z_L = \sqrt{\frac{\rho_L G_L''}{2}} \sqrt{\sqrt{Q_L^2 + 1} + Q_L} + j \sqrt{\frac{\rho_L G_L''}{2}} \sqrt{\sqrt{Q_L^2 + 1} - Q_L} \quad (15)$$

where  $Q_1 = G_1' / G_1''$  is the reverse of the loss tangent of the fluid. When the fluid is Newtonian,  $Q_1 = 0$  and the real and imaginary parts of the impedance

have the same magnitude which is depending on the density-viscosity product since  $G''_1 = \omega\eta_1$ . Eq.(12) applied to this Newtonian case give rise to the Kanazawa's equation. Sauerbrey and Kanazawa equations combined in the well-known Martin equation (see Eq.(15)) are often applied to calculate absorbed mass in chemical sensor applications or determining density/viscosity of liquids..

$$Z_L = j\omega\rho_1 h_1 + (1 + j)\sqrt{\frac{\omega\rho_1\eta_1}{2}} \quad (16)$$

Summarizing the main remarks of this section, we can conclude that the physical properties of the layers (contained in  $Z_L$ ) can be extracted directly from  $G$  and  $B$  through the TLM without any additional approximation by using network or impedance analyzers; or from  $\Delta f_s$  and  $\Delta R_m$  through the LEM under the “small surface condition”. The main advantages of using the LEM is that  $\Delta R_m$  and  $\Delta f_s$  can be directly related to the real and imaginary parts of  $Z_L$  and that they can be obtained using simple characterization interfaces.

The next section includes a brief overview of the different electronic characterization systems used for AT-cut quartz crystal microbalance in in-solution applications, which are based on the following principles: network or impedance analyzers, decay methods, oscillators and lock-in techniques. The operation mode, together with the advantages and disadvantages of each technique can be found at reference (Arnau et al., 2008).

## 1.4 Interface Electronic Systems for AT-Cut Quartz Sensors

The use of oscillators as QCR electronic interfaces has been a common practice, mainly in those applications in which the second contacting medium is gaseous. However, since the problems associated with oscillators in variable

---

damping applications were described, the use of impedance or network analyzers was extended (Johannsmann et al., 1992; Noel and Topart, 1994; Reed et al., 1990; Yang and Thompson, 1993; Yang et al., 1993). Nowadays this technique is habitually used for sensor analysis under laboratory conditions having its advantages and disadvantages.

Impedance or network analyzers measure the electrical impedance or admittance of the quartz sensor over a range of frequencies near resonance (fundamental and/or harmonics). Advantages of impedance analyzers are mainly related to the fact that the sensor is almost characterized in isolation and no external circuitry influences its electrical behaviour; additionally, electrical external influences can be excluded by calibration. Impedance analyzers provide the complete characterization of the electrical response of the device at different frequencies. This is very useful when several physical parameter of the layers deposited over the sensor must be extracted. However, its high cost and large dimensions prevent its use for in situ or remote measurements. Moreover, it is not suitable for performing a fast monitoring of the sensor parameters and neither for simultaneous multiple sensor characterization.

The drawbacks of impedance analyzers are mainly related to the fact that they are broad-spectrum instruments which are not specifically designed for the range of frequencies or impedances of typical QCM applications. New interface circuits based on a similar principle of operation, but with the frequency and impedance range adapted to QCM applications have been proposed. Adapted “impedance analyzers” which improve the portability and allow acquiring complete impedance spectrum between 1 and 5 s (assuming 1000 frequency points) has been developed (Schroöder et al., 2001). This acquisition time is not appropriate for fast QCM applications where a fast changing frequency must be monitored (Gabielli et al., 2007; Torres et al., 2008). Other alternative simple systems following the principle of passive interrogation of the sensor are

described elsewhere (Calvo et al., 1997; Kankare et al., 2006; Kurosawa et al., 1993; Niedermayer et al., 2009).

From the complete electrical response of the resonator, the values of the MSRF and motional resistance can be obtained by measuring the frequency corresponding to the conductance peak around resonance; the motional resistance is determined as the reciprocal of the conductance peak value (Arnau et al., 2000). In this way, the shifts in both parameters from a reference unperturbed state can be obtained as follows:

$$\Delta R_m = \frac{1}{G_{\max}} - \frac{1}{G_{\max}^o} \quad (17)$$

$$\Delta f_s = f_{G_{\max}} - f_{G_{\max}^o} \quad (18)$$

where the superscript “o” indicates the unperturbed state.

The evaluation of the MSRF and the motional resistance in this way is based on the suitability of the BVD model for characterizing the sensor response. In BVD circuits the relationships between MSRF and maximum conductance frequency and between the motional resistance and the reciprocal of the conductance peak value are exact. For an unperturbed resonator, the BVD circuit can very accurately represent the device response. Additionally, the range of frequencies in which the resonance happens is very narrow and therefore the frequency resolution of the instrument is very high. However, for heavy damping loads the quality factor of the device is considerably reduced and the resonance range broadens; this reduces the frequency resolution as well as the suitability of the BVD circuit for representing the sensor response. The determination of the MSRF and motional resistance by using the mentioned relationships is not as accurate as for the unperturbed situation (Arnau et al., 2000). On the other hand, an option better than a direct reading of the

---

conductance peak and its frequency from the discrete data of the conductance plot measured by the impedance analyzer, is to fit these data to a Lorentzian curve and to obtain this information from the maximum of the curve; this provides more accurate results in case of heavy loaded quartz sensors.

Additionally, an alternative parameter, probably more accurate than the motional resistance for measuring the damping and quality factor  $Q$  of the loaded sensor is the half power spectrum of the resonance ( $\Gamma$ ). The MSRF and the bandwidth ( $2\Gamma$ ) are related through the quality factor (see Eq.(18)), which in turn, is reciprocal to the dissipation factor  $D$ . A relationship among all these parameters can be obtained through the BVD model (see Eq.(19)) (Lucklum et al., 2008):

$$D = \frac{1}{Q} = \frac{2\Gamma}{f_r} \quad (19)$$

$$R = \frac{h_q^2}{8Ae_{26}^2} Z_q n\pi \frac{2\Gamma}{f} = \frac{h_q^2}{8Ae_{26}^2} Z_q n\pi D \quad (20)$$

The dissipation factor  $D$ , is habitually used in instruments based on the decay method. In these methods the piezoelectric resonator is excited with a signal generator approximately tuned to the frequency of the desired harmonic. At any given time, the signal excitation is eliminated by opening the appropriate relay. At this moment, the voltage or current, depending on whether the parallel or series resonant frequency is excited according to the electrical setup (Rodahl et al., 1996), decays as an exponentially damped sinusoidal signal. The schematics and operation principle are extensively described in references (Rodahl and Kasemo, 1996a, 1996b; Rodahl et al., 1996).

In these methods the sensor is characterized in isolation. Moreover, in series excitation mode the parallel capacitance is cancelled, and then the system

provides almost the MSRF. Although less expensive than impedance analyzers, its cost remains high, and its dimensions are large enough to prevent their use out of a laboratory. The accuracy of the decay method is high, provided that the accuracy in the data acquisition is high as well, both in phase and amplitude, which becomes complicated for strongly damping loads and for high resonance frequencies. Moreover, it becomes more sophisticated when simultaneous multiple sensor characterization at high sampling rates has to be performed.

Oscillators overcome some drawbacks of the previous mentioned interface systems, its fast operation and the low expense of circuiting makes them suitable interface systems for remote or in situ measurements, as well as, for multiple sensor characterization in HTS applications. The use of oscillators has been a common practice, however great drawbacks remain with oscillators currently used for QCM applications both in applications with variable damping conditions and high resolution applications. When changes in the load cause not only an inertial effect, but also a damping, the frequency shift provided by the sensor for the same physical change in the properties of the load is different depending on the oscillation condition used when designing the oscillator. This must be taken into account and carefully considered when using an oscillator in a specific application where the physical properties of the load can change, producing changes in both the mass loading and dissipation. The origin of these inconsistencies will be explained in detail in section 3.1.

In relation to the measurements provided by the oscillators, they can oscillate in an oscillation frequency near the true MSRF when working with  $0^\circ$  phase condition and the parallel capacitance is compensated (See section 3.1). With respect to the motional resistance, the voltage provided by the Automatic Gain Control incorporated in many oscillators is proportional to the change in the motional resistance when parallel capacitance of the sensor is compensated (Arnau et al., 2002). When the damping of the load increases, both, the

---

frequency and resistance measurements provided by an oscillator designed in the previous conditions differ from the true MSRF and motional resistance.

In spite of the drawbacks of oscillator circuits for QCR sensor applications mentioned above, the low cost of the circuitry as well as the integration capability and continuous monitoring are some features which would make the oscillators a good choice for biosensors applications in which changes in the load cause mainly an inertial effect. However, some drawbacks appear again in these interfaces when a small Limit Of Detection (LOD) is claimed. As mentioned in section 2.1.2, working with high frequency acoustic devices has not carried a parallel improvement in the resolution. An increment in the working frequency of the acoustic device leads to an improvement in the sensitivity; however, improving the LOD requires an improvement of the frequency stability.

The oscillation frequency in an oscillator is the result of a delicate balance among the phase responses of each one of the elements in the oscillator (Arnau, 2008; Arnau et al., 2008); if the phase response in one of the elements changes, the oscillation frequency shifts to find the new balance point. When working with QCM sensors, the shift in the frequency must be related with changes in the physical properties of the layers deposited over the sensor, and not with changes in the phase of some elements of the oscillator loop. Therefore, a good selection of components and appropriate configurations must be chosen to maintain the phase of the rest of the components of the oscillator as constant as possible (Auge et al., 1994; Wessendorf, 1993). If this objective is not achieved, this phase instability will produce frequency instability. The relationship between a shift in the phase and a shift in the frequency of a crystal resonator operating at its series resonance frequency  $f_0$  is given by the stability factor  $S_F$ :

$$S_F = \frac{\Delta\varphi}{\Delta f} f_o = 2Q \quad (21)$$

where  $\Delta f$  is the frequency shift necessary to provide a phase shift  $\Delta\varphi$  in the phase-frequency response of the resonator, around  $f_o$ , and  $Q$  is the series quality factor of the resonator.

According to (24) the frequency noise  $\Delta f_n$  associated to a phase noise in the circuitry  $\Delta\varphi_n$  is:

$$\Delta f_n = \frac{f_o}{2Q} \Delta\varphi_n \quad (22)$$

Consequently, because the quality factor is normally reduced proportionally to  $1/f_o$ , the frequency instability is increased in relation to the square of frequency. Moreover, the phase response of the electronic components of an oscillator gets worse with increasing the frequency, which increases, even more, the noise.

When the second contacting medium is gaseous, the  $Q$  factor of the resonator is high; therefore, changes in the phase response of the sensor due to external conditions are easily compensated for very small changes in the frequency of the resonator, and appear in the signal frequency as a small noise and/or drift. However, in in-liquid applications (as biosensors) the  $Q$  factor is reduced, therefore, even small changes in the phase response of the rest of the components in the loop of the oscillator need to be compensated for bigger shifts in the oscillator frequency. In these cases, the noise and drift are not negligible and a good control of the external variables has to be done for minimizing this problem. In this sense, two aspects should be distinguished: on one hand on the experimental set-up which must be designed to minimize the disturbances or interferences which can affect the resonance frequency of the

---

resonator such as: temperature, vibrations, pressure changes due to the fluid pumps, etc.; and on the other hand on the ability of the characterization system for an accurate measurement of the resonant frequency of the acoustic device. When the disturbances of the experimental set-up are maintained under maximum control, the frequency stability depends on the measuring system. The selection of the appropriate oscillator configuration plays an important role in minimizing the frequency shift inaccuracy. The introduction of the contribution entitled “*Improvement electronic interfaces for AT-cut quartz crystal microbalance sensors under variable damping and parallel capacitance compensation*” contains a review of principal oscillator configurations; more details can be found in reference (Arnau et al., 2008). From that review it can be concluded that although the simplicity of an oscillator makes this device very attractive for sensor applications, some limitations remain. In those applications in which the resonator damping is maintained relatively constant during the experiment and where there is not a requirement of a small LOD, although not rigorously working at MSRF, the use of oscillators has the advantages of low cost, small dimensions and fast operation. However, when damping changes during the experiment, or when small values of LOD are required, oscillators are not good electronic interfaces.

On one hand, in those applications which involve variable damping, simpler and cheaper systems which operate similarly to oscillators but implement a passive interrogation of the sensor can be used. These configurations are based on lock-in techniques which implement a manual cancellation of the parallel capacitance of the resonator (Arnau et al., 2002; Ferrari et al., 2003, 2001). These systems continuously lock the MSRF of the sensor. A comprehensive explanation of the principle of operation of these techniques, which serve as basis for the concept proposed in section 3.1 can be found elsewhere (Arnau et al., 2008).

On the other hand to implement a quasi-ideal oscillator for high frequency QCM sensors, keeping in mind the low quality factors reached by these sensors in liquid conditions, and the extremely low phase noise needed, is extremely difficult; therefore, a different characterization interface would be necessary. Recently an open loop system system for high frequency SAW and high-overtone bulk acoustic resonator (HBAR) devices has been proposed (Rabus et al., 2013, 2012). In those works, a similar approach to the proposal in section 3.2 for high frequency, high resolution applications was used.



## 2 Objectives

---

The review of the currently used interface electronic systems for AT-Cut Quartz Sensors has revealed the great efforts made in the last two decades for having available characterization systems for QCM sensors. Some drawbacks detected in those currently used interfaces justify the necessity to propose new characterization interfaces which overcome those mentioned drawbacks. The general objective of this thesis is to contribute to the improvement of the acoustic wave sensor characterization systems by proposing new interfaces, which improve the resolution and accuracy of the experimental measurements obtained, in two different, but related, fields of application:

- In-liquid QCM characterization in variable damping conditions.
- In-liquid high resolution applications.

As it was stated in the previous chapter, attending to the application, the requirements of the electronic interface can be different. For that reason, to accomplish the general Thesis objective, different specific objectives have been

---

defined for each field of application previously mentioned. Thus, the specific objectives for in-liquid QCM characterization systems in variable damping conditions are:

- 1) The system should have the ability to perform a continuous monitoring of the motional series resonant frequency, the motional resistance and the parallel capacitance of a thickness-shear mode (TSM) QCM. This system should permit the tracking of the previously mentioned parameters under variable damping media and adverse (large, variable) parallel capacitance conditions.
- 2) The system should remove or compensate for the sensor parallel capacitance, including the parasitic ones. This compensation should be done automatically in the whole frequency working range.
- 3) The sensor should be characterized by the interface system in isolation.
- 4) The circuit proposed should allow an accurate calibration of the whole system.
- 5) The system should be validated in different liquid fluids, with different damping under variable capacitance condition.

On the other hand, the specific objectives for the characterization systems in-liquid high resolution applications are:

- 1) The system should have the ability to characterize high frequency acoustic devices (in particular QCM and LM-SAW) to achieve the increment of sensitivity.
- 2) The proposed electronic interface should be a low noise system to improve the Limit of Detection, this requirement is mandatory in high resolution applications.
- 3) A fast operation of the characterization system is required in order to accomplish the ability to characterize simultaneously several sensors in real time.
- 4) The system should be validated in an application where a high resolution measurement was required. To achieve this, the system will be used in a real immunosensor application for low molecular weight compounds

detection.5) The results provided by the proposed system should be compared with those provided by other currently used technologies in the fields of high resolution detection.



## **3 Results**

---



### **3.1 Improved electronic interfaces for AT-Cut quartz crystal microbalance sensors under variable damping and parallel capacitance conditions**

Antonio Arnau, José V. García, Yolanda Jiménez, Vittorio Ferrari, Marco Ferrari

Reprinted with permission from: A. Arnau, J. V. García, Y. Jimenez, V. Ferrari and M. Ferrari, Review of Scientific Instruments, Vol. 79, 075110, (2008).

<http://dx.doi.org/10.1063/1.2960571>.

Copyright 2008, American Institute of Physics.

### **ABSTRACT**

A new configuration of automatic capacitance compensation (ACC) technique based on an oscillator-like working interface, which permits the tracking of the series resonant frequency and the monitoring of the motional resistance and the parallel capacitance of a thickness-shear mode (TSM) quartz crystal microbalance (QCM) sensor, is introduced. The new configuration permits an easier calibration of the system which, in principle, improves the accuracy. Experimental results are reported with 9 and 10MHz crystals in liquids with different parallel capacitances which demonstrate the effectiveness of the capacitance compensation. Some frequency deviations from the exact series resonant frequency, measured by an impedance analyzer, are explained by the specific non-ideal behaviour of the circuit components. A tentative approach is proposed to solve this problem that is also common to previous ACC systems.

**Keywords:** capacitance compensation, quartz microbalance, oscillators, series resonant frequency, interface circuit.

---

## I. INTRODUCTION

AT-cut quartz crystal microbalance (QCM) sensors are becoming into a good alternative analytical method in a great deal of applications. They have been extensively used as QCM sensors in gaseous media<sup>1</sup>. The work of Konash and Bastiaans in 1980<sup>2</sup>, demonstrating that the QCM could be also used for liquid-phase, and that it was possible to maintain the stability of a crystal oscillator with the resonator one-face in contact with a liquid medium, paved the way for numerous applications in different fields like electrochemistry and biology. The physical explanation of why the resonator could maintain the oscillation under the tremendous load of the contacting liquid was given later on by the well-known work of Kanawaza and Gordon<sup>3</sup>. Until the important work of Reed et al in 1990<sup>4</sup>, extending the application of the QCM to contacting viscoelastic media, few works described the use of the quartz sensor under liquid conditions<sup>5-8</sup>. The complete physical description of a viscoelastic load in contact with the quartz crystal resonator (QCR) has allowed the study of mechanical properties of different materials coated on the surface of the sensor, like viscoelastic properties of polymers<sup>9,10</sup>. In these cases concepts like “acoustically thin” or “acoustically thick” coatings are of fundamental importance<sup>11</sup>; in case of a thick viscoelastic film in contact with a liquid, a complete characterization of the sensor, together with alternative techniques, is necessary for a comprehensive explanation of certain phenomena involved during the experiments<sup>12</sup>. On the contrary, for acoustically thin films, great simplifications can be done in the physical model and the extraction of the physical properties of interest is simple by appropriate characterization of the sensor<sup>12,13</sup>. These simplifications can be done in a great deal of applications such as: fluid physical characterization, for both Newtonian and/or viscoelastic fluids<sup>12,14,15</sup>, charge transfer analysis for studying the behaviour of conductive polymers in electrochemical processes<sup>16</sup>, detection of immunoreactions and the development of biosensors<sup>17-28</sup>, etc. However, even in the simplest cases, sensor

characterization should be performed through suitable electronic interfaces that must be able to accurately measure and monitor, even continuously, appropriate sensor parameters associated with the physical properties to be evaluated.

For in gas/vapor phase applications the resonator maintains a high Q factor and oscillators are the best choice for sensor monitoring; no special requirements are necessary different from classical quartz oscillators based on the well-known Pierce, Colpitts, Miller, etc., configurations. For sensor-array it would be advantageous to have the sensing face of the resonator grounded to avoid the coupling or “cross-talk” among the oscillators, but even this recommendation has been demonstrated to be unnecessary if a certain level of isolation is maintained among the circuits<sup>29</sup>. Application of QCM sensors under in-liquid phase conditions is very much challenging and this introduction will be focused on it.

From the beginning, the use of oscillators has been a common practice in in-liquid phase QCM applications. However, the attention was quickly paid on these interfaces to explain some inconsistencies in the experiments; for instance, different frequency shifts were obtained with different oscillators in apparently the same resonator conditions<sup>5,6,13</sup>.

Since the problems associated with oscillators for a reliable monitoring of the right frequency of the QCR sensors were described, the use of impedance analyzers to characterize the quartz sensor was extended<sup>4,30-33</sup>. Nowadays this technique is habitually used as accurate tool for sensor analysis under laboratory conditions having the high cost, lack of portability and slow measuring speed its mayor disadvantages<sup>34</sup>. To circumvent these drawbacks, important efforts have been made to adapt the principle of operation of these reference instruments into smaller electronic boards configured for the specific features of QCR sensors<sup>35-40</sup>. These adapted systems maintain similar

---

specifications to high performance impedance analyzers in the range of frequencies and impedances of typical QCR sensors while improving the portability. However, the low cost of the circuitry as well as the integration capability and continuous monitoring of oscillators make them the best choice for most of chemical sensor applications. Therefore important efforts have been made to improve their behaviour as electronic interfaces for QCM sensors under liquid loading.

The first attempt was to pose the need of a common reference of the working phase of the QCR sensor in the oscillators used for in-liquid applications, and  $0^\circ$  for the phase of the sensor under oscillating conditions was proposed<sup>6</sup>. It was immediately probed that the zero-phase condition not always exists for the loaded sensor<sup>41</sup>.

In the beginning of 90's Barnes analyzed most of the typical oscillators used until then for in-liquid sensing<sup>42</sup>. In this work a clear explanation is included about the reasons of why different oscillators can provide different monitoring frequencies under the same sensor conditions. The two typical operational modes of oscillators are discussed: the parallel mode has a less restrictive range of operation than the series mode and it can be designed to force the resonator to oscillate under heavy load conditions, on the other hand the sensor phase condition is more difficult to control.

In this work Barnes introduced the main aspects, which would be in the near future the "key" points in the design of oscillators for QCR sensors: a) one face of the resonator should be grounded for electrochemical or biological applications and for a better control of the parallel capacitance, b) the evaluation of the motional series resistance would be very useful in many applications, c) an automatic gain control should be implemented to adjust the gain loop for stable operation, and d) the parallel capacitance (static and parasitic components) plays an important role in determining the oscillation

frequency, specially in parallel mode configurations<sup>43</sup>. Effectively, the evaluation of the sensor damping played an important role after the work of Martin and Granstaff in 1991<sup>13</sup>, showing that the simultaneous measuring of the frequency shift and motional resistance allowed the discrimination of different contributions on the sensor response: mass and liquid effects. Thus, automatic gain control systems were implemented in oscillators, not only for stabilization purposes but as a mean to evaluate the damping of the sensor, although some problems of this technique for the evaluation of the damping have been described elsewhere<sup>44</sup>. Finally, the parallel capacitance compensation has been one of the key aspects in the last approaches of electronic interfaces for QCM sensor characterization<sup>44-46</sup>.

From then on great efforts were made in the design of appropriate oscillators in in-liquid applications. Parallel mode oscillators, operating at strong negative phase conditions ( $\approx -76^\circ$ ) to force the oscillation of the resonator under heavy load conditions, were used<sup>47,48</sup>. However, the major efforts were made in the design of series oscillators with the resonator working at zero phase condition and with one face grounded: emitter coupled oscillators<sup>49-52</sup>, the Lever oscillator<sup>53,54</sup>, the Active bridge oscillator<sup>55,56</sup> and the Balanced bridge oscillator<sup>57,58</sup>.

The reason for developing series oscillators, working near the resonator low impedance zero-phase condition, was the assumption that the parallel capacitance has a lower effect on the oscillating frequency near the low impedance zero-phase frequency of the sensor. Moreover, if the parallel capacitance could be compensated, for instance by parallel resonance with a coil at the working frequency, a series mode oscillator would provide an oscillating frequency theoretically independent of the damping; in other words, the oscillator would be working at the series resonant frequency of the motional branch of the sensor (motional series resonant frequency - MSRF).

---

However, the use of a coil for tuning out the parallel capacitance is not habitually used because the oscillating frequency is not known “a priori”, and the tuning out of the parallel capacitance is not easy to do without additional more involved instrumentation. Under these conditions it was found, with some series configurations, that the initial design at zero-phase was not the optimal condition for the usual range of loads. Different works found that the resonator phase condition at which the frequency was reasonably closer to the MSRF, in the most usual range of loads (for motional resistances ranged from 100 to 700  $\Omega$ ), was  $-38^\circ \pm 3^\circ$  <sup>49,51,52,59</sup>. In other cases, although the zero-phase condition of the sensor was desired, the non-ideal characteristics of the circuit components result in a phase condition near but not equal to the zero-phase condition ( $\approx -6^\circ$  for the Lever oscillator<sup>53</sup> and  $\approx -3,5^\circ$  for the active bridge oscillator<sup>55,56</sup>). The balanced bridge oscillator is, in principle, able to compensate the parallel capacitance, and then the oscillating frequency is theoretically driven by the condition of zero-phase of the motional impedance<sup>57,58</sup>. Therefore, in ideal conditions the oscillating frequency would be the MSRF. However, until now no oscillator configuration has been described able to accurately drive the resonator at MSRF on a wide range of loads.

Fortunately, there are many applications in which oscillators, although not rigorously working at MSRF, are the best option. Effectively, for applications in which the resonator loss and the parallel capacitance are maintained relatively constant during experiment, the frequency shift of the resonator sensor, which is the parameter of interest, is practically independent on the resonator phase under oscillating conditions. On the contrary, when the resonator losses and parallel capacitance change during experiment, as it is the case in QCM applications, deviations in the measurements can occur and the results should be carefully interpreted. These effects are accentuated in the case of heavy acoustic loads and particularly happen when oscillators are used as QCM drivers<sup>34</sup>. In general, oscillators are not a good interface in these cases.

Passive measurements based on impedance analyzers or decay method techniques<sup>60,61</sup> are more appropriate techniques. Alternatively, simpler and cheaper systems which operate similarly to oscillators but implement a passive interrogation of the sensor could be used. These configurations are based on phase-locked loop techniques, can perform a parallel capacitance compensation of the sensor, providing a measuring of its magnitude, and allow an easy and accurate calibration of the system<sup>44-47</sup>.

In this article a new circuit configuration for automatic parallel capacitance compensation (ACC) technique is presented. The new configuration makes the calibration procedure easier and, in principle, improves its accuracy. A different approach for performing the capacitance compensation at high frequencies is introduced as well. Experimental results show the effectiveness of the parallel capacitance compensation. However, some additional improvements are necessary to increase the accuracy of the system due to the non-ideal response of some components of the circuit. A new approach is proposed to avoid these inaccuracies.

## II. THEORY

A loaded thickness-shear-mode (TSM) QCR sensor can be modeled around resonance by the lumped-element equivalent circuit shown in Fig.1.

The circuit is a generalization of the Butterworth-Van Dyke (BVD) model in which  $L_1$ ,  $C_1$ ,  $R_1$  refer to the unperturbed sensor,  $C_0$  is the so-called static capacitance of the crystal,  $C_p$  is the parasitic capacitance external to the sensor and  $Z_L$  is a complex impedance representing the contribution of the load. A detailed description of the relationships between the electrical parameters of the model and the physical and geometrical properties of the quartz crystal and the load can be found elsewhere<sup>62</sup>. For the purpose of this article the model in Fig.1 is enough to show the problem of oscillators as

drivers for QCM sensor characterization, and to understand the principle of operation of the circuit here proposed.

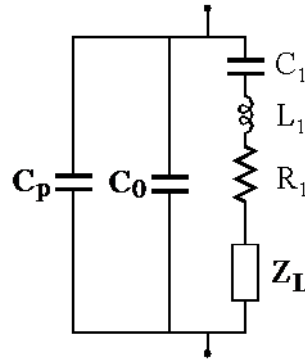


Fig. 1. Lumped-element equivalent circuit for the QCR around resonance.

Oscillators' output frequency depends on the specific loop gain and phase oscillating conditions; therefore different oscillators can provide different output frequencies for the same experiment depending on the specific designed oscillating conditions. This effect which could not be easily recognized can lead to the risk of severe misinterpretations of the authentic frequency shift of the sensor characteristic frequency. The problem is qualitatively depicted in Fig. 2. As it can be noticed, different frequency shifts,  $\Delta f_1$  and  $\Delta f_2$ , would be provided by oscillators with different sensor phase oscillating conditions,  $\alpha_1$  and  $\alpha_2$ , between two different instants of an experiment for which the conductance and phase responses of the sensor around the resonance are given by the plots 1, 1' and 2, 2' for instants 1 and 2 respectively. As it can be understood this effect is a consequence of the decrease of the steepness of the phase response of the sensor as a consequence of the damping effect due to the load. The conductance value of the sensor is also different at the two phase oscillating conditions,  $\alpha_1$  and  $\alpha_2$ ; this also implies an error in the characterization of the

sensor damping when the conductance is taken as a parameter for its characterization.

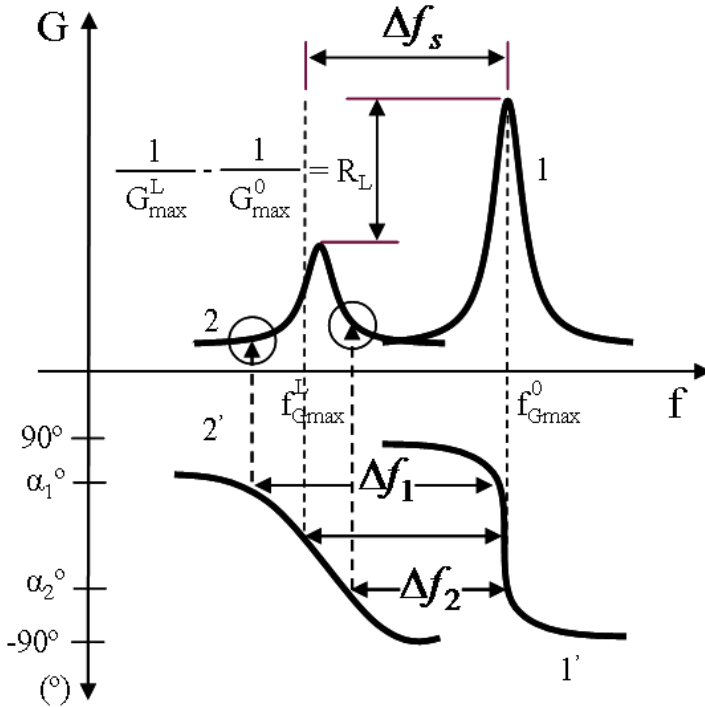


Fig. 2. Qualitative description of the problem of QCM sensor characterization.

The appropriate frequency and conductance to be monitored are those corresponding to the series resonance of the motional branch of the circuit in Fig.1, which are, for most cases, very close to those of the conductance peak of the sensor as shown in Fig. 2 ( $f_{Gmax}$  and  $G_{max}$ ). However, this point of the admittance response of the sensor is not univocally determined at a specific phase condition,  $\Phi(f_{Gmax})$ , that depends on both the total motional resistance  $R_m$  and the total parallel capacitance  $C_0^*=C_0+C_p$  through Eq. (1). Therefore, a different strategy must be designed to continuously track this characteristic point.

$$\Phi(f_{G_{\max}}) = \arctan[2\pi f_{G_{\max}} R_m C_0^*] \quad (1)$$

Figure 3 shows, qualitatively, the typical locus of the admittance of a quartz sensor under different loads. As it can be noticed, the high admittance zero-phase frequency,  $f_r$ , gives a good approximation of the maximum conductance frequency for low acoustic loads; however, when the acoustic load and/or the parallel capacitance increase the zero-phase frequency can be no longer considered as the maximum conductance frequency. On the contrary, if the parallel capacitance is compensated the zero-phase is the appropriate tracking condition for the maximum conductance monitoring.

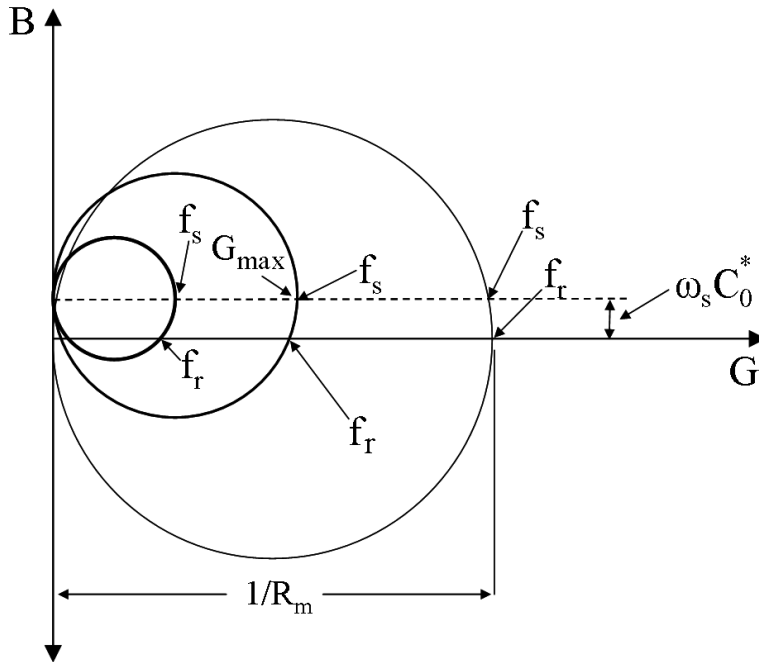


Fig. 3: Qualitative description of the change in the sensor admittance due to different loads using the admittance locus diagram.

### III. SYSTEM DESCRIPTION

The concept behind the design is the same introduced elsewhere<sup>46</sup>, that is, by simultaneous exciting the quartz crystal at two frequencies, and assuming linear behavior of the resonator at the driving level of the signals, the compensation of the parallel capacitance,  $C_0^*$ , is automatically and simultaneously made with the locking of the series resonant frequency,  $f_s$ , of the sensor.

The new approach, shown in Fig.4, was partially introduced elsewhere<sup>44</sup> for manual capacitance compensation. In the present case two phase locked loops (PLL) are used for both frequency tracking and parallel capacitance compensation. The PLL in charge of the sensor series resonant frequency tracking is based on a phase-frequency detector (PFD) instead of a multiplier as is the case elsewhere<sup>46</sup>. In this configuration the non-inverter amplifier in charge of driving the sensor has, ideally, the same response at different frequencies inside its bandwidth of linear operation, since only a resistance,  $R_v$ , is included in the feedback loop unlike the system described elsewhere<sup>46</sup>, where a resistance in parallel with a capacitance is proposed to obtain a  $90^\circ$  phase-shift of the high frequency component of the composed driving signal, necessary for a proper operation of the multiplier as a phase detector (Fig. 3 elsewhere<sup>46</sup>). Therefore, an easier and, in principle, more accurate calibration of the PLL can be performed in this new configuration by following the procedure introduced elsewhere<sup>44</sup>.

A different approach is also followed in Fig.4 for the parallel capacitance compensation, where an auxiliary high frequency signal is used to perform the capacitance compensation. The frequency of this signal is selected around four times the fundamental resonant frequency of the sensor where only capacitive behaviour of the crystal resonator is expected; only very small differences (less than 1% for AT-cut quartz resonator<sup>63</sup>) exist between the low frequency and

high frequency capacitances of the sensor. In this new approach the parallel compensation is provided by a phase sensitive circuit similar to the one used for the frequency tracking, and the calibration of this loop can be performed easily and accurately in a similar way.

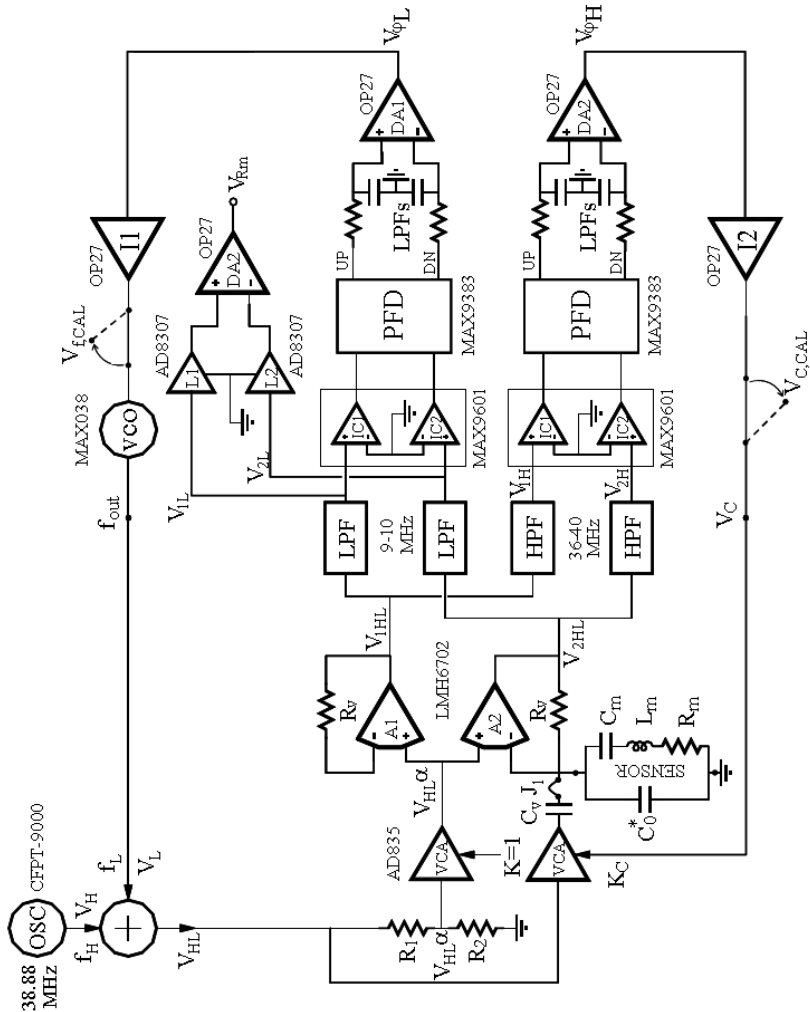


Fig. 4: Schematic circuit of the ACC system proposed.

The magnitudes governing the operation of the system are the phase-shifts between the signals  $V_{1HL}$  and  $V_{2HL}$  at the two frequencies,  $f_H$  and  $f_L$ , corresponding in this case to the signal of fixed frequency equal to 4-times the fundamental resonant frequency of the sensor and to the signal which sweeps the frequency around the series resonant frequency of the sensor, respectively. The phase-shift at the lower frequencies around the series resonant frequency of the sensor controls the PLL in charge of the frequency tracking, while the phase-shift at the auxiliary higher frequency controls the PLL in charge of the parallel capacitance compensation. Therefore, the equation governing the control of the system is:

$$V_{2HL} = \left(1 + R_v Y_m + j\omega R_v (C_0^* - C_C)\right) V_{1HL} \quad (2)$$

where  $V_{1HL} = V_{HL} \alpha$ ;  $C_C = [V_C / \alpha - 1] C_v$ ;  $\alpha = R_1 / (R_1 + R_2)$ ; and  $Y_m = [j\omega L_m + R_m + 1/j\omega C_m]^{-1}$ .

The subindex *HL* in the previous equations means that the voltage waveform considered is the sum of the two sinusoidal signals  $V_H$ , with fixed frequency  $f_H$  generated by the auxiliary oscillator whose frequency is around four times the fundamental resonant frequency of the sensor, and  $V_L$  with frequency  $f_L$  generated by the voltage controlled oscillator (VCO) around the series resonant frequency of the sensor. The high and low frequency components of  $V_1$  and  $V_2$  are separated, before being connected to the phase-frequency detectors (PFD), by appropriate filtering.

At the auxiliary frequency,  $f_H$ , where only capacitive behaviour of the sensor is expected, Eq. (2) is reduced to:

$$V_{2H} = \left(1 + j\omega R_v (C_0^* - C_C)\right) V_{1H} \quad (3)$$

and the phase shift between the signals  $V_{2H}$  and  $V_{1H}$  is given by:

$$\Phi(V_{2H}, V_{1H}) = \arctan[2\pi f_H R_v C_r] \quad (4)$$

where  $C_r = C_0^* - C_C$  is the residual uncompensated parallel capacitance.

As it can be noticed when  $C_r = 0$  the phase shift is zero and the differential amplifier DA2 gives zero voltage at its output that makes the integrator I2 to maintain a continuously stable  $dc$ -voltage at its output. This is the only stable condition for the loop out of saturation. In a different condition,  $C_r \neq 0$ , the amplifier DA2 gives a signal which is integrated by the integrator I2 until a new stable condition is reached for  $C_r = 0$ . The output voltage  $V_C$  of the integrator I2 can be used to monitor the changes in the parallel capacitance of the sensor and also for a continuous monitoring of its magnitude.

The sensitivity of the capacitance compensation is limited by the sensitivity of the phase detector. Assuming a residual error of the phase detector of  $0.1^\circ$ , for the frequency  $f_H$  around 40 MHz and  $R_v = 237\Omega$ , the uncompensated residual capacitance obtained by solving  $C_r$  from Eq. (4) is near 30fF, which is enough for most cases.

At the frequency  $f_L$ , and assuming that the parallel capacitance has been compensated ( $C_r = 0$ ), Eq. (2) is reduced to:

$$V_{2L} = (1 + R_v G_m + jR_v B_m) V_{1L} \quad (5)$$

where  $G_m = R_m / (R_m^2 + X_m^2)$  ;  $B_m = -X_m / (R_m^2 + X_m^2)$  and  $X_m = \omega L_m - 1/\omega C_m$

As it can be noticed from Eq. (5) signals  $V_{2L}$  and  $V_{1L}$  will be in phase when  $X_m$  is null and this only happens at MSRF,  $f_s = (2\pi L_m C_m)^{-1/2}$ . At this frequency the differential amplifier DA1 gives a zero voltage at its output; this makes the integrator I1 to maintain a continuously stable  $dc$ -voltage at its

output. This is the only stable condition for the loop out of saturation. If the series resonant frequency changes, a phase shift between the signals will arise at the locked frequency; a signal different from zero will appear at the output of the amplifier DA1, which will be integrated by the integrator I1, until a new stable condition is reached for the locking frequency at the new frequency  $f_s$ . It can be noticed that the voltage at the input of the VCO can be used as a direct measurement of the shift in the series resonant frequency, in case the frequency range of the VCO is narrow enough to have good frequency/voltage sensitivity. A narrow bandwidth of the VCO can reduce the dynamic range of the PLL, however this can be avoided with the system described elsewhere<sup>64,65</sup>.

At the series resonant frequency Eq. (5) is reduced to:

$$V_{2L} = \left[ 1 + \frac{R_v}{R_m} \right] V_{1L} \quad (6)$$

and by measuring the voltage levels  $V_{2L}$  and  $V_{1L}$  the magnitude of the motional resistance  $R_m$  is obtained as explained elsewhere<sup>44</sup>.

In the circuit in Fig. 4 the voltage controlled amplifier (VCA) connected to the output of the resistive divider formed by  $R_1$  and  $R_2$ , is only included for symmetry.

## IV. MATERIALS AND METHOD

### A. Circuit implementation

The circuit was made following recommendations applicable to high frequency layout design<sup>66,67</sup>, and implemented in four-layer surface-mount technology by using the integrated circuits indicated in the block diagram of Fig. 4 with the following “key” component values:  $R_v = 237 \text{ } \Omega$ ,  $C_v = 18 \text{ pF}$ ,

$1/\alpha=3$  and  $V_C$  designed to cover values ranged from  $1/3$  and  $1\text{ V}$ , which permits a capacitance compensation ranged between  $0$  and  $2C_p$  according to Eq. (2). Therefore a maximum parallel capacitance of  $36\text{pF}$  is possible to compensate for the selected value of  $C_p$ .

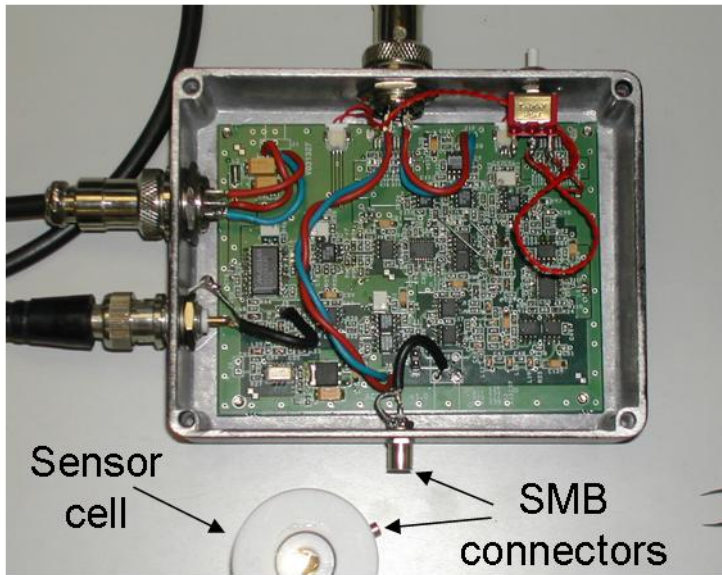


Fig. 5. Final circuit implementation of the system proposed in Fig. 4.

Filters for separating the high and low frequency components of  $V_{1HL}$  and  $V_{2HL}$  were implemented with seven-pole high-pass and low-pass filters based on Chebyshev configuration with  $0.5\text{ dB}$  ripple in the pass bandwidth. Attenuation higher than  $80\text{dB}$  was obtained between the components. Special care was taken in the board design and in the selection of the filter components in order to obtain the best symmetric configuration. The residual differences were compensated in the calibration steps explained in the next section. High frequency comparators based on PECL (positive emitter-coupled logic) technology (MAX9601) were used at the input of the PECL phase detectors (MAX9383). These ultra high speed comparators present a very low

propagation delay (500 ps) with very low dispersion ( $<30$  ps), which is important in this application for reducing the error in the phase comparison. However, they need a very high slew rate signal at the inputs. For that it was necessary to include additional comparators (not shown in the figure) after the low pass filters (LPFs) in Fig. 4 to increase the slew rate of the low frequency component (10 MHz) at the appropriate value. 38.88 MHz auxiliary frequency,  $f_H$ , for parallel capacitance compensation was selected and implemented with the CFPT-9000 oscillator from C-MAC<sup>®</sup>. This frequency is appropriate for 9 and 10 MHz quartz crystal resonators. The final circuit implementation is shown in Fig. 5.

## B. Calibration

After the implementation, the system was calibrated according to the following procedure. The automatic capacitance compensation loop (ACC loop) must be calibrated before the automatic frequency tracking loop (AFT loop):

### *1. Steps for calibration of the ACC loop.*

(a) The sensor is removed from the system and the loop is opened by taking the appropriate jumper (J1) off (Fig. 4). Under these conditions the operational amplifiers (OPAs) A1 and A2 act as followers and the phases of the signals  $V_{1HL}$  and  $V_{2HL}$  are expected to be equal assuming equal behaviour of the OPAs. If OPAs A1 and A2 have any different response, the differential configuration described and this calibration procedure tends to compensate it.

(b) Additionally, any possible feedback voltage is avoided by disconnecting the integrator output I2 and fixing the voltage  $V_C$  at a constant value ( $V_{C,CAL}$ ). In this situation, variable resistances included in the differential amplifier DA2 and/or in the integrator I2 allow the calibration of the system by assuring a stable *dc*-voltage at the integrator I2 output. Because the gain of the

integrator is infinite for a continuous  $dc$ -signal, it is almost impossible to maintain the integrator output voltage completely stable. For the same reason, a quasi-stable non-saturated  $dc$ -voltage at the integrator output assures a minimum phase error. Another possible procedure can be followed by the method 2 described elsewhere<sup>44</sup>.

### ***2. Steps for calibration of the AFT loop.***

(a) Once the capacitance compensation loop is calibrated, any parallel capacitance which appears between the terminals of the sensor connector will be compensated by the ACC loop. Therefore if any adaptor or cable is going to be used as interface to connect the sensor at the sensor terminals, it should be introduced before the calibration of the AFT loop. In this way the parallel capacitance introduced by the adaptor and/or the cable will be compensated by the ACC loop, and the OPAs A1 and A2 will act as followers, making the phases of the signals  $V_{1HL}$  and  $V_{2HL}$  to be equal again, like in step (a) in the previous calibration. Under these conditions, the calibration of the AFT loop has to be performed.

(b) To avoid any possible voltage feedback during the calibration of the AFT loop, the integrator output I1 is opened and the input of the VCO connected to a reference voltage ( $V_{f,CAL}$ ); this voltage will be appropriate to provide an output frequency around 9 or 10 MHz, depending on the resonance frequency of the sensor to be used. Under these conditions, variable resistances included in the differential amplifier DA1 and/or in the integrator I1 allow the calibration of the system by assuring a stable  $dc$ -voltage at the integrator I1 output. As mentioned above, a quasi-stable non-saturated  $dc$ -voltage at the integrator output assures a minimum phase error. Another possible procedure can be followed by the method 2 described elsewhere<sup>44</sup>

### C. System characterization

After the previous calibration, preliminary characterizations of the resistance monitoring and of the parallel capacitance compensation were performed. To make easier the preliminary characterizations and the experiments to validate the system operation presented below, an adapter was made which allowed changing the testing resistances and capacitances in an easy way. A small board was designed according to the drawing depicted in Fig. 6; the male SMB connector allows the connection of the adapter to the sensors female connector in the circuit (Fig. 5), and the female connector is used for the connexion of the sensor. A small connector included in parallel allows replacing the surface-mount testing resistances and capacitors to perform the preliminary characterizations and the subsequent validation experiments.

The resistance characterization, simulating the motional resistance, was performed in the same way as in the manual compensation system described elsewhere<sup>44</sup> and it will be not repeated here.

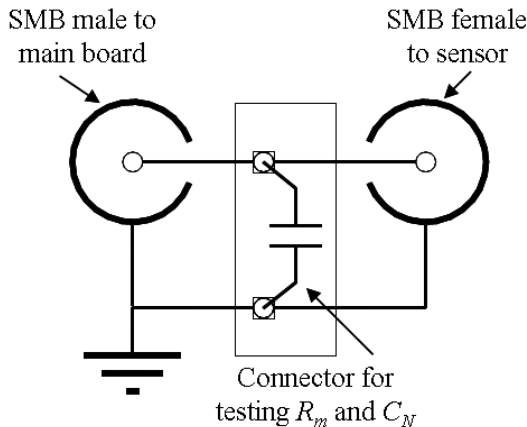


Fig. 6. Layout of the interface testing board.



Fig. 7. Sensor-cell for experiments with liquids.

The characterization of the capacitance compensation was performed in a similar way as in the case of the resistance monitoring. A set of surface-mount capacitors, whose nominal value is included in the first column of Table I, were used and connected to the sensor terminals of the system through the adapter, as indicated in Fig. 6. The true value of the capacitance was measured with an impedance analyzer (HP 4291A) which provided the data in the second column. The capacitance of the adapter alone was also measured since it is added to the real capacitance of the capacitors.

The voltage  $V_C$  can be used to monitor the parallel capacitance compensation according to Eq. (2):

$$C_C = C_v \left( \frac{V_C}{\alpha} - 1 \right) \quad (7)$$

The voltages corresponding to the different capacitors (third column in Table I) were measured with a voltmeter (HP 34401A) and introduced in Eq. (7) for each monitored value of capacitance. Values for  $C_v$  and  $1/\alpha$  were obtained which minimize the following expression:

$$\sum_{i=1}^N \left( \frac{C_{Ai} - C_{Ci}}{C_{Ai}} \cdot 100 \right)^2 \quad (8)$$

where  $C_{Ai}$  are the values measured with the impedance analyzer and  $C_{Ci}$  are the corresponding values monitored by the ACC system and calculated according to Eq. (7). The values obtained for  $C_v$  and  $1/\alpha$  according to the previous procedure were used in Eq. (7) to monitor the parallel capacitance compensation. Results will be shown and discussed below.

**Table I**

Characterization of the parallel capacitance compensation

$C_N$ (pF)	$C_A$ (pF)	$V_C$ (mV)	$C_C$ (pF)
Adapt.	3.66	400	3.68
1	4.66	417	4.65
5.6	9.24	504	9.23
6.8	10.2	523	10.2
11.2	14.7	605	14.6
15	18.4	677	18.5
18	20.6	720	20.7

#### D. Validation of the parallel capacitance compensation in liquids

After the preliminary characterization, a set of measurements of the sensor one-face in contact with liquids was performed with sensors of 9 and 10MHz nominal resonance frequency in order to validate the operation principle of the system. Bidistilled water, propylenglycol 99% and glycerol 99% were the liquids used. For each liquid and sensor, several measurements with different capacitors connected in parallel by using the adapter in Fig. 6 were made. In order to isolate one face of the sensor from the liquid a home-made cell was designed (Fig. 7). The MSRFs monitored by the system, with and without capacitance compensation, were recorded by a frequency meter (HP 53181A) and compared with the corresponding maximum conductance frequencies obtained from the impedance analyzer. The ACC loop was opened in the system to perform the measurements without capacitance compensation. The motional resistance and the compensated parallel capacitance values monitored by the system were also compared with the reciprocal of maximum conductance and parallel capacitance values of the sensor measured with the impedance analyzer. Measurements of the sensors in the cell but without liquid loading were also made for reference.

### V. RESULTS AND DISCUSSION

#### A. System Characterization

In the preliminary resistance characterization, relative errors smaller than 1.5% in the range of resistances used from 100 to 4700  $\Omega$  were found between the measurements obtained by the proposed system and those obtained from the impedance analyzer.

In the characterization of the capacitance compensation, values for  $C_p = 17.65$  pF and  $1/\alpha = 3.022$  were obtained which minimized the expression in Eq. (8). As it can be noticed the obtained values for  $C_p$  and  $1/\alpha$  are in good

agreement with the nominal values used for the implementation of the circuit ( $C_p = 18$  pF,  $1/\alpha = 3$ ). The corresponding monitored values of capacitance compensation  $C_G$  were obtained from Eq. (7) with the obtained values for  $C_p$  and  $1/\alpha$ ; the results are shown in the fourth column of Table I. It can be noticed that errors smaller than 1% are found in the range of capacitances tested.

### **B. Validation of the parallel capacitance compensation in liquids**

Results of the experiments performed in bidistilled water are presented in Figs. 8 and 9. Figure 8 shows the results corresponding to the frequency monitoring for 9 MHz (a-panel) and 10 MHz (b-panel) sensors respectively. The results of the resistances (Fig.9a) and capacitances (Fig. 9b) monitored with the system for the 10MHz sensor show a good agreement with the corresponding ones measured with impedance analyzer.

For an effective operation of the ACC system, no changes in the frequency monitoring would be expected when increasing the values of the capacitance in parallel with the sensor, because the system would be continuously locking the MSRF of the sensor which does not depend on the parallel capacitance. The same happens with the maximum conductance frequency measured by the impedance analyzer. On the contrary, a change in the parallel capacitance can produce a change in the oscillating frequency of an oscillator working at the zero-phase condition of the sensor; this is the case of the proposed system when the ACC loop is disconnected. In connection with this aspect, it is important to mention that changes in the oscillating frequency of an oscillator can occur, even for non-heavy loads, when changes in the parallel capacitance occur during the experiment.

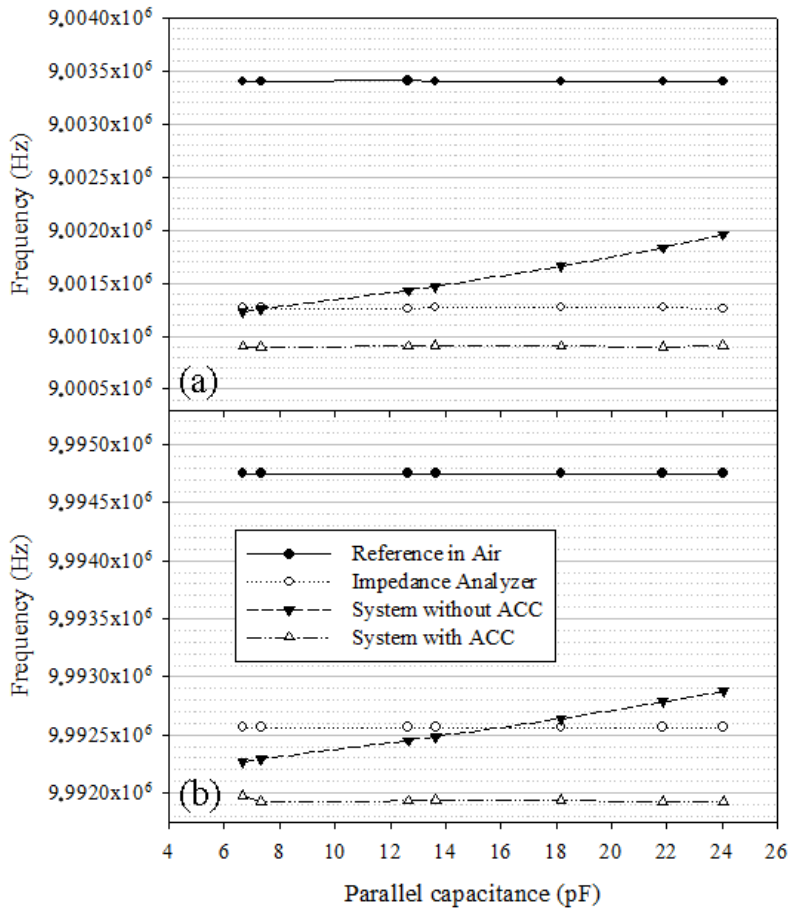


Fig. 8. Experimental results of the frequencies obtained from the impedance analyzer and from de ACC system, with and without ACC, in water loading conditions, for different parallel capacitances connected to the sensor. The frequency measured with the impedance analyzer in air loading conditions is included as reference. a) 9 MHz sensor and b) 10 MHz sensor

Results in Fig. 8 agree with the mentioned behaviour. The frequency monitoring by the system under ACC conditions does not significantly change when increasing the capacitances in parallel with the sensor. The same happens

with the maximum conductance frequency provided by the impedance analyzer. However, a frequency increase is observed in the frequency monitored by the system when the ACC loop is disconnected. This effect agrees with the operation principle of the system. Effectively, when the ACC loop is disconnected no capacitance compensation is performed and Eq. (5) has to be rewritten as follows:

$$V_{2L} = (1 + R_v G_m + jR_v(\omega C_r + B_m))V_{1L} \quad (9)$$

The AFT loop performs a continuous locking at the frequency of the sensor which makes the phases of low frequency components at points  $V_1$  and  $V_2$  equal. According to Eq. (9) this happens at the frequency  $f_L$  which complies with the following equation:

$$\omega_L C_r + B_m = 0 \quad (10)$$

An approximate expression for  $B_m$  around the series resonance frequency can be obtained as follows (see appendix):

$$B_m \approx -\frac{2\Delta f_{LS} Q_S}{f_S R_m} \quad (11)$$

where  $\Delta f_{LS} = f_L - f_S$  and  $Q_S$  is the quality factor of the sensor around the MSRF.

From the former expression and according to Eq. (10), an increase of the residual uncompensated parallel capacitance  $C_r$  is compensated by the system, when the ACC loop is not connected, with an increase in  $f_L$  relative to  $f_S$ ; in other words the system increases the frequency making the sensor to operate under a slightly inductive behaviour.

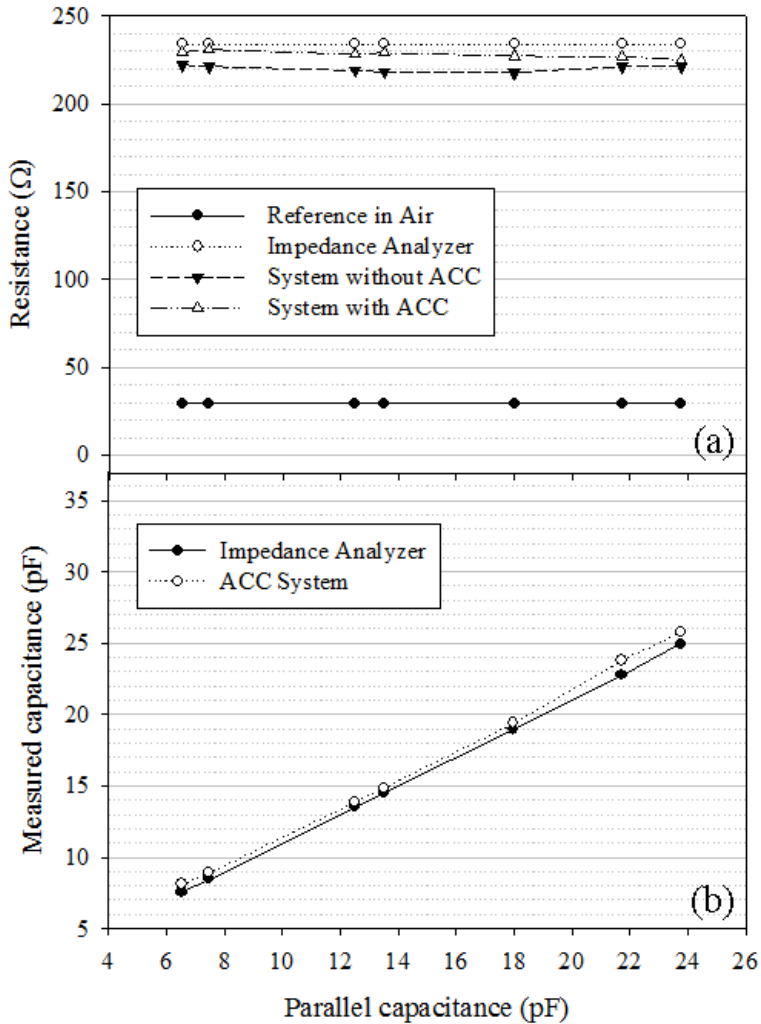


Fig. 9. Experimental results of the motional resistances and parallel capacitances measured from the impedance analyzer and from de ACC system, with and without ACC, in water loading conditions, for different parallel capacitances connected to the sensor. The motional resistance in air loading conditions is included as reference. a) 9 MHz sensor and b) 10 MHz sensor.

On the other hand, Fig. 8 also shows that a constant frequency shift exists between the maximum conductance frequency obtained from the

impedance analyzer  $f_A$  ( $f_A = f_S$ ) and the frequency locked by the system with ACC,  $f_L$ . If the correct operation of the ACC loop is assumed, this deviation can not be explained in terms of capacitance compensation. Effectively, the AFT loop was calibrated with the OPAs A1 and A2 acting as followers; however, when the sensor is operating in contact with water the motional resistance of the sensor increases the gain of the non-inverter amplifier A2 ( $1 + R_v/R_m$ ) around 2 (see in Fig. 9a values for  $R_m$ ), whereas A1 maintains its operation as a follower. The different gain of the amplifiers induces a different phase response and the signal  $V_{2L}$  suffers a delay in relation to the signal  $V_{1L}$ <sup>68</sup>. This delay produces a negative phase-shift that the system compensates by decreasing the locking frequency in relation to the MSRF,  $f_S = f_A$ . Effectively, under capacitance compensation conditions  $C_r \approx 0$  and Eqs. (9) and (11) can be combined to obtain the following approximate expression for the phase shift,  $\varphi$ , between  $V_{2L}$  and  $V_{1L}$ :

$$\tan \varphi \approx -\frac{2\Delta f_{LS} Q_S \left( \frac{R_v}{R_v + R_m} \right)}{f_S} \quad (12)$$

where it has been assumed that  $G_m \approx 1/R_m$  around series resonance.

According to Eq. (12) a negative value of  $\Delta f_{LS}$  could provide the necessary positive phase-shift to compensate the negative phase-shift due to the different gain of the amplifiers A1 and A2. In other words, the system decreases the locking frequency making the sensor to operate in a slightly capacitive behaviour; this leads the signal  $V_2$  the exact amount to compensate the previous delay.

Equation (12) allows calculating the approximate phase-shift compensated. For water conditions and 10MHz sensor (Figures 8b and 9a)  $R_v \approx R_m$ , the frequency shift necessary to compensate the phase delay is  $\Delta f_{LS} \approx -$

500 Hz from Fig. 8a, and a quality factor  $Q_S \approx L_m \omega / R_m = 2048$  was obtained from the value of  $L_m$  in the unperturbed state ( $L_m \approx 7.5\text{mH}$ ) and the motional resistance in water ( $R_m \approx 230 \Omega$  from Fig. 9a). With these data the negative phase-shift compensated by the system, obtained by Eq. (12) (changing the sign) is  $\approx -5.85^\circ$ . This result is in agreement with the data given by the manufacturer<sup>68</sup> and with the results in Fig. 8a for 9 MHz sensor. Effectively, for 9 MHz sensor the frequency shift is reduced to 350 Hz indicating the more ideal behaviour of the amplifiers as the operating frequency decreases.

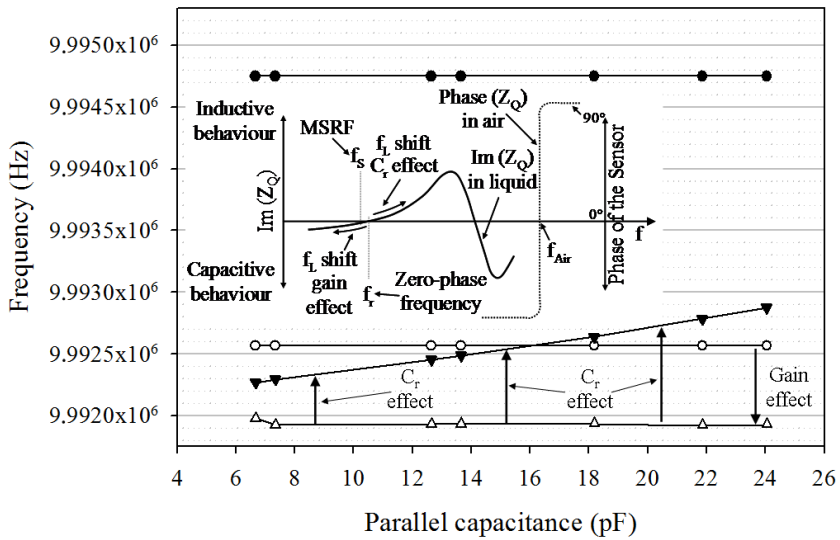


Fig 10: Graphical qualitative explanation of the deviations of the frequencies locked by the ACC system, with and without ACC, in relation to the MSRF measured with the impedance analyzer.

Figure 10 introduces a qualitative explanation of the different effects explained before: a) the frequency shift due to the compensation of the residual capacitance  $C_r$  when the ACC system is not connected (“ $C_r$  effect”), and b) the frequency shift of the locking frequency of the system due to the different gain

of the amplifiers (“gain effect”). In the experiment, both effects are combined in the results obtained with the system operating without ACC, while only the “gain effect” appears in the system operating with ACC; this is indicated in Fig. 10 using Fig. 8b as reference.

According to the previous explanation, the gain effect should diminish as the motional resistance increases, since the gain of A2 tends to 1 for increasing values of  $R_m$ . This was corroborated with experiments made with high-viscosity liquids.

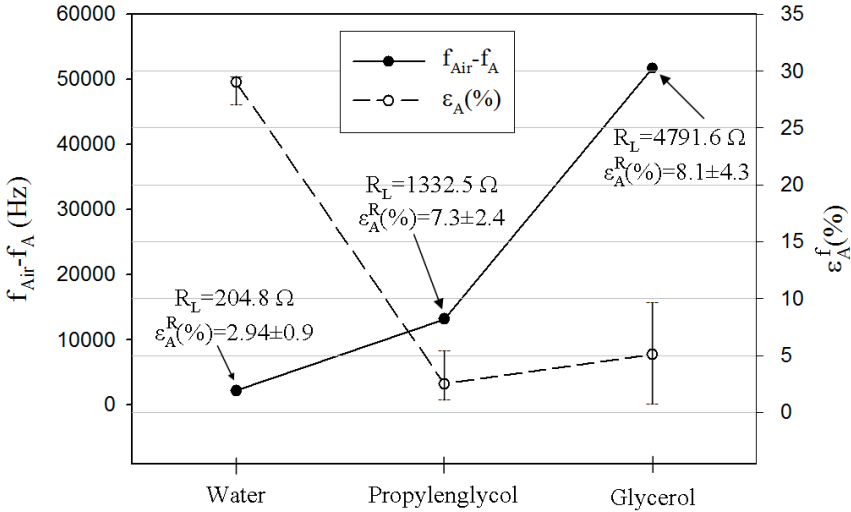


Fig. 11: Experimental results of the frequencies and resistances obtained from the impedance analyzer and from de ACC system for different liquids with a 10 MHz AT-cut QCR sensor.

Figure 11, concentrates the relevant results obtained with water, propylenglycol and glycerol (99% purity) for a 10MHz sensor. Measurements with propylenglycol and glycerol could not be performed without ACC because no locking condition at sensor zero-phase was found under these loading

conditions. In Fig. 11  $f_{Air}-f_A$  is the frequency shift between the frequency of the sensor in air and in liquid measured with the impedance analyzer.  $\mathcal{E}_A^f$  (%) for each liquid, is the average of the relative errors obtained between the frequencies in liquid obtained from the impedance analyzer ( $f_A=f_S$ ) and from the system ( $f_L$ ), for each parallel capacitance added to the sensor. Deviations ( $f_A-f_L$ ) were obtained for each liquid and for each added capacitance  $C_{Pi}$  (the same added capacitances as in the experiments shown in Fig. 8 were used); the average relative error in relation to the total frequency shift ( $f_{Air}-f_A$ ) was calculated according to the expression in Eq. (13). The dispersion of the errors is represented as well in Fig.11.

$$\mathcal{E}_A^f (\%) = \frac{1}{N} \sum_{i=1}^N \left( \frac{|f_A - f_{Li}|}{f_{Air} - f_A} \right) \times 100 \quad (13)$$

As it can be noticed the relative errors are much bigger in water than in the high-viscosity liquids. Much bigger errors would have been expected for high-viscosity liquids than for water if the parallel capacitance compensation had not been effective. With the relative frequency errors shown in Fig. 11 it is possible to demonstrate that very good parallel capacitance compensation had to be necessarily performed by the system. Effectively, as the motional resistance increases a very small residual uncompensated capacitance can produce big frequency deviations between the locking frequency and the MSRF, ( $f_A-f_L$ ) in Eq. (13). As explained before a phase shift produced by a residual capacitance has to be compensated with a shift in the locking frequency relative to the MSRF according to Eq. (9). Therefore, in the other way around it is possible to obtain the residual capacitance for a given frequency shift between the locking frequency and the MSRF ( $f_A-f_L$ ). By combining Eqs. (9) and (10), the residual uncompensated capacitance can be approximately obtained as follows:

$$C_r \approx \frac{2\Delta f_{LS} Q_S}{2\pi f_A^2 R_m} \quad (14)$$

For instance, in the case of glycerol the motional resistance was measured and found to be  $R_m = 4976 \Omega$ , the corresponding quality factor was  $Q_S \approx 94$  and the maximum frequency error was around 5 kHz ( $\varepsilon_A^f (\%) = 10\%$ ). For these values a maximum residual capacitance of  $\approx 0.3$  pF is obtained from Eq. (14). This very low residual capacitance is coherent with the error dispersion obtained for high-viscosity liquids, since any non-ideal response of the capacitors used to simulate the added parallel capacitance could provide unexpected frequency shifts. This non-ideal behaviour is only made evident as the motional resistance increases as can be noticed with the low dispersion of the frequency errors under water conditions. This confirms that the system performs good capacitance compensation and that the frequency deviations for water conditions are due to the “gain effect”.

In Fig. 11 the contribution of each liquid to the motional resistance ( $R_L = R_m - R_I$ ) measured with the impedance analyzer is included as well together with the average relative error obtained with the ACC system and its corresponding dispersion. The average error in the resistance,  $\varepsilon_A^R (\%)$ , was obtained through Eq. (15), in a similar way as in the case of Eq. (13):

$$\varepsilon_A^R (\%) = \frac{1}{N} \sum_{i=1}^N \left( \frac{|R_m^A - R_{mi}^{ACC}|}{R_m^A - R_{Air}^A} \right) \times 100 \quad (15)$$

where  $R_m^A$  is the motional resistance obtained from the impedance analyzer and  $R_{mi}^{ACC}$  is the one monitored by the ACC system for each parallel

---

capacitance added to the sensor. The errors are calculated in relation to the motional resistance shift relative to air  $R_{air}^A$ .

The relative errors increase as the motional resistance increases. This is due to the reduction in the resolution of the system as the motional resistance increases. The gain of the amplifier A2 tends to be 1 as the motional resistance increases and the ability of the system to discriminate resistance changes at very heavy loads diminishes. In any way, the error is maintained around 10% for very high viscosity liquids, such as glycerol 99%.

The average relative error obtained by the ACC system in the measuring of the parallel capacitances, taking the values measured by the impedance analyzer as reference, is smaller than 4% in all the range with dispersion smaller than 2.5%. This error, although small in all the cases, must be carefully considered since it is very difficult to assure that the parallel capacitances to be compensated are the same when the sample setup to be tested (cell + sensor + adapter + parallel capacitors) is moved from the system to the analyzer and viceversa. Inevitable experimental errors could change the parallel capacitance in the order of tenths of picofarad.

The frequency deviations due to the gain effect for low-viscosity liquids, like water, can be avoided by decreasing the value of the resistance  $R_v$ , or by designing a new strategy for an automatic gain control of the input stage of the system formed by the amplifiers A1 and A2. In the next section a tentative approach is described for this purpose.

## VI. TENTATIVE APPROACH FOR FUTURE DEVELOPMENTS

Figure 12 shows a tentative approach for an ACC system designed to control the gain of the amplifiers of the input stage to avoid the inconveniences described in the previous section.

The loop in charge of the frequency locking has the same design previously described. In this approach the ACC is performed at low frequencies following the system described elsewhere<sup>46</sup>; the reasons for making the ACC at low frequencies will be explained later on. Then the high frequency signals  $V_{1H}$  in this approach correspond to the frequencies near the series resonant frequency, while the low frequency component  $V_L$  corresponds to the auxiliary low frequency signal used for parallel capacitance compensation (50 kHz).

The proposed configuration includes a new VCA with a resistance  $R_3$  connected to the amplifier A1, which is converted into a non-inverter amplifier. A new loop is included to control the gain,  $K_R$ , of the VCA. The equation governing the new loop, assuming that the signals  $V_{1H}$  and  $V_{2H}$  are in phase and that the parallel capacitance is compensated, is the following:

$$V_{2H} - V_{1H} = V_H \alpha R_v \left[ \frac{1}{R_m} - \frac{1}{R_C} \right] \quad (16)$$

where  $R_C = R_3 / (1 - K_R)$ .

The integrator I3 maintains a constant value output voltage for a zero voltage at its input. This condition, which is the only stable loop condition out of saturation, is only possible when the multiplier M2 provides zero voltage at its output. For signals  $V_H$  and  $V_{2H} - V_{1H}$  at the inputs of the multiplier M2, the output provides zero voltage only for  $R_C = R_m$ . Under this condition the voltages  $V_{2H}$  and  $V_{1H}$  will have the same amplitude at the locking frequencies and the amplifiers A1 and A2 will work with the same equivalent gain.



amplifiers A1 and A2 at the auxiliary high frequency signal, proposed in the first configuration, for parallel capacitance compensation. Effectively, the conversion of the amplifier A1 in a non-inverter amplifier, and the introduction of the resistance R3, makes this amplifier to work with gain different from 1 at the selected auxiliary frequencies used for capacitance compensation, while amplifier A2 is working as a follower at these frequencies, once the parallel capacitance is compensated. The very different responses of these amplifiers at high frequencies would make the accurate capacitance compensation difficult. This is avoided at low frequencies where small differences in the gains of the input stage amplifiers have not relevant effects in their phase response.

## APPENDIX

The motional admittance of the sensor can be written as follows:

$$Y_m = \frac{R_m}{R_m^2 + X_m^2} - j \frac{X_m}{R_m^2 + X_m^2} = G_m + jB_m \quad (17)$$

where  $X_m$  is given by:

$$X_m = L_m \omega_L - \frac{1}{C_m \omega_L} = \frac{1}{C_m \omega_L} \frac{\omega_L^2 - \omega_S^2}{\omega_S^2} \approx \frac{2\Delta f_{LS} Q_S R_m}{f_S} \quad (18)$$

where  $\omega_S = (L_m C_m)^{-1/2}$ ,  $Q_S = (\omega_S R_m C_m)^{-1}$  is the quality factor of the sensor under loading conditions,  $\Delta f_{LS} = f_L - f_S$  and it has been assumed that  $\omega_L \approx \omega_S$ .

From Eq. (18) it can be solved the following expression:

$$\left(\frac{X_m}{R_m}\right)^2 = \left(\frac{2\Delta f_r Q_R}{f_S}\right)^2 \ll 1 \quad (19)$$

which is true for most practical cases.

Therefore, the approximate expressions for  $B_m$  and  $G_m$  are given by:

$$B_m = -\frac{X_m/R_m^2}{1+(X_m/R_m)^2} \approx \frac{X_m}{R_m^2} \approx \frac{2\Delta f_{LS} Q_S}{f_S R_m} \quad (20a)$$

$$G_m = \frac{1}{R_m} \cdot \frac{1}{1+(X_m/R_m)^2} \approx \frac{1}{R_m} \quad (20b)$$

### ACKNOWLEDGEMENTS

The authors are grateful to the Spanish Ministry of Science and Technology for financially supporting this research under contract reference: AGL2006-12147/ALI.

## REFERENCES

- <sup>1</sup> A.W. Czanderna and C. Lu, in *Applications of Piezoelectric Quartz Crystal Microbalances*, edited by C. Lu and A.W. Czanderna (Elsevier, Amsterdam, 1984), Vol. 7, p.1.
- <sup>2</sup> P.L. Konash and G.J. Bastiaans, *Analytical Chemistry* **52**, 1929 (1980)
- <sup>3</sup> K.K. Kanazawa and J.G. Gordon II, *Analytica Chimica Acta* **175**, 99 (1985)
- <sup>4</sup> C.E. Reed, K.K. Kanazawa and J.H. Kaufman, *Journal of Applied Physics* **68** (5), 1993 (1990)
- <sup>5</sup> S. Kurosawa and E. Tawara, *Analytica Chimica Acta* **230** (1), 41 (1990)
- <sup>6</sup> R. Schumacher, *Angew. Chem. Int. Ed. In English* **29** (4), 329 (1990)
- <sup>7</sup> K.A. Davis and T.R. Leary, *Anal. Chem.* **61**, 1227 (1989)
- <sup>8</sup> Z.A. Shana and D.E. Radtke, *Analytica Chimica Acta* **231** (2), 317 (1990)
- <sup>9</sup> C. Behling, R. Lucklum, and P. Hauptmann, *Sensors and Actuators, A* **61**, 260 (1997)
- <sup>10</sup> C. Behling, R. Lucklum, and P. Hauptmann, *Meas. Sci. Technol.*, **9**, 1886 (1998)
- <sup>11</sup> R. Lucklum, C. Behling, and P. Hauptmann, *Anal. Chem.*, **71**, 2488 (1999)
- <sup>12</sup> Y. Jiménez, M. Otero, A. Arnau, "QCM Data Analysis and Interpretation", in *Piezoelectric Transducer and Applications*, 2nd Ed., pp 331-398, A. Arnau Ed., Springer-Verlag Berlin Heidelberg (2008). In press.
- <sup>13</sup> S.J. Martin, V. E. Granstaff, G.C. Frye, *Anal. Chem.* **63**, 2272 (1991)
- <sup>14</sup> S.W. Lee, W.D. Hinsberg and K. Kanazawa, *Anal. Chem.* **74** (1), 125 (2002)
- <sup>15</sup> A. Arnau, Y. Jiménez and T. Sogorb, *J. Appl. Phys.* **88**, 4498 (2000)

- 
- <sup>16</sup> C. Gabrielli, H. Perrot, D. Rose, A. Rubin, M.C. Pham and B. Piro, *Review Scientific Instruments* **78** (7): 6 pages (2007)
- <sup>17</sup> A. Janshoff, H-J Galla and C. Steinem, *Angew. Chem. Int. Ed.* **39**, 4004 (2000)
- <sup>18</sup> MA. Cooper and VT. Singleton, *Journal of Molecular Recognition* **20** (3), 154 (2007)
- <sup>19</sup> TA. Camesano, YT. Liu and M. Datta, *Advances in Water Resources* **30** (6-7), 1470 (2007)
- <sup>20</sup> O. Lazcka, FJ. Del Campo and FX, Muñoz, *Biosensors & Bioelectronics* **22** (7), 1205 (2007)
- <sup>21</sup> TS. Hug, *Assay and Drug Development Technologies* **1** (3), 479 (2003)
- <sup>22</sup> FL. Dickert, P. Lieberzeit and O. Hayden, *Analytical and Bioanalytical Chemistry* **377** (3), 540 (2003)
- <sup>23</sup> KA. Marx, *Biomacromolecules* **4** (5), 1099 (2003)
- <sup>24</sup> KA. Fahrnich, M. Pravda and GG. Guilbault, *Analytical Letters* **35** (8), 1269 (2002)
- <sup>25</sup> J. Wegener, A Janshoff and C. Steinem, *Cell Biochemistry and Biophysics* **34** (1), 121 (2001)
- <sup>26</sup> CK. O'Sullivan and GG. Guilbault, *Biosensors & Bioelectronics* **14** (8-9), 663 (1999)
- <sup>27</sup> CK. O'Sullivan, R. Vaughan and GG. Guilbault, *Analytical Letters* **32** (12), 2353 (1999)
- <sup>28</sup> K.Bizet, C. Grabielli and H. Perrot, *Analisis EurJAC* **27**, 609 (1999)
- <sup>29</sup> R. Ni, XB. Zhang, W. Liu, GL. Shen and RQ. Yu, *Sensors and Actuators B* **88**, 198 (2003)

- <sup>30</sup> D. Johannsmann and K. Mathauer, *Physical Review B* **46** (12), 7808 (1992)
- <sup>31</sup> M. Yang and M. Thompson, *Langmuir* **9**, 802 (1993)
- <sup>32</sup> M. Yang and M. Thompson, *Analytica Chimica Acta* **282**, 505 (1993)
- <sup>33</sup> M. Noël and P.A. Topart, *Analytical Chemistry* **66** (4), 484 (1994)
- <sup>34</sup> A. Arnau, V. Ferrari, D. Soares, H. Perrot, "Interface Electronic Systems for AT-Cut QCM Sensors. A comprehensive review", in *Piezoelectric Transducers and Applications*, 2nd Ed., pp 117-186, A.Arnau Ed., Springer-Verlag Berlin Heidelberg, (2008). In press.
- <sup>35</sup> M. Schmid, E. Benes and R. Sedlaczek, *Meas. Sci. Technol.* **1**, 970 (1990)
- <sup>36</sup> J. Schröder, R. Borngläber, R. Lucklum and P. Hauptmann **72** (6), 2750 (2001)
- <sup>37</sup> J. Schröder, R. Borngläber, F. Eichelbaum and P. Hauptmann, *Sensors and Actuators A* **97-98**, 543 (2002)
- <sup>38</sup> J. Auge, k. Dierks, F. Eichelbaum and P. Hauptmann, *Sensors and Actuators B* **95**, 32 (2003)
- <sup>39</sup> S. Doerner, T. Schneider, J. Schröder and P. Hauptmann "Universal impedance spectrum analyzer for sensor applications" in *Proceedings of IEEE Sensors* **1**, pp. 596-594 (2003)
- <sup>40</sup> R. Schnitzer, C. Reiter, KC. Harms, E. Benes and M. Gröschl, *IEEE Sensors Journal* **6** (5), 1314 (2006)
- <sup>41</sup> Z. Tiean and L.H. Nie, *Journal of Electro-analytical Chemistry* **293** (1-2), 1 (1990)
- <sup>42</sup> C. Barnes, *Sensors and Actuators A-Physical* **29** (1), 59 (1991)
- <sup>43</sup> C. Barnes, *Sensors and Actuators A-Physical* **30** (3), 197 (1992)

- 
- <sup>44</sup> A. Arnau, T.Sogorb, Y. Jiménez, *Rev. Sci. Instrum.* **73** (7), 2724 (2002)
- <sup>45</sup> V. Ferrari, D. Marioli, and A. Taroni, *IEEE Trans. Instrum. Meas.* **50**, 1119 (2001)
- <sup>46</sup> V. Ferrari, D. Marioli, A. Taroni "ACC oscillator for in-liquid quartz crystal microbalance sensors" in *Proc. IEEE Sensors 2003*, vol 2, pp. 849-854 (2003)
- <sup>47</sup> C. Riesch and B. Jakoby, *IEEE Sens. J.* 7,464 (2007).
- <sup>48</sup> G. Hayward, *Analytica Chimica Acta* **264** (1), 23 (1992)
- <sup>49</sup> G. Hayward and G.Z. Chu, *Analytica Chimica Acta* **288** (3), 179 (1994)
- <sup>50</sup> F. Eichelbaum, R. Borngräber, J. Schröder, R. Lucklum, and P. Hauptmann, *Rev. Sci. Instrum.* **70**, 2537 (1999)
- <sup>51</sup> R. Borngräber, J. Schröder, R. Lucklum and P. Hauptmann, *IEEE Trans. Ultrason. Ferroelect. Freq. Contr.* **49** (9), 1254 (2002)
- <sup>52</sup> D. Soares, *Meas. Sci. Technol.* **4**, 549 (1993)
- <sup>53</sup> C. Fruböse, K. Doblhofer and D. Soares, *Ber. Bunsenges. Phys. Chem.* **97** (3), 475 (1993)
- <sup>54</sup> K.O. Wessendorf "The lever oscillator for use in high resistance resonator applications" in *Proceedings of the 1993 IEEE International Frequency Control Symposium*, pp. 711-717 (1993)
- <sup>55</sup> K.O. Wessendorf "Oscillator circuit for use with high loss quartz resonator sensors" US Patent 5416448 (1995)
- <sup>56</sup> K.O. Wessendorf "The active bridge oscillator" in *Proceeding of IEEE International Frequency Control Symposium*, pp. 361-369 (1998)
- <sup>57</sup> K.O. Wessendorf "The active-bridge oscillator for use with liquid loaded QCM sensors" in *Proceedings of IEEE International Frequency Control Symposium and PDA Exhibition*, pp. 400-407 (2001)

<sup>58</sup> E. Benes, M. Gröschl, W. Burger and M. Schmid, *Sensors and Actuators A* **48**, 1 (1995)

<sup>59</sup> E. Benes, M. Schmid, M. Gröschl, P. Berlinger, H. Nowotny and K.C. Harms "Solving the cable problem between crystal sensor and electronics by use of a balanced bridge oscillator circuit" in *Proceedings of the Joint Meeting of the European Frequency and Time Forum and the IEEE International Frequency Control Symposium*, Vol. 2, pp.1023-1026 (1999)

<sup>60</sup> D. Soares, W. Kautek, C. Fruböse and K. Doblhofer, *Ber. Bunsenges. Phys. Chem.* **98** (2), 219 (1994)

<sup>61</sup> M. Rodahl and B. Kasemo, *Rev. Sci. Instrum.* **67**, 3238 (1996)

<sup>62</sup> M. Rodahl and B. Kasemo, *Sensors and Actuators B* **37**, 111 (1996)

<sup>63</sup> R. Lucklum, D. Soares and K. Kanazawa, "Models for Resonant", in *Piezoelectric Transducers and Applications*, 2nd Ed., pp 63-96, A.Arnau Ed., Springer-Verlag Berlin Heidelberg, (2008). In press

<sup>64</sup> W.G. Cady, *Piezoelectricity. An introduction to the theory and applications of electromechanical phenomena in crystals.* Dover, New York, 1964.

<sup>65</sup> R. Torres, A. Arnau, H. Perrot, J. García. and C. Grabielli, *Electronics Letters* **42** (22), 1272 (2006)

<sup>66</sup> R.Torres, A.Arnau, H. Perrot, "Fast, Continuous and Accurate Frequency Shift Measurement in the AC Electrogravimetry Technique", *2007 European Freq. and Time Forum & IEEE Int'l Frequency Control Symposium* , Geneva, Switzerland May 29 - June 1, (2007).

<sup>67</sup> H. Johnson, "High-Speed Digital Design: A Handbook of Black Magic", Prentice Hall, (1993)

<sup>68</sup> M. Montrose , "Emc & the Printed Circuit Board: Design, Theory, & Layout Made Simple", Wiley-IEEE Press, (1998).

<sup>69</sup> LMH6702 Data Sheet, National Semiconductor, [www.national.com](http://www.national.com) (2005).



### **3.2 A different point of view on the sensitivity of quartz crystal microbalance sensors**

Antonio Arnau, Yeison Montagut, José V. García, Yolanda Jiménez

Measurement Science and Technology, Volume 20, Number 12, (2009)

This is an author-created, un-copyedited version of an article published in Measurement Science and Technology. IOP Publishing Ltd is not responsible for any errors or omissions in this version of the manuscript or any version derived from it.

The Version of Record is available online at <http://dx.doi.org/10.1088/0957-0233/20/12/124004>.

### Abstract

In this paper the sensitivity of a quartz crystal microbalance (QCM) sensor is analyzed and discussed in terms of the phase change versus the surface mass change, instead of the classical sensitivity in terms of the resonant frequency change derived from the well-know Sauerbrey equation. The detection sensitivity derived from the Sauerbrey equation is a theoretical detection capability in terms of the frequency change versus mass change, which increases with the square of frequency. However, when a specific application and measuring system are considered, the detection capability of the QCM sensor must be considered from a different point of view. A new equation is obtained,  $\Delta\varphi \cong -\Delta m_c / (m_q + m_L)$ , which quantifies the phase shift,  $\Delta\varphi$ , of a fixed frequency signal corresponding to the series resonant frequency of the sensor versus a change in the coating mass,  $\Delta m_c$ ;  $m_q = \eta_q \pi / 2 v_q$ , where  $\eta_q$  is the loss viscosity of the unperturbed sensor and  $v_q$  is the wave propagation speed in the quartz, is a parameter which only depends on physical parameters of the unperturbed resonator and fixes the maximum sensitivity of the sensor and  $m_L = \rho_L \delta_L / 2$ , where  $\rho_L$  and  $\delta_L$  are, respectively, the liquid density and the wave penetration depth of the wave in the liquid, is the equivalent surface mass density associated with the oscillatory movement of the surface of the sensor in contact with a fluid medium. This equation is an approximate equation around series resonant frequency of the sensor. The simulation results for 10, 50 and 150MHz resonance frequency QCM sensors probe its validity. A new electronic system is proposed for QCM biosensor applications based on the equation introduced.

## 1. Introduction

The use of the AT-cut quartz crystal resonator as the so-called quartz-crystal microbalance (QCM) sensor has been based on the well-know Sauerbrey equation<sup>i</sup>. The Sauerbrey equation establishes the fact that the decrease in the resonance frequency of the resonator is proportional to the increase in the surface mass density of the coating on the sensor surface. When a Newtonian semi-infinite liquid medium is in contact with the resonator surface, the Kanazawa equation provides the associated frequency shift due to the contacting fluid<sup>ii</sup>. For a QCM sensor with one face in contact with an “acoustically thin layer” contacting a semi-infinite fluid medium, Martin’s equation (equation (1)) can be applied<sup>iii</sup>, which combines both the mass effect of the coating (Sauerbrey effect) and the mass effect of the liquid (Kanazawa effect) on the frequency shift:

$$\Delta f = -\frac{2f_s^2}{Z_{cq}}(\rho_c h_c + \frac{1}{2}\rho_L \delta_L) \quad (1)$$

In equation (1), the first term in the brackets corresponds to the Sauerbrey effect and the second to the Kanazawa effect, where  $f_s$  is the sensor resonance frequency,  $Z_{cq}$  is the characteristic acoustic impedance of the quartz,  $\rho_c$  and  $h_c$  are the density and thickness of the coating, and  $\rho_L$  and  $\delta_L$  are the liquid density and the wave penetration depth of the acoustic wave in the liquid, respectively;  $\frac{1}{2}\rho_L \delta_L$  is, in fact, the equivalent surface mass density associated with the oscillatory movement of the surface of the sensor in contact with a fluid medium.

According to Eq. (1), for a certain surface mass density of the coating, the associated frequency shift increases directly proportional to the square of the resonant frequency. Consequently, it seems logic to think that the higher the

resonant frequency the higher the sensitivity. In fact the resonant frequency of the resonator has been always the main parameter for sensor characterization.

### 1.1. QCM Monitoring Systems

Effectively, in practice, all the techniques used for QCM sensor characterization have been used in the way to determine, among other relevant sensor parameters, the resonant frequency shift of the resonator<sup>iv,v</sup>: Network or impedance analysis are used to sweep the resonant frequency range of the resonator and determine the maximum conductance frequency<sup>vi,vii</sup>, which is almost equivalent to the motional series resonant frequency of the resonator-sensor; impulse excitation and decay method techniques are used to determine the series-resonant or the parallel-resonant frequency depending on the measuring set-up<sup>viii</sup>; oscillator techniques are used for a continuous monitoring of a frequency which corresponds to a specific phase shift of the sensor in the resonance bandwidth<sup>ix,x,xi,xii,xiii</sup>; this frequency can be used, in many applications, as reference of the resonant frequency of the resonator-sensor; and the lock-in techniques, which can be considered as sophisticated oscillators, are designed for a continuous monitoring of the motional series resonant frequency or the maximum conductance frequency of the resonator-sensor<sup>xiv,xv,xvi,xvii,xviii,xix</sup>.

The main reason to monitor the resonant frequency of the resonator-sensor is that a simple relationship exists between its variation and the physical parameters to be monitored in a real application: mass change and/or fluid properties (Eq. 1). In many applications, for example in QCM based biosensors which cover a great deal of process monitoring<sup>xx</sup>, the experimental frequency shifts obtained are usually small, in the order of tens of Hertz. Therefore, a big effort is taking place to improve the sensitivity of the resonator-sensor; in most approaches, it is trying to do by increasing the resonance frequency of the resonator, as Eq. (1) suggests. Now, the first question arises: is the resonant frequency the only parameter to be taken into account to improve the

sensitivity? The immediate answer is clear: no. The sensitivity will not be improved if the frequency stability is not improved as well. Now, the main question is: how to improve the frequency stability? Two aspects can be distinguished. The frequency stability depends, on one hand on the experimental set-up which must be designed to minimize the disturbances or interferences which can affect the resonant frequency of the resonator such as: temperature, vibrations, pressure changes due to the fluid pumps, etc.; and on the other hand on the ability of the characterization system for an accurate measuring of the parameter of interest, in this case the appropriate resonant frequency of the resonator-sensor. Assuming that the experimental set-up is maintained under maximum control, the frequency stability depends on the measuring system.

The different characterization methods mentioned can be classified in two types: 1) Those which passively interrogate the sensor which is maintained external to the measuring system, and 2) Those in which the sensor forms part of the characterization system. In the first group impedance or network analyzers and decay methods are included. Advantages of impedance analyzers are acknowledged and are mainly related to the fact that the resonator-sensor is almost characterized in isolation and no external circuitry influences the electrical behaviour of the sensor; additionally, electrical external influences can be excluded by calibration. The accuracy of decay methods is high provided that the accuracy in the data acquisition is high as well, both in phase and amplitude, which becomes very complicated for high resonant frequencies. Therefore, for high frequency resonators, more than 50MHz, only impedance analysis provides accurate results, but its high cost and large dimensions, prevent its use for sensor applications. Consequently, oscillators are taken as alternative for sensor resonant frequency monitoring; their low cost of the circuitry as well as the integration capability and continuous monitoring are some features which make the oscillators to be the most common alternative

for high resonant frequency QCM sensors. Therefore, it is very important to consider now the aspect of frequency stability in oscillators. Starting from this aspect a different point of view in the concept of sensitivity will appear. The new concept will be very useful in the understanding of the limitations of the QCM sensor sensitivity and the causes; it will provide as well a suitable basis on which to propose a measuring system for minimizing the instabilities and improving the sensitivity.

### 1.2. Stability in Oscillators

The problem of frequency stability in oscillators can be understood making use of the block schema shown in Fig.1a, where an active part (A) and a feedback network form a loop. The feedback network has been divided, for didactic purposes in two parts, one associated with the resonator sensor (X) and the other part which includes the rest (B). One of the conditions the loop has to comply with in order to oscillate is the so-called “*phase-loop condition*”. This condition establishes that the total phase shift of the signal in the loop must be zero; it is to say:  $\varphi_A + \varphi_B + \varphi_X = 0$ . This condition is achieved at certain frequency of the signal which is the oscillation frequency. However, the phase response of the different blocks is not continuously constant; it changes due to small changes in the values of the components of the block; these changes occur due to different causes such as: changes in the environmental conditions, aging or drift of the components, changes in the magnitudes of the signal, current or voltage, mainly in the active components, etc. A phase shift in one of the blocks must be compensated with a contrary phase shift of the same magnitude in another block. Normally the phase-shift is absorbed in the component which has the most sharp phase-frequency response in the loop, usually the resonator, by changing the oscillating frequency a small amount. This amount depends on the sharpness of the slope of the phase-frequency response of the resonator. This effect is shown in Fig.1b where a phase shift of

magnitude  $-\alpha$ , for example in the active block (A), is absorbed in the resonator by changing the oscillating frequency in the loop exactly the necessary amount to compensate that phase-shift. The shift in the oscillation frequency could be small ( $\Delta f_1$ ) or big ( $\Delta f_2$ ) depending on the sharpness of the slope of the phase-frequency response of the resonator,  $\varphi_X$  vs.  $f$ . These frequency changes occur continuously, mainly due to the continuous change of the small-signal parameters in the active components, giving place to a phase noise which is transferred into frequency instability. This instability is more pronounced the higher the frequency.

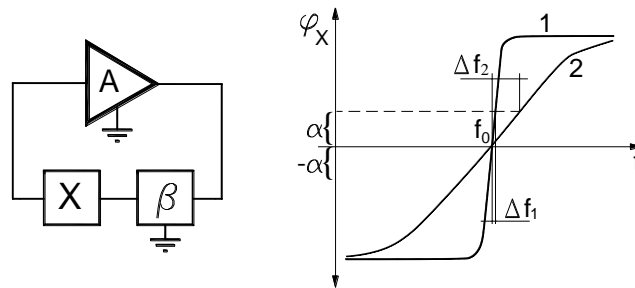


Fig. 1 a) Block diagram of an oscillator, and b) plot of the phase-frequency response of the resonator-sensor where the effect of frequency instabilities, due to a phase-noise in the loop, can be observed.

This analysis has pointed out that the origin of the frequency instability is the phase instability, whatever the origin of the phase instability is: temperature change, non-linearity of the components of the circuit, magnitude of the signals, etc; therefore when we are interested in monitoring the resonant frequency with an oscillator we should keep in mind that the sensitivity will not be given only by the resonant frequency but by the stability in phase of the rest of the components of the loop, which is very difficult to control, mainly the inherent phase noise of the active components. It is important to notice that crystal resonators are normally used in oscillators with the objective of stabilizing the oscillating frequency, in this cases the high Q of the resonator is

used to absorb the phase instabilities of the rest of the components of the feedback system. On the contrary, when a resonant sensor is used in an oscillator it should be kept in mind that the objective is to evaluate the change in the resonator response; consequently the higher the stability of the rest of the components of the system the higher the capability to detect changes in the sensor and, therefore, the higher the sensitivity of the global system.

However, we can think in the other way around: why not to interrogate the sensor at constant frequency and then measure the change in the phase response of the sensor due to the experimental process to be monitoring, for example an increase in the surface density of the coating?<sup>xxi</sup>.

The advantage of this approach is that the sensor is interrogated with an external source which can be designed to be very stable. Oven controlled crystal oscillators can be easily found with frequency stabilities higher than  $10^{-8}$  (it means 1Hz stability in 100 MHz), and starting from this frequency the desired frequency can be synthesized with a very small frequency-noise. In Fig.2a the mentioned approach is shown: the phase-response of the resonator sensor in a reference state is described by plot 1, and the phase response of the sensor in a second state is described by plot 2. If the sensor is continuously interrogated with an appropriate testing frequency  $f_i$ , the change in the phase response of the resonator will be followed by a phase shift,  $\Delta\phi$ , of the signal of frequency  $f_i$ . This phase shift can be monitored with a very simple circuit shown in Fig.2b, where a mixer is used as a phase detector. A more specific circuit will be proposed for this application later on, and additional advantages of the measuring system will be described.

Now the following question is: what is the phase shift expected for a certain surface mass density change in the coating? This relationship will be derived next.

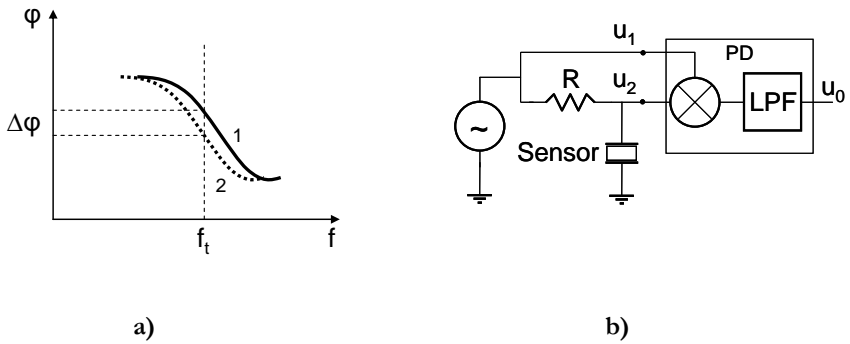


**Fig. 2** *a)* Representation of the phase-shift obtained when the resonator sensor is interrogated at constant frequency, and *b)* Simple system for measuring the phase-shift.

## 2. Theoretical Background

A loaded thickness-shear-mode (TSM) QCR (quartz crystal resonator) sensor can be modeled around resonance by the lumped-element equivalent circuit shown in Fig.3a<sup>xxii, xxiii</sup>. The circuit is a generalization of the Butterworth-Van Dyke (BVD) model in which  $L_q$ ,  $C_q$ ,  $R_q$  refer to the unperturbed sensor,  $C_0$  is the so-called static capacitance of the crystal,  $C_p$  is the parasitic capacitance external to the sensor and  $Z_{mL}$  is a complex impedance representing the contribution of the load. Consequently, the complete admittance of a loaded QCR is given by the following expression:

$$Y = \frac{1}{Z} = j\omega C_0^* + \frac{1}{Z_m} \quad (2)$$

where  $C_0^* = C_0 + C_p$  is the parallel capacitance,  $\omega$  is the angular frequency of the signal and  $Z_m = Z_{m0} + Z_{mL}$ , is the so-called motional impedance where  $Z_{m0}$  is the impedance of the series circuit formed by  $L_q$ ,  $C_q$ ,  $R_q$  and  $Z_{mL}$  is given by the following expression<sup>xxii</sup>:

$$Z_{mL} = \frac{1}{\omega C_0} \frac{\alpha}{4K^2} \frac{Z_L}{Z_{cq}} \frac{1}{1 - \frac{j \frac{Z_L}{Z_{cq}}}{2 \tan \frac{\alpha}{2}}} \quad (3)$$

where  $K$  is the complex electromechanical coupling factor for a lossy quartz,  $a$  is the complex acoustic wave phase across the lossy quartz, and  $Z_L$  is the acoustic load impedance. The parameters  $L_q$ ,  $R_q$ ,  $C_q$ ,  $C_0$ ,  $K$ ,  $a$ , and  $Z_{cq}$  depend on intrinsic properties of quartz (Table I), on the crystal thickness  $h_q$ , the electrode area  $A_s$ , and the quartz crystal losses  $\eta_q$ , in the following way<sup>xxii</sup>:

$$L_q = \frac{\rho_q h_q^3}{8A_s e_q^2}, C_q = C_0 \frac{8K_0^2}{\pi^2}, R_q = \frac{\eta_q}{\bar{c}_{66} C_q}, C_0 = \epsilon_{22} \frac{A_s}{h_q}, \quad (4)$$

$$K^2 = \frac{e_{26}^2}{\epsilon_{22} \bar{c}_{66}}, K_0^2 = \frac{e_{26}^2}{\epsilon_{22} \bar{c}_{66}}, \alpha = h_q \omega \sqrt{\frac{\rho_q}{\bar{c}_{66}}}, Z_{cq} = \sqrt{\rho_q \bar{c}_{66}}, \bar{c}_{66} = \bar{c}_{66} + j\omega\eta_q$$

The physical and geometrical properties of the load deposited on the crystal are included in the acoustic load impedance  $Z_L$ .

For small loads ( $Z_L/Z_{cq} \ll 2 \tan \alpha/2$ ) the contribution of the load on the motional impedance (Eq.3) can be approximated to:

$$Z_{mL} = \frac{1}{\omega C_0} \frac{\alpha}{4K^2} \frac{Z_L}{Z_{cq}} = \bar{K}_t Z_L \quad (5)$$

where, after applying Eq. 4,  $\bar{K}_t = h_q^2 / 4e_{26}^2 A_s$ ,

$Z_L$  in the former equation is the acoustic load impedance acting at the surface of the quartz plate. For an “acoustically thin” coating contacting a semi-infinite Newtonian fluid the expression of  $Z_L$  can be approximated to<sup>xxii</sup>:

$$Z_L = j\omega\rho_c h_c + (1 + j)\sqrt{\frac{\omega\rho_L\eta_L}{2}} \quad (6)$$

where  $\eta_L$  is the semi-infinite fluid viscosity.

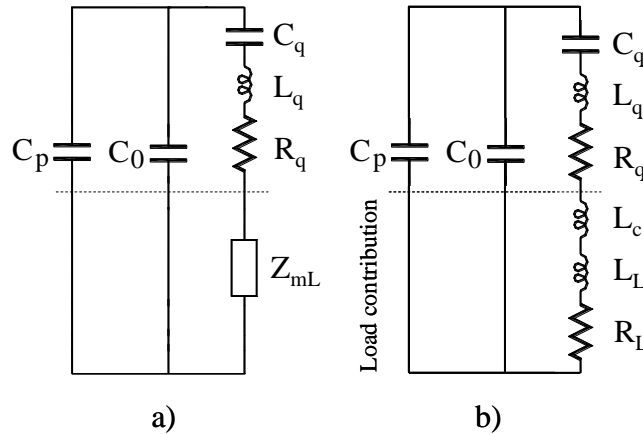


**Fig. 3** *a)* Lumped element model of the QCM sensor, and *b)* Simplified lumped element model for the QCM sensor in contact with an “acoustically thin” coating contacting a semi-infinite fluid medium.

The former expression can be re-written as follows:

$$Z_L = m_L\omega + j\omega(m_c + m_L) \quad (7)$$

where  $m_c$  is the surface mass density of the coating ( $\rho_c h_c$ ) and  $m_L = \rho_L \delta_L / 2$ , is the equivalent surface mass density of the contacting liquid associated with the oscillatory movement of the surface of the sensor, where  $\delta_L = (2\eta_L / \omega\rho_L)^{1/2}$  is the wave penetration depth of the wave in the liquid.

**Table I.** Properties of the AT quartz

Quartz Parameter	Value	Description
$e_{26}$ (A s m <sup>-2</sup> )	$9.657 \times 10^{-2}$	Piezoelectric constant
$\epsilon_{22}$ (A <sup>2</sup> s <sup>4</sup> Kg <sup>-1</sup> m <sup>-3</sup> )	$3.982 \times 10^{-11}$	Permittivity
$c_{66}$ (N m <sup>-2</sup> )	$2.947 \times 10^{10}$	Piezoelectrically stiffened shear modulus
$\rho_q$ (Kg m <sup>-2</sup> )	2651	Density
$v_q = (c_{66}/\rho_q)^{1/2}$ (m s <sup>-2</sup> )	3334.15	Wave propagation speed
$K_o^2$	$7.947 \times 10^{-3}$	Electromechanical coupling factor
$Z_{cq}$ (Kg m <sup>-2</sup> s <sup>-1</sup> )	$8.839 \times 10^6$	Quartz characteristic impedance
$\eta_q$ (Pa s) (*)	$9.27 \times 10^{-3}$	Effective quartz viscosity
$m_q = \eta_q \pi / 2 v_q$ (ng/mm <sup>-2</sup> ) (**)	4.367	Effective quartz-resonator surface mass density

(\*) This is an effective viscosity obtained for a 10MHz quartz crystal resonator in air, starting from the experimental values of  $R_q$  and  $C_q$  obtained from an impedance analyzer. Therefore this quartz viscosity is an effective viscosity which includes other sources of loss like the effect of the contacts to the connector and the air. Therefore, the results obtained using this parameter must be considered an approximation.

(\*\*) This is an author definition since  $m_q$  only depends on quartz parameters and has surface density dimensions (see Eq. 17)

From Eqs. 5-7, the lumped-element equivalent model in Fig. 3a turns into the equivalent model in Fig. 3b, where the contribution of the load on the motional branch of the equivalent circuit is taken into account by means of an inductance  $L_c$  representing the inertial effect of the coating, and by a series circuit formed by an inductance  $L_L$  and a resistance  $R_L$  representing, respectively, the inertial effect of the equivalent mass of fluid displaced by the oscillatory movement of the sensor surface and the corresponding loss effect.

Consequently, the motional impedance  $Z_m$  of a loaded resonator sensor in those applications, like in piezoelectric biosensor applications, in which the effects of the coating layer and the liquid on the acoustic impedance can be

considered additive, according to Eqs 6-7 (Martin's equation), can be written as follows:

$$Z_m = R_m + jX_m = R_q + R_L + j \left( \omega(L_q + L_c + L_L) - \frac{1}{\omega C_q} \right) \quad (8)$$

where  $L_c = K_t m_c$ ,  $R_L = \omega K_t m_L$ , and  $L_L = K_t m_L$ .

Starting from Eq.8 the frequency shift of the motional series resonant frequency (MSRF) due to the load can be easily obtained. Effectively, the motional series resonant angular frequency is given by the following expression:

$$\omega_s^2 = \frac{1}{C_q L_q} \quad (9)$$

Consequently, its variation can be obtained by taken the derivatives in both members of the equation as follows:

$$\Delta \omega_s = -\frac{\omega_s}{2L_q} \Delta L \quad (10)$$

where  $\Delta L = K_t (m_c + m_L)$ .

After some trivial calculations and solving for  $\Delta f_s$ , the following expression is obtained, which corresponds to Eq.1.

$$\Delta f_s = -\frac{2f_s^2}{Z_{cq}} (m_c + m_L) \quad (11)$$

Next, we are interested in obtaining the change in the phase response of the resonator sensor due to small changes in the load.

### 3. Phase-Shift vs. Mass Density Change

According to the equivalent model introduced in Fig. 3b in conjunction with Eq.8, the change of the phase-frequency response of the resonator sensor due to small changes in the load will be a consequence of the change in the phase-frequency response of the motional impedance  $Z_m$ . An approximate expression for the phase-shift which suffers a signal of a constant frequency near the MSRF,  $f_s$ , passing through the motional impedance, when small changes in the load occur, is obtained next.

The phase provided by the motional branch in a reference state, 1, is given by:

$$\varphi_1 = \arctan \frac{X_{m1}}{R_{m1}} \quad (12)$$

Around series resonance  $X_m$  is small and the tangent can be approximated to the phase, therefore  $\varphi_1 \approx X_{m1}/R_{m1}$ . After changing the mass of the coating, the new phase would be:  $\varphi_2 \approx X_{m2}/R_{m1}$  and the phase-shift is given by:

$$\Delta\varphi = \varphi_1 - \varphi_2 = \frac{X_{m1} - X_{m2}}{R_{m1}} \quad (13)$$

On the other hand, at the testing frequency  $f_t$ ,  $X_m = L_m \omega_t - 1/C_m \omega_t$ , where  $L_m = L_q + L_c + L_L$  and  $C_m = C_q$  (see Eq.8). Therefore the following approximation can be written for  $X_m$ :

$$X_m = \frac{1}{C_m \omega_t} \left( \frac{\omega_t^2}{\omega_s^2} - 1 \right) \approx \frac{2\Delta\omega}{C_m \omega_s^2} \quad (14)$$

where  $\Delta\omega = \omega_t - \omega_s$ .

Therefore, the phase-shift in Eq.13 is given by:

$$\Delta\varphi = \frac{2(\Delta\omega_1 - \Delta\omega_2)}{R_{m1}C_m\omega_s^2} = \frac{2(\omega_{s2} - \omega_{s1})}{R_{m1}C_m\omega_s^2} = \frac{2\Delta\omega_s}{R_{m1}C_m\omega_s^2} = \frac{2\Delta\omega_s}{(R_q + R_L)C_q\omega_s^2} \quad (15)$$

The change in the motional series resonant angular frequency due to small changes in the load, according to Eq. 11, is given by:

$$\Delta\omega_s = -\frac{\omega_s^2}{\pi Z_{cq}}(\Delta m_c + \Delta m_L) \quad (16)$$

Using Eq. 16 and the relationships given by Eqs. 4-5 in Eq. 15, the following expression is obtained for the phase-shift:

$$\Delta\varphi = -\frac{\Delta m_c + \Delta m_L}{m_q + m_L} \quad (17)$$

where  $m_q = \eta_q \pi / 2v_q$ , being  $v_q = (\bar{c}_{66} / \rho_q)^{1/2}$  the wave propagation speed in the quartz. The validity of this approximation around series resonance will be proved later on.

When only mass changes occur in the coating the expression for the phase-shift is reduced to:

$$\Delta\varphi \text{ (rad)} = -\frac{\Delta m_c}{m_q + m_L} \quad (18)$$

The former equation is very simple but makes a very important aspect clear; in contrast with Sauerbrey equation in which the frequency shift associated with a change in the surface mass density of the coating does not

depend on the medium, Eq.18 includes the additional consideration of the medium. From the previous equation it is clear that the bigger  $m_L$  the bigger  $\Delta m_c$  for a given phase-shift detection limit. This equation makes clear the higher sensitivity of the QCM in gas than in liquid, independently of the reduction of the quality factor  $Q$  of the sensor due to the contact with the liquid, for a given phase stability. In other words, Sauerbrey equation predicts the same shift in the resonant frequency for a sensor in vacuum or in liquid for a given change in the surface mass of the coating; however the corresponding phase-shift for the same change in the surface mass of the coating is much smaller for the sensor in liquid than in vacuum. Therefore, although the Sauerbrey equation ideally predicts the same frequency-mass sensitivity, much higher phase stability of the system is necessary for the case of the sensor in liquid than in vacuum to have, in practice, the same mass sensitivity.

Moreover,  $m_L$  in the previous equation is reduced with the wave penetration depth in the liquid. This reduction is proportional to  $\omega^{1/2}$ ; therefore the phase-mass sensitivity in a given liquid medium, for a given phase noise, could be improved by increasing the frequency but only proportionally to  $\omega^{1/2}$ .

The maximum sensitivity in terms of phase-shift per unit of mass change occurs for the sensor in vacuum, where  $m_L$  is null. Table II shows the theoretical detection capability of QCM sensors of different resonant frequencies, and in contact with different media, for a given phase-shift detection limit of  $0.1^\circ$ ; the corresponding frequency shift according to Sauerbrey equation is included as well.

As can be observed the same phase-mass sensitivity is obtained in vacuum for all the sensors. This is because the same value of  $\eta_q$  (see Table I) has been used, therefore the same value of  $\Delta m_c$  is necessary for obtaining the same  $\Delta\varphi = 0.1^\circ$ . Thus, for increasing the sensitivity in vacuum it is necessary to increase the wave propagation speed using a different material or to decrease

---

the sources of loss. However, this is irrelevant because most of applications which we are interested in are performed in liquid. In this case, the results in water are relevant; as can be observed an increase in the mass sensitivity is obtained as the wave penetration depth in the fluid decreases when increasing the frequency. A strong increase in the series resonant frequency shift occurs when increasing the resonant frequency, as Sauerbrey predicts; however, it must be recognized that this frequency-shift corresponds to the same phase-shift of  $0.1^\circ$ . Therefore, although the frequency-mass sensitivity has increased 225 times from the sensor of 150MHz to that of 10MHz ( $150^2/10^2$ ), the phase-mass sensitivity has been increased only 3.4 times ( $\approx(150/10)^{1/2}$ ). A phase-shift below  $0.1^\circ$  can be detected by modern phase detectors (mixers) even at very high frequencies; consequently, if the phase stability of the system is not reduced below  $0.1^\circ$ , the real improvement in the sensitivity will be 3.4 times and not 225 times. Thus, the most important aspect for increasing the mass sensitivity is to improve the phase stability of the characterization system as much as possible and, at the same time, to make the system capable to detect very tiny phase shifts in the sensor response; on the contrary it will be irrelevant to increase the “frequency-mass sensitivity” by using high frequency resonator-sensors, because the frequency noise would be of the same magnitude that the measurable frequency shift associated with the surface mass change of the coating, making impracticable the improve of the sensitivity.

Assuming the experimental set-up has been designed in the most appropriate way to reduce the disturbances, the remaining goal is to design optimally the characterization electronic system to reduce the frequency and phase noise. This can be made, as mentioned, by interrogating the sensor with an appropriate fixed frequency from a very stable external source, and to detect the phase-shift in the signal when the phase-frequency response of the resonator-sensor changes, due to changes in the surface mass density of the coating. In principle the idea is simple, but an appropriate circuit must be

proposed to select the appropriate interrogating frequency and to monitor the phase-shift in a suitable way to reduce the interference of the circuit.

**Table II.** Mass sensitivity for 0.1° phase detection limit or phase noise

			$f_{s0}$ (MHz)	10	50	150
Medium	$\rho_L$ (Kg/m <sup>3</sup> )	$\eta_L$ (Pa·s)				
Vacuum	0	0	$\Delta m_c$ (pg/mm <sup>2</sup> )	7.62	7.62	7.62
Hydrogen	0.08988	$8.6 \times 10^{-6}$		7.76	7.68	7.66
Air	1.18	$1.783 \times 10^{-5}$		8.34	7.94	7.81
Water	1000	0.001		163.32	77.25	47.82
Vacuum			$\Delta f_s$ (Hz)	0.17	4.31	38.81
Hydrogen				0.18	4.35	38.99
Air				0.19	4.49	39.75
Water				3.70	43.70	243.47

#### 4. Description of the System Proposal

As mentioned the interesting characterization parameter for our purposes is the phase-shift associated with the motional impedance  $Z_m$ ; however this impedance can not be measured in isolation, and an appropriate circuit must be used to avoid that the rest of the necessary components in the characterization system attenuate its contribution. The general schematic for the proposed system is introduced in Fig.4; specific considerations about the values of some components in the circuit will be made later on.

Two parts can be distinguished in the circuit. The sensor circuit (inside the dashed line), which includes the sensor, and the rest of the circuit which can be considered as the measure and control part of the system.

The sensor circuit is formed by two parallel branches forming a differential circuit. At first glance, a change in the phase-shift between the signals  $u_1$  and  $u_2$  will be due to a change in the phase-frequency behaviour of the motional impedance of the sensor, assuming that the phase-frequency

response of the rest of the components of the sensor circuit is maintained constant.

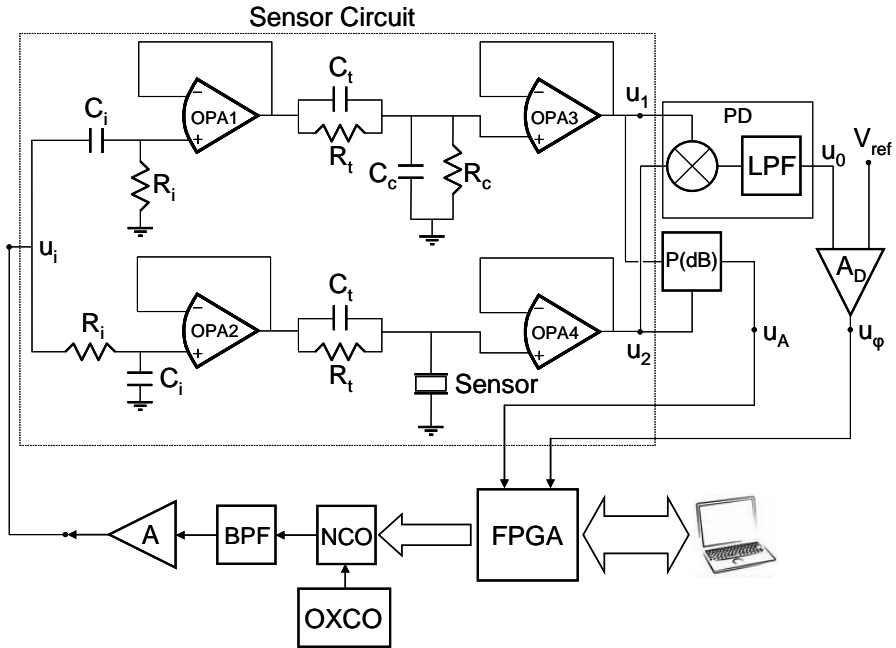


**Fig. 4** Block diagram of the proposed system

Therefore, the change in the phase-shift between  $u_1$  and  $u_2$  can be related to the phase-shift given in Eq.18. This relationship will be obtained next. The change in the phase-shift between  $u_1$  and  $u_2$  can be continuously monitored by a phase-detector. The mixer and the low-pass filter (LPF) connected in series behind the signals  $u_1$  and  $u_2$  act as a phase detector (PD). Effectively, for  $u_1$  and  $u_2$  being sinusoidal signals of peak-amplitude  $U_1$  and  $U_2$ , respectively, angular frequency  $\omega$  and phase-shifted an amount  $90^\circ - \varphi_D$ , the output signal of the mixer (multiplier) would be:

$$\begin{aligned}
 u_1 \cdot u_2 &= U_1 \sin \omega t \cdot U_2 \sin(\omega t + 90^\circ - \varphi_D) = \\
 &= \frac{U_1 U_2}{2} [\sin(\varphi_D) - \cos(2\omega t + \varphi_D + 90^\circ)]
 \end{aligned} \tag{19}$$

Therefore at the output of the low pass-filter the following signal  $u_0$  is obtained:

$$u_0 = \frac{U_1 U_2}{2} \sin(\varphi_D) \approx (\text{for small phase - shifts}) \approx k_m \varphi_D \tag{20}$$

where  $k_m = U_1 U_2 / 2$ .

As can be observed the behaviour of a phase detector based on a mixer provides a voltage proportional to the phase-shift, for small phase-shifts around  $90^\circ$ . Therefore, for a proper operation it is convenient to phase-shift, in advance, the testing signals in each branch of the sensor circuit  $90^\circ$ ; for this purpose the networks formed by  $R_i$  and  $C_i$  at the inputs of the sensor circuit have been included. The phase-shifting networks formed by  $R_i$  and  $C_i$  must be designed coherently with the resonant frequency of the sensor in order to obtain two signals  $90^\circ$  phase-shifted and of similar amplitude. This requirement makes the parallel branches in the sensor circuit necessary in order to have two signals  $90^\circ$  shifted with simple passive circuits. This could be avoided with other type of phase-detectors, such as phase-frequency detectors based on digital circuits; however the phase-jitter of digital phase detectors is not convenient for our purposes since it increases the phase noise of the system. Moreover, the differential system is convenient since the phase-noise in the original signal  $u_i$  is transmitted in both branches and cancelled in the phase detector.

A differential amplifier  $A_D$  enhances the signal of the phase-detector. The voltage  $V_{ref}$  is used to appropriately fix the output of the amplifier at zero

volts in the reference state to compensate any offset; this allows increasing the gain of the differential amplifier to provide maximum resolution on the phase-shift monitoring, which will be given by the output signal  $u_\phi$ .

On the other hand, an additional measurement of the power ratio of the signals  $u_1$  and  $u_2$ , provided at the output signal  $u_A$  of the P(dB) block, allows obtaining a complete characterization of the sensor. This combination of phase and power measurements permits to select the appropriate testing frequency by a suitable control system. The control system is formed by a Field Programmable Gate Array (FPGA) which continuously monitors the phase and the level ratio of the signals  $u_1$  and  $u_2$  through the acquisition of the magnitudes  $u_\phi$  and  $u_A$ . The FPGA controls the frequency of the signal synthesized by a Numeric Control Oscillator (NCO) whose frequency reference source is an Oven Crystal Control Oscillator (OXCO) with very high frequency stability and very small phase noise. The output signal of the NCO is filtered, to obtain a sinusoidal signal with minimum spurious components in the appropriate bandwidth around sensor resonance, and amplified to the appropriate level at the input of the sensor circuit.

The change in the phase-shift between the signals  $u_1$  and  $u_2$  is the main parameter, which must be related to the change in the phase of the motional branch of the sensor. This relationship will be obtained next. This analysis will be useful as well for designing the sensor circuit in the most appropriate way to avoid any reduction in the phase sensitivity.

After some basic analysis, the equations governing the operation of the sensor circuit are obtained as follows:

$$u_1 = \frac{R_c(1 + j\omega R_t C_t)}{R_t + R_c + j\omega R_t R_c (C_t + C_c)} \frac{j\omega R_t C_t}{1 + j\omega R_t C_t} u_i \quad (21)$$

$$u_2 = \frac{(R_m + jX_m)(1 + j\omega R_t C_t)}{R_t + R_m - \omega R_t (C_t + C_0)X_m + j[X_m + \omega R_t R_m (C_t + C_0)]} \frac{1}{1 + j\omega R_t C_t} u_i \quad (22)$$

In the obtaining of the former equations it has been assumed that the OPAs are operating as ideal followers.

Starting from Eqs. (21) and (22) it is possible to obtain the expression for the change in the phase-shift between  $u_1$  and  $u_2$ . Effectively, the phase of the signals  $u_1$  and  $u_2$  relative to  $u_i$  will be:

$$\varphi_1 = \varphi_{Z_t} - \varphi_{Z_{ct}} + 90^\circ - \varphi_{Z_i} \quad (23a)$$

$$\varphi_2 = \varphi_{Z_m} + \varphi_{Z_t} - \varphi_{Z_{mt}} - \varphi_{Z_i} \quad (23b)$$

where  $\varphi_{Z_t} = \text{atan } \omega_t R_t C_t$ ,  $\varphi_{Z_{ct}} = \text{atan } \omega_t R_t R_c (C_t + C_c) / (R_t + R_c)$ ,  
 $\varphi_{Z_i} = \text{atan } \omega_t R_t C_i$ ,  $\varphi_{Z_m} = \text{atan } X_m / R_m$ , and  
 $\varphi_{Z_{mt}} = \text{atan } [X_m + \omega_t R_t R_m (C_t + C_0)] / [(R_t + R_m) - \omega_t R_t (C_t + C_0) X_m]$ .

Therefore, the phase-shift between  $u_1$  and  $u_2$  will be given by:

$$\varphi_2 - \varphi_1 = \varphi_{Z_m} - \varphi_{Z_{mt}} + \varphi_{Z_{ct}} - 90^\circ \quad (24)$$

Hence, the exact change in the phase-shift from a reference state “1” to a second state “2”, keeping in mind that the testing frequency,  $\omega$ , is constant will be:

$$\Delta(\varphi_2 - \varphi_1)_1^2 = \Delta(\varphi_{Z_m} - \varphi_{Z_{mt}})_1^2 \quad (25)$$

After some calculations and approximations (see Appendix) the following expression is obtained starting from Eq.(25):

$$\Delta(\varphi_2 - \varphi_1)_1^2 \approx \Delta\varphi \frac{R_t}{R_t + R_m} \quad (26)$$

where  $\Delta\varphi$  is the phase-shift in the motional impedance of the sensor given by Eq.(18). Therefore the former expression results:

$$\Delta(\varphi_2 - \varphi_1)_1^2 \approx -\frac{\Delta m_c}{m_q + m_L} \frac{R_t}{R_t + R_m} \quad (27)$$

This simple expression will be compared in the next paragraph with the exact expression in Eq. (25) keeping in mind the definitions given in Eq. (23). As can be observed from Eq. (27), for  $R_t \gg R_m$  the second term in the second member tends to 1 and the change in the phase-shift between the signals  $u_1$  and  $u_2$  tends to the change in the phase-shift given by the motional impedance (Eq. 18). For practical reasons, in order not to reduce too much the level of the signals, it is enough that  $R_t \approx 10R_m$ .

Since the testing frequency is maintained constant, the  $R_c$ - $C_c$  network has not contribution in the change of the phase-shift; however it is convenient to select  $R_c$  and  $C_c$  similar to  $R_m$  and  $C_0$ , respectively. Effectively, under these conditions, and at the MSRF of the sensor, the level of the signals at the output of the OPAs 3 and 4 is similar, which is convenient for the operation of the phase-detector, and the output voltage  $u_A$  is zero. This configuration is useful as well for the search of the suitable testing frequency because both voltages  $u_\varphi$  and  $u_A$  are zero at the MSRF of the sensor. This and other considerations will be made in the next paragraph, where a numerical and graphical analysis will demonstrate the validity of expression in Eq.(18), as an approximation of the phase-shift associated with the motional impedance, and in Eq. (27) as an approximation of the exact expression given by Eq. (23-25).

A final consideration is that the proposed system can be also used to follow the change of MSRF of the sensor. Effectively, since the phase and level ratio of the magnitudes at the output of the sensor circuit are continuously monitored, the excitation frequency can be changed in such a way to maintain the voltages  $u_p$  and  $u_A$  at zero and, consequently, to follow the shift of the MSRF of the sensor; this would convert the circuit in a configuration similar to that described in Refs<sup>xiv,xvi,xvii</sup>. However, in case of small changes in the MSRF of the sensor, it is better to maintain the testing frequency fixed to improve the stability.

### 5. Numerical Validation of the Phase-Mass Equations

In order to prove the validity of Eq. (18) and (27) numerical simulations were made using the model in Fig.3b for representing the electrical behaviour of the sensor. This model is proved to be suitable for many applications and mainly for those applications in which the sensor is in contact with a very “acoustically thin” coating contacting a semi-infinite Newtonian fluid medium; this is the case in most of applications dealing with the characterization of biological process, such as in piezoelectric biosensors which we are interesting with, and in many electrochemical applications.

The numerical simulations were made for three quartz resonator sensors with resonant frequencies of 10, 50 and 150MHz, in contact with a thin coating layer of 100nm thickness and density equal to water; the Newtonian medium was considered like water. The parameters of the equivalent model were calculated according to the expressions given in Eq. (4), (5) and (8) with quartz properties in Table I, starting from the resonant frequency of the resonator (thickness) and the diameter of the electrode for typical commercial sensors. For 10MHz sensors a value of 5,2 mm for the diameter of the electrode mask was selected, which corresponds to typical sensors of 14 mm quartz blank diameter. For 50 and 150MHz quartz resonators 1,5 mm for the diameter of

the electrode was selected which corresponds to typical values for inverted MESA quartz resonators. The effective viscosity of the quartz  $\eta_q$  was calculated from the value of  $R_q$  obtained for the 10MHz crystal in air with an impedance analyzer (approx.  $10\Omega$ ). The thickness of the quartz was obtained from the resonant frequency through the approximate expression:  $h_q \approx v_q/2f_i$ . The rest of the parameters of the model and other relevant magnitudes are included in Table III.

Under these conditions the mass change in the coating was simulated by changing the thickness of the coating in steps of  $1\text{\AA}$  (Armstrong), it is to say in steps of  $100\text{pg}/\text{mm}^2$ , from  $-50\text{nm}/\text{mm}^2$  to  $50\text{nm}/\text{mm}^2$ . For each step the parameters in Eq. (24):  $\varphi_{Z_m}$  and  $\varphi_{Z_m}$  were calculated; as it can be observed by simple analysis of Eq. (21) and (22) the capacitor  $C_t$  does not provide advantages and can be made null without any restriction, therefore  $\varphi_{Z_d}=0$ , which improves the operation at high frequencies. Finally, the simulated change in the phase-shift was evaluated taking as reference the state of the sensor for  $\Delta m_c=0$ ; this change in the phase-shift was compared with the one given by Eq. (27).

Table IV shows a part of the calculations made for the 10MHz sensor taking  $R_c=R_m$  and  $R_t=10R_m$ ; the constant testing frequency was selected as the MSRF of the reference state, it is to say for  $\Delta m_c=0$ , and the change in the MSRF has been included for reference. The  $90^\circ$  phase-shift between  $u_1$  and  $u_2$  provided by the  $R_t$ - $C_t$  networks has not been considered here. These numbers are represented in Fig.5 (upper panel) with the results for 50 (middle panel) and 150MHz lower panel; the changes in the phase-shift corresponding to the motional impedance  $\Delta\varphi_{Z_m}$  are included as well for comparison. As can be observed Eq. (18) is a simple and good approximation of the response phase-shift vs. mass change of the QCM sensor around the MSRF.

3.2. A different point of view on the sensitivity of quartz crystal microbalance sensors

**Table III.** Properties of the resonator and parameters of the model shown in Fig.3b for three different sensors loaded with a coating layer, of 100nm thickness and water-like properties, contacting a fluid medium like water.

Parameter				Description
$f_{s0}$ (Hz)	10000000	50000000	150000000	Nominal unperturbed MSRF
$h_q$ (m)	$1.667 \times 10^{-4}$	$3.334 \times 10^{-5}$	$1.111 \times 10^{-5}$	Thickness of the quartz crystal
$d_e$ (m)	$5.20 \times 10^{-3}$	$1.50 \times 10^{-3}$	$1.50 \times 10^{-3}$	Diameter of the electrode
$A_e$ (m <sup>2</sup> )	$2.12 \times 10^{-5}$	$1.77 \times 10^{-6}$	$1.77 \times 10^{-6}$	Electrode Area
$C_o$ (pF)	5.07	2.11	6.33	Static capacitance
$C_p$ (pF)	2.00	2.00	2.00	Parasitic parallel capacitance
$C_o^*$ (pF)	7.07	4.11	8.33	Total parallel capacitance
$C_q$ (fF)	32.7	13.6	40.8	Motional capacitance
$L_q$ (μH)	7751.8	745.28	27.603	Unperturbed motional inductance
A	3.1416	3.1416	3.1416	Quartz acoustic wave phase
$\frac{K_t}{(\Omega \text{ m}^2 \text{ s kg}^{-1})}$	$3.51 \times 10^{-2}$	$1.69 \times 10^{-3}$	$1.87 \times 10^{-3}$	Electroacoustic constant
$\eta_q$ (*) (Pa s)	$9.27 \times 10^{-3}$	$9.27 \times 10^{-3}$	$9.27 \times 10^{-3}$	Effective quartz viscosity
$R_q$ (*) (Ω)	9.63	23.14	7.71	Unperturbed motional resistance
<b>Loaded sensor equivalent circuit parameters</b>				
$m_c$ (ng/mm <sup>2</sup> )	100	100	100	Coating surface mass density
$L_c$ (μH)	3.51	1.69	0.187	Motional inductance of the coating
$\delta_L$ (nm)	178.4	79.79	46.07	Wave penetration depth in water
$m_L$ (ng/mm <sup>2</sup> )	89.21	39.89	23.03	Equivalent surface mass density in water
$L_L$ (nH)	3129	672.8	43.16	Motional inductance of the water
$L_m$ (μH)	7758.5	747.64	27.833	Total motional inductance
$R_L$ (Ω)	196.63	211.36	40.68	Motional resistance of the water
$R_m$ (Ω)	206.25	234.49	48.39	Total motional resistance
$C_m$	32.7	13.6	40.8	Total motional capacitance
$f_{sL}^0$	9995721.5	49921051.2	149377514.8	Loaded MSRF

**Table IV.** Partial data of the calculations for obtaining the plot in Fig.6a

$\Delta m_c$ (ng/mm <sup>2</sup> )	$\Delta f_s$ (Hz)	$\varphi_{Zm}$ (deg)	$\varphi_{Zmt}$ (deg)	$\Delta\varphi_{Eq.(25)}$ (deg)	$\Delta\varphi_{Eq.(27)}$ (deg)
-1.00	22.60	-0.61	4.70	-0.55	-0.56
-0.90	20.34	-0.55	4.71	-0.50	-0.50
-0.80	18.08	-0.49	4.71	-0.44	-0.45
-0.70	15.82	-0.43	4.72	-0.39	-0.39
-0.60	13.56	-0.37	4.73	-0.33	-0.33
-0.50	11.30	-0.31	4.73	-0.28	-0.28
-0.40	9.04	-0.24	4.74	-0.22	-0.22
-0.30	6.78	-0.18	4.74	-0.16	-0.17
-0.20	4.52	-0.12	4.75	-0.11	-0.11
-0.10	2.26	-0.06	4.76	-0.05	-0.06
0.00	0.00	0.00	4.76	0.00	0.00
0.10	-2.26	0.06	4.77	0.05	0.06
0.20	-4.52	0.12	4.77	0.11	0.11
0.30	-6.78	0.18	4.78	0.16	0.17
0.40	-9.04	0.24	4.78	0.22	0.22
0.50	-11.30	0.31	4.79	0.28	0.28
0.60	-13.56	0.37	4.80	0.33	0.33
0.70	-15.82	0.43	4.80	0.39	0.39
0.80	-18.08	0.49	4.81	0.44	0.45
0.90	-20.34	0.55	4.81	0.50	0.50
1.00	-22.60	0.61	4.82	0.55	0.56

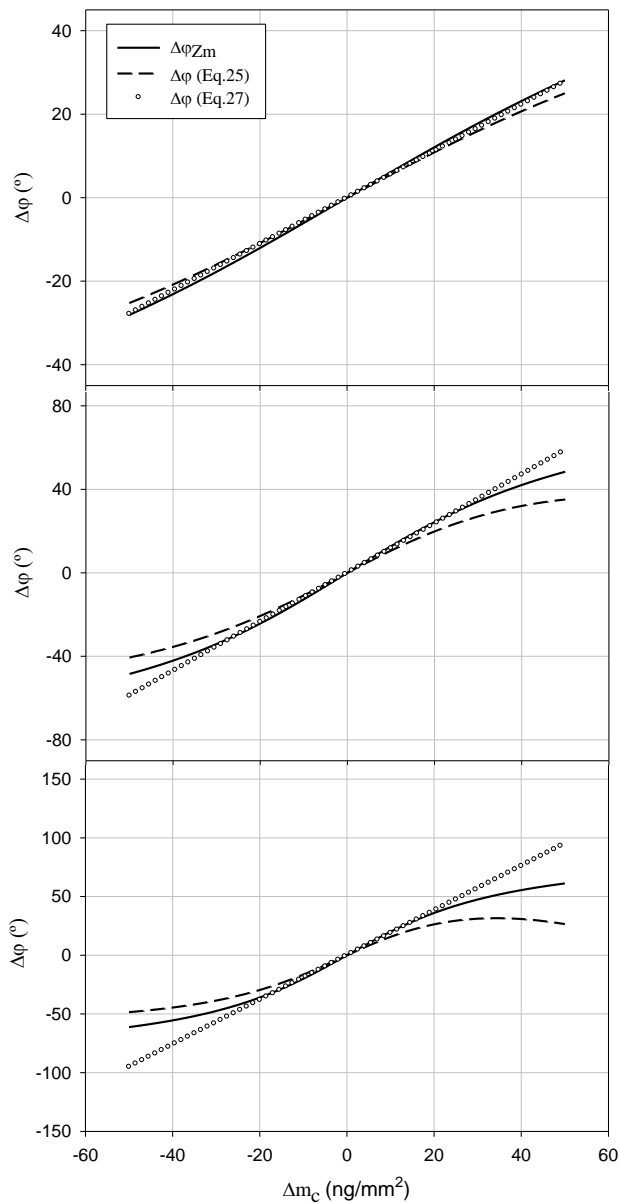


**Fig. 5** Graphical representation of the phase-shift in the motional impedance given by Eq. (12), the phase shift given by Eq.(25) with the exact definitions in Eq.(23), and the approximation given by Eq.(27), for three QCM sensor of 10MHz (upper panel), 50MHz (middle panel) and 150MHz (lower panel)

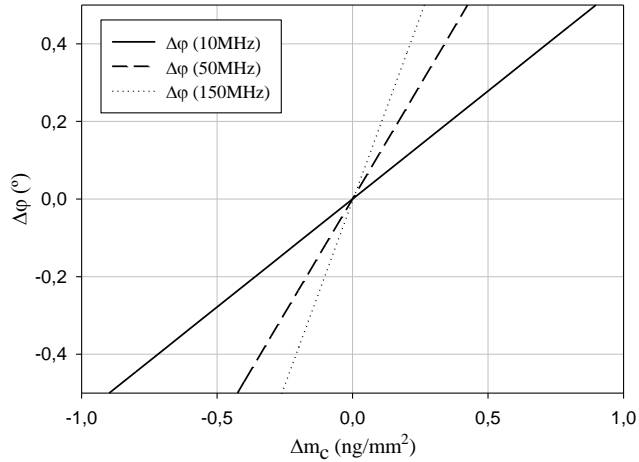


**Fig. 6** Graphical comparison, obtained from Fig.5 with the phase-shift given by Eq. (27), of the phase-mass sensitivities of three QCM sensors of 10MHz, 50MHz and 150MHz fundamental resonant frequency

Figure 6 is a zoom, extracted from Fig.5, which shows a comparison of the sensitivities of the three QCM sensors (10, 50 and 150MHz), in terms of phase-shift vs. mass change.

## 6. Conclusions

The sensor phase-mass-sensitivity increases with the resonant frequency but this increase is much smaller than the corresponding increase in the frequency-mass-sensitivity. However, the frequency and phase are intimately related in feedback systems like oscillators; therefore, for taking advantage of the great increase in the frequency sensitivity of the QCM sensor when increasing the resonant frequency, it is necessary, at the same time, to improve the phase stability of the system. In other words, if the phase stability of a feedback system, whose oscillating frequency is controlled by the sensor, is not improved and the resonant frequency of the sensor is increased, the sensitivity

of the setup system-sensor will be only increased in the same degree that the wave penetration depth in the liquid is reduced, this is proportionally to  $(\omega)^{1/2}$ .

The circuit proposed in this article is appropriate for characterizing the phase-response vs. mass change of the QCM and a simple equation has been derived which provides quantitative information. The proposed circuit interrogates the sensor at fixed frequency, which reduces the frequency and phase instabilities. The sensor circuit has a very simple differential configuration which allows the cancellation of the phase instabilities of the external source and, consequently, the capability to detect changes in the sensor response is improved.

## Appendix

Starting from Eq. (25)

$$\Delta(\varphi_2 - \varphi_1)|_1^2 = \Delta(\varphi_{Zm} - \varphi_{Zmt})|_1^2 = \Delta\varphi_{Zm}|_1^2 - \Delta\varphi_{Zmt}|_1^2 \quad A.1$$

Keeping in mind the definitions in Eq.(23):

$$\varphi_{Zm} = \arctan \frac{X_m}{R_m}; \varphi_{Zmt} = \arctan \frac{\frac{X_m}{R_t + R_m} + \frac{R_t R_m}{R_t + R_m} \omega_t (C_t + C_0)}{1 - \frac{R_t X_m}{R_t + R_m} \omega_t (C_t + C_0)} \quad A.2$$

Thus,  $\Delta\varphi_{Zm}|_1^2 = \varphi_{Zm1} - \varphi_{Zm2}$ , can be approximated, around the MSRF and according Eq.(13), to:

$$\Delta\varphi_{Zm}|_1^2 \approx \frac{X_{m1} - X_{m2}}{R_m} \quad A.3$$

For  $\Delta\varphi_{Zmt}|_1^2 = \varphi_{Zmt1} - \varphi_{Zmt2}$  we can do the following calculations:

$$\tan \Delta\varphi_{Zmt}|_1^2 = \tan(\varphi_{Zmt1} - \varphi_{Zmt2}) = \frac{\tan \varphi_{Zmt1} - \tan \varphi_{Zmt2}}{1 + \tan \varphi_{Zmt1} \tan \varphi_{Zmt2}} \quad A.4$$

and near MSRF  $\varphi_{Zmt}$  can be approximated to:

$$\varphi_{Zmt} \approx \arctan \frac{X_m}{R_t + R_m} + \frac{R_t R_m}{R_t + R_m} \omega_t (C_t + C_0) \quad A.5$$

The product of tangents in the denominator of Eq. (A.4) is much smaller than 1, and because the testing frequency is constant, Eq. (A.4) can be approximated to:

$$\tan \Delta\varphi_{Zmt}|_1 \approx \frac{X_{m1} - X_{m2}}{R_t + R_m} \quad \text{A.6}$$

Near the MSRF the tangent can be approximated to the angle and Eq.(A.6) results:

$$\Delta\varphi_{Zmt}|_1 \approx \frac{X_{m1} - X_{m2}}{R_t + R_m} \quad \text{A.6}$$

Consequently, Eq. (A1) reduces to:

$$\Delta(\varphi_2 - \varphi_1)|_1^2 = \Delta\varphi_{Zm}|_1^2 - \Delta\varphi_{Zmt}|_1^2 \approx \frac{X_{m1} - X_{m2}}{R_m} \left( \frac{R_t}{R_m + R_t} \right) \quad \text{A.7}$$

which converts to Eq.(27) keeping in mind Eq.(13) and (18).

#### Acknowledgment

The authors are grateful to the Spanish Ministry of Science and Technology for financially supporting this research under contract reference: AGL2006-12147/ALI.

---

<sup>i</sup> G. Sauerbrey (1959) "Verwendung von schwingquarzen zur wägung dünner schichten und zur mikrowägung" *Zeitschrift Fuer Physik* 155 (2): 206-222

<sup>ii</sup> K.K. Kanazawa and J.G. Gordon II (1985) "The oscillation frequency of a quartz resonator in contact with a liquid" *Analytica Chimica Acta* 175:99-105

- 
- iii S.J. Martin, V.E. Granstaff and G.C. Frye (1991) "Characterization of quartz crystal microbalance with simultaneous mass and liquid loading" *Anal. Chem.* 63:2272-2281
- iv A. Arnau, V. Ferrari, D. Soares, H. Perrot, "Interface Electronic Systems for AT-Cut QCM Sensors. A comprehensive review", in *Piezoelectric Transducers and Applications*, 2nd Ed., pp 117, A.Arnau Ed., Springer-Verlag Berlin Heidelberg, (2008)
- v F. Eichelbaum, R. Borngräber, J. Schröder, R. Lucklum, and P. Hauptmann (1999) "Interface circuits for quartz crystal microbalance sensors" *Rev. Sci. Instrum.* 70:2537-2545
- vi J. Schröder, R. Borngräber, R. Lucklum and P. Hauptmann (2001) "Network analysis based interface electronics for quartz crystal microbalance" *Review Scientific Instruments* 72 (6):2750-2755
- vii S. Doerner, T. Schneider, J. Schröder and P. Hauptmann (2003) "Universal impedance spectrum analyzer for sensor applications" in Proceedings of IEEE Sensors 1, pp. 596-594
- viii M. Rodahl and B. Kasemo (1996) "A simple setup to simultaneously measure the resonant frequency and the absolute dissipation factor of a quartz crystal microbalance" *Rev. Sci. Instrum.* 67:3238-3241
- ix H. Ehhoun, C. Gabrielli, M. Keddou, H. Perrot and P. Rousseau (2002) "Performances and limits of a parallel oscillator for electrochemical quartz crystal microbalances" *Anal. Chem.* 74:1119-1127
- x C. Barnes (1992) "Some new concepts on factors influencing the operational frequency of liquid-immersed quartz microbalances" *Sensors and Actuators A-Physical* 30 (3):197-202
- xi K.O. Wessendorf (1993) "The lever oscillator for use in high resistance resonator applications" in Proceedings of the 1993 IEEE International Frequency Control Symposium, pp. 711-717
- xii R. Borngräber, J. Schröder, R. Lucklum and P. Hauptmann (2002) "Is an oscillator-based measurement adequate in a liquid environment?" *IEEE Trans. Ultrason. Ferroelect. Freq. Contr.* 49 (9):1254-1259
- xiii S. J. Martin, J. J. Spates, K. O. Wessendorf, T. W. Schneider and R. J. Huber (1997) "Resonator/oscillator response to liquid loading" *Anal. Chem.* 69:2050-2054
- xiv A. Arnau, T.Sogorb, Y. Jiménez (2002) "Circuit for continuous motional series resonant frequency and motional resistance monitoring of quartz crystal resonators by parallel capacitance compensation" *Rev. Sci. Instrum.* 73 (7): 2724-2737
- xv V. Ferrari, D. Marioli, and A. Taroni (2001) "Improving the accuracy and operating range of quartz microbalance sensors by purposely designed oscillator circuit" *IEEE Trans. Instrum. Meas.* 50:1119-1122
- xvi A. Arnau, J.V. García, Y. Jiménez, V. Ferrari and M. Ferrari (2007) "Improved Electronic Interfaces for Heavy Loaded at Cut Quartz Crystal Microbalance Sensors" in Proceedings of Frequency Control Symposium Joint with the 21st European Frequency and Time Forum. IEEE International, pp.357-362
- xvii M. Ferrari, V. Ferrari, D. Marioli, A. Taroni, M. Suman and E. Dalcanale (2006) "In-liquid sensing of chemical compounds by QCM sensors coupled with high-accuracy ACC oscillator" *IEEE Trans. Instrum. Meas.* 55 (3):828-834

- <sup>xviii</sup> B. Jakoby, G. Art and J. Bastemeijer (2005) "A novel analog readout electronics for microacoustic thickness shear-mode sensors" *IEEE Sensors Journal* 5 (5):1106-1111
- <sup>xix</sup> C. Riesch and B. Jakoby (2007) "Novel Readout Electronics for Thickness Shear-Mode Liquid Sensors Compensating for Spurious Conductivity and Capacitances" *IEEE Sensors Journal* 7 (3): 464-469
- <sup>xx</sup> MA. Cooper and VT. Singleton (2007) "A survey of the 2001 to 2005 quartz crystal microbalance biosensor literature: applications of acoustic physics to the analysis of biomolecular interactions" *Journal of Molecular Recognition* 20 (3):154-184
- <sup>xxi</sup> D.M. Dress, *et al* (1999) "Method and system for detecting material using piezoelectric resonators" US Patent 5932953
- <sup>xxii</sup> R. Lucklum, V. D. Soares and K.K. Kanazawa, "Models for resonant sensors", in *Piezoelectric Transducers and Applications*, 2nd Ed., pp 63, A.Arnau Ed., Springer-Verlag Berlin Heidelberg, (2008)
- <sup>xxiii</sup> R. W. Cernosek, S. J. Martin, A. R. Hillman and H.L. Bandey (1998) "Comparison of lumped-element and transmission-line models for thickness-shear-mode quartz resonator sensors" *IEEE Trans. Ultrason. Ferroelect. Freq. Contr.* 45:1399-1407

### **3.3 High-Frequency phase shift measurement greatly enhances the sensitivity of QCM immunosensors**

Carmen March, José V. García, Ángel Sánchez, Antonio Arnau, Yolanda Jiménez, Pablo García, Juan J. Manclús, Ángel Montoya

Biosensors and Bioelectronics, Volume 65, 15 March 2015, Pages 1-8,  
ISSN 0956-5663

<http://dx.doi.org/10.1016/j.bios.2014.10.001>

Copyright (2015), with permission from Elsevier

### ABSTRACT

In spite of being widely used for in liquid biosensing applications, sensitivity improvement of conventional (5-20 MHz) quartz crystal microbalance (QCM) sensors remains an unsolved challenging task. With the help of a new electronic characterization approach based on phase change measurements at a constant fixed frequency, a highly sensitive and versatile high fundamental frequency (HFF) QCM immunosensor has successfully been developed and tested for its use in pesticide (carbaryl and thiabendazole) analysis. The analytical performance of several immunosensors was compared in competitive immunoassays taking carbaryl insecticide as the model analyte. The highest sensitivity was exhibited by the 100 MHz HFF-QCM carbaryl immunosensor. When results were compared with those reported for 9 MHz QCM, analytical parameters clearly showed an improvement of one order of magnitude for sensitivity (estimated as the  $I_{50}$  value) and two orders of magnitude for the limit of detection (LOD):  $30 \mu\text{g L}^{-1}$  *vs*  $0.66 \mu\text{g L}^{-1}$   $I_{50}$  value and  $11 \mu\text{g L}^{-1}$  *vs*  $0.14 \mu\text{g L}^{-1}$  LOD, for 9 and 100 MHz, respectively. For the fungicide thiabendazole,  $I_{50}$  value was roughly the same as that previously reported for SPR under the same biochemical conditions, whereas LOD improved by a factor of 2. The analytical performance achieved by high frequency QCM immunosensors surpassed those of conventional QCM and SPR, closely approaching the most sensitive ELISAs. The developed 100 MHz QCM immunosensor strongly improves sensitivity in biosensing, and therefore can be considered as a very promising new analytical tool for in liquid applications where highly sensitive detection is required.

Key Words: High Fundamental Frequency; HFF QCM; Immunosensor; Sensitivity enhancement.

## 1. Introduction

Throughout the last two decades, quartz crystal microbalance (QCM) resonators have gained an increasing relevance for biological and biochemical research. Since acoustic QCM sensors can detect mass and viscosity alterations on its surface by means of variations on their resonance frequency (Marx, 2003), they have found widespread acceptance as valuable tools for biomolecular interactions and related phenomena analysis. Their scientific merits, simple operation principles and affordable basic elements have been extensively discussed (Marx, 2007; Sagmeister et al., 2009; Speight and Cooper, 2012).

Already established and commercially available systems usually employ frequencies ranging from 5 to 20 MHz (Stehrer et al., 2010; Uttenthaler et al., 2001; Yoshimine et al., 2011). According to Sauerbrey's relation (Sauerbrey, 1959), since mass sensitivity is directly proportional to the square of its resonance frequency  $f_0$ , the performance of a QCM sensor depends crucially on its fundamental resonance frequency. This relationship is expressed as follows:

$$\Delta f = -2f_0^2 / \sqrt{\rho\mu} \cdot \Delta m \quad (1)$$

where  $\Delta f$  is the frequency shift produced as a consequence of a mass alteration per unit active area  $\Delta m$ ;  $f_0$  is the fundamental resonance frequency with no attached mass;  $\rho$  the quartz density (2648 g cm<sup>-3</sup>); and  $\mu$  the quartz shear modulus (29.47 dyn cm<sup>-2</sup>, for AT-cut).

Operation at suitable high fundamental frequencies (HFF) turns to be imperative for in liquid applications in which the sensitive detection of small changes is required. Uttenthaler and coworkers first developed a HFF-QCM biosensor for phage detection in liquids (Uttenthaler et al., 2001), but very few research groups have been working with HFF resonators in liquid media since

this first application was demonstrated. HFF resonators are usually described as small, fragile and difficult to implement in flow-cell systems (Lin et al., 1993; Sagmeister et al., 2009; Stehrer et al., 2010). Moreover, these sensors do not quite get a stable resonance frequency signal in the presence of even minute fluctuations of hydrostatic pressure (Sota et al., 2002).

The fabrication of HFF sensors involves a reduction of their plate thickness. The thinned resonator region needs to be essentially carved into a thicker quartz plate otherwise mechanical stability and easy handling and installation in a flow-cell system would be restricted. These requirements, together with those derived from working in liquid media, are accomplished by a suitable “inverted mesa” design. This way, the thickness is achieved by chemically etching of only a small sensor central circular area. Likewise, the surrounding thicker material provides better stability whereas the sensitive central area could be as thinner as 8.3  $\mu\text{m}$  for up to 200 MHz high frequencies (Michalzik et al., 2005; Sagmeister et al., 2009).

As mentioned above, higher sensitivity can be achieved when frequency increases. However, in oscillators mainly used with conventional low fundamental frequency resonators, unsteady frequency signal is largely caused because phase noise increases with higher frequencies. This way, resonance signal becomes unstable and therefore the pursued improvement remains unsolved. In order to reduce this noise, a new electronic characterization system has recently been proposed by our group (Montagut et al., 2011), based on the phase/mass relationship at a fixed frequency:

$$\Delta\varphi \approx -(\Delta m / m_L) \quad (2)$$

where  $\Delta\varphi$  is the phase shift produced by a mass alteration  $\Delta m$  on the sensor surface; and  $m_L$  is the liquid mass perturbed by the resonator. When fundamental resonance frequency increases because crystal thickness decreases,

---

$\Delta\varphi$  rises as  $m_L$  is reduced. Therefore, if frequency is fixed and changes in phase are measured, operation at high frequencies without a significant increase of noise would be allowed and suitable phase shift ( $\Delta\varphi$ ) responses will be obtained.

Affinity interactions are often real-time monitored by means of transducer systems which allow label-free detection of the binding reaction. Although the most popular are optical systems based on surface plasmon resonance (SPR), the application of mass sensitive transducers as HFF QCM could turn this acoustic technology into a competitive tool for sensitivity improvement. In a previous work we described a piezoelectric immunosensor for pesticide determination (March et al., 2009), based on a conventional 9 MHz QCM sensor. The achieved immunosensor sensitivity was enough for pesticide determination in fruit juice samples. However, it still was far from that required by more demanding applications, such as the measurement of pesticide residues at European regulatory levels in drinking water.

It is well known that enhanced sensitivity in competitive immunoassays for low molecular weight compounds can be achieved by lowering immunoreagent concentrations. The signal produced in biomolecular interactions must be, meantime, high enough even at low immunoreagent and analyte concentrations. Taking advantage of QCM measurements based on the phase/mass approach above described, in the present work we report the development of an HFF-QCM immunosensor for the high-sensitivity determination of carbaryl and thiabendazole pesticides. Carbaryl, the first successful carbamate insecticide with a broad-spectrum efficacy, was chosen as a model analyte because it has become a reference analyte for immunoassay comparison, from ELISA to immunosensors (Abad et al., 1997; March et al., 2009; Mauriz et al., 2006). Thiabendazole (TBZ) is a widespread fungicide used in postharvest control of fungal diseases on fruit and vegetables. Moreover, it is

one of the most widely detected pesticides in Europe and USA. The structures of both analytes are provided as supplementary information, Fig S1.

## 2. Material and Methods

### 2.1. Chemicals and immunoreagents

Bovine serum albumin (BSA) fraction V was purchased from Roche Diagnostics (Mannheim, Germany). Tween-20 was supplied by Fluka-Aldrich Chemie (Buchs, Switzerland). All other chemicals were of analytical grade.

*Reagents for covalent immobilization:* 1-ethyl-3-(3-dimethyl-amino-propyl) carbodiimide hydrochloride (EDC) and N-hydroxysuccinimide (NHS) were purchased from Pierce (Rockford, IL); thioctic acid (TA), mercaptohexadecanoic acid (MHDA) and 11-mercaptoundecanol (MUD) were supplied by Sigma-Aldrich Chemie (Steinheim, Germany); ethanolamine blocking agent was obtained from Sigma (St. Louis, MO).

*Analytical pesticide standards:* Carbaryl was purchased from Dr. Ehrenstorfer (Augsburg, Germany) and TBZ from Riedel-de Hën (Seelze, Germany).

*Immunoreagents:* For carbaryl assay, BSA-CNH protein-hapten conjugate and LIB-CNH45 monoclonal antibody (MAb) were produced as previously described (Abad et al., 1997). For TBZ assay, BSA-TN3C protein-hapten conjugate and LIB-TN3C13 MAb were previously prepared as described (Abad et al., 2001).

### 2.2. HFF-QCM sensor set-up

#### 2.2.1. HFF-QCM sensor chip and flow-cell assembly

Sensors were from AWSensors (Valencia, Spain, [www.awsensors.com](http://www.awsensors.com)). They were based on square shaped 50 and 100 MHz AT-cut, inverted mesa crystals, with 36 mm<sup>2</sup> of total area and an etched area thickness of

---

approximately 33 and 17  $\mu\text{m}$ , for 50 and 100 MHz, respectively. Electrode active surface ranged from 0.196 to 3.142  $\text{mm}^2$  (for 0.5 to 2.0 mm electrode diameter). Sensors were assembled on a polyether ether ketone (PEEK) support with a conical hole to expose the active surface of the gold electrode where interface events as immunoassays will take place (supplementary information, Fig S2-A).

HFF-QCM chips were subsequently mounted into a flow-cell suitable for operation at high frequencies. The flow-cell was made up of two main components: the upper and the lower cell housing. Sensor chips were placed on the aluminum lower housing. Thereafter, they were sandwiched between this lower piece and a polymethyl methacrylate (PMMA) upper lid. The upper and lower pieces were held together by means of two screws making a 2.75  $\mu\text{l}$  internal volume flow-through cell chamber that was sealed either with a Polydimethylsiloxane (PDMS) or a nitrile O-ring. This way, only one face of the sensor was allowed to be in contact with the fluid (supplementary information, Fig. S2-B).

### 2.2.2. *Measurement platform*

The flow cell was included in the AWS A10 test platform from AWSensors. This platform consists basically on an automated flow-through equipment controlled by syringe pumps (Hamilton, Bonaduz, GR, Switzerland) and thermostated at 25  $^{\circ}\text{C}$  combined with an electronic characterization system based on the fixed frequency phase-shift measurement technique described elsewhere (Montagut et al., 2011) (supplementary information, Fig S2-C). By means of this platform, before and after covalent functionalization, HFF-sensor chips were electronically characterized by impedance analysis performed in working buffer to determine the optimum operation frequency. In this work the chosen frequency was that at which the sensor showed the maximum conductance.

AWS A10 platform allows the remote control of fluidics, as well as data acquisition and analysis by AW-BIO v1.8 dedicated software (AWSensors, Spain). Phase, amplitude and temperature were therefore measured, recorded and processed through the assays. Samples were delivered to the flow cell by means of the syringe pump at a constant flow rate. Teflon tubing, internal diameter 0.25 and 0.80 mm were used for flow-through in and out port connections, respectively (Valco Vici, Switzerland and Supelco, Bellefonte, PA).

### *2.3. Gold electrode surface functionalization*

#### *2.3.1. Clean up of crystals.*

50 and 100 MHz HFF-QCM crystals assembled in the PEEK support were subjected to UV-ozone radiation for 15-20 min using a UV/Ozone ProCleaner from BioForce Nanosciences (Ames, IA). After the cleaning treatment, crystals were rinsed with distilled water and ethanol and blown dry with a stream of nitrogen gas.

#### *2.3.2. Covalent immobilization.*

Surface functionalization of HFF-QCM sensors was based on the classical amide chemistry to obtain self-assembled monolayers (SAM). All procedures were performed on only one face of the crystal following the previously described protocol (March et al., 2009), with the exception of:

- For carbaryl assays, the thiolated compounds used for SAM formation were TA or MHDA at concentrations ranging from 5  $\mu\text{M}$  to 10 mM for BSA-CNH conjugate immobilization. For TBZ, a 250  $\mu\text{M}$  solution of MHDA and MUA (50:1 molar ratio) was used for BSA-TN3C conjugate immobilization.

- BSA-hapten conjugates in 0.1 M sodium phosphate buffer, pH 7.5 was placed on the crystal active surfaces at concentrations ranging from 1.0  $\mu\text{g mL}^{-1}$  to 10.0  $\text{mg mL}^{-1}$  (carbaryl) or 20.0  $\mu\text{g mL}^{-1}$  (TBZ), for 4 h.

---

Functionalized sensors could be used for at least 75 times.

#### 2.4. *Immunoassay format*

The indirect competitive immunoassays developed to determine carbaryl and TBZ were binding inhibition tests based on the conjugate-coated format. For the inhibition assays, a fixed amount of the respective monoclonal antibody was mixed with standard solutions of the analyte, and the mixture was pumped over the sensor surface previously immobilized with the assay conjugate. Since analyte inhibits antibody binding to the respective immobilized conjugate, increasing concentrations of analyte will reduce the phase decrease of the piezoelectric sensor (a general scheme showing the sensing interface and the signal transduction strategy is provided as supplementary information, Fig. S3). Carbaryl and TBZ standard solutions ranging from  $10^{-3}$  to  $2.0 \times 10^3 \mu\text{g L}^{-1}$  were prepared from 1 mM stock solutions in dimethylformamide (stored at  $-20\text{ }^\circ\text{C}$  in dark vials) by serial dilutions in PBS (10 mM phosphate buffer solution, 0.9% NaCl, pH 7.4). For carbaryl assays, depending on the crystal operational fundamental frequency, the standards were mixed with different fixed concentrations of LIB-CNH45 MAb in PBS:  $2.5 \mu\text{g mL}^{-1}$  for 50 MHz and  $2.0 \mu\text{g mL}^{-1}$  for 100 MHz resonators. For TBZ,  $1.0 \mu\text{g mL}^{-1}$  of LIB-TN3C13 MAb was used in combination with 100 MHz crystals. Analyte-antibody mixture solutions were incubated for 1 h at room temperature and then 250  $\mu\text{L}$  of this mixture were brought onto the sensor surface. Variations in phase response were monitored in real time as the binding between free antibody and the immobilized conjugate took place. Regeneration of the functionalized surfaces was accomplished with 0.1 M HCl to break the antibody-hapten conjugate association in carbaryl immunoassays and 0.1M NaOH to break the antibody-conjugate interaction in TBZ assays.

All standards and samples were run at least in duplicate. Standard curves were obtained by plotting the phase decrease *versus* analyte concentration. The experimental points were fitted to the four-parameter logistic equation:

$$y = y_0 + [(A - y_0) / 1 + (x/x_0)^B] \quad (3)$$

where  $y$  is the HFF-QCM signal (variation of phase at the fixed fundamental frequency  $\Delta\varphi$ ),  $y_0$  is the asymptotic minimum (background signal),  $A$  is the asymptotic maximum (maximum signal in absence of analyte,  $S_{\max}$ ),  $x$  is the analyte concentration,  $x_0$  is the analyte concentration giving 50% inhibition ( $I_{50}$ ), and  $B$  is the slope of the sigmoidal curve at the inflection point.

Mean standard curves were obtained by averaging several individual standard ones. These curves were normalized by expressing the phase decrease provided by each standard concentration as the percentage of the maximum response (maximum signal,  $S_{\max} = 100\%$ ) in the absence of analyte.

### 2.5. Immunoassay protocol

To block non-specific MAb adsorption to the functionalized gold surface, prior to the first assay on every freshly immobilized crystal, blocking buffer (PBS containing 0.5 % BSA) was pumped for 15 min at 20  $\mu\text{L min}^{-1}$ . At this stage, only very low variations of phase ( $\Delta\varphi$  measured as voltage variation,  $\Delta u\varphi \leq 10$  mV) were obtained and signal baseline was easily recovered with working buffer (PBST: PBS containing 0.005 % Tween 20). The assay procedure was as follows:

(1) 4-5 min flow of working buffer (PBST) to stabilize the baseline signal.

(2) Sample injection (250  $\mu\text{L}$ ) and 15 min flow of working buffer.

(3) Regeneration (4 min) with 0.1 M HCl (carbaryl) or NaOH (TBZ) followed by working buffer (1-2 min).

At steps (1) and (2) the flow rate was of  $20 \mu\text{L min}^{-1}$ . For step (3) it was raised to 250 or  $150 \mu\text{L min}^{-1}$  for carbaryl or TBZ assays, respectively. A complete assay cycle, including regeneration, takes around 25 min. Once the last assay had finished, everyday crystals were washed with double distilled water, air-dried and stored at  $4^\circ\text{C}$ .

### 3. Results and discussion

#### 3.1 50 MHz HFF-QCM carbaryl immunosensor

As for most immunosensors, operating with HFF QCMs requires the assessment of the optimal concentrations of immunoreagents involved in the antigen-antibody binding. As known, low molecular weight compounds as carbaryl and thiabendazole should be measured by means of competitive immunoassays (Abad et al., 2001; March et al., 2009). Moreover, indirect competitive immunoassays, in combination with covalent protein immobilization via SAM, provide the highest sensor sensitivity, regeneration capability and reproducibility. In the present work, optimization of immunoreagent concentrations was performed for carbaryl as a model analyte.

##### 3.1.1. Immunoassay optimization: Selection of the optimal assay conjugate concentration and electrode diameter

The pair [BSA-CNH conjugate] - [LIB CNH45 monoclonal antibody] was previously selected as the optimal carbaryl antigen-antibody pair for QCM immunoassays (March et al., 2009). First, 5 and  $10 \text{ mg mL}^{-1}$  of BSA-CNH were immobilized onto 50 MHz QCM SAM-activated electrodes with electrode diameter ranging from 1.0 to 2.0 mm. The concentrations of thiolated compounds were roughly proportional to their respective conjugate concentration and low enough as to produce well organized and compacted monolayers (Chaki and Vijayamohan, 2002). LIB-CNH45 MAb concentration was fixed at  $15.6 \mu\text{g mL}^{-1}$  and, once delivered to the flow cell,

changes in phase response in mV ( $\Delta\mu\phi$ ) were measured as antigen (BSA-CNH) - antibody (LIB-CNH45) interaction took place.

For 5 and 10 mg mL<sup>-1</sup> of immobilized conjugate, electrode surfaces of 2.0 and 1.5 mm diameter gave the highest and very similar signals, whereas 1 mm electrode diameter provided poorer phase shifts. The longest electrode diameter (2.0 mm) also produced the highest baseline drifts and signal noise. Under the same conditions, resonators with 1.5 mm electrode diameter appeared to be the most efficient since they gave the highest signal variation to electrode diameter ratio (average  $\Delta\mu\phi/\varnothing$  of 1568 for 1.5 mm *vs* 825 for 2.0 mm, see supplementary data, table S1).

In relation to the thiolated compounds used for SAM formation, signal variations were fairly similar for both MHDA and TA. MHDA has the longest aliphatic chain, a quality that empowers the assembly of well-ordered monolayers and therefore enhances the efficiency of the covalent binding. Subsequently, lower conjugate concentrations ranging from 0.001 to 1.0 mg mL<sup>-1</sup> were immobilized only on 1.5 mm diameter electrode sensors, employing MHDA as the thiol compound for SAM generation. For BSA-CNH conjugate concentrations in the 0.01 - 1.0 mg mL<sup>-1</sup> range, the obtained phase shifts were the highest and very similar among them (see supplementary data, table S1). BSA-CNH conjugate immobilized at 0.01 mg mL<sup>-1</sup> produced the highest signal variation with the lowest immunoreagent expense.

#### *3.1.2. Immunoassay optimization: Selection of the optimal monoclonal antibody concentration*

Several concentrations of MAb (LIB-CNH45) ranging from 1.0 to 50.0  $\mu\text{g mL}^{-1}$  were assayed in combination with 1, 10 and 100  $\mu\text{g mL}^{-1}$  of BSA-CNH conjugate immobilized on 50 MHz sensor chips with 1.5 mm electrode diameter. Obtained results are displayed in Fig. 1 (triangles). For every conjugate concentration, the HFF-QCM signal was plotted against its

corresponding MAb dose. As expected, higher binding corresponded to increasing both MAb and conjugate concentrations. For 50 MHz sensors, 20  $\mu\text{g mL}^{-1}$  of antibody provided signals near saturation. Furthermore, to fulfill the requirements for competitive immunoassays, the selected MAb concentration should not exceed 50% of the maximum measured signal. Subsequently, the optimum LIB-CNH45 MAb concentration should be  $\leq 5 \mu\text{g mL}^{-1}$ . At any antibody concentration the binding signal obtained for 10  $\mu\text{g mL}^{-1}$  conjugate was almost identical to that of 100  $\mu\text{g mL}^{-1}$ , whereas it drastically dropped at the lowest conjugate concentration (1  $\mu\text{g mL}^{-1}$ ).

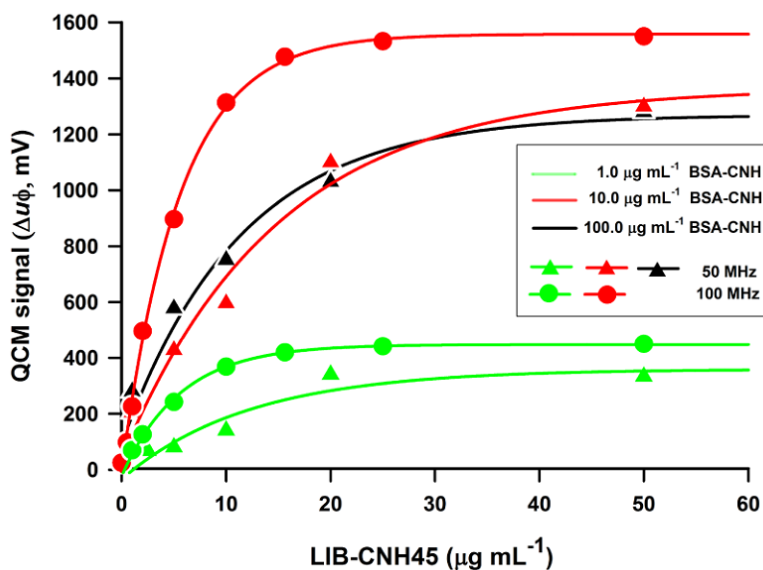


**Fig. 1.** Optimization of the HFF-QCM carbaryl immunoassay. Signal variation obtained with 50 MHz (triangles) and 100 MHz (circles) QCM resonators as a function of LIB-CNH45 MAb concentration for three BSA-CNH conjugate concentrations: 1  $\mu\text{g mL}^{-1}$  (green), 10  $\mu\text{g mL}^{-1}$  (red), and 100  $\mu\text{g mL}^{-1}$  (black).

In summary, for 50 MHz sensor chips these results confirmed the selection of 10  $\mu\text{g mL}^{-1}$  BSA-CNH as the optimal conjugate concentration for

### 3.3 High-Frequency phase shift measurement greatly enhances the sensitivity of QCM immunosensors

immobilization. As regards to antibody optimal concentration,  $2.5 \mu\text{g mL}^{-1}$  of MAb provided optimal signals with the lowest immunoreagent consumption.

#### 3.1.3. 50 MHz HFF-QCM standard curves: Assay sensitivity

Fig. 2 shows a representative real-screen record of signals obtained for different carbaryl concentrations subjected to competitive immunoassays in the same experiment. The lower record represents the phase shifts produced when conjugate-MAb binding occurred. The real-time sensograms include interaction (binding events) and regeneration steps. The interaction took approximately 15 min. As expected for competitive assays, phase shifts decreased when carbaryl concentrations increased. MAb solution was injected every two or three assays to control the constant and slight baseline dropping throughout the assays.

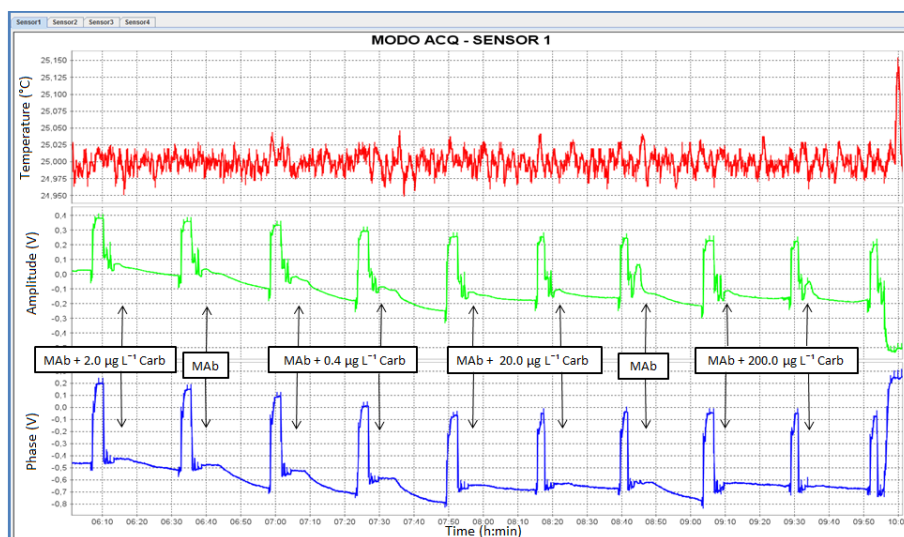


**Fig. 2.** HFF-QCM immunosensor response to analyte concentration. Upper, middle and lower record: real-time monitoring of temperature, amplitude and phase, respectively. The three records correspond to consecutive carbaryl immunoassays performed with a constant, optimized LIB-CNH45 MAb concentration. Arrows indicate sample injection. Regeneration steps appear as high peaks.

Two more additional parameters were measured and recorded simultaneously: amplitude (middle record) and temperature (upper record). As

---

shown, temperature was nearly constant ( $25.00 \pm 0.05$  °C) through the whole experiment. Regarding amplitude, it also changed with binding events. At low carbaryl concentrations, phase shifts were higher than amplitude ones. However, as analyte concentration increased, the observed amplitude variations were higher than those of phase.

Biochemical processes that take place on the sensor surface (adsorption, binding, etc.) cause changes in both phase ( $\Delta\varphi$ ) and amplitude ( $\Delta A$ ):  $\Delta\varphi$  corresponds to the amount of bound mass and  $\Delta A$  to conformation of the bound biomolecules or viscoelastic properties at the sensor-liquid interface (Mitsakakis and Gizeli, 2011). The amplitude change to phase change ratio ( $\Delta A/\Delta\varphi$ ) provides an insight on viscosity changes occurring at the sensor-liquid interface. Some researchers concluded that experimental high  $\Delta A/\Delta\varphi$  ratios are reliable indicators of viscous interactions, whereas small ratios indicate a rigid layer (Tsortos et al., 2008), as desirable for reliable microgravimetric measurements (Kanazawa and Gordon, 1985). Taking into account that carbaryl assays in the immunosensor are competitive, the larger changes in phase than in amplitude obtained for low carbaryl concentrations and the smaller changes in phase than in amplitude produced by high carbaryl concentrations, strongly suggest that  $\Delta\varphi$  mainly accounts for mass changes on the sensor surface. For the purpose of this work, measuring phase changes was indeed enough to quantify the antibody-antigen interactions. Thus, the immunosensor was working in the microgravimetric mode.

Hence, phase shifts were used to generate carbaryl immunosensor standard curves. They were obtained by averaging three individual ones performed with at least two assays per carbaryl concentration. Voltage phase shifts ( $\Delta u\varphi$ ) were normalized by expressing them as:  $100 \times \Delta u\varphi / \Delta u\varphi_0$ , where  $\Delta u\varphi_0$  is the voltage phase decrease at zero analyte concentration (maximum

signal). Experimental points were fitted to the mathematical logistic function according to equation [3].

As depicted in Fig. 3 (triangles, black line), the carbaryl standard curve for the 50 MHz QCM immunosensor showed the typical sigmoidal shape of competitive assays, where signal decreases as analyte concentration increases. I50 value, which is an estimate of assay sensitivity, was  $1.95 \mu\text{g L}^{-1}$ ; the limit of detection (LOD: I90 value) was  $0.23 \mu\text{g L}^{-1}$ , and the working range (WR: I80-20 range) was  $0.50 - 7.20 \mu\text{g L}^{-1}$ .

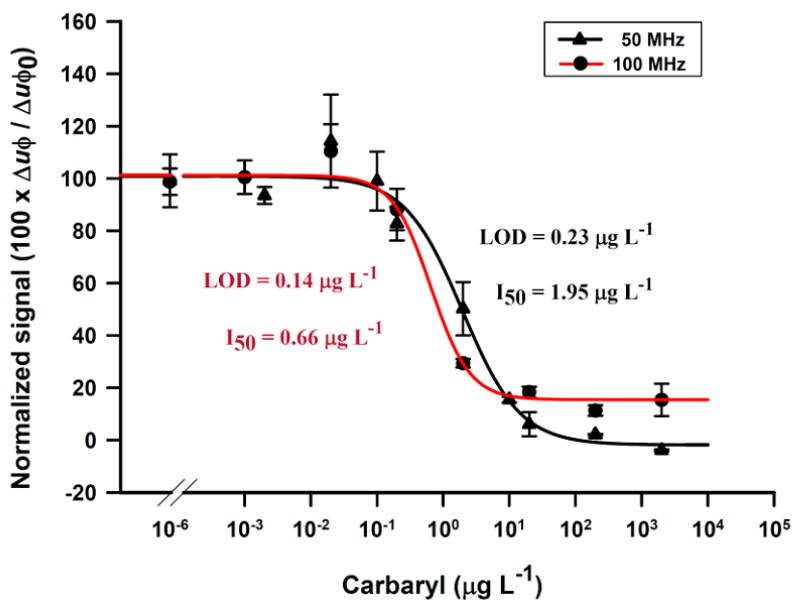


Fig. 3. HFF-QCM carbaryl standard calibration curves performed with 50 MHz (triangles) and 100 MHz (circles) resonators under optimized conditions.

---

### 3.2. 100 MHz<sub>z</sub> HFF-QCM immunosensors

#### 3.2.1. Carbaryl immunoassay optimization: Selection of the immunoreagent concentrations

For 100 MHz QCM immunosensors, carbaryl was also used as a model analyte. Antigen-antibody dose-response curves were performed for only two BSA-CNH conjugate concentrations: 1 and 10  $\mu\text{g mL}^{-1}$ . In this case saturation was again reached close to 20  $\mu\text{g mL}^{-1}$  (Fig 1, circles). Slopes were higher than those of 50 MHz at the same conjugate doses. Not surprisingly, the lowest signals were obtained with the lowest conjugate concentration (1  $\mu\text{g mL}^{-1}$ ). The binding signal for 10  $\mu\text{g mL}^{-1}$  conjugate was high enough as not to consider higher conjugate concentrations worthwhile to be assayed. These results are in agreement with those of 50 MHz and confirm the selection of 10  $\mu\text{g mL}^{-1}$  as the optimal concentration for BSA-CNH conjugate immobilization, for either 50 or 100 MHz resonators. The higher responses obtained with 100 MHz enabled lowering the LIB-CNH45 MAb concentration for the competitive assay down to 2.0  $\mu\text{g mL}^{-1}$ .

In previous works with conventional 9 MHz QCM sensors, the MAb dose-response curve at 10  $\text{mg mL}^{-1}$  assay conjugate reached saturation at around 200  $\mu\text{g mL}^{-1}$  MAb (March et al. 2009). For 50 and 100 MHz resonators, the saturating concentration was roughly one order of magnitude lower than that of 9 MHz sensors, which certainly pointed towards an improvement of at least one order of magnitude in sensor sensitivity. This improvement allowed us to significantly reduce not only the MAb but also the conjugate concentration: they were around one and three orders of magnitude, respectively, lower than those employed for the 9 MHz carbaryl immunosensor.

#### 3.2.2. Carbaryl standard curves: Electrode diameter selection and assay sensitivity

For 100 MHz QCM immunosensors, preliminary experiments were performed with the same electrode diameter previously selected for the 50

MHz immunosensor: 1.5 mm. But, when the highest carbaryl concentrations were assayed, phase variations were too large and yielded poor calibration curves with unacceptable asymptotic minimum over 30% of the maximum assay signal (data not shown). Other drawbacks found were baseline drifts and some unsteady sensor response. This unsuitable behavior seemed to decrease when lower electrode surfaces (1.0 and 0.5 mm diameter) were used. The performance of 0.5 mm diameter sensors was not adequate because signal decayed to undesirable levels. In contrast, immunoassays performed on functionalized 1.0 mm diameter electrodes provided standard curves with quite good sensitivity, similar to that of 1.5 mm but with an acceptable asymptotic minimum below 20% of the maximum signal.

The inadvisable response provided by 1.5 mm in relation to that of 1.0 mm electrode diameter 100MHz resonators could be explained in terms of theoretical considerations on the crystal quality factor. In brief, HFF-QCM resonators have lower quality factors than conventional low frequency ones. In addition, this factor further decreases in usual liquid applications, such as biosensors, in comparison with “in air”. That is, in liquid media, as evidenced from the conductance-frequency relationship, a dramatic increase in the width of the conductance peak as well as a decrease in the maximum conductance accompanies liquid loading (Lin et al., 1993). This fact can account for the overlapping between spurious signals and fundamental resonance peak. In order to minimize this effect in HFF-QCM resonators, additional studies pointed towards a reduction of the electrode diameter in consonance with the quartz thickness decrease (Kao et al., 2008). Ever since 1964, King Jr. postulated that the sensitivity of detection was inversely proportional to the square of the electrode diameter and the resonator thickness. Recently, Liang et al. (2013) reported that for HFF-QCM chips of about 73 MHz, quality factor increases as electrode diameter decreases for a given range. Thus, there is a need to find out a crystal design compromise in order to get the optimal

---

electrode diameter to crystal thickness ratio for a given HF frequency. In our case, 1.0 mm seemed to be better than 1.5 mm electrode diameter for our 100 MHz HFF-QCM immunosensor application.

Calibration curves were then obtained on 100 MHz, 1.0 mm electrode diameter sensors, functionalized with  $10 \mu\text{g mL}^{-1}$  of BSA-CNH conjugate and using  $2.0 \mu\text{g mL}^{-1}$  of LIB-CNH45 MAb. As for that of 50 MHz, the 100 MHz carbaryl standard curve depicted in Fig. 3 (circles, red line) is the mean of three individual ones.  $I_{50}$  value was  $0.66 \mu\text{g L}^{-1}$ , LOD was  $0.14 \mu\text{g L}^{-1}$  and WR was 0.26 -  $1.73 \mu\text{g L}^{-1}$ .

From these analytical parameters, an effect on the sensitivity could be observed with 100 MHz in relation to 50 MHz QCM sensor chips: sensitivity parameters for 100 MHz chips were around twice smaller than those of 50 MHz ( $0.66 \mu\text{g L}^{-1}$  vs  $1.95 \mu\text{g L}^{-1}$   $I_{50}$ , and  $0.14 \mu\text{g L}^{-1}$  vs  $0.23 \mu\text{g L}^{-1}$  LOD, for 100 and 50 MHz, respectively). These results confirmed those obtained in antigen-antibody dose-response curves depicted in Fig. 1, in which slopes for 100 MHz were higher than slopes for 50 MHz. Moreover, as expected, lowering the antibody concentration as allowed by 100 MHz QCM sensors lead to improved analytical sensitivity parameters.

### 3.2.3. *Thiabendazole HFF-QCM immunosensor*

To further explore the potential applications of HFF-QCM technology for sensitive pesticide determination, a TBZ immunosensor was also developed. To this purpose, experimental parameters like SAM composition, assay conjugate and MAb concentrations were fixed according to those reported for SPR (Estevez et al., 2012). Briefly,  $1.0 \mu\text{g mL}^{-1}$  of LIB-TN3C13 MAb was used on sensors functionalized with  $20 \mu\text{g mL}^{-1}$  of BSA-TN3C conjugate. The resonator employed was 100 MHz with 1.0 mm diameter active electrode, in accordance with those previously selected as optimal fundamental frequency and electrode size HFF-QCM sensor chip for carbaryl.

Fig. 4 represents the mean of two individual TBZ curves. Phase shifts obtained for TBZ standards in the  $10^{-3}$ -  $5.0 \times 10^2 \mu\text{g L}^{-1}$  range were very similar to those obtained for carbaryl. As regards to the functionalized surface regeneration, a strong basic solution (0.1 M NaOH) had to be employed for a shorter time period (1-2 min), in order to ensure the effective LIB-TN3C13 monoclonal antibody detachment from the sensor surface. The  $I_{50}$  value, LOD and working range were: 0.80, 0.06 and  $0.16$ - $3.68 \mu\text{g L}^{-1}$  respectively. These analytical parameters are roughly the same order of magnitude as those previously reported for TBZ in ELISA (Abad et al., 2001) and in the SPR immunosensor (Estevez et al., 2012).

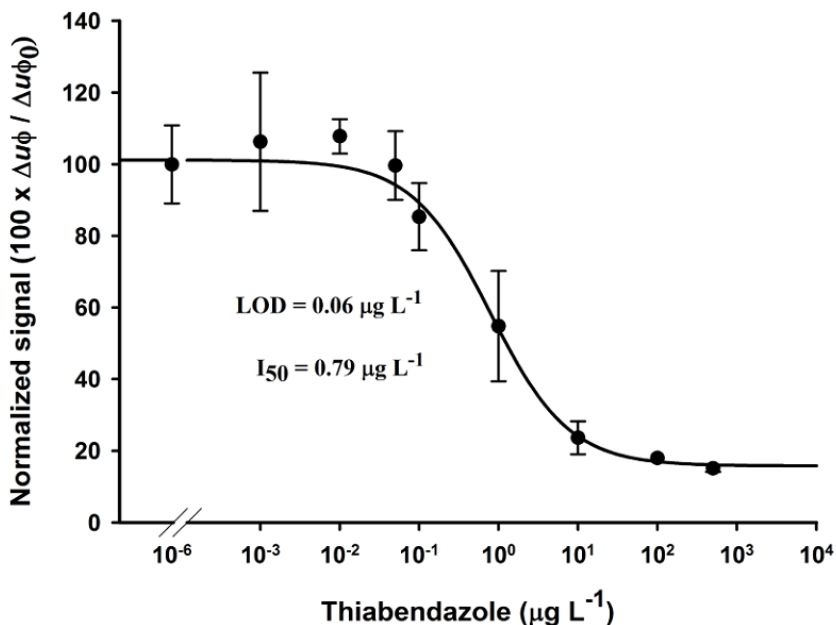


**Fig. 4.** Standard calibration curve for thiabendazole performed with 100 MHz QCM resonator, under optimized conditions.

### 3.3 Comparison between pesticide immunosensors and ELISAs

The parameters obtained from carbaryl standard curves with the 50 MHz QCM sensor (Fig. 3, triangles, black line) entailed a 50-fold decrease in the LOD with respect to that for conventional 9 MHz QCM crystals (March et al., 2009). Further LOD improvement (up to two orders of magnitude) was achieved by increasing twice the sensor fundamental frequency (100 MHz, Fig. 3, circles, red line). These results are summarized in Table 1, where the performance of different carbaryl immunosensors, under roughly the same biochemical conditions, is compared. As shown, for the three analytical parameters studied ( $I_{50}$  value, LOD and WR), QCM immunosensors operating at high fundamental frequency (50 or 100 MHz) gave lower values than SPR. The limit of detection and  $I_{50}$  value achieved with 100 MHz resonators were one order of magnitude and five-fold lower than their respective values reported for SPR (Mauriz et al., 2006).

**Table 1**

Analytical performance comparison between different carbaryl immunosensors and ELISA.

Analytical parameters ( $\mu\text{g L}^{-1}$ )	ELISA		SPR <sup>3</sup>	QCM: Fundamental Resonance Frequency (MHz)			
	Standard <sup>1</sup>	Optimized <sup>2</sup>		9 <sup>4,a</sup>	10 <sup>5,b</sup>	50 <sup>b</sup>	100 <sup>b</sup>
LOD	0.13	0.01	1.41	13.30	4.00	0.23	0.14
$I_{50}$	0.72	0.06	3.12	30.34	16.70	1.95	0.66
WR	0.23-2.36	0.02-0.18	1.91-5.75	18.30-50.30	7.00-35.00	0.50-7.20	0.26-1.72

<sup>1</sup> Standard ELISA performed with the same immunoreagents as SPR and QCM immunosensors (Abad et al., 1997)

<sup>2</sup> Abad and Montoya, 1997

<sup>3</sup> Mauriz et al., 2006

<sup>4</sup> March et al., 2009

<sup>5</sup> Montagut et al., 2011

<sup>a</sup> Frequency shift measurements

<sup>b</sup> Phase shift measurements at a fixed frequency.

Nevertheless, the three immunosensing methodologies (conventional QCM, SPR and HFF QCM) still yielded higher  $I_{50}$  values (indicating a lower sensitivity) than the previously reported optimized ELISA (Abad and Montoya, 1997). This ELISA was in fact around one order of magnitude more sensitive than the best QCM immunosensor (100 MHz). However, the immunoreagents employed in the optimized ELISA could not be used in the high frequency QCM because of the immunosensor regeneration requirements. Anyway, if the comparison was established between the 100 MHz QCM immunosensor and the ELISA performed under the same biochemical conditions (Abad et al., 1997), HFF QCM reached the same analytical performance. As regards to the working ranges for high frequency QCM, they were wider than those reported for SPR and conventional QCM and closer to ELISA working range.

**Table 2**

Analytical performance comparison between HFF-QCM and SPR immunosensors and ELISA for thiabendazole.

---

Analytical parameters ( $\mu\text{g L}^{-1}$ )	ELISA <sup>1</sup>	SPR <sup>2</sup>	100 MHz HFF-QCM
LOD	0.02	0.13	0.06
$I_{50}$	0.2	0.64	0.80
WR	0.05 – 0.90	0.23 – 1.88	0.16 – 3.68

---

<sup>1</sup> Abad et al, 2001

<sup>2</sup> Estevez et al., 2012

For the thiabendazole fungicide, LOD was about 3 times higher than in ELISA and 2 times lower than in SPR performed under the same biochemical conditions (Table 2). Moreover, as expected from the lower slope of the HFF-QCM immunosensor standard curve, its working range was two-fold widened

---

with respect to that of SPR (Estevez et al., 20012), thus reaching the same width as the reference ELISA (Abad et al., 2001).

#### 4. Conclusions

Despite the widespread use of QCM technology, some challenges such as the improvement of the sensitivity and the limit of detection of QCM biosensors still remained unsolved. With the help of a new electronic sensor characterization approach, a sensitive HFF-QCM immunosensor has successfully been developed and tested for its use in pesticide determinations. This novel technology is based on the phase/mass relationship and allows a sensitive mass sensing by means of phase change measurements. Moreover, it also admits not only phase but also amplitude measurements, which could in turn allow the analysis of mass and viscosity changes during bio-interactions on the basis of the acoustic ratio (Dewilde et al., 2013).

Carbaryl insecticide chosen as a model analyte allowed us to compare the analytical performance of several immunosensors with respect to that of ELISA taken as the reference immunoassay. Analytical parameters ( $I_{50}$  value, LOD and working range) of the 100 MHz HFF-QCM carbaryl immunosensor indicated enhanced sensitivity as regards to that of either QCM or SPR immunosensors. The highest improvement was attained for LOD: around 10 and 100-fold improvement with respect to those of SPR and conventional QCM, respectively. Hence, sensitivity parameters approached the previously reported for the optimized ELISA. These features proved that lower immunoreagent consumption is needed and higher analytical sensitivity is achieved when signal is empowered. With regards to the standard curve for TBZ fungicide immunosensor, sensitivity parameters were the same order of magnitude as those of SPR immunosensor and ELISA performed under the same conditions.

To the best of our knowledge, this is the first high frequency QCM immunosensor successfully developed for demanding analytical applications,

such as pesticide detection. Despite the high sensitivity and versatility of the developed HFF-QCM platform, further work is still required. The influence of electrode diameter/crystal thickness ratio on the signal, as well as the relationship between amplitude/phase and viscoelastic phenomena occurring at the sensor-liquid interface, should be dealt with promptly. Experiments aimed to increase sensitivity by improving immobilization methods, and to elucidate the contribution of the electrode diameter on signal quality, are now in progress.

### **Acknowledgments**

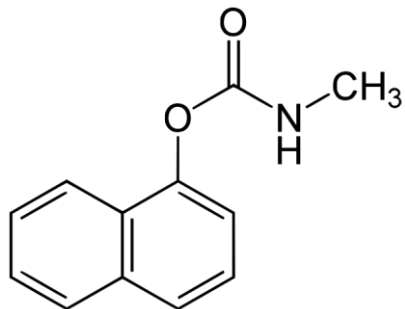
We would like to acknowledge Federico Martin and Juan Antonio Buitrago for their excellent technical assistance. This work was supported by European Regional Development Fund (ERDF) and the Spanish Ministry of Economy and Competitiveness (DETECTA IPT-2012-0154-300000 project).

### **References**

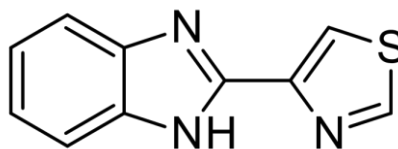
- Abad, A., Manclús, J.J., Moreno, M.J., Montoya, A. 2001. *J. AOAC Int.* 84, 156-161.
- Abad, A., Montoya, A., 1997. *J. Agric. Food Chem.* 45, 1495-1501.
- Abad, A., Primo, J., Montoya, A., 1997. *J. Agric. Food Chem.* 45, 1486-1494.
- Chaki, N.K., Vijayamohan, K., 2002. *Biosens. Bioelectron.* 17, 1-12.
- Dewilde, A.H., Wang, G., Zhang, J., Marx, K.A., Therrien, J.M., 2013. *Anal. Biochem.* 439, 50-61.
- Estevez, M.C., Belenguer, J., Gomez-Montes, S., Miralles, J., Escuela, A.M., Montoya, A., Lechuga, L.M., 2012. *Analyst* 137, 5659-5665.
- Kanazawa, K.K., Gordon, J.G., 1985. *Anal. Chim. Acta* 175, 99-105.
- Kao, P., Patwardhan, A., Allara, D. Tadigadapa, S., 2008. *Anal. Chem.* 80, 5930-5936.
- King, Jr., W.H., 1964. *Anal. Chem.* 36, 1735-1739.
- Liang, J., Huang, J., Zhang, T., Zhang, J., Xuefeng Li, Ueda T., 2013. *Sensors* 13, 12140-12148.

- 
- Lin, Z., Yip, C.M., Joseph, I.S., Ward, M.D., 1993. *Anal. Chem.* 11, 1546-1551.
- March, C., Manclús, J.J., Jiménez, Y., Arnau, A., Montoya, A., 2009. *Talanta* 78, 827-833.
- Marx, K.A. 2003. *Biomacromolecules* 4, 1099-1120.
- Marx, K.A., 2007. The quartz crystal microbalance and the electrochemical QCM : applications to studies of thin polymer films, electron transfer systems, biological macromolecules, biosensors, and cells, in : Steinem, C., Janshoff, A., (Eds), *Piezoelectric Sensors*. Springer, Berlin, pp. 371-429.
- Mauriz, E., Calle, A., Abad, A., Hildebrant, A., Barceló, D., Montoya, A., Lechuga, L.M., 2006. *Biosens. Bioelectron.* 21, 2129-2136.
- Michalzik, M., Wendler, J., Rabe, J., Büttgenbach, S., Bilitewski, U., 2005. *Sensor. Actuat. B* 105, 508-515.
- Mitsakakis, K., Gizeli, E., 2011. *Anal. Chim. Acta* 699, 1-5.
- Montagut, Y.J., García, J.V., Jiménez, Y., March, C., Montoya, A., Arnau, A., 2011. *Sensors* 11, 4702-4720.
- Sagmeister, B.P., Graz, I.M., Schwödiauer, R., Gruber, H., Bauer, S., 2009. *Biosens. Bioelectron.* 24, 2643-2648.
- Sauerbrey, G., 1959. *Z. Phys.* 155, 206-222.
- Sota, H., Yoshimine, H., Whittier, R.F., Gotoh, M., Shiohara, Y., Hasegawa, Y., Okahata, Y., 2002. *Anal. Chem.* 74, 3592-3598.
- Speight, R., Cooper, M.A., 2012. *J. Mol. Recognit.* 25, 451-473.
- Stehrer, B.P., Schwödiauer, R., Bauer, S., Graz, I.M., Pollheimer, P.D., Gruber, H., 2010. *Procedia Engineering* 5, 835-837.
- Tsartos, A., Papadakis, G., Mitsakakis, K., Melzak, K. A., Gizeli, E., 2008. *Biophys. J.* 94, 2706-2715.
- Uttenthaler, E., Schráml, M., Mandel, J., Drost, S., 2001. *Biosens. Bioelectron.* 16, 735-743.
- Yoshimine, H., Kojima, T., Furusawa, H., Okahata, Y., 2011. *Anal. Chem.* 83, 8741-8747.

### Appendix A: Supplementary Material



**Carbaryl**



**Thiabendazole**

**Fig. S1:** Analyte structures

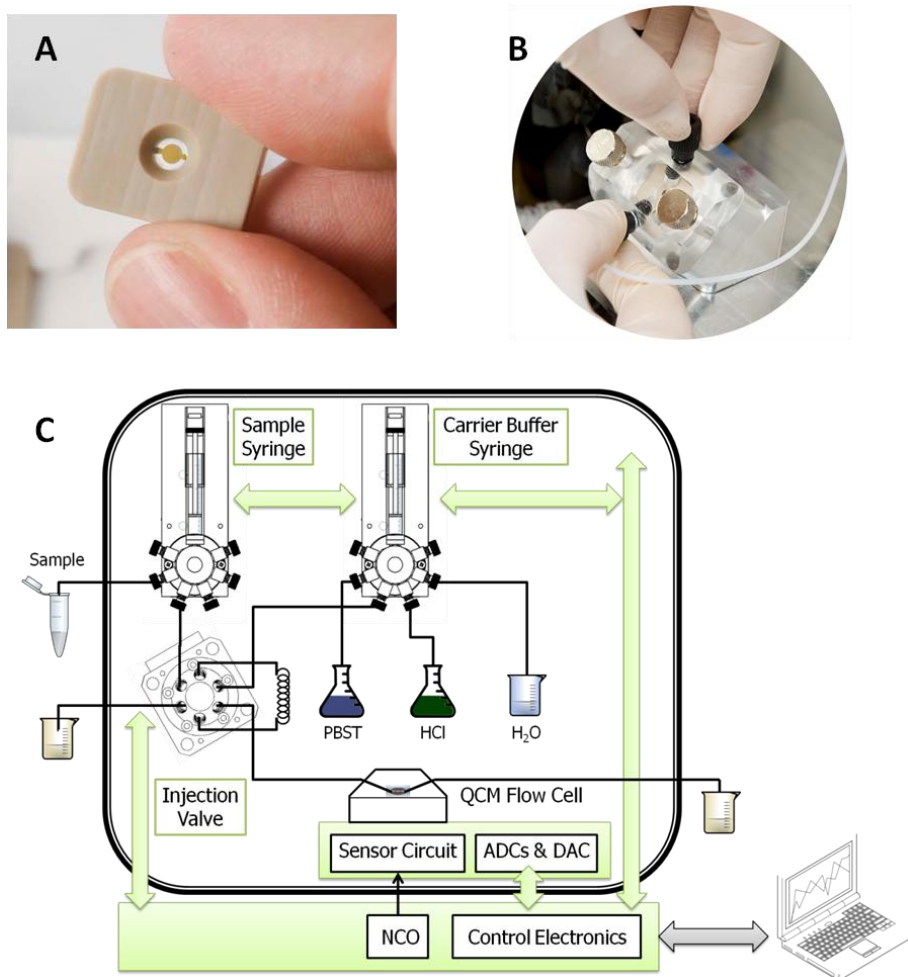


**Fig. S2:** HFF-QCM immunosensor set-up. (A) HFF-QCM chip. (B) Flow cell assembly ([www.awsensors.com](http://www.awsensors.com)). (C) Scheme of the AWS A10 test platform, showing the flow-through system and electronic subsystems.

3.3 High-Frequency phase shift measurement greatly enhances the sensitivity of QCM immunosensors

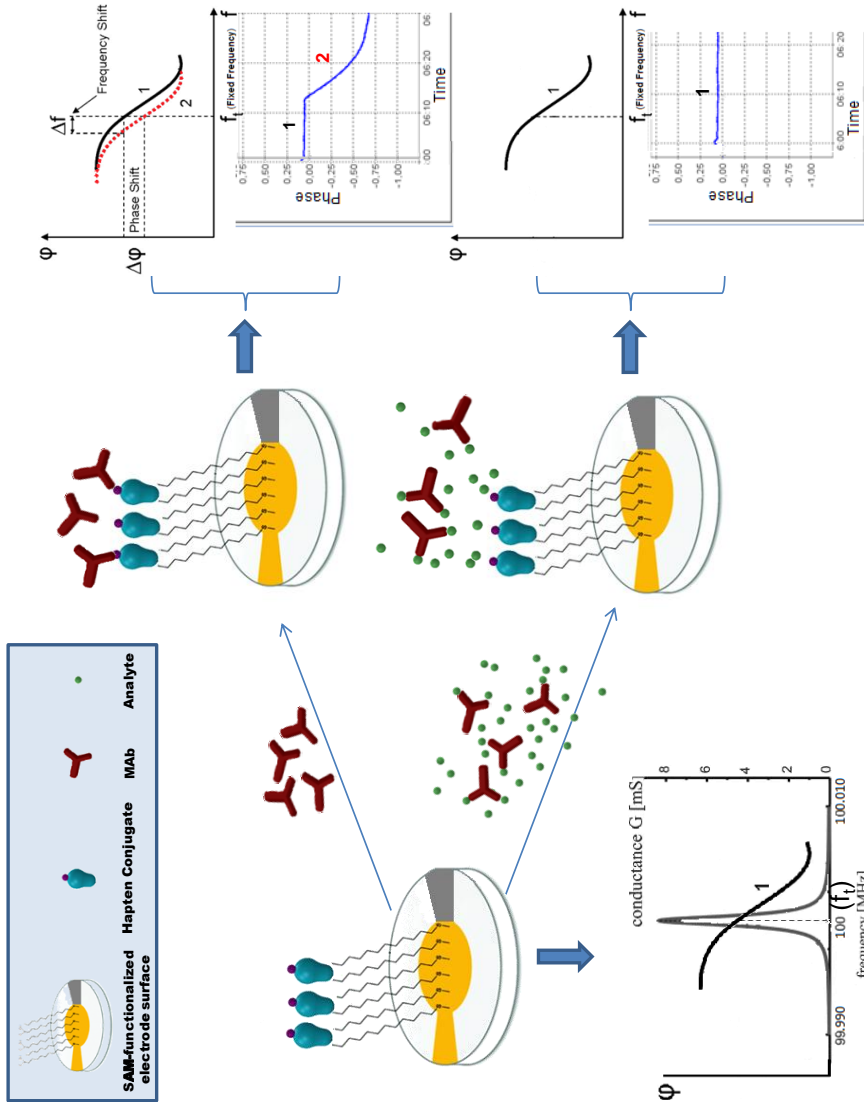


Fig. S3: Scheme of the sensing interface and signal transduction strategy.

**Table S1**

Evaluation of 50 MHz QCM signals produced by the interaction between LIB-CNH45 monoclonal antibody ( $15.6 \mu\text{g mL}^{-1}$ ) and the immobilized BSA-CNH conjugate at different concentrations. The conjugate was covalently bound on SAM activated gold surfaces with electrode diameters ranging from 1.0 to 2.0 mm.

Gold electrode diameter $\varnothing$ (mm)	Thiolated compound (mM)		[BSA-CNH] ( $\text{mg mL}^{-1}$ )	Phase shift		$\Delta u\varphi/\varnothing$ ( $\text{mV mm}^{-1}$ )
				$\Delta u\varphi$ (mV)	rSD (%) <sup>3</sup>	
2.0	TA <sup>1</sup>	10.0	10.0	2200	11.0	1100
	MHDA <sup>2</sup>	1.0	5.0	1650	5.3	825
1.5	TA	10.0	10.0	2000	10.6	1333
		1.0	5.0	2450	10.4	1633
	MHDA	1.0	5.0	2255	7.75	1503
		1.0	1.0	900	15.9	600
		0.5	0.1	1100	11.9	733
		0.05	0.01	1142	2.7	761
1.0		0.005	0.001	235	9.2	157
	TA	10.0	10.0	470	12.0	470
	MHDA	1.0	5.0	525	12.1	525

<sup>1</sup> TA: Thioctic acid

<sup>2</sup> MHDA: Mercaptohexadecanoic acid

<sup>3</sup> Relative standard deviations (rSD) were calculated from at least three independent measurements.

3.3 High-Frequency phase shift measurement greatly enhances the sensitivity of QCM immunosensors

---

### **3.4 Love Mode Surface Acoustic Wave and High Fundamental Frequency Quartz Crystal Microbalance immunosensors for the detection of carbaryl pesticide**

J.V. García, M.I. Rocha, C. March, P. García, L.A. Francis, A. Montoya, A. Arnau, Y. Jimenez

Procedia Engineering, Volume 87, 2014, Pages 759-762, ISSN 1877-7058,

<http://dx.doi.org/10.1016/j.proeng.2014.11.649>.

© 2014 The Authors. Published by Elsevier Ltd.

Peer-review under responsibility of the scientific committee of Eurosensors 2014.

**Abstract**

In this work we determined the Sensitivity (estimated as the I50 value) and Limit of Detection (LOD) for the immunodetection of carbaryl pesticide with two different types of acoustic wave sensors: High Fundamental Frequency Quartz Crystal Microbalance (HFF-QCM) and Love Mode Surface Acoustic Wave (LM-SAW). Results were compared with others previously reported using different sensors and techniques, like traditional QCM, Surface Plasmon Resonance (SPR) and Enzyme-Linked ImmunoSorbent Assay (ELISA). We used the AWS-A10 research platform (AWSensors, Spain) to perform the experiments. We obtained I50 values of 0.31  $\mu\text{g/L}$  and 0.66  $\mu\text{g/L}$ , and LODs of 0.09  $\mu\text{g/L}$  and 0.14  $\mu\text{g/L}$ , for 120 MHz LM-SAW and 100 MHz HFF-QCM devices, respectively. Both the sensitivities and LODs of the immunosensors improved previously reported SPR and QCM results by one and two orders of magnitude, respectively, and reached those of ELISA.

**Keywords:** "Acoustic wave sensor; Biosensor; Immunosensor; Carbaryl; Pesticide; QCM; SAW; Love wave; High Fundamental Frequency"

---

## 1. Introduction

Acoustic wave sensors are widely used in in-liquid biosensing applications [1]. One of these applications is the label-free pesticide analysis in fruit and juices [2]. However, the sensitivity and LOD of acoustic immunosensors should be improved to comply with regulations and to extend their applicability to more demanding applications, such as the analysis of drinking water. In this work we propose two acoustic technologies, HFF-QCM and LM-SAW, for the detection of a Low Molecular Weight (LMW) compound, carbaryl pesticide. Carbaryl was chosen as model analyte since it was used as a reference LMW compound by previous works, both for acoustic and other techniques such as SPR and ELISA [2,3,4] We sought to enhance the analytical performance of the proposed acoustic biosensors by improving the sensitivity of the transducer devices -using sensors working at higher frequencies than those previously used in this application -, and by reducing the readout system noise and improving the flow injection analysis (FIA) system - using a dedicated system to perform the experiments -.

## 2. Materials and methods

### 2.1. LM-SAW sensors, HFF-QCM sensors and flow cells

The Love-Mode sensors used were based on a 17×8.4 mm and 0.35 mm thick single-side polished Z-propagating AT-cut quartz substrates. The silicon dioxide (SiO<sub>2</sub>) guiding layer had a thickness of 3 μm. The input and output IDT consisted of 100 double-finger pairs designed for a sensor synchronous frequency of 120 MHz. The sensing area consisted of 10 nm of chrome and 50 nm of gold.

The HFF-QCM sensors used were based on AT-cut 100 MHz HFF-QCM inverted mesa resonators. The electrode had 1mm of diameter and its structure consisted of a gold layer of 90 nm deposited over a 5 nm chromium

adhesion layer. The resonators were bonded permanently to a support made of polyether ether ketone (PEEK) using an epoxy adhesive. The electrical contact between resonator electrodes and copper pads in the lower part of the peek support was made by a conductive epoxy.

Flow cells for both types of sensors were designed and manufactured considering the mechanical, electrical and chemical requirements of the application. They allowed a fast and easy installation and replacement of the sensors, and a convenient interface to the system (Figure 1b).

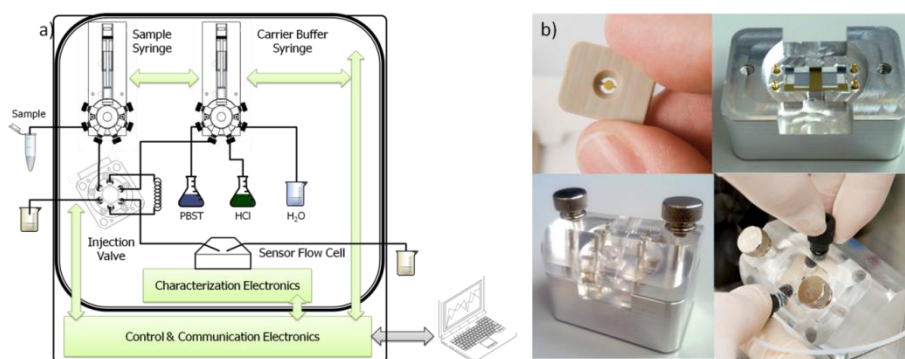


**Fig. 1.** (a) Block diagram of the AWS A10RP system; (b) Picture of the sensors and flow cells used in this work.

## 2.2. Experimental set-up

We used the research platform AWS-A10 (Advanced Wave Sensors S.L., Spain) to perform the experiments. The platform consists of an electronic characterization system, an automated FIA system, and a control and communications system (Figure 1a). The proposed system allows the comparison of both devices, measured by the same characterization system and under similar experimental conditions. The electronic characterization system is based on the open loop phase detection technique at a fixed frequency, which allows the characterization of very high frequency acoustic sensors without a significant increase of noise [5,6,7]. A PC software collects data from the

---

characterization system and controls all the elements of the AWS-A10 Platform, including the FIA system. All measurements were performed at a temperature of 25°C ± 0.1°C.

### 2.3. Functionalization protocol

The sensing areas of the sensors were functionalized following a similar procedure, chemicals and reagents as described [2]. Sensors were cleaned by exposure to UV/ ozone using the UV/Ozone ProCleaner (BioForce Nanosciences Inc., USA). After exposure, sensors were rinsed with distilled water and ethanol, and dried with nitrogen gas. Active areas were functionalized by immobilizing BSA-CNH carbaryl hapten conjugates (10 µg/mL) through the formation of a mercaptohexadecanoic acid self-assembled monolayer (SAM).

### 3. Results

The immunoassays were competitive inhibition tests based on the conjugate coated format. A fixed concentration of 2 µg/mL of the monoclonal antibody (Mab) LIB-CNH45 [3] was mixed with standard solutions of the analyte at different concentrations. In this format the analyte inhibits the antibody binding to the immobilized conjugate. Thus, increasing concentrations of analyte reduce the measured signal changes.

Figure 2a shows the immunoassay cycle followed for each sample. The protocol consisted of pumping phosphate buffer solution containing 0.005% Tween (PBST) at a flow rate of 20 µL/min at least for 5 min (only 1 min. shown in figure), next injecting the sample (250 µL) into the main flow for 15 min at the same flow rate. At this point, the change in the phase signal with respect to that obtained at the time of sample injection was measured ( $\Delta u\varphi = u\varphi - u\varphi_0$ ). The regeneration of the active area was performed by pumping 0.1M HCl for 4 min and PBST again for 4min., at a flow rate of 250 µL/min.

3.4. Love Mode Surface Acoustic Wave and High Fundamental Frequency Quartz Crystal Microbalance immunosensors for the detection of carbaryl pesticide

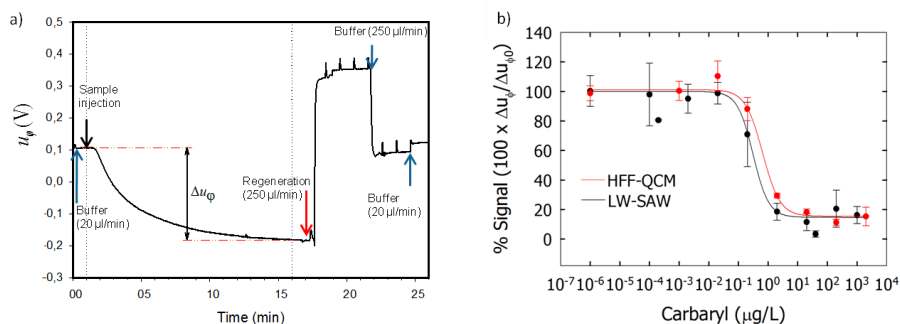


**Fig. 2.** (a) Immunoassay cycle; (b) LM-SAW and HFF-QCM standard calibration curves for carbaryl determination

All samples were injected and measured at least in duplicate. Figure 2b shows the standard curves obtained by representing the phase signal change versus the analyte concentration. The measurements were normalized as the percentage of the maximum signal (the phase signal change in the absence of analyte). Experimental points were fitted to a four-parameter logistic equation and the analytical parameters were extracted from the fitted curve.

**Table 1.** Analytical performance of carbaryl determination for different immunosensing techniques

	ELISA [3]	SPR [4]	QCM 10MHz $\Delta f$ [2]	QCM 10MHz $\Delta \phi$ [8]	HFF-QCM 100MHZ	LM-SAW 120MHZ
Sensitivity ( $\mu\text{g}/\text{L}$ )	0.72	3.12	30.00	16.70	0.66	0.31
L.O.D ( $\mu\text{g}/\text{L}$ )	0.13	1.41	11.00	4.00	0.14	0.09
Working Range ( $\mu\text{g}/\text{L}$ )	0.23 - 2.36	1.90 - 5.75	15.00 – 53.00	7.00 – 35.00	0.26 – 1.73	0.14 – 1.63

The developed immunosensors achieved I50 values of 0.31  $\mu\text{g}/\text{L}$  and 0.66  $\mu\text{g}/\text{L}$ , and LODs of 0.09  $\mu\text{g}/\text{L}$  and 0.14  $\mu\text{g}/\text{L}$ , for 120 MHz LM-SAW and 100 MHz HFF-QCM devices, respectively (Table 1). We compared these results with previously reported ones, using different technologies but the same

---

target analyte and immunoreagents. The sensitivities and LODs of the developed immunosensors improved those of SPR [4] and QCM (with classical frequency shift measurement [2] and the phase shift measurement approach [8]). The improvement was in the range of one and two orders of magnitude respectively. Analytical parameters also approached ELISA's ones [3].

#### **4. Conclusions**

We have developed both HFF-QCM and LM-SAW immunosensors for the detection of a LMW compound, the Carbaryl pesticide. The enhancement of the analytical performance sought was accomplished. Compared with QCM results previously reported, we achieved an improvement of about two orders of magnitude in sensitivity and LOD with both technologies. The obtained I50 and LOD values also exceed by one order of magnitude those reported for SPR and reached those of ELISA. The high sensitivity reached by these immunosensors could allow label free pesticide analysis at concentrations close to the European Maximum Residue Levels for drinking water.

#### **Acknowledgements**

The authors acknowledge: the Spanish Ministry of Economy and Competitiveness and the European Regional Development Fund (ERDF) for their financing support through the grant of the INNPACTO 2012 project (DETECTA IPT-2012-0154-300000) and J.V. García's Fellowship, ref. AP2007-03745 of the FPU (Formación de Profesorado Universitario) program; the Mexican Consejo Nacional de Ciencia y Tecnología (CONACyT) for M.I. Rocha-Gaso's PhD CONACyT Fellowship.

#### **References**

[1] R.E. Speight, M.A. Cooper, A survey of the 2010 quartz crystal microbalance literature, *J Mol Recognit.* 25 (2012) 451-73.

[2] C. March, J.J. Manclús, Y. Jiménez, A. Arnau, A. Montoya, A piezoelectric immunosensor for the determination of pesticide residues and metabolites in fruit juices, *Talanta* 78 (2009) 827-33.

[3] A. Abad, J. Primo, A. Montoya, Development of an Enzyme-Linked Immunosorbent Assay to Carbaryl. 1. Antibody Production from Several Haptens and Characterization in Different Immunoassay Formats, *J. Agric. Food Chem.* 45 (1997) 1486-1494.

[4] E. Mauriz, A. Calle, A. Abad, A. Montoya, A. Hildebrandt, D. Barceló, L.M. Lechuga, Determination of carbaryl in natural water samples by a surface plasmon resonance flow-through immunosensor, *Biosens Bioelectron.* 21 (2006) 2129-36.

[5] A. Arnau, Y. Montagut, J.V. García, J.V., Y. Jiménez, A different point of view on the sensitivity of quartz crystal microbalance sensors, *Meas. Sci. Technol.* 20 (2009) 124004.

[6] Arnau, A., García, P., García, J.V., Jiménez, Y., Montagut, Y., Reig, A., (WO2010149811) Method and device for nanogravimetry in fluid media using piezoelectric resonators.

[7] Y.J. Montagut, J.V. García, Y. Jiménez, C. March, A. Montoya, A. Arnau, Frequency-shift vs phase-shift characterization of in-liquid quartz crystal microbalance applications, *Rev. of sci. instrum.* 82 (2011) 064702.

[8] Y. Montagut, J.V. García, Y. Jiménez, C. March, A. Montoya, A. Arnau, Validation of a Phase-Mass Characterization Concept and Interface for Acoustic Biosensors, *Sensors (Basel)*. 11(5) (2011) 4702-4720.

## 4 Concluding remarks

---

During the development of this thesis the main objectives of the proposed work have been accomplished. Two different electronic characterization systems have been proposed, designed and validated.

For the automatic capacitance compensation system proposed in chapter 3.1, we can conclude that we managed to cover the goals we set ourselves. The proposed circuit is capable of continuously monitoring the required sensor parameters, providing different signals that allow the monitoring of experimental processes. Furthermore, a data acquisition system, presented in Appendix I, has been developed to fulfill the requirements that any standalone system must have. In relation of the experimental results presented in this chapter, we can conclude that the designed circuit compensates effectively and accurately the parallel capacitance, allowing a proper circuit operation even for high dampening loads. Furthermore, this compensation is made automatically and simultaneously with the MSRF monitoring. So, parallel capacitance changes

---

that can occur during the measurement may be compensated without user intervention.

During the validation process of the system, we have observed and identified different discrepancies between the results provided by the system and those provided by a reference impedance analyzer. These discrepancies have been clearly identified, and a feasible solution based on a quite similar principle of operation to overcome them has been proposed.

The instrument is completely autonomous, it has an internet connection and a power source, can be controlled remotely, and you can have access to experiment data from any PC with appropriate software. Future lines to improve the sensor system are aimed to improve the accuracy of measurements by the electronic circuitry and to improve the sensitivity in detecting various physical properties using QCM sensors. This approach would face the problem of the different gain of the amplifiers, which at higher frequencies is even more pronounced. To address this problem, a new system, which is proposed, would be necessary.

Regarding the high resolution characterization system whose concept has been introduced in chapter 3.2, we can conclude that the measurements carried out with the developed high frequency system were satisfactory for working in liquid media and high resolution applications. The proposed system is simple, small, fast and with a high integration capacity. The improvement of sensitivity has been accomplished as the proposed system has the ability to characterize acoustic resonators of higher fundamental frequencies. The system provides both the phase-shift and attenuation of HFF-QCM and traditional QCM sensors, as well as, phase shift and Insertion Loss for Love Wave devices with a high signal to noise ratio.

In Chapter 3.3 and 3.4 experiments were performed with the aim of validating the contributions of this Thesis as suitable for biosensing

applications. The proposed electronic characterization system was proven to be valid for both HFF-QCM and LM-SAW immunosensors for the detection of a low molecular weight compound, the Carbaryl pesticide. A conjugate-coated immunoassay format was chosen, since it allows the regeneration of the sensor surface. Hence, competitive assays were performed where the carbaryl analyte competed with the immobilized hapten-conjugate for binding to a fixed and limited amount of antibody in the solution. The regeneration of the immunosensor was possible using hydrochloric acid. The enhancement of the analytical performance sought was accomplished. Compared with QCM results previously reported, we achieved an improvement of about two orders of magnitude in sensitivity and LOD with both technologies. The obtained I50 and LOD values also exceed by one order of magnitude those reported for SPR and reached those of ELISA. The high sensitivity reached by these immunosensors could allow label free pesticide analysis at concentrations close to the European Maximum Residue Levels for drinking water.

The developed characterization system is not reliable for measuring high attenuations, but a measurement principle similar to that used in impedance or network analyzers can be implemented by interrogating the sensor with different frequencies in the resonance wideband. A tracking mode for continuously monitoring the frequency of maximum conductance and the maximum conductance value can be implemented to make the system reliable for measuring high damping loads. This would be implemented in a future work. Following a similar principle, the characterization of the system at multiple overtones in traditional QCM sensors can be achieved. This would be very useful for the extraction of the physical and geometrical parameters of the material deposited over the sensor.

The fast operation and low cost of the system proposed makes easier the simultaneous characterization of several sensors, making possible a multi-array

---

implementation. This is one of the main challenges which remains with acoustic wave technologies. To face with this challenge, the ability to miniaturization of quartz resonators can be used. This capability makes it possible to integrate multiple sensors in an array configuration. This is a promising new technology, because miniaturization of the resonator implies further advantages such as reduced cost, reduced consumption of samples and reagents, and reduced assay time trial.

## **Appendix I. Design and implementation of a QCM characterization system with automatic parallel capacitance cancellation**

---

In this appendix, we are presenting the electronic design of the system presented in Chapter 3.1. In order to provide a complete autonomous system, an FPGA based embedded system with a built-in microprocessor has been developed. This embedded system implements the frequency counter for the MSRF measurement, and the data acquisition system for the resistance and capacitance voltage signals. The system sends the measurements via an Ethernet connection to a custom developed PC application, for data visualization and storage.

In summary, this complete system includes:

- The circuit for automatic capacitance compensation and resonant frequency monitoring.
- The data acquisition system including: the supporting circuitry for the embedded hardware module, the digital design of the system

---

with the built-in microprocessor based on FPGA, and the microprocessor's firmware.

- The low noise symmetric power supply circuit of the system

We have used the OrCad™ 16.0 design package (Cadence Design Systems, Inc.) both for the schematic capture and for the printed circuit board (PCB) layout design. To implement the FPGA based microprocessor system we have used the Xilinx ISE Design Suite and the Embedded Development Kit (Xilinx, Inc.). Next, we will present the design and implementation of this design. Advanced Wave Sensors S.L. commercialized the system under the name *ACC-QCM-09*.

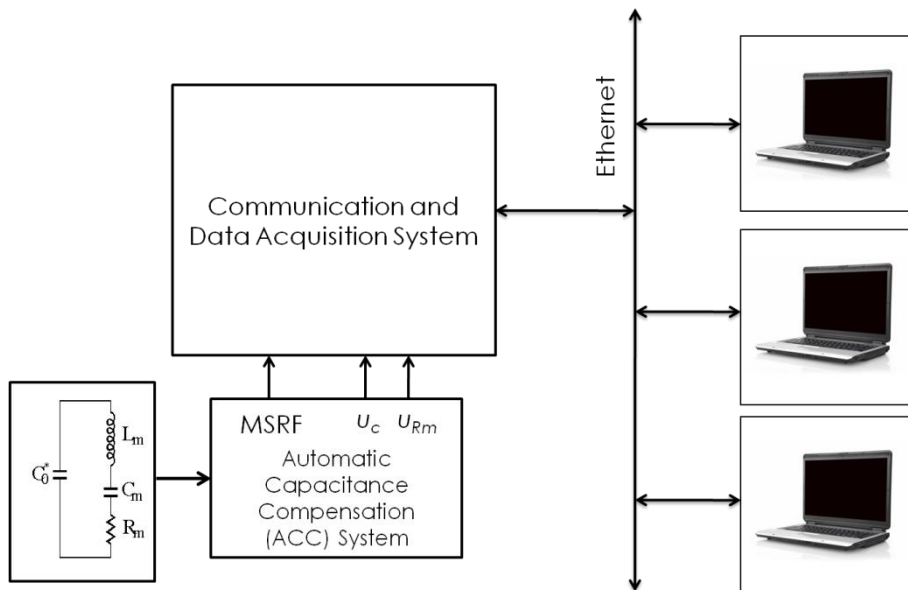


Figure I.1. Block diagram of the complete system including the ACC system and the FPGA based communications and data acquisition system.



## I.1.i. Design schematics

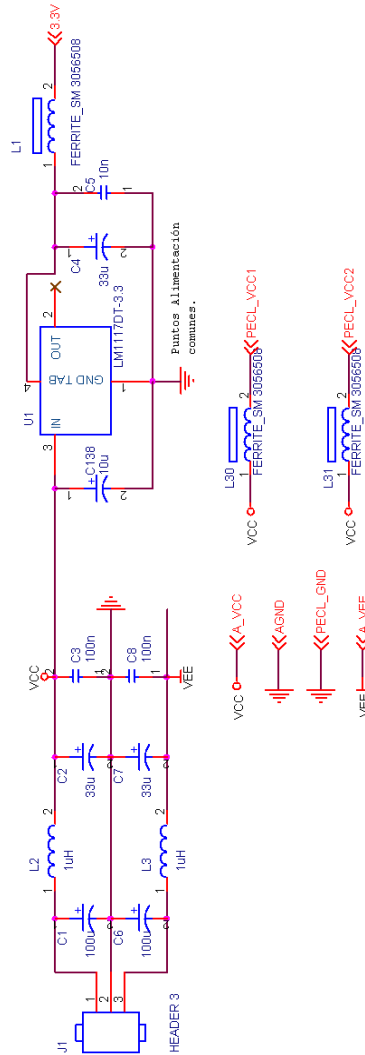


Figure I.3. ACC circuit power supply filter section. The circuit is powered by the symmetric power supply of  $\pm 5$  V presented in following sections through connector J1. Figure shows the input filtering for the local analog symmetric supply of  $+5$  V. The  $+5$  V (VCC) line serves as input for the LM1117, a 3.3 V output linear regulator (National semiconductor). This supply is exclusively used by the 38 MHz oscillator circuitry. In addition, PECL\_VCC1 and PECL\_VCC2 voltages are derived from this line after separation by two ferrite beads. These two lines will supply the high-speed PECL digital logic of the circuit. Separation from the analog power supply lines to prevent noise coupling is mandatory.

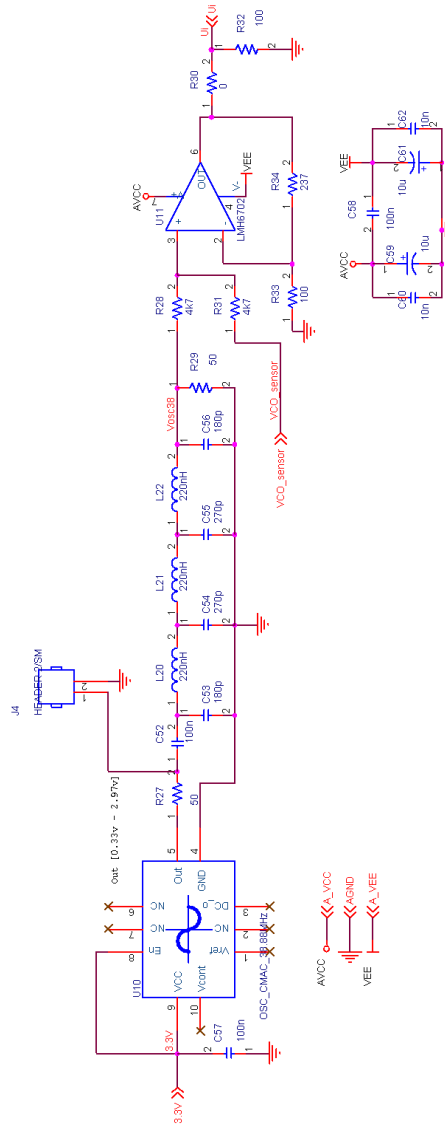


Figure I.4. Oscillator circuit of 38.88 MHz for the automatic capacitance compensation loop. The circuit is based on the CMOS output temperature compensated crystal oscillator (TCXO) CFPT 9000 (C-MAC, Inc.)(C-MAC MicroTechnology, 2005). Frequency stability of the TCXO output is better than 1 ppm for the whole temperature range. Figure shows the 7 poles ladder LC filter needed to obtain a sine wave signal from the squared output. This filtered signal feeds one of the summing inputs of an operational amplifier configured as an adder. The other input come from the VCO of the MSRF loop. The output of this adder is the signal  $u_i$  which feeds the input stage presented previously.

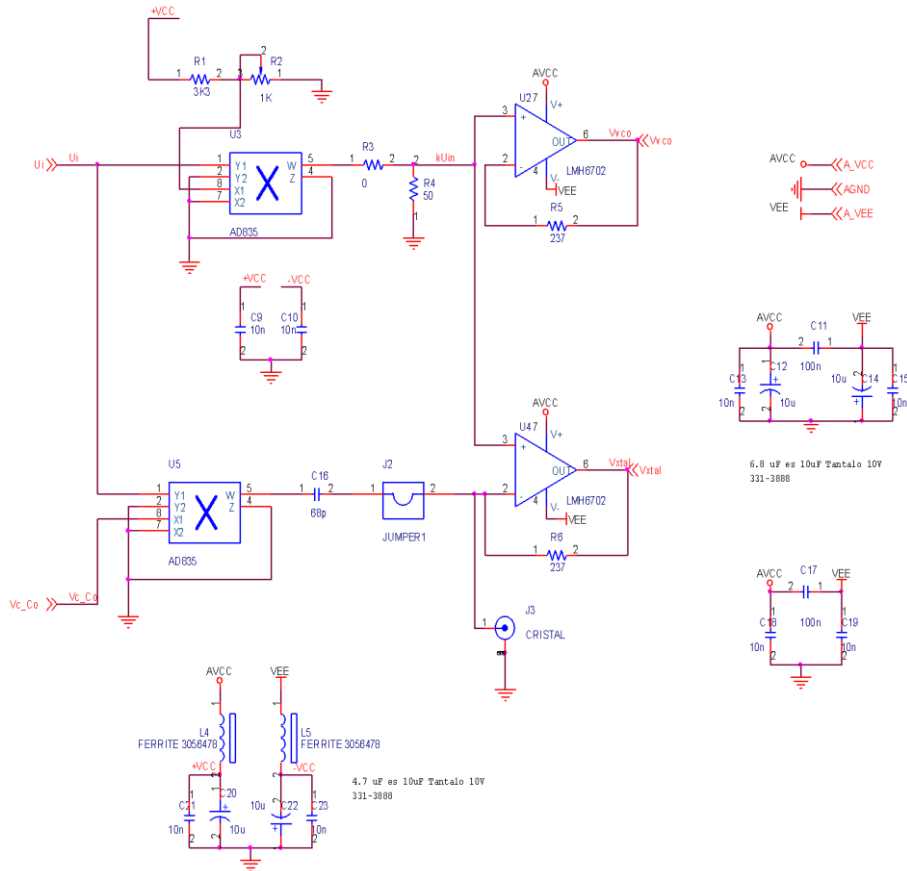


Figure I.5. Differential stage of the implemented ACC system. The signal  $u_i$ , summing signal for the VCO output and the 38.88 MHz oscillator, splits into two branches and drives the differential inputs of two four-quadrant multipliers (AD835AR, Analog Devices, Inc.) (Analog Devices, 2003). Although signal scaling in the reference branch ( $\alpha$  factor in equation 2, chapter 3.1) could have been done by a voltage divider, we used a multiplier in order to maintain the signal's phase shift between both branches. Scaling factor  $\alpha$  is adjusted during the calibration procedure via the multiturn potentiometer R2. The LMH6702 current feedback operational amplifiers (OPA) (National Semiconductor, Inc.) have a bandwidth of 1.7 GHz and provide ultra low distortion and very low phase shift between input and output (Texas Instruments, 2002). The OPAs output signals will drive the separation filters as shown next.

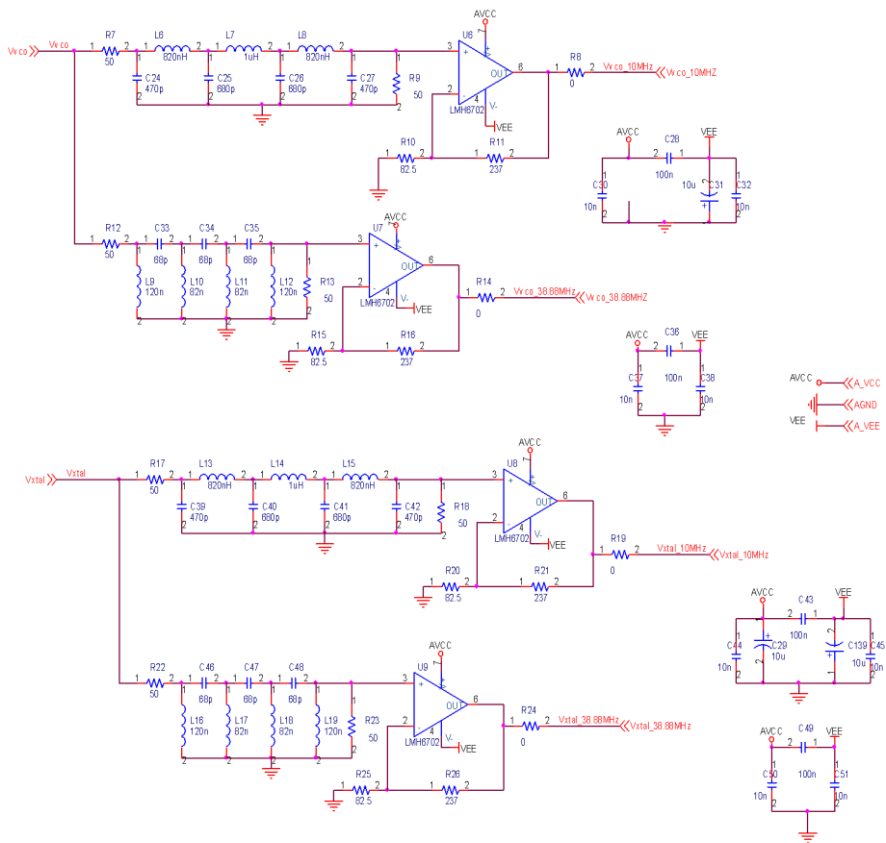


Figure I.6. LC ladder high pass and low pass filters for separating the different frequency signals of interest. Filters were designed from a Chebyshev prototype of 7 poles, with 0.5 dB ripple in the band pass and 80 dB of attenuation in the stop band. Filtered signals are amplified to accomplish the input slew rate criteria from the high speed comparators connected next. Filtered signals are amplified to accomplish the input slew rate criteria from the high speed comparators connected next.



---

Figure I.7. PLL for the MSRF monitoring loop. The signals from both branches of the differential stage feed the high-speed comparators after being filtered to remove the high frequency components. The MAX9601 (Maxim Integrated) is a positive emitter-coupled logic (PECL) high-speed comparator, with a very low delay time between input and output (500 ps) and a very low dispersion in the propagation delay (below 30 ps) (Maxim Integrated, 2002). These properties are essential to our application since the propagation dispersion will result in phase noise (and thus frequency noise at the VCO output) in the measurement. The output signals of both comparators drive the high-speed PECL phase-frequency detector (PFD) MAX9383 (Maxim Integrated). The PFD outputs are filtered and connected to the differential amplifier which provides a voltage signal proportional to the phase difference. This signal is integrated by an inverted integrator circuit. The differential amplifier and integrator are implemented by the OP297 (Analog devices), a dual, low noise, precision operational amplifier circuit. The integrator output controls the MAX038 generated sine wave signal's frequency through the frequency adjustment input (Maxim Integrated, 2007). The signal is low pass filtered to reduce the harmonic distortion to a minimum (seven poles Chebyshev LC filter with an attenuation at 20 MHz of 70 dB). After filtering, the signal will feed the adder presented in the previous section, hence closing the loop. The measurement of this signal's frequency will serve as MSRF measurement.



---

Figure I.8. PLL for the automatic capacitance cancellation (ACC) loop. The filtered signals from both branches corresponding to the high frequency component feed the MAX9601 high-speed comparators. The output signals of both comparators drive the high-speed PECL phase-frequency detector (PFD) MAX9383 (Maxim Integrated) and its outputs are filtered and connected to the OP297 based differential amplifier and inverter integrator as described in previous section. The integrator's output is scaled and level shifted through a resistive network. Once conditioned to the proper levels, the signal will drive the multiplier for the capacitance compensation shown in the differential stage, hence closing the loop for the capacitance compensation. Also, monitoring this signal will serve as sensor's parallel capacitance measurement.

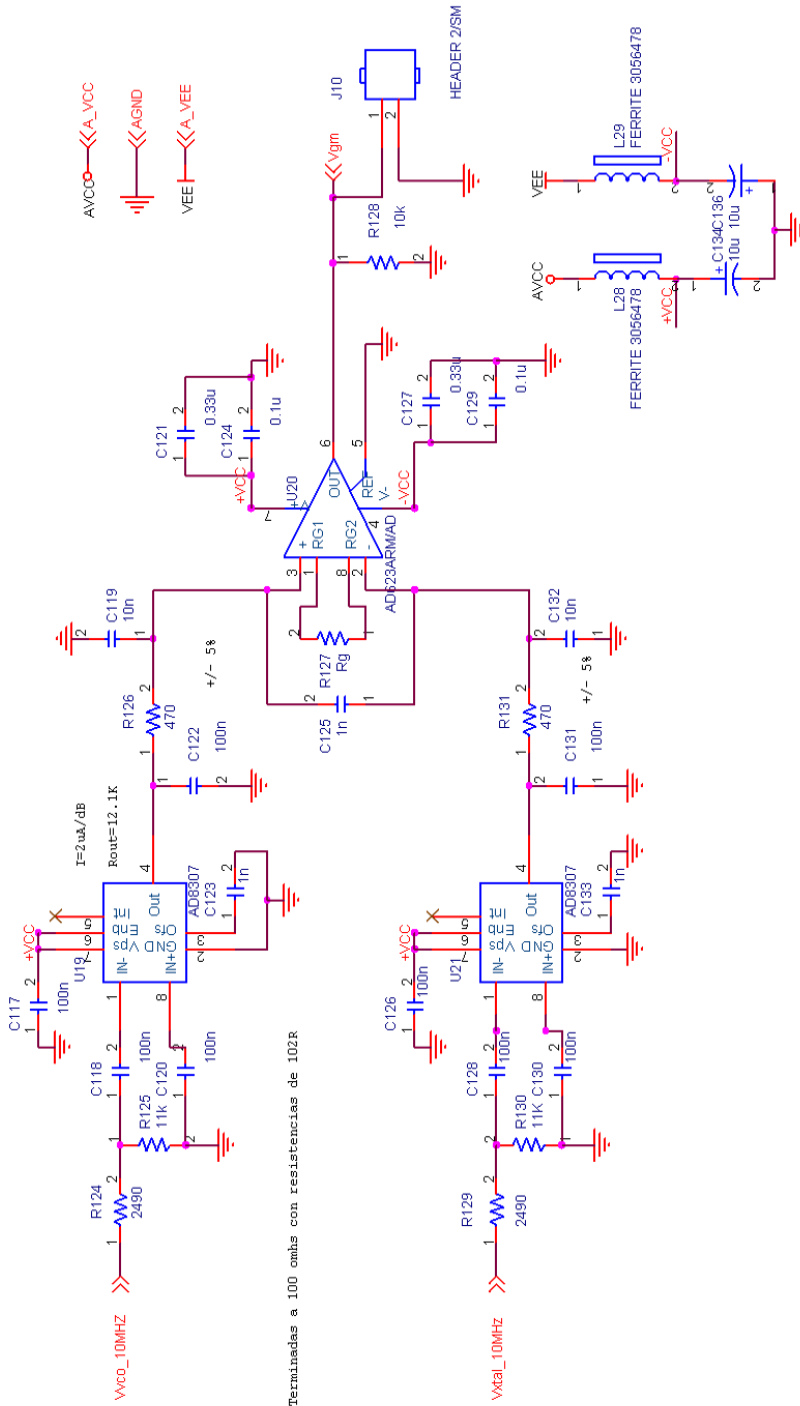


Figure I.9. Motional resistance measurement circuit. The circuit is based on two logarithmic amplifiers and an instrumentation amplifier. The output of the differential amplifier AD623 (Analog Devices, Inc.) provides a voltage signal,  $V_{Rm}$  proportional to the logarithm of the quotient between the peak amplitudes of  $V_{1L}$  and  $V_{2L}$  (as named in Figure I.2), the filtered low frequency signals of both branches of the differential stage previously presented. The signal  $V_{Rm}$  is monitored, providing the measurement of the motional resistance of the sensor (see Eq.(I.1) where  $\alpha$  and  $\beta$  are constants to be experimentally determined through the system calibration. Combining Eq.(6) in section 3.1 with Eq.(I.1) results in Eq.(I.2)). The AD8307 (Analog Devices, Inc.) logarithmic amplifiers provide a wide bandwidth of 500 MHz and a dynamic margin of 92 dB with a sensitivity of 25 mV/dB(Analog Devices, 2006).

$$V_{Rm} = \alpha + \beta \cdot \log \frac{V_{2L}}{V_{1L}} \quad (I.1)$$

$$R_m = \frac{R_V}{10^{\frac{u_{Rm} - \alpha}{\beta}} - 1} \quad (I.2)$$

---

## I.1.ii. Printed circuit board design

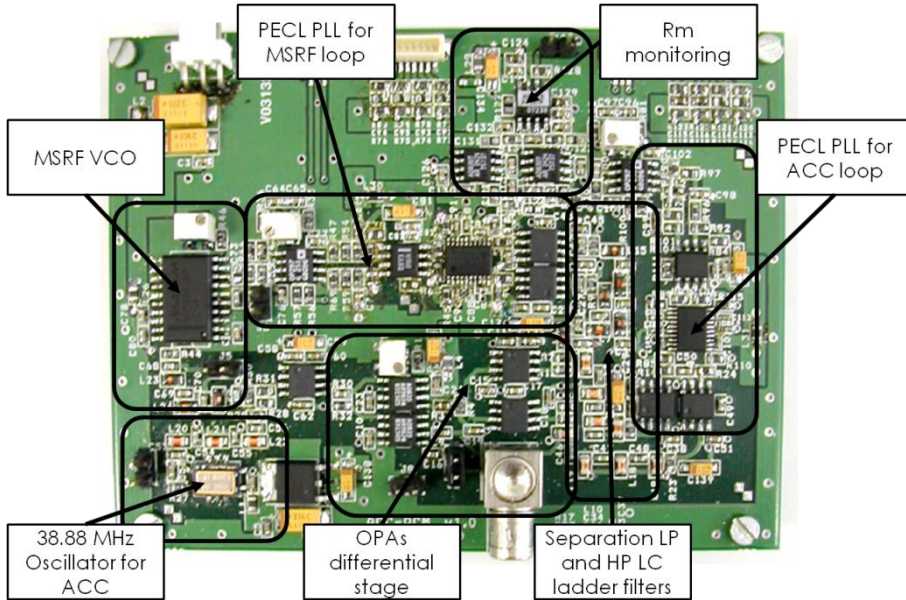


Figure I.10. Implemented circuit showing the placement location of the components for the different parts of the design schematic, as described above.

Given the complexity of the design, the size restrictions and the high operation frequencies, we have performed the design in four routing layers; two of them (the internal ones) used as power supply planes.

We have routed almost all signal traces in the top layer of the PCB, placing the components with maximum packing strategy and looking for minimize the connection length. We have been especially careful for the high frequency signals involved in the PLLs of the circuit. We have controlled the routing length of those traces involved in the PFD detection to minimize the phase difference in order to obtain the best symmetric configuration.

We have followed the general recommendations for the design of the high frequency layout (Johnson and Graham, 1993; Montrose, 1998) and the indications of the manufacturers of the different electronic components used.

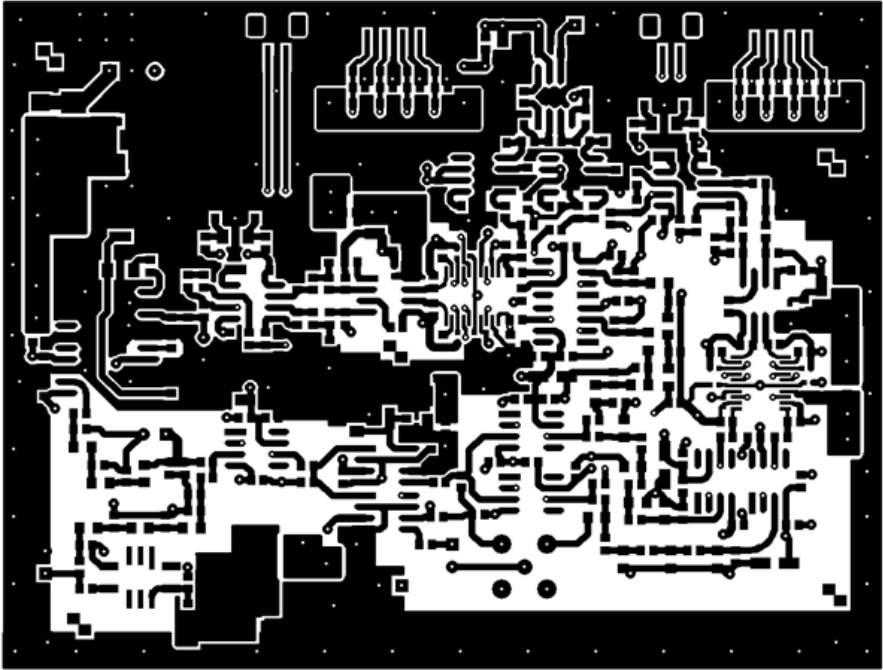


Figure I.11. Top layer fabrication mask. The ground plane of this layer has been placed far from the high frequency traces in which we want to control the phase shift, to avoid unwanted parasitic capacitances which could affect the symmetry of the design.

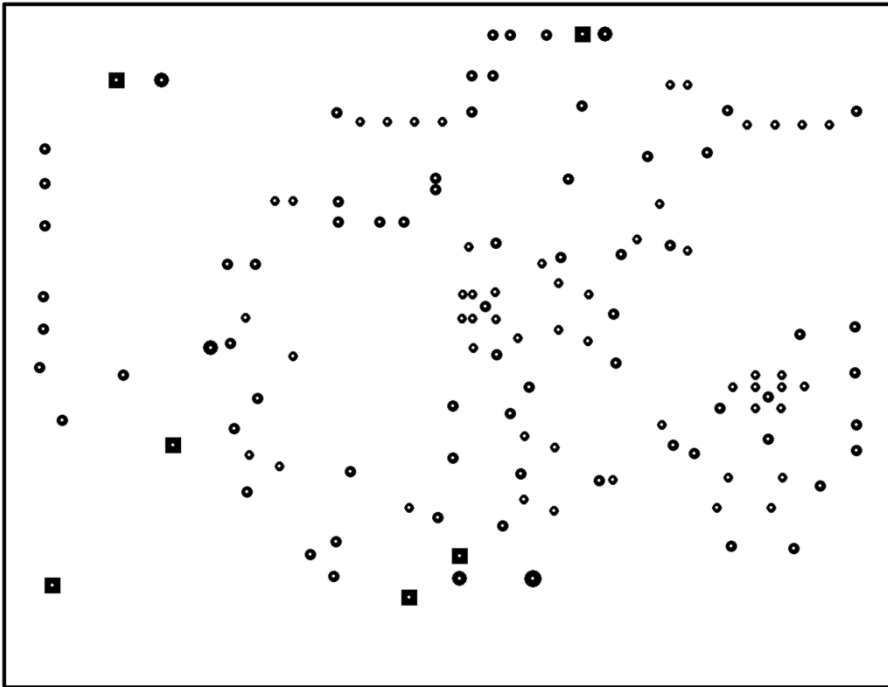


Figure I.12. Ground plane fabrication mask (negative view, black areas mean copper removal). We used a solid ground plane for the whole circuit. All components of this pcb are analog subsystems, except the PECL comparators and PFD. However, since the PECL subsystems use the positive supply of 5V as return current path, we do not need to break the plane of ground beneath these integrated circuits for noise confinement and isolation.

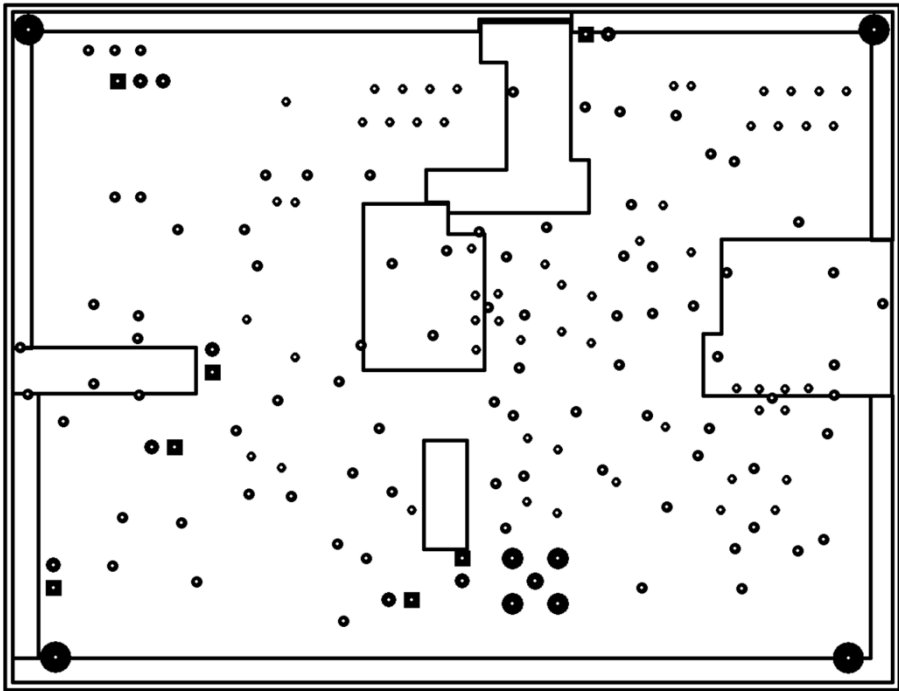


Figure I.13. Power plane fabrication mask (negative view). Although main plane is for the positive power supply voltage of +5V, several plane islands can be shown in the figure. These local planes correspond to the local filtered power supplies of some of the components previously described. The edge of this layer has been isolated also from the power supply plane and it has been connected to the ground plane by multiple connection vias.

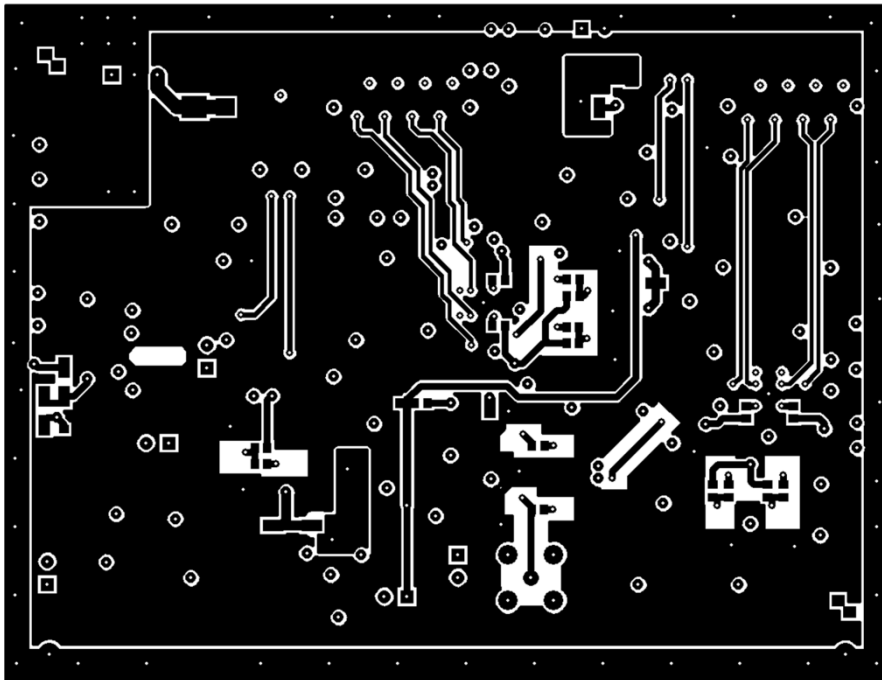


Figure I.14. Bottom layer fabrication mask. Some of the low frequency signals of the circuitry have been routed through this layer. Most of the surface was used as power plane for the negative power supply voltage (-5 V). The external edge of this layer has been also isolated and connected to the ground plane of the circuit. This technique is recommendable in high frequency designs in order to improve the electromagnetic compatibility of the design.

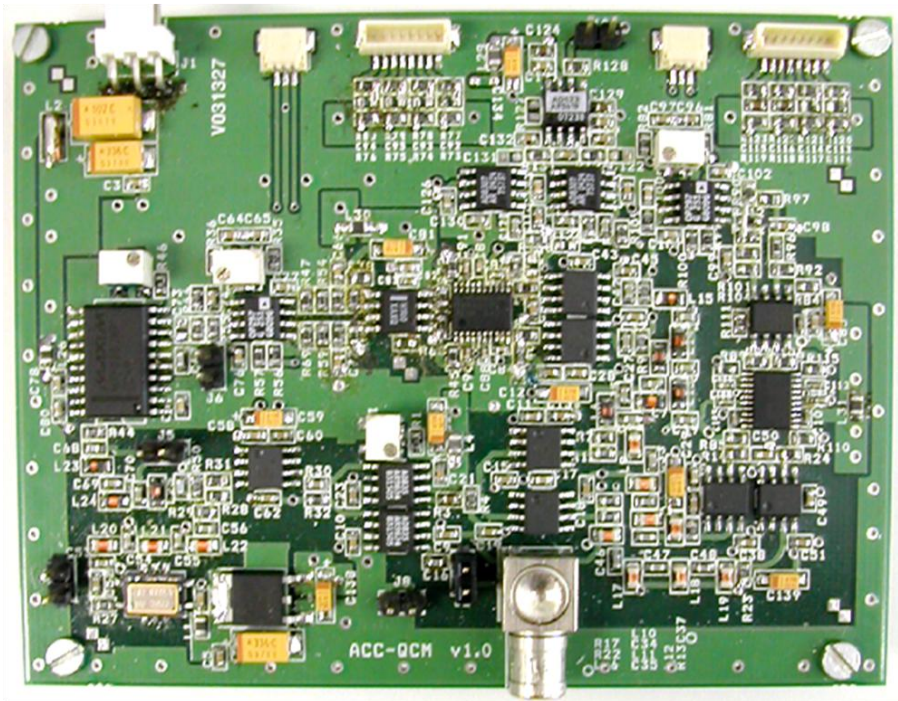


Figure I.15. Top view of the assembled ACC circuit. Final dimensions for the implemented circuit are 100 mm x 76 mm.

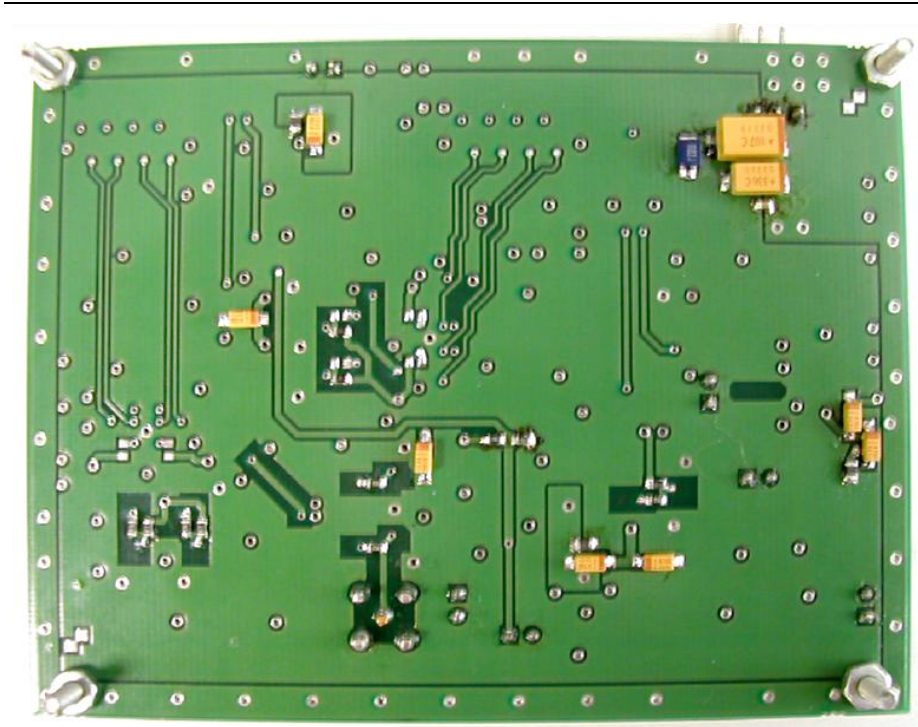


Figure I.16. Bottom view of the assembled ACC circuit.

---

## I.2. FPGA based Communications and Data Acquisition system

As shown in previous sections, the automatic capacitance compensation circuit provides a series of signals, which allow characterizing the QCM sensor. As summary the signals of interest, which must be monitored and acquired, are:

- The frequency of the sine wave signal provided by the MAX038 VCO ( $f_{out}$ ), for MSRF monitoring.
- The analog voltage signal ( $V_{Rm}$ ) for sensor's motional resistance monitoring
- The analog voltage signal ( $V_d$ ) for sensor's parallel capacitance monitoring

Thus, the embedded system must be able to perform the frequency measurement of at least one high frequency sine wave signal and measure at least two different low frequency analog voltage signals. For the frequency measurement, we have specified a resolution better than 1 Hertz, with a time between measurements lower than 1 second. For the analog signals measurement we have established a resolution better than 5 mV.

We have chosen an FPGA based system for the implementation in order to have a flexible and highly reconfigurable solution during the design stage. For the development, we opted to a hardware/software co-design, using an FPGA based embedded processor for controlling the communication and measurement tasks, and custom designed programmable logic cores to perform the frequency measurement and the interfacing between the processor and the analog to digital converter selected, the AD7864 from Analog devices, Inc.

The FPGA model used is a Virtex® 4 FX12 (Xilinx, Inc.) which includes an embedded 32 bits Power PC processor core and an Ethernet medium access controller (EMAC) for the Ethernet communications. These cores are independent hardware modules embedded in the FPGA fabric and they do not

use any resources of the programmable logic of the FPGA for its implementation. We have chosen the commercially available Virtex-4 FX12 Mini-Module (Avnet, Inc.) to implement the FPGA modules of the system.

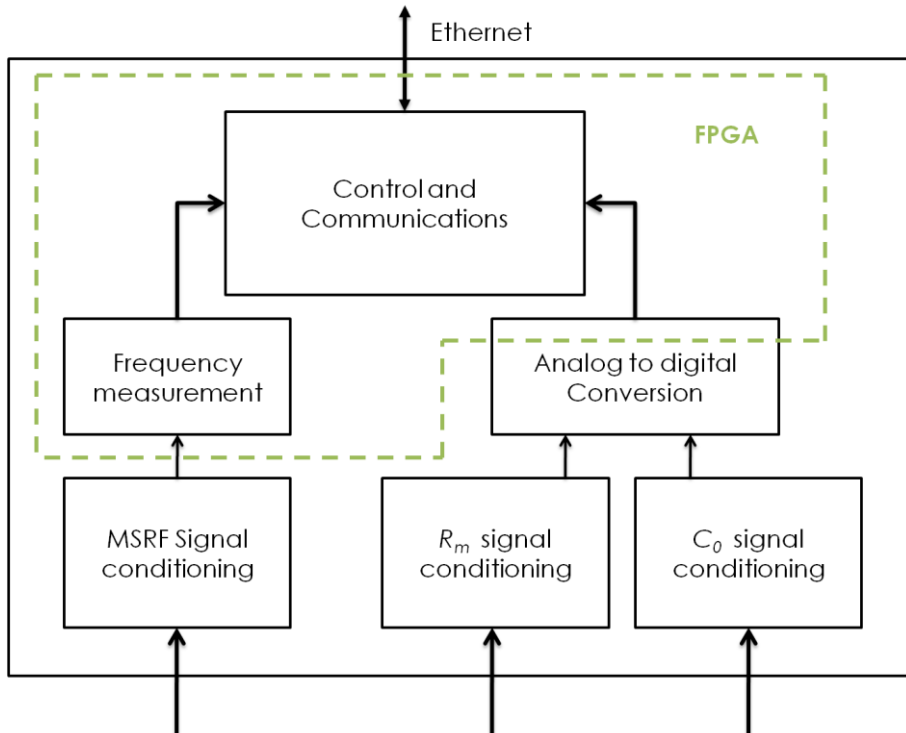


Figure I.17. Block Diagram of the FPGA based proposed system.

This module includes a Virtex-4 FX12-SF363 FPGA, 64 MB of DDR SDRAM memory, 4 MB Flash memory, a Platform Flash memory to store the FPGA configuration and a 100 MHz oscillator based clock generator. It also includes a 10/100/1000 Ethernet physical layer interface through a Broadcom BCM5461 and a RJ45 connector to provide a complete gigabyte Ethernet solution when used in conjunction with the hardware EMAC core.

We have designed a dedicated hardware module for the frequency measurement and a hardware interface for the AD7864 analog to digital

converter. Those modules are connected to the local bus processor (PLB) to be accessed by the embedded processor. The modules have been written in VHDL (VHSIC Hardware Description Language) in order to be implemented in the FPGA programmable logic. Additionally to this, a support circuitry has been designed to perform the signal conditioning of the measured signals and provide electrical and mechanical support to the FPGA module.

We will present next the details of the design and implementation of the embedded system.

### I.2.i. FPGA based logic

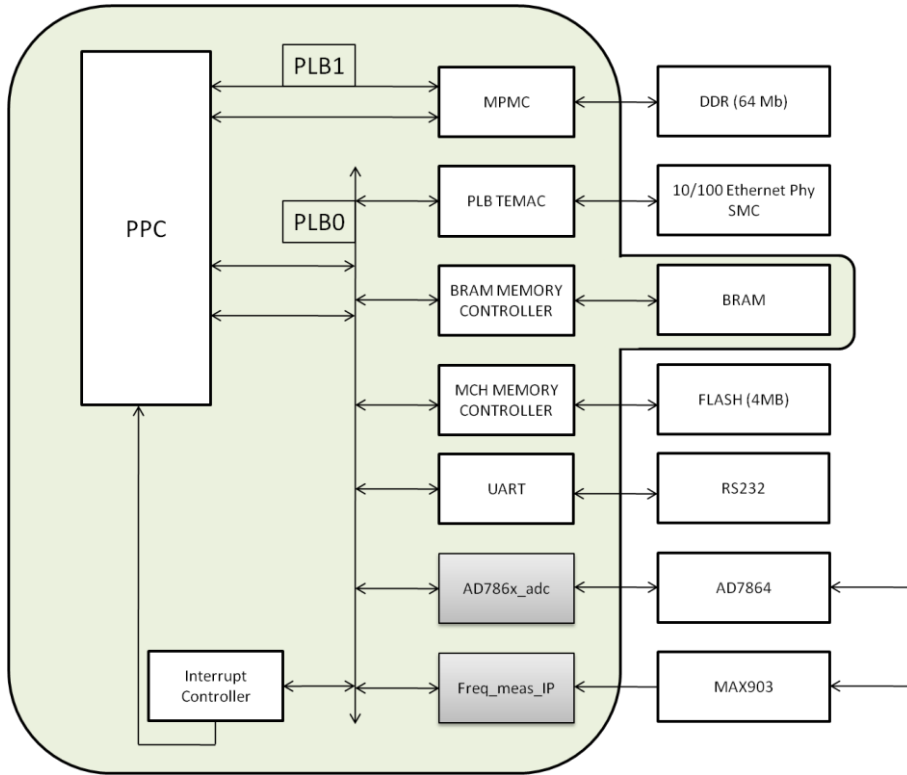


Figure I.18. Block diagram of the implemented FPGA based embedded system. Modules implemented directly in the FPGA are inside the green area. The frequency counter core (Freq\_meas\_IP) and the ADC converter interface (AD786x\_adc) cores connect to the PLB0. The bus is shared with the Ethernet MAC, an UART core for debugging, and two memory controllers: the flash memory controller and a block RAM memory controller for FPGA implemented RAM. The processor accesses the module DDR memory through the Multi-Port Memory controller (MPMC), via a dedicated PLB1.

### I.2.i.a. *Reciprocal frequency counter core*

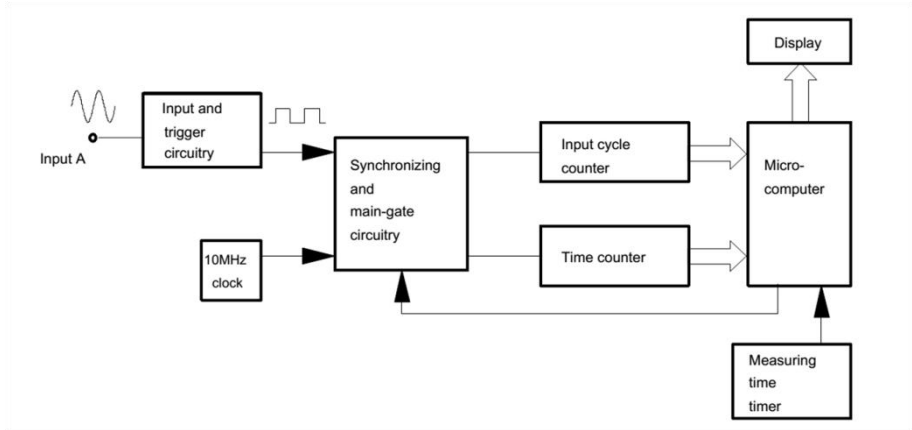
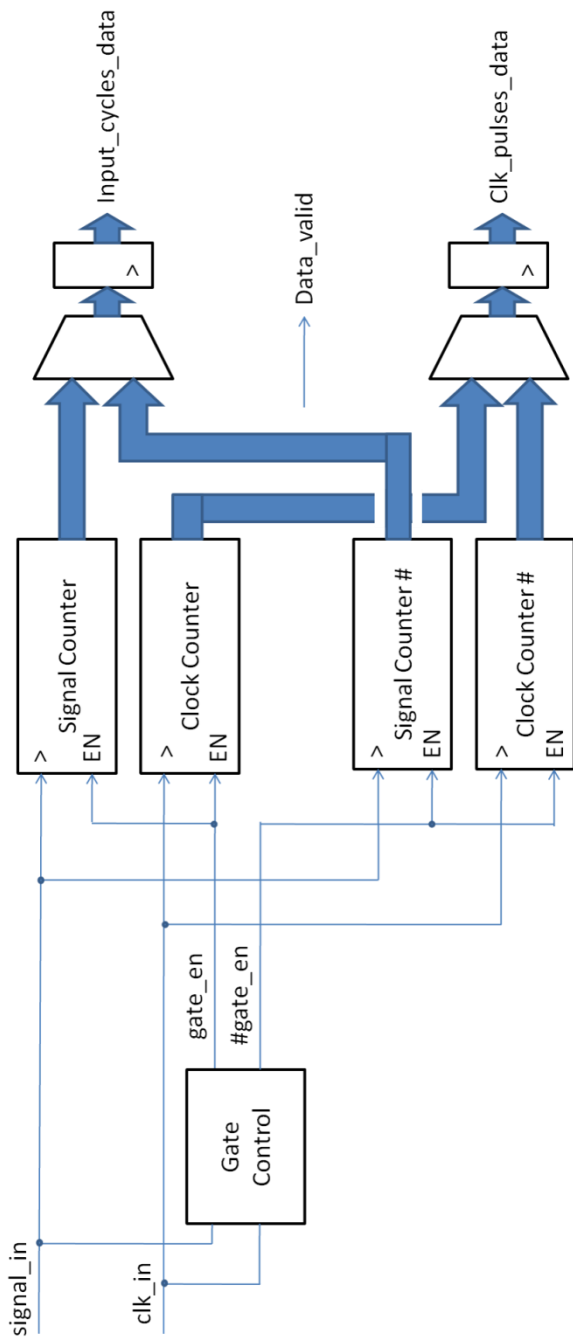


Figure I.19. Block diagram illustrating the reciprocal counting principle. © 2005 IEEE (Johansson, 2005). It contains two counting registers, one for counting the number of input cycles and other for measuring the time duration of the measurement, which is implemented by counting the pulses of a known frequency clock signal. In a conventional counter the number of events triggered by the input signal are counted during an exact period of time. Uncertainty of counting, as gate is not synchronized with input signal, is  $\pm 1$  cycle count, therefore, for 1 second gate time and a 10 MHz input signal, resolution is 1 Hz. In a reciprocal counter, the actual measuring time is synchronized to the input triggering signal, so measurement contains an exact number of input cycles and uncertainty is  $\pm 1$  clock pulse. Frequency is calculated as the number of signal input cycles divided the counted clock pulses multiplied by the clock cycle time. In this case, for a gate time of approximately 1 second and a clock signal of 100 MHz (FPGA system's clock) resolution is around 0.1 Hz (Hewlett-Packard Company, 1997; Johansson, 2005).



---

Figure I.20. Block diagram of the implemented reciprocal frequency-counting core. At least two counting registers are needed to perform the measurement, one for the input signal and other for the clock signal. With only a pair of counters, it would be necessary to implement a START/STOP control to reset the counters once the measured value is stored. In addition, during that time (several system's clock cycles) the measurement of frequency would not be performed. We chose to perform a continuous measurement of the frequency, duplicating the number of counters. So, at least one pair of signal/clock registers will be active at all the time, either the ones of the positive gate control or the ones of the negative gate control. When the data of a new measurement is available, a signal `data_valid` is generated and the reset of the working counters is performed while the other pair of counters is habilitated. The control of habilitation gate signals is performed in the block `gate_control`. By means of this circuit, we generate and synchronize the enable signals of the counters with the input signal. We will always count complete cycles of the input signal with no uncertainty in the measurement of that counter. The existence of different clock domains is essential to perform a correct reciprocal measurement, because the counters must be directly attacked both for the input signal to be measured and for the system clock signal. To avoid the possible appearance of metastability in the circuit we have introduced the corresponding synchronizers for the different clock domains in the design. The system's clock signal can be driven either by the onboard low performance 100 MHz crystal oscillator or by an external one.

```

library ieee;
use ieee.std_logic_1164.all;
use ieee.numeric_std.all;

entity gate_control is

  port (
    clk_sys : in std_logic;      -- Reloj del sistema (100MHz)
    rst     : in std_logic;      -- reset del sistema
    signal_in : in std_logic;    -- señal de entrada a medir
    gate_div_data : in std_logic_vector (31 downto 0); -- factor de division
                                                    -- para generacion de
                                                    -- señal de control

    gate_out : out std_logic ;
    gate_out_n : out std_logic
  ); -- gate control que habilita las cuentas (para contadores positivos o negativos)

end gate_control;

architecture behav of gate_control is

  signal gate, gate_q0, gate_q1, gate_sync : std_logic; -- auxiliar para control de puerta
  signal gate_n_q0, gate_n_q1, gate_n_sync : std_logic; -- auxiliar para control de puerta
  signal cuenta_div : std_logic_vector(31 downto 0); -- cuenta para division

begin -- behav

  -- purpose: Generacion de señal de toggle mediante divisor para gate control del contador
  -- type : sequential
  -- inputs : clk_sys, rst, gate_div_data
  -- outputs: toggle
  DIVISOR : process (clk_sys, rst)
  begin -- process DIVISOR
    if rst = '1' then -- asynchronous reset (active low)
      gate <= '0';
      cuenta_div <= (others => '0');
    elsif clk_sys'event and clk_sys = '1' then -- rising clock edge
      if (cuenta_div = gate_div_data) then
        gate <= not gate;
        cuenta_div <= (others => '0');
      else
        gate <= gate;
        cuenta_div <= STD_LOGIC_VECTOR(UNSIGNED(cuenta_div) + 1);
      end if;
    end if;
  end process DIVISOR;

  -- purpose: sincronizador de la señal de gate con la señal de entrada a medir,
  -- de forma que se mida siempre ciclos enteros de la señal de entrada
  -- type : sequential
  -- inputs : signal_in,
  -- outputs: names]>
  SYNCHRO: process (signal_in, rst)
  begin -- process SYNCHRO
    if rst = '1' then -- asynchronous reset (active low)
      gate_q0 <= '0';
      gate_q1 <= '0';
      gate_sync <= '0';

      gate_n_q0 <= '0';
      gate_n_q1 <= '0';
      gate_n_sync <= '0';
    elsif signal_in'event and signal_in = '1' then -- rising clock edge
      gate_q0 <= gate;
      gate_q1 <= gate_q0;
      gate_sync <= gate_q1;
    end if;
  end process SYNCHRO;

```

```
gate_n_q0 <= not gate;
gate_n_q1 <= gate_n_q0;
gate_n_sync <= gate_n_q1;

end if;
end process SYNCHRO;

gate_out <= gate_sync;
gate_out_n <= gate_n_sync;

end behav;
```

Code 1. gate\_control.vhd

```

library IEEE;
use IEEE.std_logic_1164.all;
use IEEE.numeric_std.all;

entity freq_counter is

  port (
    clk_sys      : in std_logic; -- reloj del sistema (100MHz)
    rst          : in std_logic; -- reset general sistema
    signal_in    : in std_logic; -- señal procedente del oscilador
    gate_div_data : in std_logic_vector (31 downto 0);
    input_cycles_data : out std_logic_vector (31 downto 0); -- ciclos de entrada contados
    clk_pulses_data : out std_logic_vector (31 downto 0); -- pulsos de reloj contados
    data_valid   : out std_logic; -- señal de datos validos a la salida
  )

end freq_counter;

architecture rtl of freq_counter is

  signal signal_count_data, clk_count_data, signal_count_data_n, clk_count_data_n : std_logic_vector
    (31 downto 0);
  signal gate_en, gate_en_q1, gate_en_q2, data_regs_en : std_logic;
  signal gate_en_n, gate_en_n_q1, gate_en_n_q2, data_regs_en_n : std_logic;

  signal counter_rst, counter_rst_h, counter_rst_n, counter_rst_h_n : std_logic;

component gate_control
  port (
    clk_sys      : in std_logic;
    rst          : in std_logic;
    signal_in    : in std_logic;
    gate_div_data : in std_logic_vector (31 downto 0);
    gate_out     : out std_logic;
    gate_out_n   : out std_logic;
  )
end component;

begin

  GATE_U1: gate_control
  port map (
    clk_sys    => clk_sys,
    rst        => rst,
    signal_in  => signal_in,
    gate_div_data => gate_div_data,
    gate_out   => gate_en,
    gate_out_n => gate_en_n);

  -- rtl

  -- purpose: Contador para Nº de ciclos de la señal de entrada
  -- type : sequential
  -- inputs : signal_in, rst, gate_en
  -- outputs: signal_count_data
  SIGNAL_COUNT : process (signal_in, rst, counter_rst)
  begin -- process SIGNAL_COUNT
    if rst = '1' or counter_rst = '1' then -- asynchronous reset (active low)
      signal_count_data <= (others => '0');
    elsif signal_in'event and signal_in = '1' then -- rising clock edge
      if gate_en = '1' then
        signal_count_data <= STD_LOGIC_VECTOR(UNSIGNED(signal_count_data) + 1);
      end if;
    end if;
  end process SIGNAL_COUNT;

  -- purpose: Contador para Nº de ciclos de la señal de entrada

```

```

-- type : sequential
-- inputs : signal_in, rst, gate_en
-- outputs: signal_count_data
SIGNAL_COUNT_N : process (signal_in, rst, counter_rst_n)
begin -- process SIGNAL_COUNT
  if rst = '1' or counter_rst_n = '1' then -- asynchronous reset (active low)
    signal_count_data_n <= (others => '0');
  elsif signal_in'event and signal_in = '1' then -- rising clock edge
    if gate_en_n = '1' then
      signal_count_data_n <= STD_LOGIC_VECTOR(UNSIGNED(signal_count_data_n) + 1);
    end if;
  end if;
end process SIGNAL_COUNT_N;

-- purpose: Contador para N° de ciclos de la señal de reloj
-- type : sequential
-- inputs : clk_sys, rst, gate_en
-- outputs: signal_count_data
CLOCK_COUNT : process (clk_sys, rst, counter_rst)
begin -- process SIGNAL_COUNT
  if rst = '1' or counter_rst = '1' then -- asynchronous reset (active low)
    clk_count_data <= (others => '0');
  elsif clk_sys'event and clk_sys = '1' then -- rising clock edge
    if gate_en = '1' then
      clk_count_data <= STD_LOGIC_VECTOR(UNSIGNED(clk_count_data) + 1);
    end if;
  end if;
end process CLOCK_COUNT;

-- purpose: Contador para N° de ciclos de la señal de reloj
-- type : sequential
-- inputs : clk_sys, rst, gate_en
-- outputs: signal_count_data
CLOCK_COUNT_N : process (clk_sys, rst, counter_rst_n)
begin -- process SIGNAL_COUNT
  if rst = '1' or counter_rst_n = '1' then -- asynchronous reset (active low)
    clk_count_data_n <= (others => '0');
  elsif clk_sys'event and clk_sys = '1' then -- rising clock edge
    if gate_en_n = '1' then
      clk_count_data_n <= STD_LOGIC_VECTOR(UNSIGNED(clk_count_data_n) + 1);
    end if;
  end if;
end process CLOCK_COUNT_N;

-- purpose: Generacion de señal de habilitacion para registrar las salidas de los contadores
-- type : sequential
-- inputs : clk_sys, rst, gate_en
-- outputs: regs_en
REGS_SYNCHRO : process (clk_sys, rst)
begin -- process REGS_SYNCHRO
  if rst = '1' then -- asynchronous reset (active low)
    gate_en_q1 <= '0';
    gate_en_q2 <= '0';

    gate_en_n_q1 <= '0';
    gate_en_n_q2 <= '0';
  elsif clk_sys'event and clk_sys = '1' then -- rising clock edge
    gate_en_q1 <= gate_en;
    gate_en_q2 <= gate_en_q1;

    gate_en_n_q1 <= gate_en_n;
    gate_en_n_q2 <= gate_en_n_q1;
  end if;
end process REGS_SYNCHRO;

```

```

    end if;
end process REGS_SYNCHRO;

data_regs_en <= (not gate_en_q1 and gate_en_q2); -- Habilitamos enable de
-- contador gate =1 en el
-- flanco negativo
data_regs_en_n <= (not gate_en_n_q1 and gate_en_n_q2); -- Lo mismo para el
-- flanco positivo y
-- contador de gate=0

-- purpose: retardo de un ciclo para reset de contadores
-- type : sequential
-- inputs : clk_sys, rst
-- outputs:
CLEAR_COUNT: process (clk_sys, rst)
begin -- process CLEAR_COUNT
if rst = '1' then -- asynchronous reset (active low)
    counter_rst <='0';
    counter_rst_n <='0';
elseif clk_sys'event and clk_sys = '1' then -- rising clock edge
    counter_rst <= data_regs_en;
    counter_rst_n <= data_regs_en_n;
end if;
end process CLEAR_COUNT;

-- purpose: Registros de datos donde se almacena la frecuencia. Los datos de
-- entrada se seleccionan en funcion de la señal de enable habilitada. Si no se
-- lo traga habra qu ecrear un mux combinacional antes
-- type : sequential
-- inputs : clk_sys, rst,
DATA_REGS : process (clk_sys, rst)
begin -- process DATA_REGS
if rst = '1' then -- asynchronous reset (active low)
    input_cycles_data <= (others => '0');
    clk_pulses_data <= (others => '0');

elseif clk_sys'event and clk_sys = '1' then -- rising clock edge
if data_regs_en = '1' then
    input_cycles_data <= signal_count_data;
    clk_pulses_data <= clk_count_data;
elseif data_regs_en_n = '1' then
    input_cycles_data <= signal_count_data_n;
    clk_pulses_data <= clk_count_data_n;
end if;
end if;

end if;
end process DATA_REGS;

DATA_VALID_FLAG: process (clk_sys, rst)
begin -- process
if rst='1' then
    data_valid <= '0';
elseif clk_sys'event and clk_sys='1' then
    data_valid <= data_regs_en or data_regs_en_n;
end if;
end process;

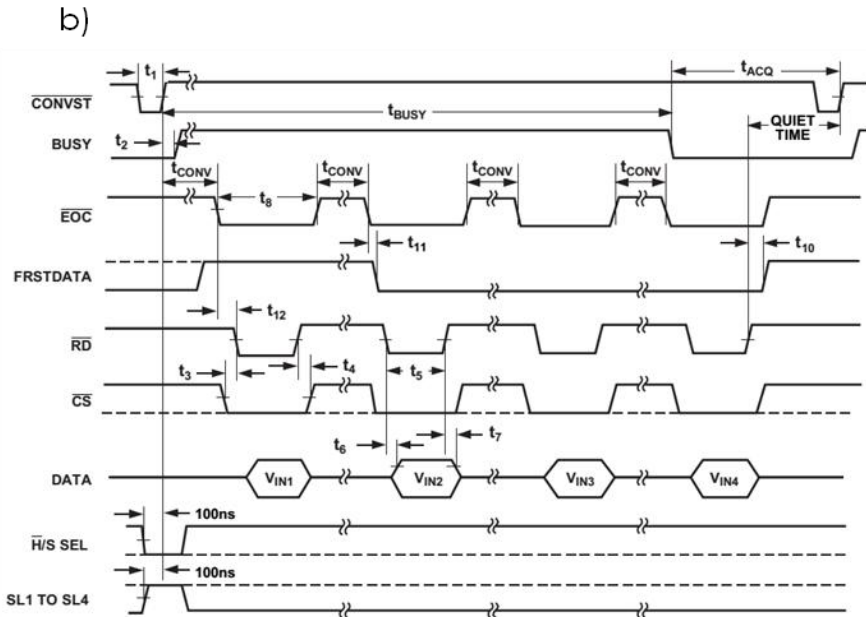
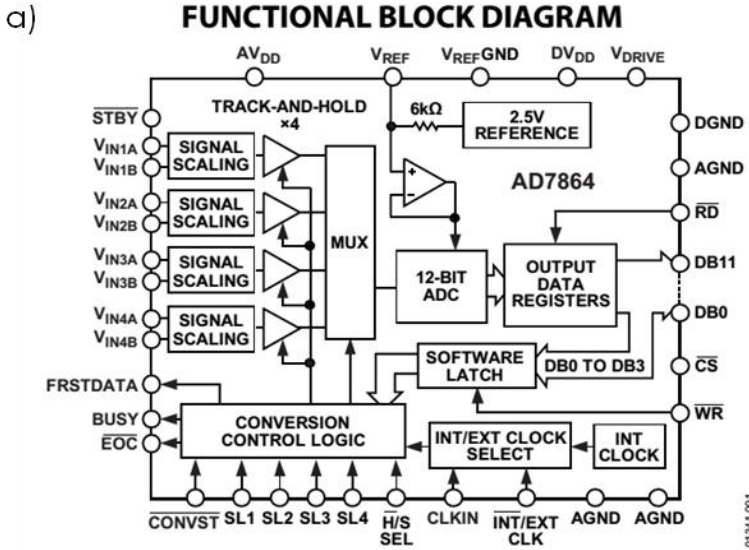
end rtl;

```

## Code 2. freq\_counter.vhd



I.2.i.b. *AD7864 ADC driver interface core*



---

Figure I.21. Functional block diagram (a) and timing diagram (b) of the AD7864, a four channels, 12 bits simultaneous sampling ADC (Analog Devices, 2009) © 2009 Analog Devices, Inc. The AD7864 interface core has been designed for a reading between conversions mode of operation as shown in (b). After the conversion start signal of a given duration is generated, the analog signals are sampled simultaneously in all the channels, and the conversion of each of them proceeds sequentially. The digital converted value for each sampled channel is presented sequentially in the data bus. The generation of the necessary signals is implemented in the custom developed core by a sequential state machine.

```

library IEEE;
use IEEE.std_logic_1164.all;

entity AD786x_IP is

  generic (
    Nbits      : integer := 12;  -- Numero de bits = 12 para AD7862
    NConvSt_cycles : integer := 10;  -- Numero de ciclos de reloj de
    -- duracion señal ConvSt
  )
  port (
    clk_sys : in std_logic;  -- reloj del sistema
    rst     : in std_logic;  -- reset general del sistema (activo nivel alto)

    INIT_CONV : in std_logic;  --Inicio conversión. Ponemos a 1 para que se
    --realice una conversión

    ADC_data_in : in std_logic_vector (0 to Nbits-1);  -- Bus de datos del ADC
    EOC_n       : in std_logic;  -- Señal de control que indica que ha finalizado una conversión
    ConvSt      : out std_logic;

    ADC0_data_out : out std_logic_vector (0 to Nbits-1);  --
    ADC1_data_out : out std_logic_vector (0 to Nbits-1);  --
    ADC2_data_out : out std_logic_vector (0 to Nbits-1);  --
    ADC3_data_out : out std_logic_vector (0 to Nbits-1);  --
    data_valid    : out std_logic;  -- Señal que indica inicio de conversión
  )
end AD786x_IP;

architecture RTL of AD786x_IP is

  type estado_t is (IDLE, CONV0, CONV1, CONV2, CONV3, DATAVALID);
  type delays_t is (IDLE, DELAY, ENDING);

  signal estado, next_estado      : estado_t;
  signal delay_state, next_delay_state : delays_t;

  signal next_genConvSt, gen_ConvSt          : std_logic;
  signal next_clrCounter, clrCounter, next_enCounter, enCounter, next_ConvSt : std_logic;

  signal Start, Start_comb          : std_logic;
  signal init_conv_d, init_conv_d1 : std_logic;

  signal flag_EOC, EOC_n_q1, EOC_n_q2 : std_logic;

  signal delay_counter          : integer range 0 to
  NConvSt_cycles+1;
  signal reg_en0, next_reg_en0, reg_en1, next_reg_en1, reg_en2, next_reg_en2, reg_en3, next_reg_en3
  : std_logic;

  signal next_datavalid : std_logic;

begin  -- RTL

  -----
  -----
  -----
  -- Maquina de estados principal. Bloque combinacional.
  -----
  FSM_main_comb : process (estado, Start, flag_EOC)
  begin

    case (estado) is

      when IDLE =>
        if (Start = '1') then
          next_genConvSt <= '1';  -- Cuando se produzca flanco CLK comienza conversión.
          next_estado <= CONV0;  -- pasa al estado conversión.
          reg_en0 <= '0';
          reg_en1 <= '0';
        end if
      end case
    end process
  end begin

```

```

reg_en2 <= '0';
reg_en3 <= '0';
next_datavalid <= '0';
else
next_genConvST <= '0'; -- Cuando se produzca flanco CLK comienza conversion.
next_estado <= IDLE; -- pasa al estado conversion.
reg_en0 <= '0';
reg_en1 <= '0';
reg_en2 <= '0';
reg_en3 <= '0';
next_datavalid <= '0';

end if;

when CONV0 =>

if (flag_EOC = '1') then
next_genConvST <= '0'; -- Cuando se produzca flanco CLK comienza conversion.
next_estado <= CONV1; -- pasa al estado conversion.
reg_en0 <= '1';
reg_en1 <= '0';
reg_en2 <= '0';
reg_en3 <= '0';

next_datavalid <= '0';
else
next_genConvST <= '0'; -- Cuando se produzca flanco CLK comienza conversion.
next_estado <= CONV0; -- pasa al estado conversion.
reg_en0 <= '0';
reg_en1 <= '0';
reg_en2 <= '0';
reg_en3 <= '0';
next_datavalid <= '0';
end if;

when CONV1 =>

if (flag_EOC = '1') then
next_genConvST <= '0'; -- Cuando se produzca flanco CLK comienza conversion.
next_estado <= CONV2; -- pasa al estado conversion.
reg_en0 <= '0';
reg_en1 <= '1';
reg_en2 <= '0';
reg_en3 <= '0';
next_datavalid <= '0';
else
next_genConvST <= '0'; -- Cuando se produzca flanco CLK comienza conversion.
next_estado <= CONV1; -- pasa al estado conversion.
reg_en0 <= '0';
reg_en1 <= '0';
reg_en2 <= '0';
reg_en3 <= '0';
next_datavalid <= '0';
end if;

when CONV2 =>

if (flag_EOC = '1') then
next_genConvST <= '0'; -- Cuando se produzca flanco CLK comienza conversion.
next_estado <= CONV3; -- pasa al estado conversion.
reg_en0 <= '0';
reg_en1 <= '0';
reg_en2 <= '1';
reg_en3 <= '0';
next_datavalid <= '0';
else
next_genConvST <= '0'; -- Cuando se produzca flanco CLK comienza conversion.
next_estado <= CONV2; -- pasa al estado conversion.
reg_en0 <= '0';
reg_en1 <= '0';
reg_en2 <= '0';

```

```

    reg_en3 <= '0';
    next_datavalid <= '0';
end if;

when CONV3 =>
    if (flag_EOC = '1') then
        next_genConvSt <= '0'; -- Cuando se produzca flanco CLK comienza conversion.
        next_estado <= DATAVALID; -- pasa al estado conversion.
        reg_en0 <= '0';
        reg_en1 <= '0';
        reg_en2 <= '0';
        reg_en3 <= '1';
        next_datavalid <= '0';
    else
        next_genConvSt <= '0'; -- Cuando se produzca flanco CLK comienza conversion.
        next_estado <= CONV3; -- pasa al estado conversion.
        reg_en0 <= '0';
        reg_en1 <= '0';
        reg_en2 <= '0';
        reg_en3 <= '0';
        next_datavalid <= '0';
    end if;

when DATAVALID =>
    next_genConvSt <= '0'; -- Cuando se produzca flanco CLK comienza conversion.
    next_estado <= IDLE; -- pasa al estado conversion.
    reg_en0 <= '0';
    reg_en1 <= '0';
    reg_en2 <= '0';
    reg_en3 <= '0';
    next_datavalid <= '1';

when others => next_estado <= IDLE;

end case;
end process FSM_main_comb;

-----
-- Cambio de estado. Proceso secuencial.
-----
FSM_main_sec : process (CLK_SYS, RST)
begin
    if (rst = '1') then
        estado <= IDLE;
    elsif (CLK_SYS'event and CLK_SYS = '1') then
        estado <= next_estado;
    end if;
end process FSM_main_sec;

-----
-- Registro de las salidas de la maquina de estados principal
-----
FSM_main_out_reg : process (clk_sys, rst)
begin -- process fsm_out_reg
    if rst = '1' then -- asynchronous reset (active low)
        gen_ConvSt <= '0';
        data_valid <= '0';

    elsif clk_sys'event and clk_sys = '1' then -- rising clock edge
        gen_ConvSt <= next_genConvSt;
        data_valid <= next_datavalid;

    end if;
end process fsm_main_out_reg;
-----
-----

```

```

--
-- Generacion de señal de Start a partir de deteccion de flanco positivo en
-- INIT CONV
--
-----
start_pulse_dect : process (rst, clk_sys)
begin
  if (RST = '1') then
    Init_conv_d <= '0';
    Init_conv_d1 <= '0';
    Start <= '0';
  elsif clk_sys'event and clk_sys = '1' then
    Init_conv_d <= INIT_CONV;
    Init_conv_d1 <= Init_conv_d;
    Start <= Start_comb;
  end if;
end process;

Start_comb <= ((not Init_conv_d1) and Init_conv_d);
-----

-- Sincronizamos la señal EOCn (activa a nivel bajo)
-- se activa el flag cuando hay una transicion de 0 a 1
-- en EOC_n
-----

flag_EOC <= (EOC_n_q1 and (not EOC_n_q2));

EOC_SYNCHRO : process (clk_sys, rst)
begin -- process EOC_SYNCHRO
  if rst = '1' then -- asynchronous reset (active low)
    EOC_n_q1 <= '1';
    EOC_n_q2 <= '1';

  elsif clk_sys'event and clk_sys = '1' then -- rising clock edge
    EOC_n_q1 <= EOC_n;
    EOC_n_q2 <= EOC_n_q1;
  end if;
end process EOC_SYNCHRO;
-----

-- Generación de pulso de mas de 35ns en la señal ConvSt
-----
-- purpose: maquina de estados para generar señal ConvSt de mas de 35ns de duración
-- type : combinational
-- inputs : next_ConvSt
-- outputs:
fsm_convST : process (gen_ConvSt, delay_counter, delay_state)
begin -- process fsm_convST

  case delay_state is

    when IDLE =>
      if gen_ConvSt = '1' then
        next_delay_state <= DELAY;
        next_clrCounter <= '0';
        next_enCounter <= '1';
        next_ConvSt <= '0';
      else
        next_delay_state <= IDLE;
        next_enCounter <= '0';
        next_clrCounter <= '1';
        next_ConvSt <= '1';
      end if;

    when DELAY =>

      if delay_counter = NConvSt_cycles then
        next_delay_state <= IDLE;
        next_clrCounter <= '1';
        next_enCounter <= '0';
      end if;
    end case;
  end process;
end process fsm_convST;

```

```

    next_ConvSt    <= '1';
else
    next_delay_state <= DELAY;
    next_clrCounter <= '0';
    next_enCounter  <= '1';
    next_ConvSt    <= '0';

end if;

when others => next_delay_state <= IDLE;

end case;

end process fsm_convST;

fsm_convSt_seq : process (clk_sys, rst)
begin -- process fsm_convSt_seq
if rst = '1' then -- asynchronous reset (active low)
    delay_state <= IDLE;
elseif clk_sys'event and clk_sys = '1' then -- rising clock edge
    delay_state <= next_delay_state;
end if;
end process fsm_convSt_seq;

FSM_ConvSt_regout : process (clk_sys, rst)
begin -- process FSM_ConvSt_regout
if rst = '1' then -- asynchronous reset (active low)
    enCounter <= '0';
    ConvSt <= '1';
    clrCounter <= '0';
elseif clk_sys'event and clk_sys = '1' then -- rising clock edge
    enCounter <= next_enCounter;
    ConvSt <= next_ConvSt;
    clrCounter <= next_clrCounter;
end if;
end process FSM_ConvSt_regout;

ConvSt_cunter : process (clk_sys, rst, clrCounter)
begin -- process ConvSt_cunter
if (rst = '1' or clrCounter = '1') then -- asynchronous reset (active low)
    delay_counter <= 0;
elseif clk_sys'event and clk_sys = '1' then -- rising clock edge
    if enCounter = '1' then
        delay_counter <= delay_counter+1;
    end if;
end if;
end process ConvSt_cunter;

-----
-- Registros de almacenamiento de los datos de salida
-----

-- purpose: registro de datos ADC0
-- type : sequential
-- inputs : clk_sys, rst
-- outputs:
--
--
REGADC0 : process (clk_sys, rst)
begin -- process REGADC
if rst = '1' then -- asynchronous reset (active low)
    ADC0_data_out <= (others => '0');
elseif clk_sys'event and clk_sys = '1' then -- rising clock edge
    if reg_en0 = '1' then
        ADC0_data_out <= ADC_data_in;
    end if;
end if;
end process REGADC0;

```

```
REGADC1 : process (clk_sys, rst)
begin -- process REGADC
if rst = '1' then -- asynchronous reset (active low)
ADC1_data_out <= (others => '0');
elseif clk_sys'event and clk_sys = '1' then -- rising clock edge
if reg_en1 = '1' then
ADC1_data_out <= ADC_data_in;
end if;
end if;
end process REGADC1;

REGADC2 : process (clk_sys, rst)
begin -- process REGADC
if rst = '1' then -- asynchronous reset (active low)
ADC2_data_out <= (others => '0');
elseif clk_sys'event and clk_sys = '1' then -- rising clock edge
if reg_en2 = '1' then
ADC2_data_out <= ADC_data_in;
end if;
end if;
end process REGADC2;

REGADC3 : process (clk_sys, rst)
begin -- process REGADC
if rst = '1' then -- asynchronous reset (active low)
ADC3_data_out <= (others => '0');
elseif clk_sys'event and clk_sys = '1' then -- rising clock edge
if reg_en3 = '1' then
ADC3_data_out <= ADC_data_in;
end if;
end if;
end process REGADC3;

end RTL;
```

Code 3. AD786x\_IP.vhd

### 1.2.i.c. PowerPC firmware

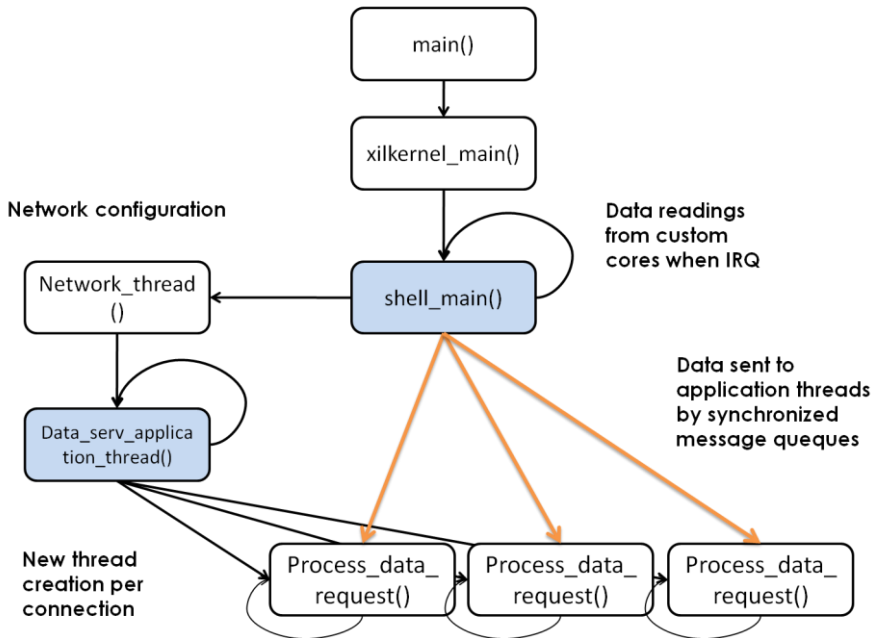


Figure 1.22. Flow diagram of the firmware application running in the PowerPC processor. The application is a simple data server, based on the small weight operative system Xilkernel from Xilinx, that accepts TCP connections to a named port and sends the measured data to each client connected. TCP/IP communications are handled by the Xilinx implementation of the lwIP 3.0 library. The system is constantly performing the frequency measurements and the ADC conversions. When a new data is available, an interrupt request is generated and the main application reads the data from the interrupting core. If a client is connected to the server, the application sends the data to the corresponding thread through a protected message queue for data communication between threads. The data is sent to the PC client in ASCII format.

```

#include <stdio.h>

#include "xmk.h"
#include "xenv_standalone.h"
#include "xparameters.h"
#include "xstatus.h"
#include "freq_meas_ip.h"
#include "ad786x_adc.h"
#include "xgpio_1.h"

#include "netif/xadapter.h"

#include "lwip/inet.h"
#include "lwip/sockets.h"
#include "lwip/sys.h"
#include "lwipopts.h"

// sema y queques

#include "semaphore.h"
#include "sys/msg.h"
#include "sys/ipc.h"
#include "errno.h"

// #include "data_server.h"

#define DHCP_TIMEOUT_MS 50000

//void echo_application_thread();
//void echo_application_header();

struct data_message_s {
    double freq0;
    double freq1;
    Xuint32 adc0;
    Xuint32 adc1;
    Xuint32 adc2;
    Xuint32 adc3;
};

struct str_message_s {
    char freq0[32];
    char freq1[32];
    char adc0[32];
    char adc1[32];
    char adc2[32];
    char adc3[32];
};

};

static sem_t mutex;
static char conexiones;
static struct data_message_s data;
static char new_data;

u16_t DATA_PORT = 7;

struct netif server_netif;
unsigned char mac_ethernet_address[] = { 0x00, 0x0a, 0x35, 0x00, 0x01, 0x02 };

/* thread spawned for each connection */
void process_data_request(void *p)
{
    int sd = (int)p;
    int RECV_BUF_SIZE = 2048;
    char rcv_buf[RECV_BUF_SIZE];
    int n, nwrote;
    char conId;
    int msgid;

```

```

struct data_message_s data_tx;
static struct str_message_s str_data;

xil_printf("data server sd: %d\n\r", sd);

// Seccion critica, Aumentamos N° de conexiones y colas
if( sem_wait(&mutex) < 0 ) {
    printf("SEM: shell_main sem_wait error.\r\n");
    goto err;
}

    conexiones = conexiones +1;
    conId = conexiones;
    printf("con Id %d",conId);
    if (conId > 10){
        conexiones = conexiones -1;
    }

if( sem_post(&mutex) < 0 ) {
    printf("SEM: shell_main sem_post error.\r\n");
    goto err;
}
// Fin de seccion critica
printf("con Id_out %d",conId);

if (conId > 10){
    printf("error: Conexiones por encima del limite \n\r");
    goto err;
}

    printf("creamos cola %d",conId-1);
    msgid = msgget (conId-1, IPC_CREAT ) ;

    if( msgid == -1 ) {
        printf("ERROR while opening Message Queue in SOCKET. Erno:
%d\r\n", errno) ;
        goto err;
    }

    printf("cola creada %d",conId-1);

    while (1) {

        if( msgrcv( msgid, &data_tx, sizeof(struct data_message_s), 0,0 ) !=
sizeof(struct data_message_s) ) { // blocking recv
            printf (" msgrcv of queue(%d) ran into ERROR. Erno: %d.
Halting..\r\n", conId, errno);
            goto err;
        }

        sprintf(str_data.freq0,"%f",data_tx.freq0);
        sprintf(str_data.freq1,"%f",data_tx.freq1);
        sprintf(str_data.adc0,"%d",data_tx.adc0);
        sprintf(str_data.adc1,"%d",data_tx.adc1);
        sprintf(str_data.adc2,"%d",data_tx.adc2);
        sprintf(str_data.adc3,"%d",data_tx.adc3);

        /* Sent data received in queue */
        if ((nwrote = write(sd, &str_data, sizeof(struct str_message_s))) < 0) {
            printf("%s: ERROR responding to client echo request. received =
%d, written = %d\n\r",
                __FUNCTION__, n, nwrote);
            goto err;
        }
    }

    /* close connection */
err:

    if( sem_wait(&mutex) < 0 ) {

```

```

        printf("SEM: data_proc sem_wait closing error.\r\n");
        goto cls;
    }

    conexiones = conexiones - 1;

    if (sem_post(&mutex) < 0 ) {
        printf("SEM: data_proc sem_post closing error.\r\n");
    }
cls:
    xil_printf("Closing socket %d\n\r", sd);
    close(sd);
    // Fin de seccion critica
}

void data_serv_application_thread()
{
    int sock, new_sd;
    struct sockaddr_in address, remote;
    int size;

    if ((sock = lwip_socket(AF_INET, SOCK_STREAM, 0)) < 0)
        return;

    address.sin_family = AF_INET;
    address.sin_port = htons(DATA_PORT);
    address.sin_addr.s_addr = INADDR_ANY;

    if (lwip_bind(sock, (struct sockaddr *)&address, sizeof(address)) < 0)
        return;

    lwip_listen(sock, 5);

    size = sizeof(remote);

    while (1) {
        new_sd = lwip_accept(sock, (struct sockaddr *)&remote, &size);
        sys_thread_new(process_data_request, (void*)new_sd,
DEFAULT_THREAD_PRIO);
    }
}

void* netif_config_thread(void *arg)
{
    struct netif *app_netif;
    struct ip_addr ipaddr, netmask, gw;

    int mscnt = 0;

    app_netif = &server_netif;

    // Clear the IP address, Subnet Mask, and Gateway
    ipaddr.addr = 0;
    netmask.addr = 0;
    gw.addr = 0;

    // Set up the lwIP network interface
    // Allocate and configure the app's netif

    if (!xemac_add(app_netif, &ipaddr, &netmask, &gw, mac_ethernet_address,
XPAR_LLTEMAC_0_BASEADDR)) {
        xil_printf("Error adding N/W interface\n\r");
        return;
    }
    netif_set_default(app_netif);
}

```

```

/* start packet receive thread - required for lwIP operation */
sys_thread_new((void*)(void*))xemacif_input_thread, app_netif, DEFAULT_THREAD_PRIO);

// Start the DHCP "Client Daemon"
print("Starting DHCPClient...\r\n");
dhcp_start(app_netif);

while (1) {
    sleep(DHCP_FINE_TIMER_MSECS);
    dhcp_fine_tmr();
    mscnt += DHCP_FINE_TIMER_MSECS;
    if (mscnt >= DHCP_COARSE_TIMER_SECS*1000) {
        dhcp_coarse_tmr();
        mscnt = 0;
    }
}

}

void network_thread(void *p)
{
    struct netif *app_netif;
    struct ip_addr ipaddr, netmask, gw;

    app_netif = &server_netif;
    int mscnt = 0;

    print("-- Entering network_thread --\r\n");
    // sleep(20);

    // Start network configuration (+DHCP) thread
    print("Configuring IP via DHCP...\r\n");
    sys_thread_new ((void*)(void*))netif_config_thread, 0, 0);

    // Wait for DHCP IP configuration
    while (1) {
        sleep(DHCP_FINE_TIMER_MSECS);
        if (app_netif->ip_addr.addr) {
            print("DHCP request success\r\n");
            print_ip("Board IP: ", &ipaddr);
            break;
        } else {
            print("No ip yet\r\n");
            ipaddr=app_netif->ip_addr;
            print_ip("Board IP: ", &ipaddr);
        }
        mscnt += DHCP_FINE_TIMER_MSECS;
        if (mscnt >= DHCP_TIMEOUT_MS) {
            print("Oh No!\r\n");
            print("ERROR: DHCP request timed out\r\n");

            print("*****\r\n");
            print("***** IP FIJA *****\r\n");

            netif_set_down(app_netif);

            IP4_ADDR(&ipaddr, 192, 168, 1, 75);
            IP4_ADDR(&netmask, 255, 255, 255, 0);
            IP4_ADDR(&gw, 192, 168, 1, 69);

            /* Add network interface to the netif_list, and set it as default */
            if (!xemac_add(app_netif, &ipaddr, &netmask, &gw, mac_ethernet_address,
XPAR_LLTEMAC_0_BASEADDR)) {
                xil_printf("Error adding N/W interface\n\r\n");
                return ;
            }

            netif_set_default(app_netif);
            /* specify that the network if is up */
            netif_set_up(app_netif);
            /* start packet receive thread - required for lwIP operation */

```

```

        sys_thread_new(xemacif_input_thread, app_netif, DEFAULT_THREAD_PRIO);

    return;
}
}
print("IP configuration done\r\n");

/* print out IP settings of the board */
print("\n\r\n\r");
print_ip_settings(&app_netif->ip_addr, &app_netif->netmask, &app_netif->gw);

/* now we can start application threads */
// print_echo_app_header();
sys_thread_new(data_serv_application_thread, 0, DEFAULT_THREAD_PRIO);

/* print_web_app_header(); */
/* sys_thread_new(web_application_thread, 0, DEFAULT_THREAD_PRIO); */

return;
}

/*****/

void freq_interrupt(int num){

    Xuint32 sigIn_cycles=0;
    Xuint32 clk_cycles=0;
    Xuint32 Reg32Value;

    int led_value;
    double Freq;

    // Escribimos en el Interrupt Status Register para borrar interrupcion
    FREQ_MEAS_IP_mWriteReg((void *)XPAR_FREQ_MEAS_IP_0_BASEADDR,
    FREQ_MEAS_IP_INTR_DISR_OFFSET, 0);

    // Leemos los registros para calculo de frecuencia mediante reciproco
    sigIn_cycles = FREQ_MEAS_IP_mReadSlaveReg2((void *)XPAR_FREQ_MEAS_IP_0_BASEADDR, 0);
    clk_cycles = FREQ_MEAS_IP_mReadSlaveReg3((void *)XPAR_FREQ_MEAS_IP_0_BASEADDR,
0);

    Freq = (((double)sigIn_cycles)/((double)clk_cycles))* 100000000.00;

    // Almacenamos en
    data.freq0 = Freq;
    data.freq1 = 0.0;

    //printf(" Frecuencia en 0 (user_count/clk_count) * f_clk == %.2Lf \n\r", Freq);

    // Ponemos a 0 Reg4 para provocar conversion con transicion 0-1 en Reg4(0)
    AD786X_ADC_mWriteSlaveReg4((void *)XPAR_AD786X_ADC_0_BASEADDR, 0, 0);

    Reg32Value = AD786X_ADC_mReadSlaveReg0((void *)XPAR_AD786X_ADC_0_BASEADDR,
0);
    data.adc0 = Reg32Value;
    Reg32Value = AD786X_ADC_mReadSlaveReg1((void *)XPAR_AD786X_ADC_0_BASEADDR,
0);
    data.adc1 = Reg32Value;
    Reg32Value = AD786X_ADC_mReadSlaveReg2((void *)XPAR_AD786X_ADC_0_BASEADDR,
0);
    data.adc2 = Reg32Value;
    Reg32Value = AD786X_ADC_mReadSlaveReg3((void *)XPAR_AD786X_ADC_0_BASEADDR,
0);
    data.adc3 = Reg32Value;

    // Ponemos a 0 Reg4 para provocar conversion con transicion 0-1 en Reg4(0)
    AD786X_ADC_mWriteSlaveReg4((void *)XPAR_AD786X_ADC_0_BASEADDR, 0, 0xFFFFFFFF);

    new_data=1;

    return;
}

```

```

int init_freq(){

    Xuint32 sigIn_cycles=0;
    Xuint32 Reg32Value;
    XStatus status;

    print("-- Entering init_freq --\r\n");

    /* Hacemos el selftest de los IP para freq metering */

    xil_printf("***** \n\r");
    xil_printf(" Starting FREQ_MEAS_IP_0 Selftest \n\r");
    xil_printf("***** \n\r");

    status = FREQ_MEAS_IP_SelfTest ((void *)XPAR_FREQ_MEAS_IP_0_BASEADDR);
    if (status != XST_SUCCESS) {
        xil_printf ("freq_count selftest: XIntc_Initialize failed.\r\n");
        return;
    }
    xil_printf(" IP FREQ_MEAS_IP_0 test ended \n\r");

    xil_printf("***** \n\r");
    xil_printf(" Starting AD786X Selftest \n\r");
    xil_printf("***** \n\r");

    xil_printf(" - write 5 to slave register 4 word 0\n\r");
    AD786X_ADC_mWriteSlaveReg4(XPAR_AD786X_ADC_0_BASEADDR, 0, 5);
    Reg32Value = AD786X_ADC_mReadSlaveReg4(XPAR_AD786X_ADC_0_BASEADDR, 0);
    xil_printf(" - read %d from register 4 word 0\n\r", Reg32Value);

    if ( Reg32Value != (Xuint32) 5 ){
        xil_printf(" - slave register 4 word 0 write/read failed\n\r");
        return;
    }
    xil_printf(" - slave register write/read passed\n\r");
    xil_printf(" IP AD786X test ended \n\r");

    sleep(2);

    xil_printf(" - Escribimos en (gate_div_data) el valor 99999999 para fijar gate time \n\r");
    xil_printf(" - Divisor sys_clk (100MHz) sincronizado con señal de entrada \n\r");

    FREQ_MEAS_IP_mWriteSlaveReg1((void *)XPAR_FREQ_MEAS_IP_0_BASEADDR,
0,99999999);

    /* Initialize exception handling */

    xil_printf("***** \n\r");
    xil_printf("**** Inicializamos manejo Interrupciones **** \n\r");
    xil_printf("***** \n\r");
    status= register_int_handler(XPAR_XPS_INTC_0_FREQ_MEAS_IP_0_IP2INTC_IRPT_INTR,
(XInterruptHandler)freq_interrupt,
25);

    if (status != XST_SUCCESS) {
        xil_printf ("freq_meas 0 intc: reg failed.\r\n");
        return;
    }

    xil_printf("***** \n\r");
    xil_printf("**** Habilitamos Interrupciones IP **** \n\r");
    xil_printf("***** \n\r");
    enable_interrupt(XPAR_XPS_INTC_0_FREQ_MEAS_IP_0_IP2INTC_IRPT_INTR);

    return;

}

/*****/

int shell_main()
{

```

```

struct data_message_s data_tx;
int led_value;
char Ncolas_tx;
int msgid;
int key;

print("-- Entering main_thread --\r\n");

// inicializamos COMUNICACIONES ENTRE PROCESOS
if( sem_init(&mutex, 1, 1) < 0 ) {
printf("SEM: Error while initializing semaphore mutex.\r\n");
return;
}

conexiones = 0;
new_data = 0;

/* initialize lwIP before calling sys_thread_new */
lwip_init();
/* any thread using lwIP should be created using sys_thread_new */
sys_thread_new(network_thread, NULL, DEFAULT_THREAD_PRIO);

// Inicializamos medida de parametros

sleep (15000);
init_freq();

while(1){
sleep(200);

if(led_value = 1){
led_value = 0;
XGpio_mSetDataReg(XPAR_BASEBOARD_LEDS_3BIT_BASEADDR, 1,
0);
} else {
led_value = 1;
XGpio_mSetDataReg(XPAR_BASEBOARD_LEDS_3BIT_BASEADDR, 1,
0xFFFFFFFF);
}

printf("New Data %d \n\r", new_data);
if (new_data == 1) {

data_tx = data;

printf("*** Frecuencia Sensor0 (user_count/clock_count) * f_clk == %f
\n\r", data_tx.freq0);
printf("*** Frecuencia Sensor1 (user_count/clock_count) * f_clk == %f
\n\r", data_tx.freq1);

printf("*** Voltaje ADC0 == %d \n\r", data_tx.adc0);
printf("*** Voltaje ADC1 == %d \n\r", data_tx.adc1);
printf("*** Voltaje ADC2 == %d \n\r", data_tx.adc2);
printf("*** Voltaje ADC3 == %d \n\r", data_tx.adc3);

// Seccion critica, consulta N° de conexiones y colas
if( sem_wait(&mutex) < 0 ) {
print("SEM: shell_main sem_wait error.\r\n");
goto err;
}

Ncolas_tx = conexiones;
printf("N_conexiones0 %d \n\r", Ncolas_tx);

if( sem_post(&mutex) < 0 ) {
print("SEM: shell_main sem_post error.\r\n");
goto err;
}
// Fin de seccion critica

```

```

        printf("N_conexiones1 %d \n\r", Ncolas_tx);

        for (key=0;key < Ncolas_tx; key=key+1){
            printf("Dentro key %d \n\r", key);
            msgid = msgget (key, IPC_CREAT );
            if( msgid == -1 ) {
                printf("ERROR while opening Message Queue.
Errno: %d\r\n", errno) ;
            }

            if( msgsnd (msgid, &data_tx, sizeof(struct
data_message_s), 0) < 0 ) { // blocking send
                printf (" msgsnd of queue(%d) ran into
ERROR. Errno: %d. Halting..\r\n", key, errno);
            }

            } // for
            new_data=0;
        } // new data

    } //while
err:
    return 0;
} // shell_main

int main()
{
    /* enable caches */
    XCACHE_ENABLE_ICACHE();
    XCACHE_ENABLE_DCACHE();

    xil_printf("***** \n\r");
    xil_printf("***** Baseboard_IPtest ***** \n\r");
    xil_printf("***** \n\r\n\r\n\r");

    xilkernel_main(); // llama a shell_main

    return 0;
}

```

Code 4. data\_server.c

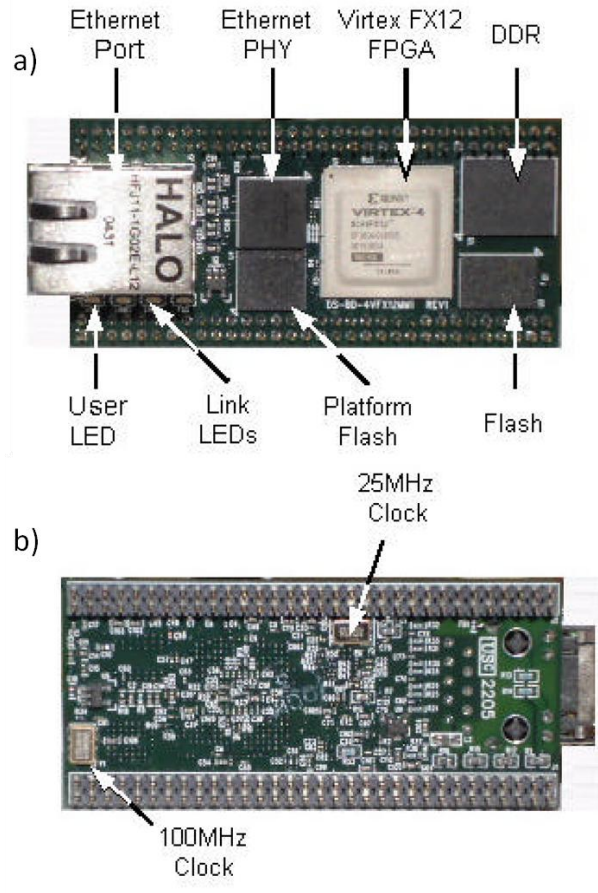
**I.2.ii. Design schematics**

Figure I.23. Top and bottom view of the Virtex-4 FX12 Mini Module. Physical placement for the components composing the module as described before is shown in the figure. The module has dimensions of 70.5mm x 30 mm. Two 2x32 2mm I/O headers provide connectivity to the module. The module is plugged in the support circuitry which provides the appropriate socket for connection.

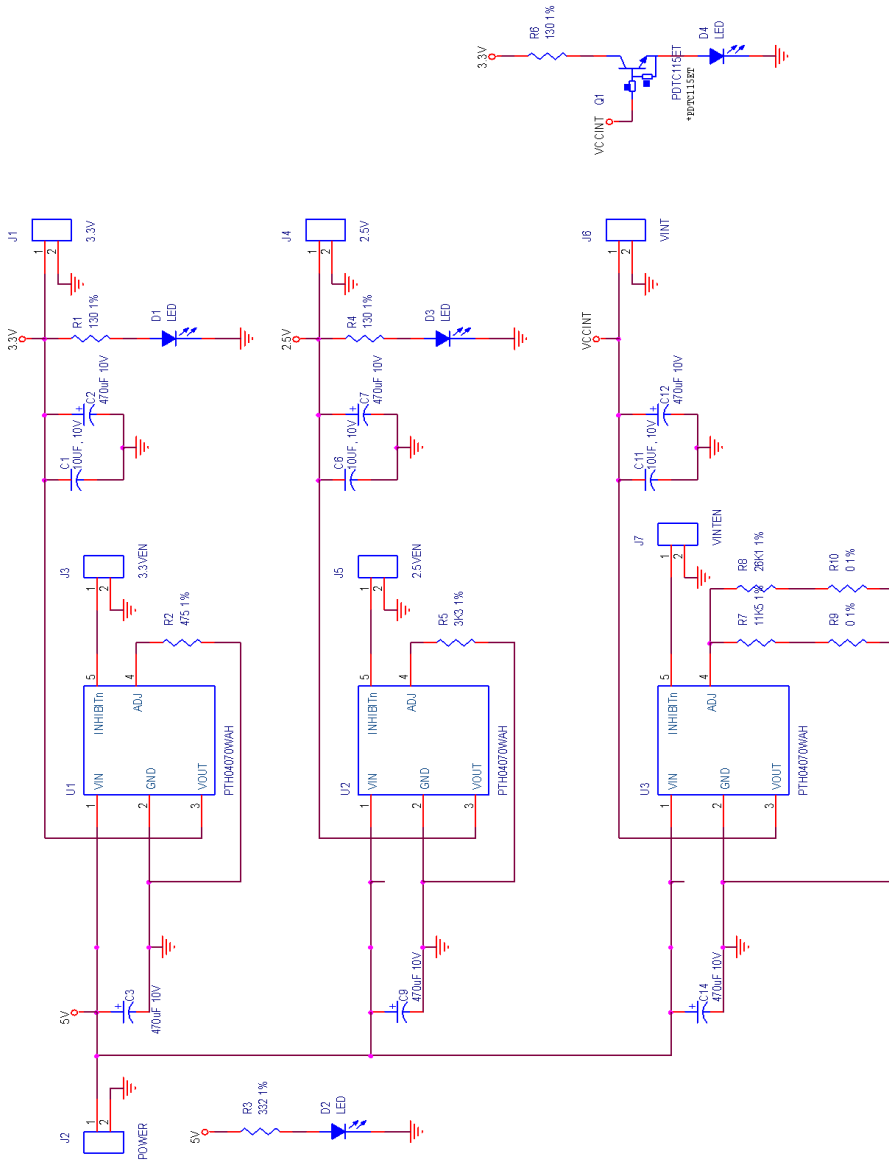


Figure I.24. Power supply circuitry for the FPGA subsystem, The FPGA subsystem is powered by a 5 V voltage through connector J2. The power supply design mainly consist on three DC/DC switching regulators modules (PTH04070WAH, Texas Instruments, Inc.). Those modules provide the 3.3 V, 2.5 V and 1.8 V supply voltages needed by the FPGA module.

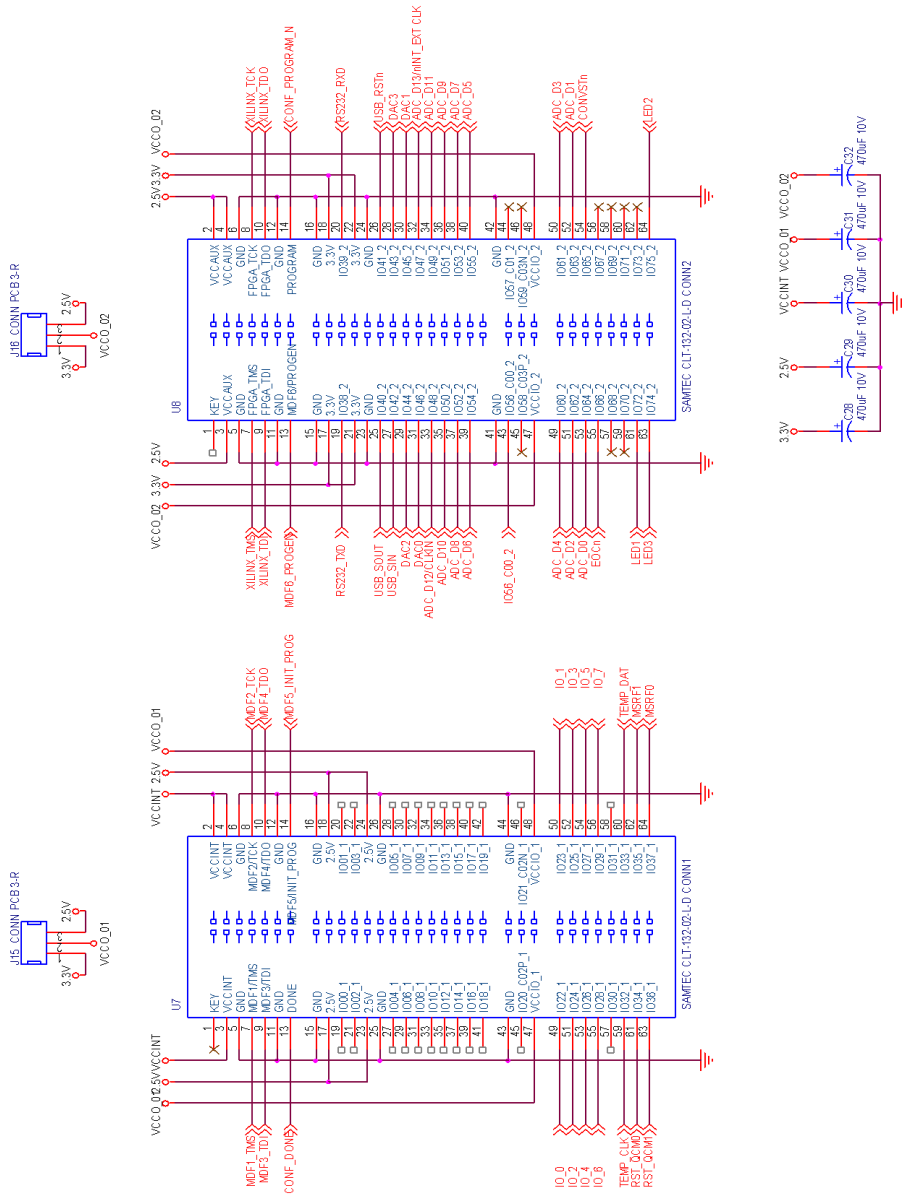


Figure I.25. Connection headers for the Virtex-4 FX12 Mini module. Figure also shows the bulk tantalum decoupling capacitors for the mini module power supply lines and two jumpers for selecting the appropriate power supply for the FPGA I/O interfacing lines.



Figure I.26. AD7864 based data acquisition frontend. A preconditioning signal stage based on the AD713 (Analog Devices, Inc.), a quad, high-speed and precision, BiFET operational amplifier, is included. This stage was not assembled on the final implementation as the signal levels from the ACC system were well adapted to the input range of the ADC circuit. The throughput of the ADC system when enabling all four channels in the read during conversion mode of operation is 130 kSPS. Cut off frequency of the low pass filters before the ADC is 48 KHz.

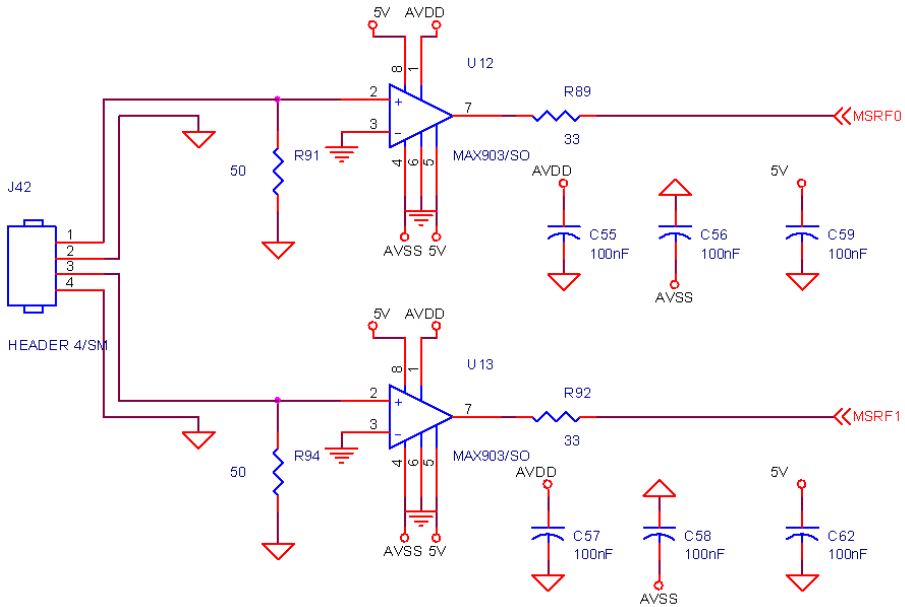


Figure I.27. High frequency comparators for frequency measurements trigger conditioning. Two different sine wave signals can be conditioned with the two different high speed MAX903 comparators (Maxim Integrated). These comparators can be powered from separate analog and digital supplies. The input range include negative voltages. The comparator transforms the sine wave signal from the VCO into a square wave digital signal with FPGA compatible voltage levels.

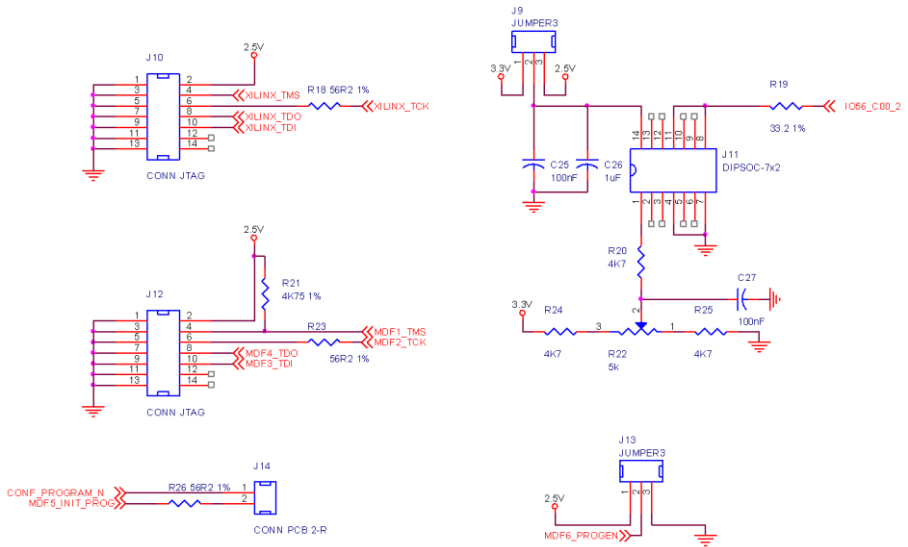


Figure I.28. FPGA programming and JTAG debug interface headers and external oscillator socket.

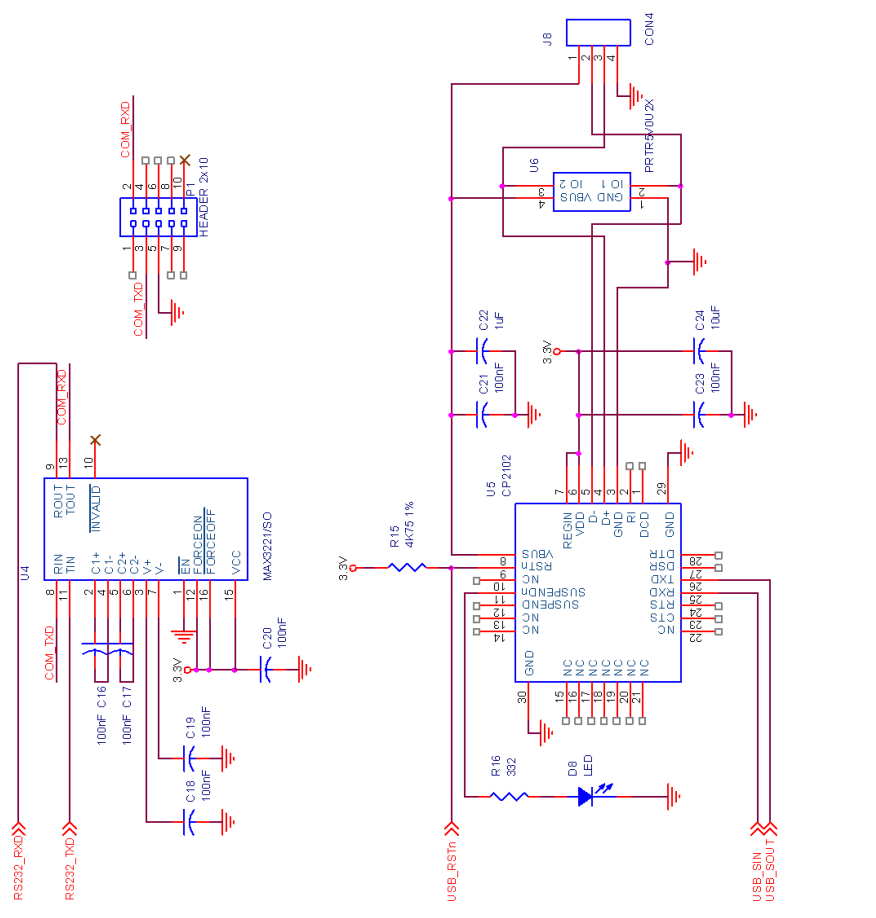
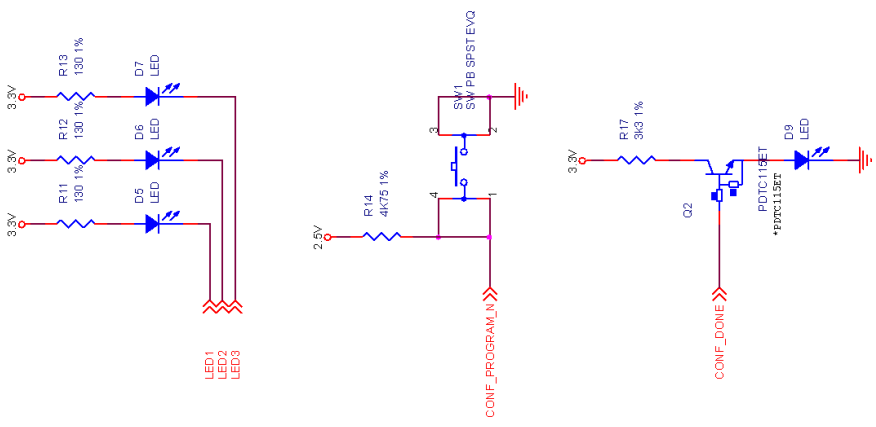


Figure I.29.USB and RS232 UART debugging interfaces. Two additional interfaces have been implemented for debugging and future expansion purposes. Although USB connection was not used in the final implementation of the system, a low cost CP2102 (Silicon Labs) USB to UART bridge offers a simple solution for a full-speed USB 2.0 compliant connectivity. For the UART serial interface, MAX232 (Maxim Integrated) performs the level translation between the RS-232 levels of the serial line and the 3.3 V LVCMOS levels of the FPGA.

### I.2.iii. Printed circuit board design

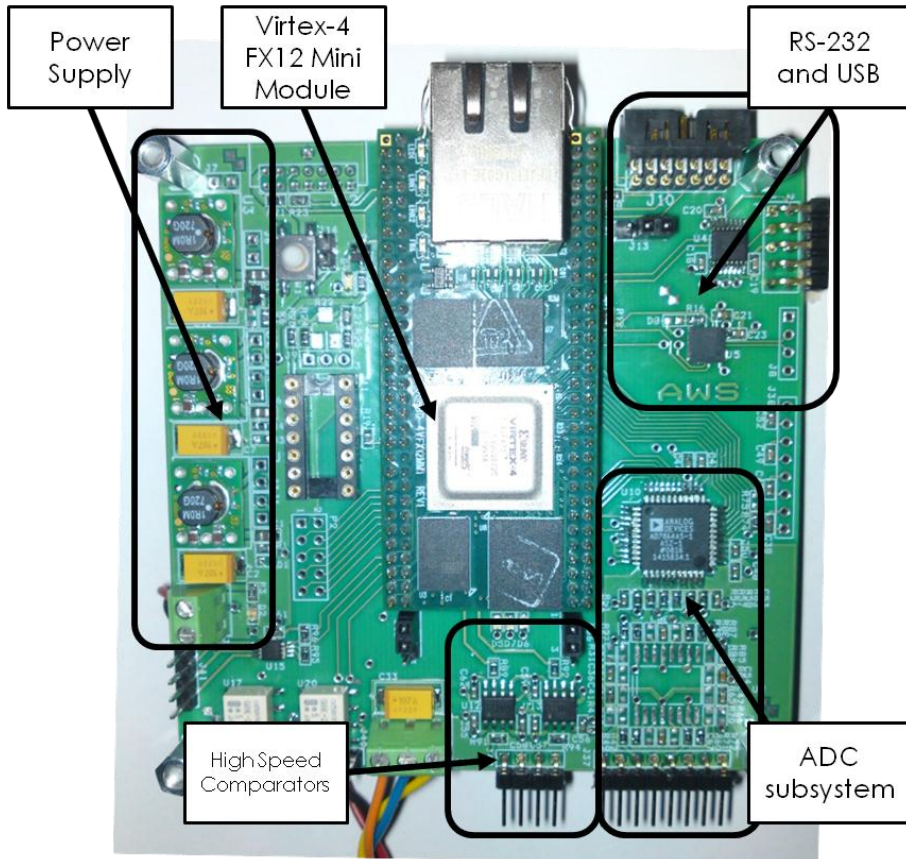


Figure I.30. Implementation of the system, showing the distribution of each subsystem in the printed circuit board.

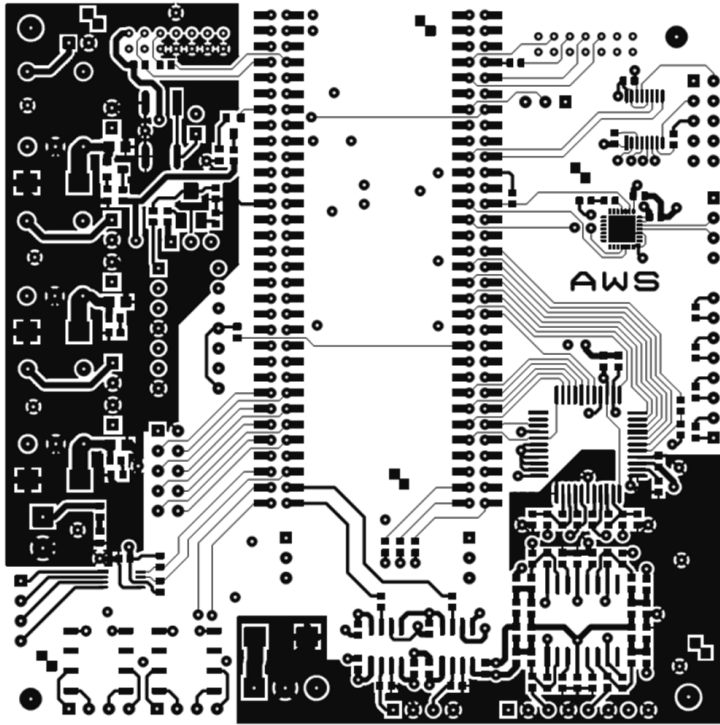


Figure I.31. Top Layer fabrication mask. Analog areas around power supply and ADC subsystem are surrounded by an analog ground copper pour.

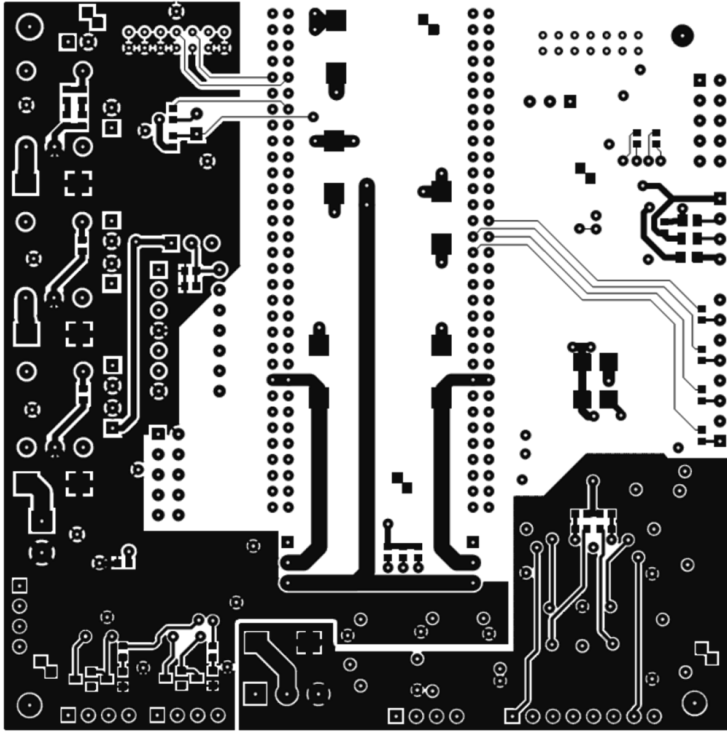


Figure I.32. Bottom Layer fabrication mask.

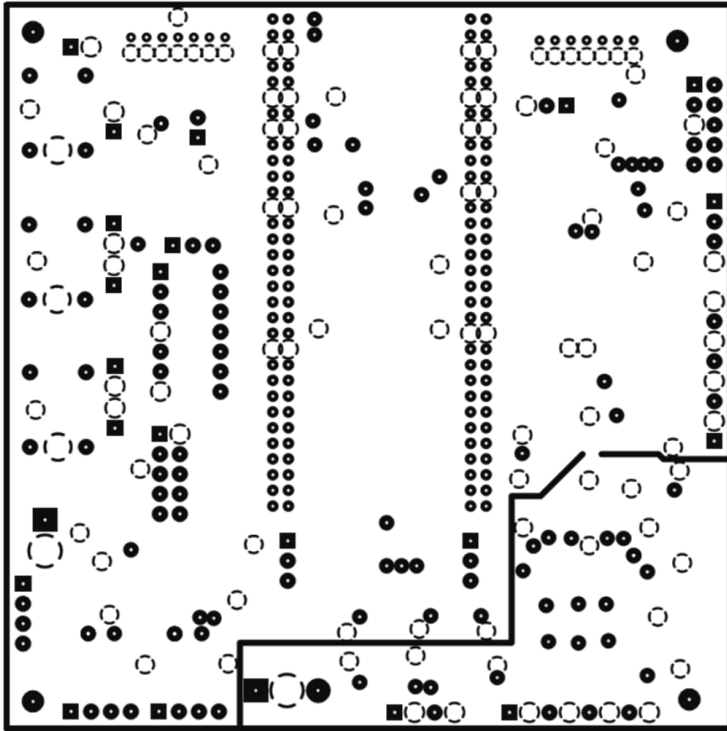


Figure I.33. Ground plane internal layer fabrication mask (negative view). Figure shows a split plane configuration for the ground plane. Digital and analog grounds are only joined at one point, beneath the analog to digital converter placement.

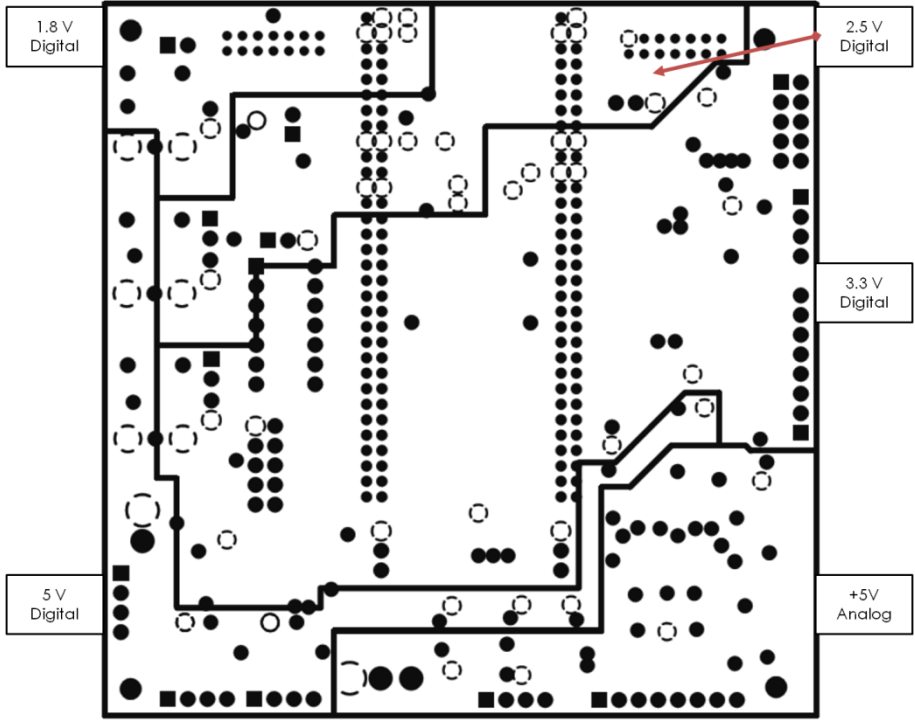


Figure I.34. Power supply plane. Figure shows the different voltage domains of the system.



Figure I.35. Assembled communications and data acquisition circuit. Top view.



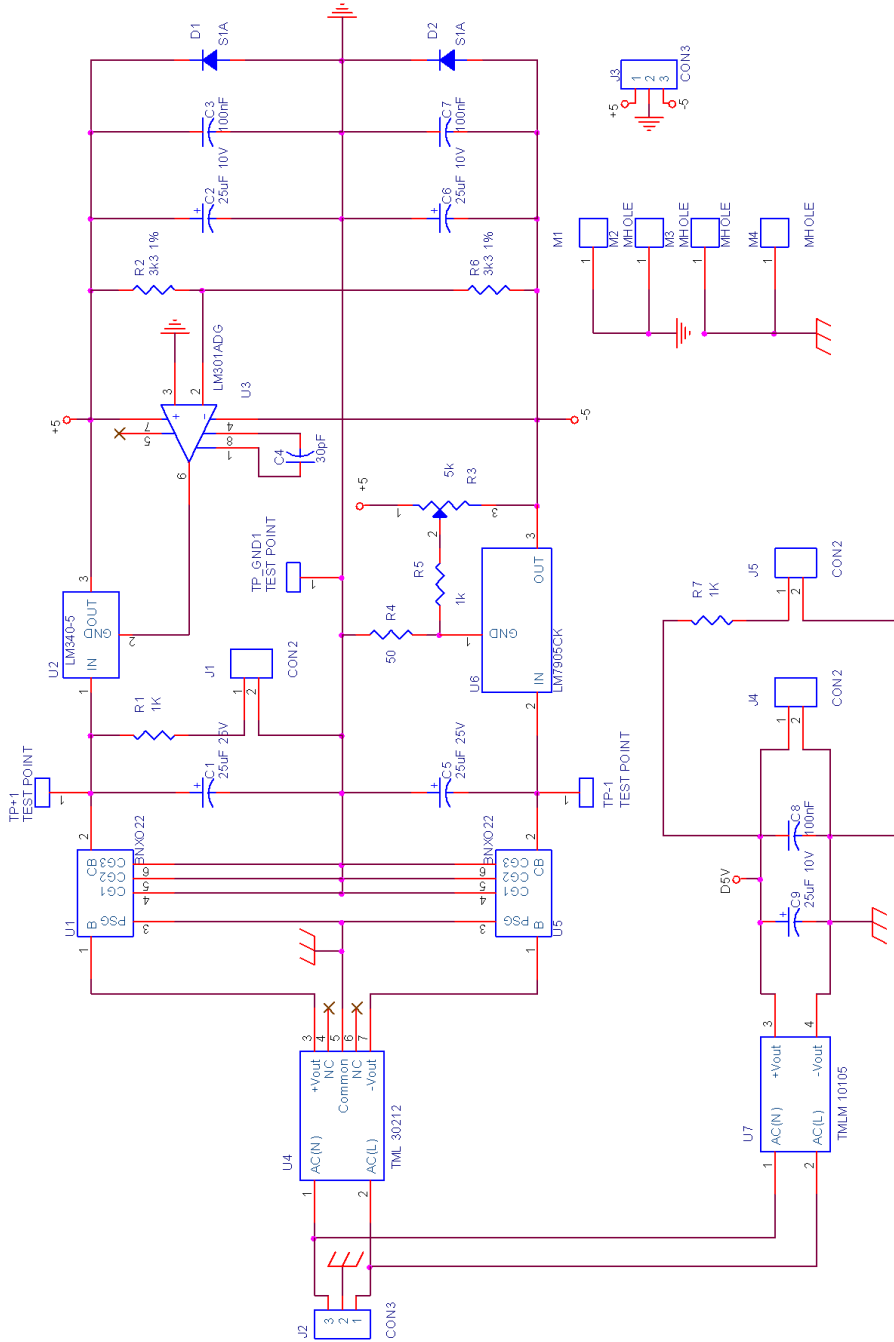
### **I.3. Symmetrical power supply**

The power supply is the circuit that supplies the electric energy needed by the rest of the circuits of the system. It generates the different direct current (DC) voltages needed by the different subsystems from the mains supply.

For the digital part of the communications and data acquisition circuit we need to supply a continuous supply of 5 Volts, with a current of 2 Amperes. We have used a commercial AC/DC power supply, model TMLM 10105 (TRACO Electronic AG) for PCB mounting, for this.

The ACC sensor circuit needs a symmetric supply that shall meet some special requirements. The design should be performed so that the symmetry of the regulated tensions will remain at the highest degree, providing a voltage of +5 Volts for a current of 1.5 Amperes at the output. This is important for the operation of the sensor circuit, because any asymmetry in the supply voltage can introduce errors in the comparison thresholds of the comparators of the PLL loops. This mismatch can introduce errors during the detection of the phase in the PLL and thus add noise and errors in the measurements performed by the system (Sogorb, 2003). Details of the implementation are shown next.

### I.3.i. Design schematics



---

Figure I.36. Symmetric power supply designed. For the digital power supply a commercial module TMLM 10105 supplies 5 V and up to 2 A. Another AC/DC commercial module generates  $\pm 12$  V symmetrical at the output with a current up to 1.3 A. Those outputs are filtered, before being connected to the regulators and the symmetry circuit, by means of the suppressor element BNX022 (muRata). This circuit introduces an attenuation of at least 35dB in the range of frequencies between 1MHz and 1GHz. The linear regulators LM340 and LM7905 (National Semiconductor) are used for generating the  $\pm 5$  V symmetric supply. To ensure the symmetry, a feedback circuitry based on the LM301 OPA is used. The circuit guarantees a symmetrical voltage output at all times if a pair of well-matched resistors, R2 and R6, are used.

I.3.ii. Printed circuit board design

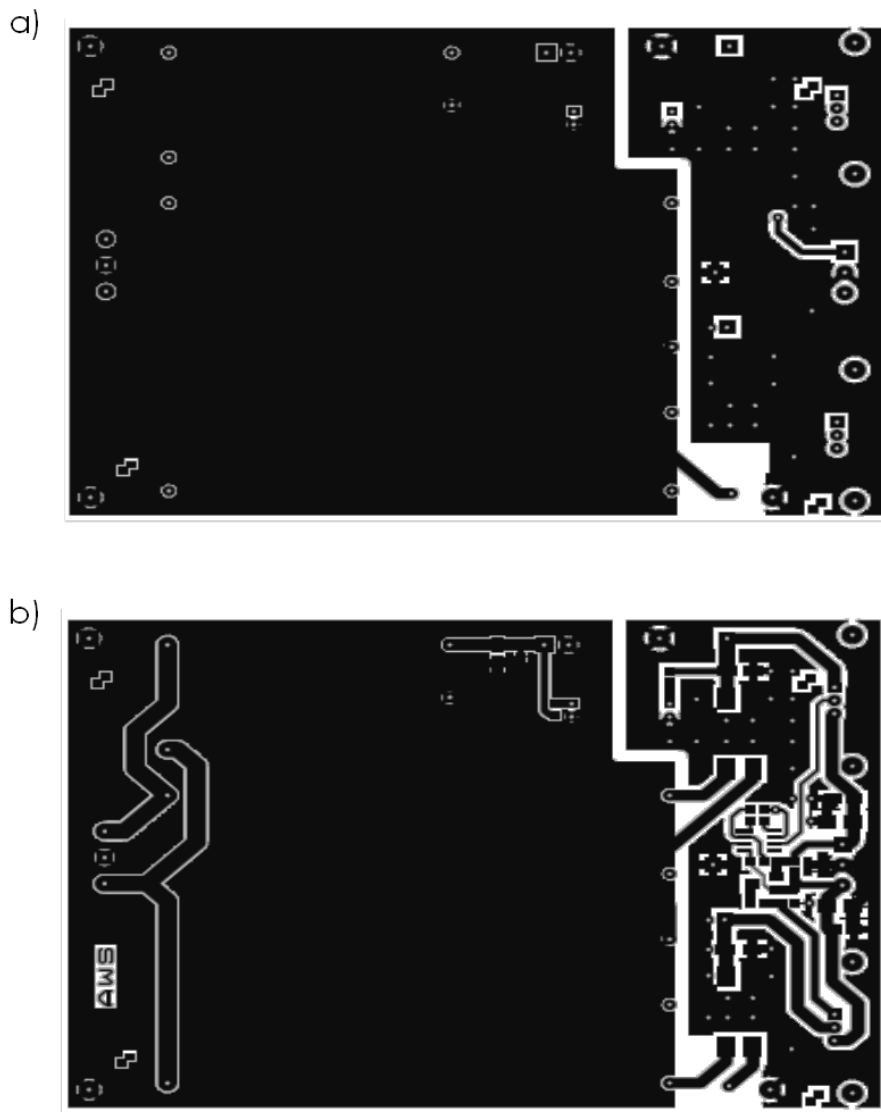


Figure I.37. Fabrication masks for the power supply circuit



Figure I.38. Assembled Power supply circuit.

---

#### I.4. Instrument's enclosure. AWS ACC-QCM-09

Finally, the whole system has to be put in a box. The instrument has a SMB frontal connector for the measurement cell that contains the quartz crystal. In the rear panel we have the connector for the AC mains supply, a panel opening for accessing the mini module RJ45 connector, and two BNC connectors for auxiliary analog connection to the  $R_m$  and  $C_o$  voltage signals of the system. We have performed two small holes in the lower part of the enclosure to reach the calibration potentiometers with the closed instrument.



Figure I.39. ACC-QCM-09 Instrument. Subsystems assembled and distributed inside the enclosure.



Figure I.40. ACC-QCM-09 Instrument (Awsensors S.L.).



## **Appendix II. Design and implementation of an integrated platform for high frequency QCM sensors in high-resolution applications**

---

In this appendix, we are describing the design and implementation of the integrated platform for acoustic wave based sensors used for the experiments presented in sections 3.3 and 3.4

The platform consists of an electronic characterization system, an automated flow injection analysis (FIA) system, and a control and communications system, controlled remotely by a PC software interface. Advanced Wave Sensors S.L., commercialized the platform under the name *AWS-A10 Research Platform* (see Figure II.1).

The characterization system, based on the proposed system in section 3.2. and previous works for QCM sensors [MONTAGUT 2011 SENSORS] [MONTAGUT 2011 RSI], was re-designed to be able to characterize QCM, HFF-QCM and SGAW type sensors, with operation frequencies in a range between 5 MHz and 150 MHz This allowed the comparison of different type of

acoustic wave sensor devices, measured by the same characterization system and under similar experimental conditions. The system was conceived as a multichannel system, being able to characterize up to four sensor devices, of any type, simultaneously, although the prototype manufactured included only one characterization channel.

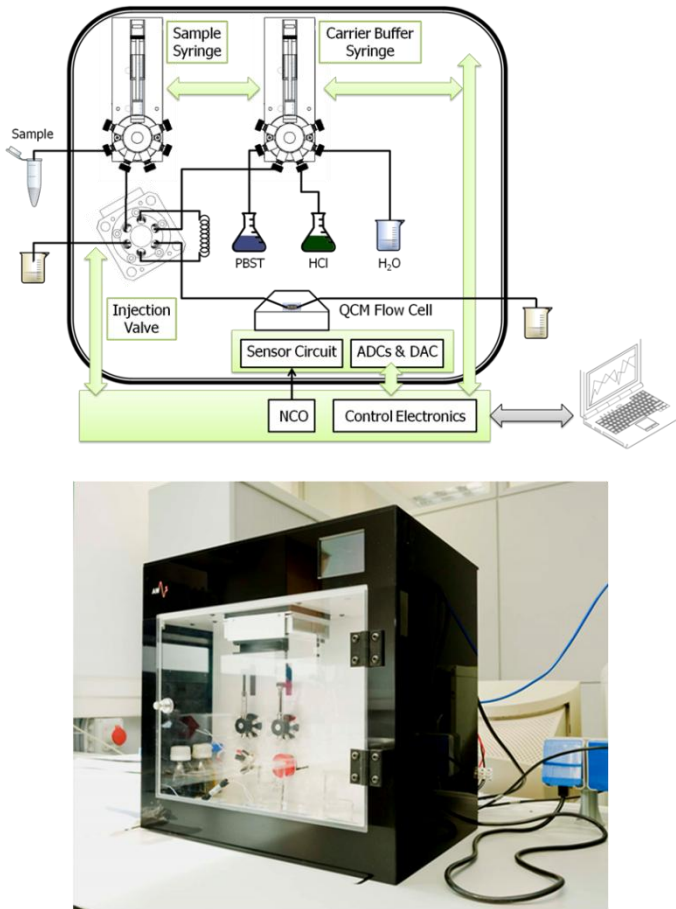


Figure II.1. AWS-A10 Research Platform: block diagram (top) and implemented system (bottom).

Per each channel, the proposed FIA system consisted on a syringe pump, a distribution valve and an injection valve. In addition, a flow cell custom designed for each type of sensor was used to provide mechanical

support for the sensor, electrical connection of the acoustic device to the characterization system, and flow confinement in the active areas of the devices. Two syringe pumps were available in the manufactured system so one of the syringes was used for flowing the different buffers over the sensor, and the other was used for loading the samples into the sample loops in a precise and repetitive way.

The systems enclosure was designed in such a way that the FIA elements and temperature sensitive parts of the characterization system were confined inside a thermostatic chamber. An air-to air peltier based thermoelectric assembly and a programmable controller, implementing a PID algorithm, were selected as the thermal management solution for the system. This allowed us to maintain a thermally stable environment when performing the measurements ( $25\text{ }^{\circ}\text{C} \pm 0.1\text{ }^{\circ}\text{C}$ ), both for the fluidic system (avoiding bubble generation due to temperature gradients) and the sensors characterization (avoiding temperature-induced changes in the acoustic sensor response or the characterization electronics).

The PC software collected the data from the characterization system and controlled all the elements of the AWS-A10 Platform, including the FIA system.

Details of the design and implementation of this system will be shown next.



will produce a change in its electrical response which, in turn, causes the phase and magnitude shift between  $u_1$  and  $u_2$ .

The phase and magnitude measurements are based on the AD8302 integrated circuit. A pair of matched logarithmic amplifiers provide the magnitude ratio measurement and a multiplier-type phase detector provides the phase difference measurement (Analog Devices, 2002). For the magnitude measurement, the default input range is -30 dB to + 30 dB with the analog output signals ranging from 0 V to 1.8 V and a sensitivity around 30 mV/dB. For the phase measurement, the detector has a sensitivity of 10 mV/ degree, for an input range of  $0^\circ$  to  $180^\circ$ .

For operation in the optimal set point of the detector (maximum linearity and accuracy), signals  $u_1$  and  $u_2$  should have similar levels and near 90 degrees of phase shift. For this, it is convenient to phase-shift the reference and sensor signals with the networks formed by  $R_i$  and  $C_i$ . In addition, the passive circuit elements of the reference branch ( $R_c$ ,  $C_c$ ,  $R_1$ ) are chosen to phase shift and attenuate the signal path of the reference branch in a similar way as it does in the sensor branch. Those phase-shifting networks are coherently designed for each sensor's type and operating frequency.

For example, when in operation with a QCM type sensor, it is convenient to use  $R_c$  and  $C_c$  components with values similar to the values of motional resistance,  $R_m$ , and parallel capacitance,  $C_0^*$ , of the sensor's model. A modular design, where those passive networks are implemented in different interchangeable modules, allow us to connect different type of sensors, of different operating frequencies, to the same characterization circuit (see Figures II.2 and II.3).

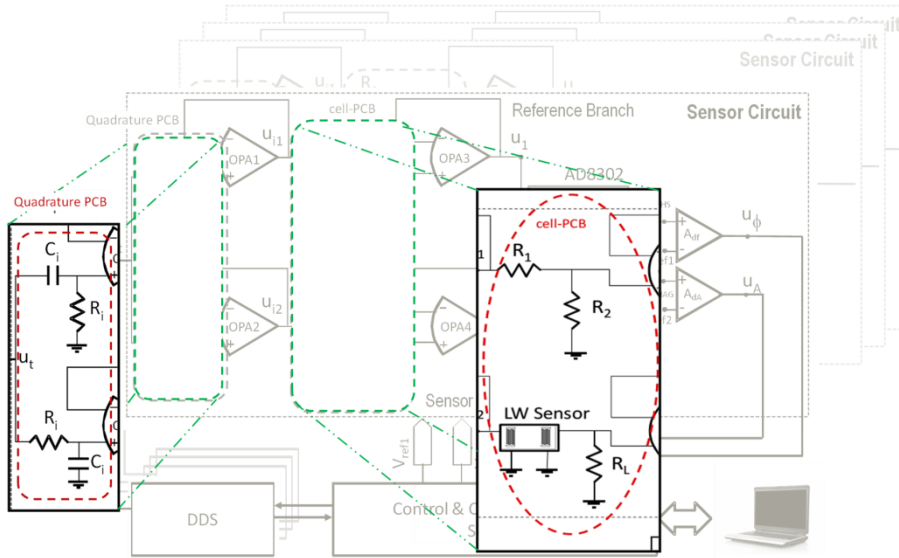


Figure II.3. Diagram shows components of the circuit implemented in different modules to allow interchangeability. Figure shows the configuration for characterization with a Love Mode SAW sensor. A different  $R_i$  and  $C_i$  network, what we call quadrature circuit, and a different reference branch network, physically implemented in a pcb integrated on the sensor's flow cell, are used.

Wide bandwidth operational amplifiers OPA1–4 are used to isolate the sensor and the reference network  $R_c$ - $C_c$  from the rest of the circuitry avoiding loading effects.

The AD8302 output signals are amplified with two low noise fixed gain differential amplifiers ( $A_{df}$  and  $A_{DA}$  in Figure II.2), which drive two high-resolution analog to digital converters (ADCs). After amplification, the obtained sensitivities are 622.9 mV/ degree and 1868.7 mV/dB. With such a high gain, the measurement range is reduced and the amplifiers and converters may saturate if big changes on the phase or magnitude happen.

When saturation is detected on the measured values, the voltages  $V_{ref1-2}$  (see Figure II.2), generated with a dual, low noise, digital to analog converter (DAC), are programmed to remain in the amplifiers and converters linear

operation range. Moreover, the voltages  $V_{ref\ 1-2}$  are used to adjust the output voltages of amplifiers  $A_{df}$  and  $A_{dA}$  at zero in the reference state.

A microcontroller-based control and communication system is in charge of programming the proper applied reference voltages  $V_{ref\ 1-2}$ , programming the operational frequency of the DDS, and reading the measured data from the ADCs, for each connected sensor circuit. In addition, this microcontroller manages the FIA operations and interfaces with the PC user's interface through an Ethernet connection.

An additional microcontroller based bus bridge is used to interconnect the four sensor circuits, interfaced via an SPI bus, to the control and communication system main bus (I2C based). This has been omitted from figures for clarity, but implementation details will be shown in next sections.

## II.1.i. Electronic Characterization System Implementation

### II.1.i.a. Signal Generator

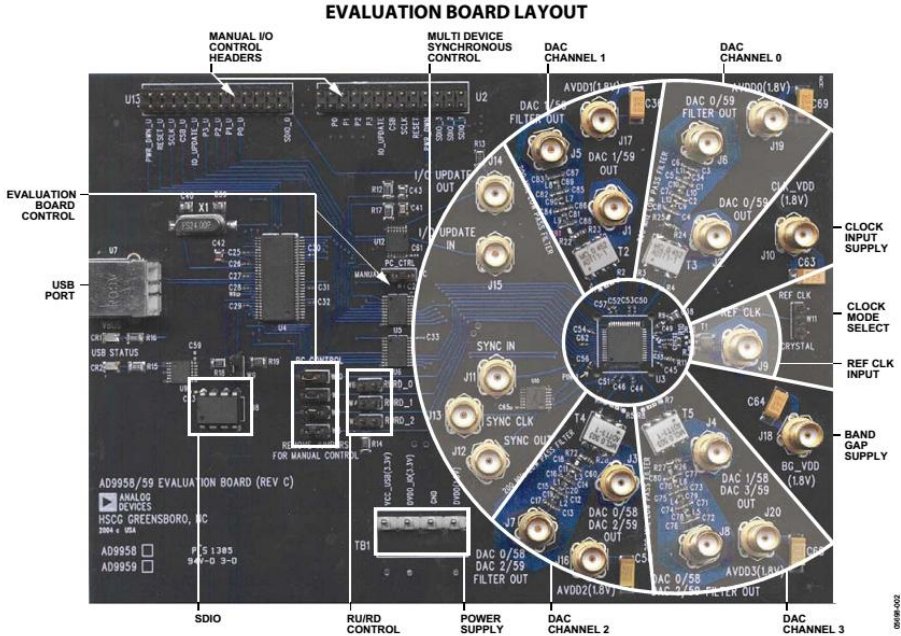


Figure II.4. Picture of the four channel signal generator used in the system © 2005 Analog Devices. The signal generator is based on the AD9959 circuit (Analog Devices, Inc.). The AD9959 consists of four direct digital synthesizer (DDS) cores that provide independent frequency, phase, and amplitude control on each channel. The clock source can drive directly the system's clock line, shared by all the DDS cores, or can be used in combination with an integrated clock multiplier (PLL based) up to a maximum of 500 MSPS. The PLL multiplication factor is programmable from 4 to 20, in integer steps (Analog Devices, 2008). To speed-up the design, the AD9959 evaluation board was used for the implementation. The board was connected to the control system via the SPI bus, accessible at the I/O manual control headers. The four DAC output channels feed the quadrature modules for 90° phase shifting before each sensor circuit. An Oven Controlled Crystal Oscillator (OCXO) generating a 100 MHz signal drives the system clock.



Figure II.5 DDS reference clock board. The circuit was designed to be compatible with two different 100 MHz high performance OCXOs: the AOCJY3-B from Abracon LLC. and the O-3311AT from KVG Quartz Crystal Technology GmbH (Abracon Corporation, 2011; KVG Quartz Crystal Technology GmbH, 2007). Although it is common to find 10 MHz high performance OCXO-based reference clocks, the selected output frequency was 100 MHz. We opted for this frequency to minimize the phase noise multiplication factor introduced by the PLL clock multiplier (Calosso et al., 2012; Rubiola, 2010). We were able to work at the highest sample rate of the DDS (500 MSPS) with a low PLL factor of 5, minimizing the signal generator system's phase noise introduced by the reference clock.

## II.1.i.b. Quadrature Coupler Circuit

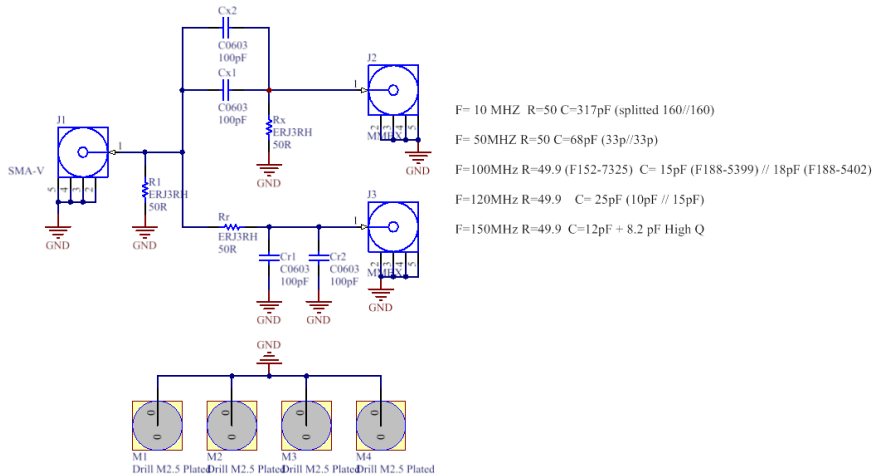


Figure II.6. Quadrature module schematic. The components' values for each operating frequency are stated at right side of the figure. The signal from the DDS output is connected to the SMA connector J1 and routed through the low pass ( $-45^\circ$  phase shift at cut frequency) and high pass ( $+45^\circ$ ) filters. Two RF MMBX board to board connectors are used to plug the module directly to the sensor circuit board. The MMBX connectors maintain an excellent electrical performance while allowing some mechanical misalignments in axial and radial directions.

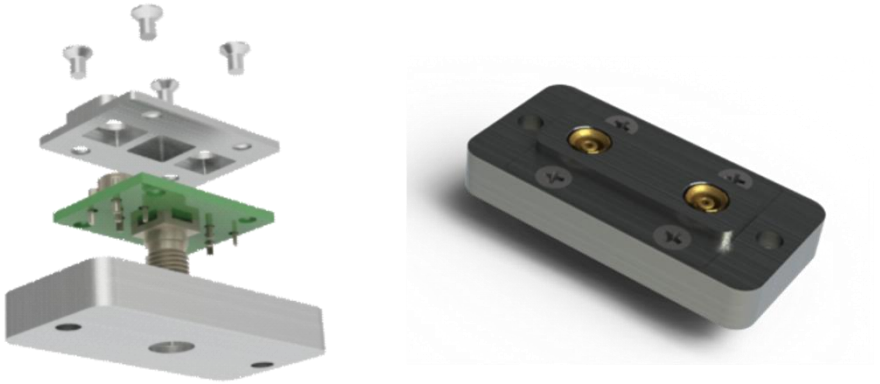
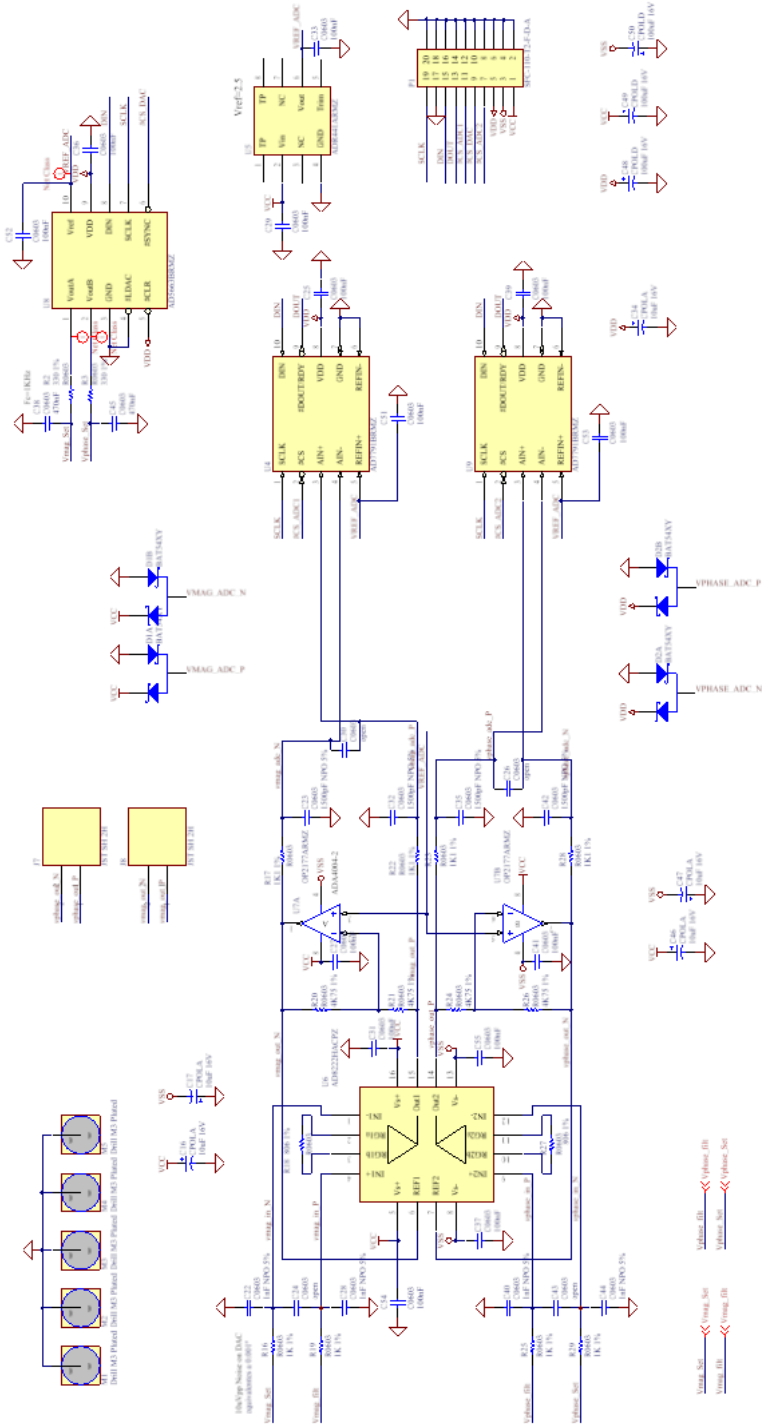


Figure II.7. Quadrature module holder 3D views: (a) Exploded view showing different parts including pcb (b) assembled.



---

Figure II.8. Radio frequency section of the sensor circuit. Signals from the quadrature module are connected to the MMBX connectors J1 and J6. Isolating amplifiers are based on the dual ADA4817-2 operational amplifiers. Those amplifiers are unity gain stable, high bandwidth (1 GHz), low noise ( $4 \text{ nV}/\sqrt{\text{Hz}}$ ), FET input amplifiers. Four additional MMBX connectors, J2 - J5, are used for connection to the sensor's cell module. As shown in previous section, the AD8302 is used as magnitude and phase detector. The detector's bandwidth was reduced (using the capacitors at PFLT and MFLT inputs) to reduce the measurement noise. In addition, the voltage outputs of the detector are low pass filtered before connecting to the next stage.



---

Figure II.9 Low frequency section of the sensor circuit. The output signals from the AD8302 are filtered before being amplified by the differential input output amplifier formed by the combination of the AD8222 instrumentation amplifier and the low noise OP2177 operational amplifier. The differential outputs of the amplifier drive the inputs of the AD7791, a 24-Bit Sigma Delta A/D Converter. This converter is accessed via an SPI communication. The reference voltages driving the negative input of the differential amplifier are generated by a dual 16-Bit DAC, the AD5663, also interfaced via the SPI bus.

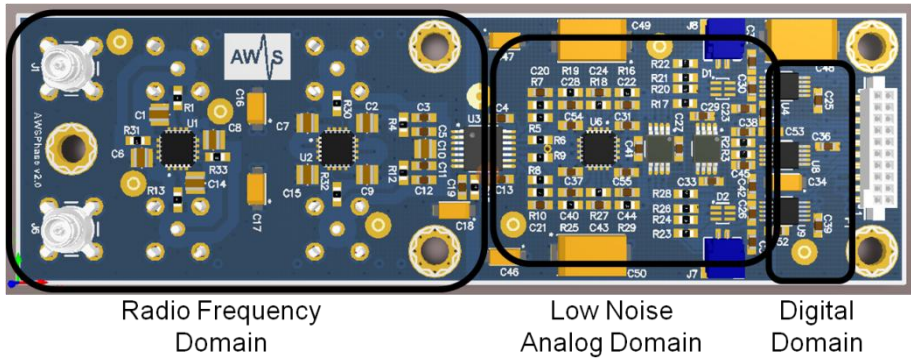


Figure II.10. 3D top view of the sensor circuit implementation. Figure shows the placement of the components of the circuit. The printed circuit board has been implemented on four layers and has dimensions of 100 mm x 30 mm.

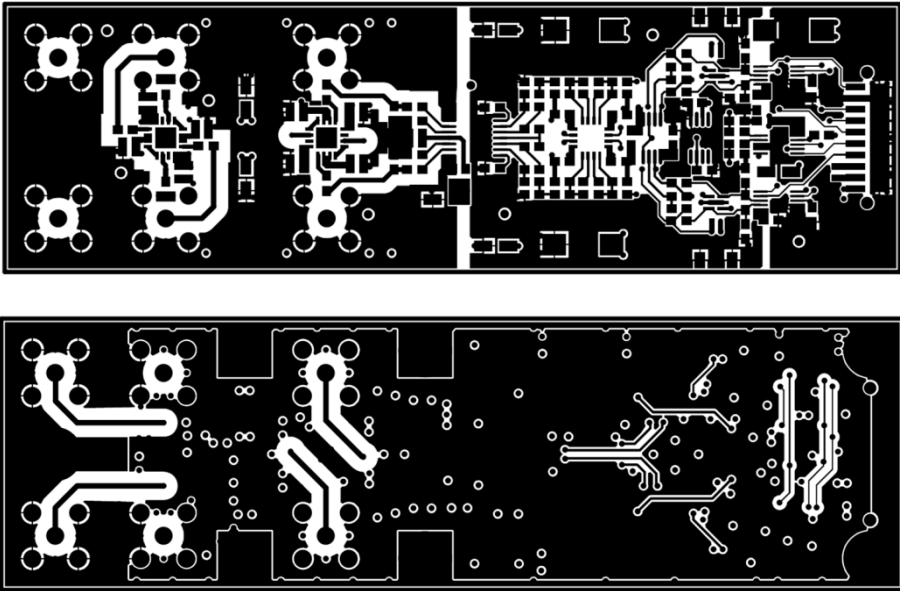


Figure II.11. PCB fabrication masks for top layer and bottom layer. The length of the high frequency signals traces has been controlled and maintained equalized to minimize the phase shift difference. Also, design is symmetrical, minimizing differences on parasitic components that can lead to phase mismatches. Part of the bottom layer copper has been used as -5 V power plane.

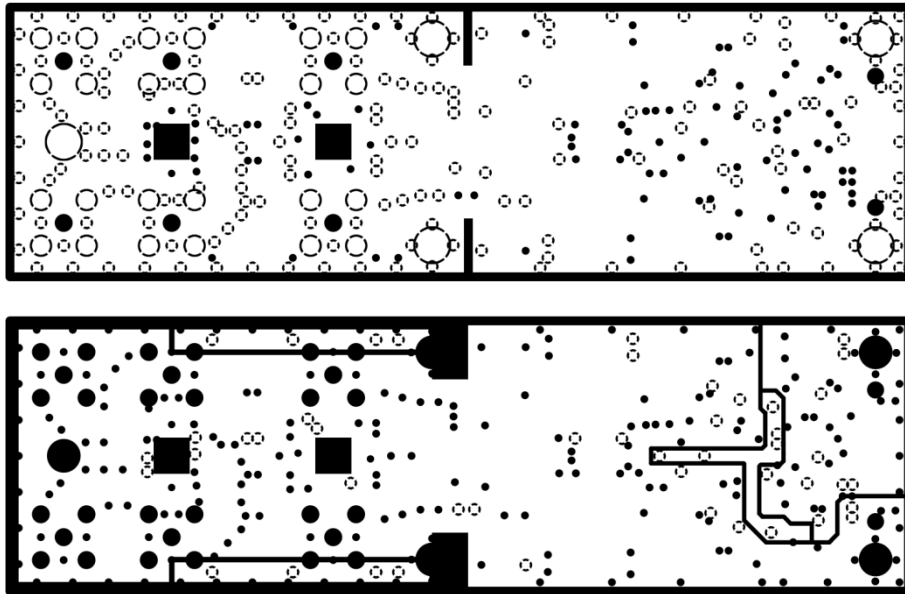


Figure II.12. PCB fabrication masks for internal GND and PWR planes (negative view). The ground plane is solid over the hole circuit, except beneath the high frequency operational amplifiers, where copper plane can increase parasitic capacitances at amplifier inputs and lead to unwanted oscillatory behavior. Power plane has been split. Digital and analog power supply voltages are connected through their plane connection.



Figure II.13 Picture of the assembled sensor circuit. Top and bottom views.

## II.1.i.d. Bus Adapter Circuit

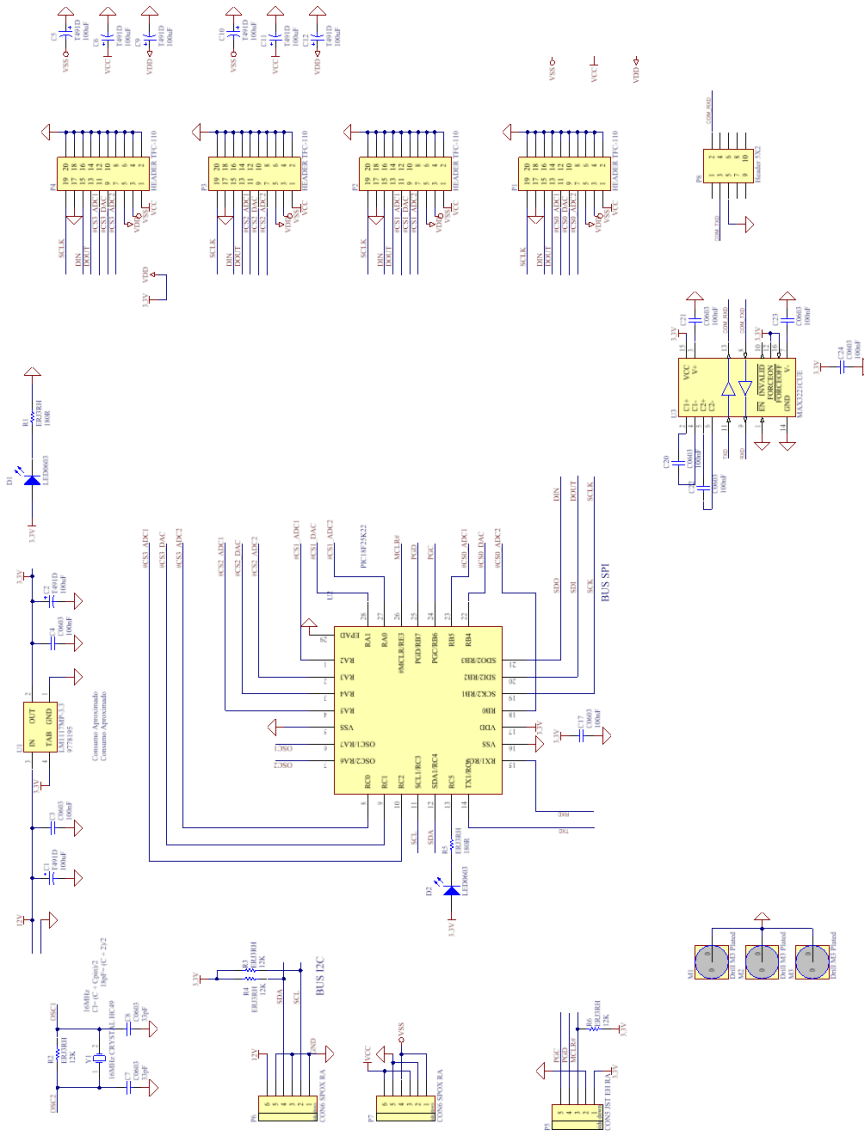


Figure II.14. Microcontroller based SPI to I2C bus bridge. A microcontroller based (PIC18F25K22, Microchip Technology, Inc.) bus adapter circuit has been designed to serve as communications bridge between up to four SPI interfaced sensor circuits and the I2C interface of the control and communications system. The microcontroller performs periodic reads from the sensor circuits' ADCs and sends the data when requested by the control system.

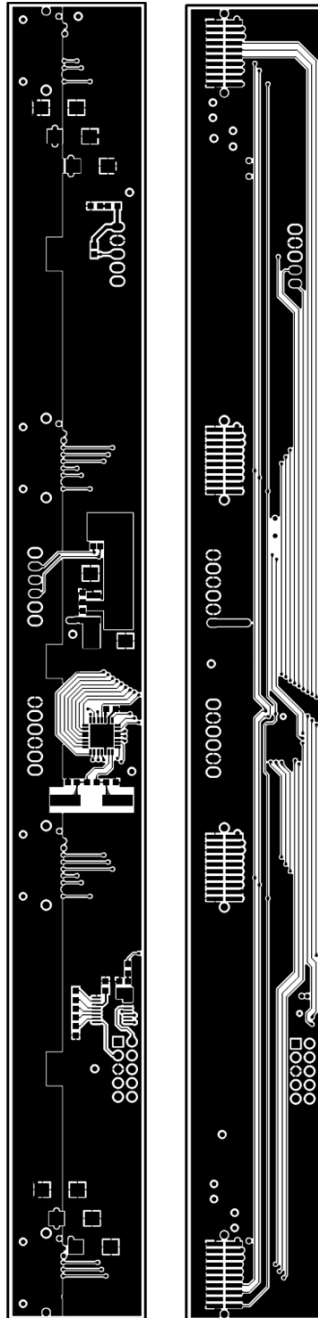


Figure II.15. Top and bottom layer fabrication masks of the bus adapter circuit.

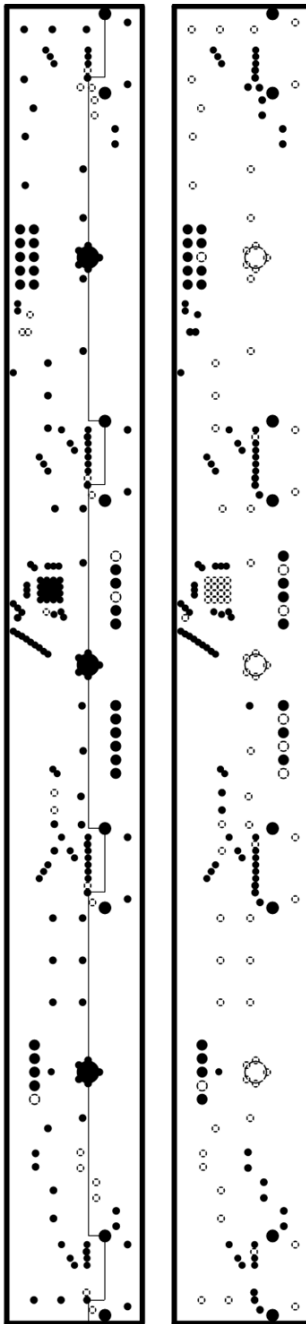


Figure II.15. Power and ground planes fabrication masks of the bus adapter circuit.



Figure II.16. Assembled bus adapter circuit. Top and bottom views.

## II.1.i.e. Control and Communications System

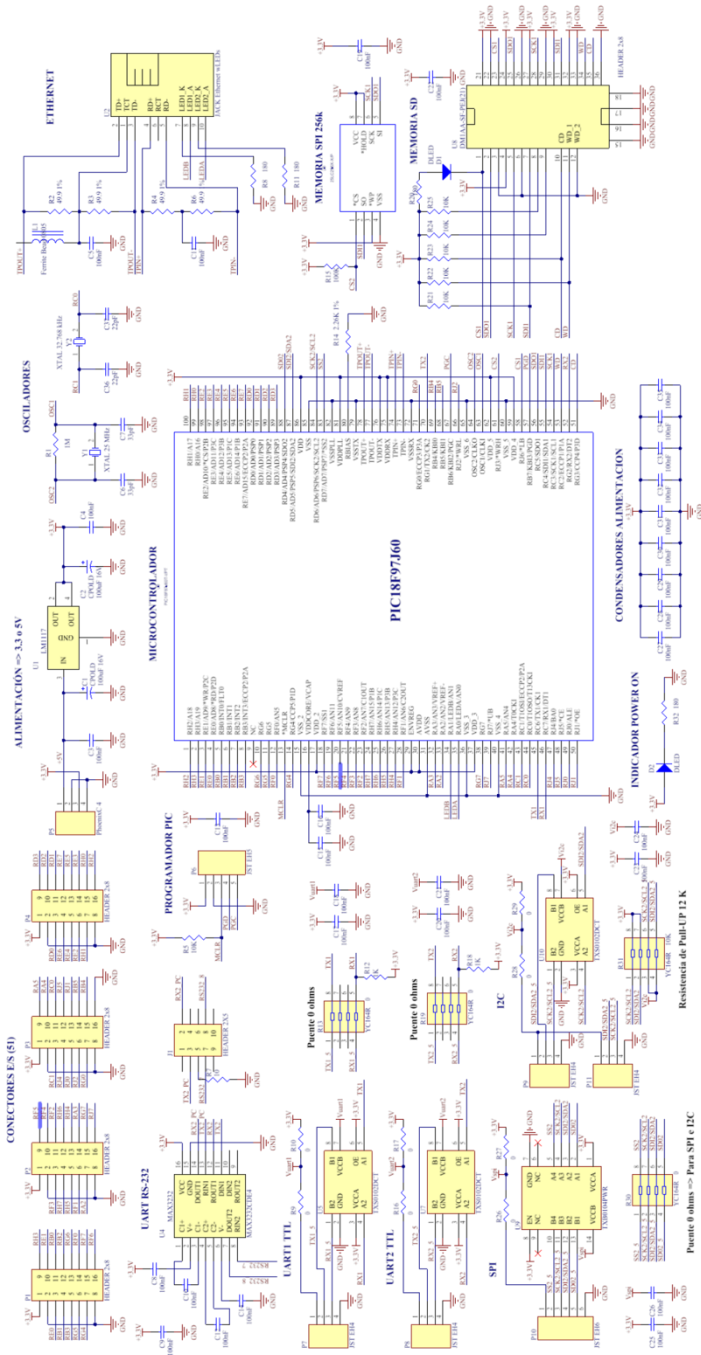


Figure II.17. Microcontroller based (PIC18F97J60, Microchip Technologies, Inc.) control and communication circuit. The implemented circuit is in charge of the control of all the elements of the platform. This includes the DDS frequency programming (SPI interface), data acquisition from the sensor circuits, and FIA system control (I2C interface). Communication with the temperature controller is performed through an RS-232 serial interface. The microcontroller features an integrated 10 Mbps Ethernet communications peripheral (MAC and 10BASE-T PHY) which only requires an external RJ45 connector with integrated transformer to implement the Ethernet communication with the PC user interface.

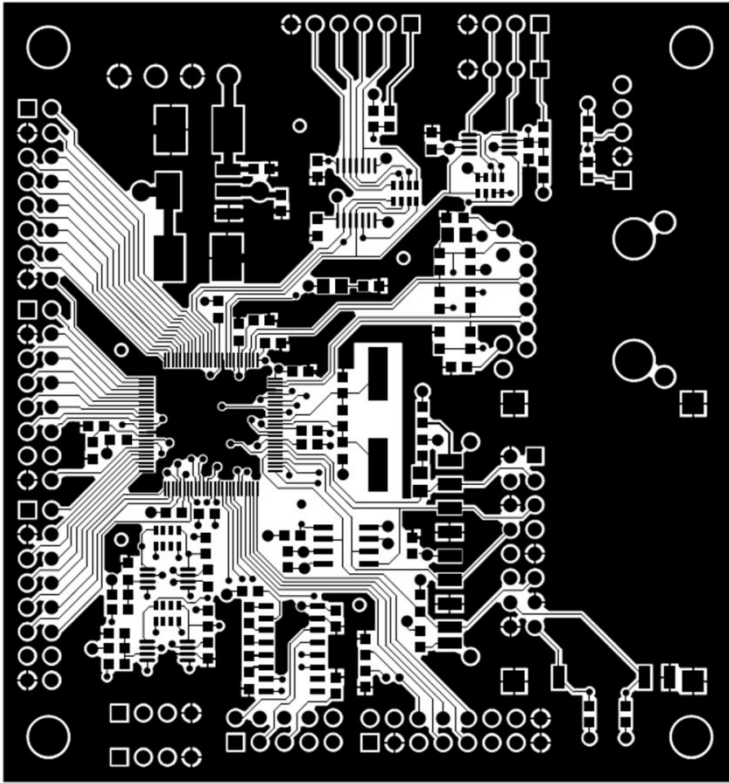


Figure II.18. Top layer Control circuit PCB fabrication mask.

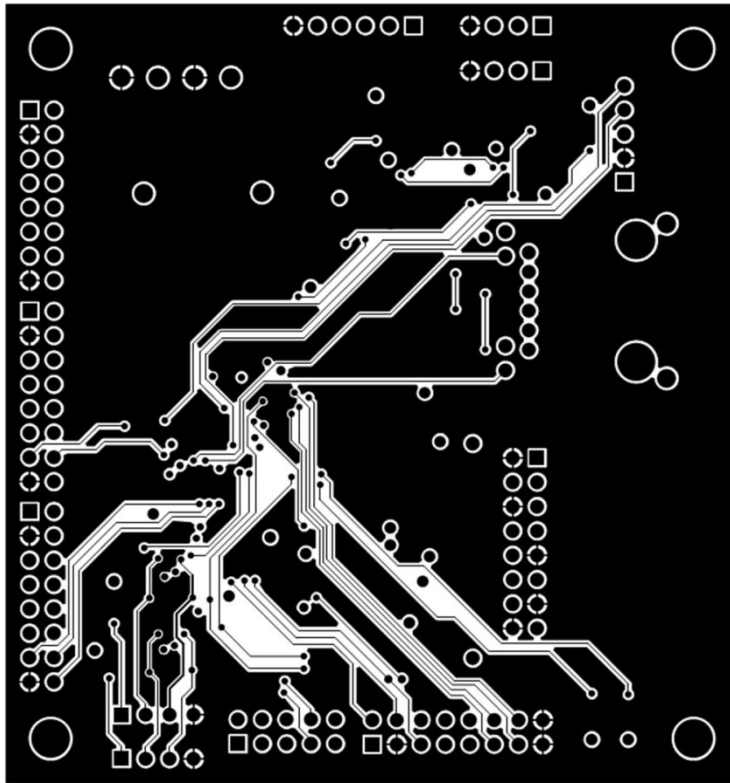


Figure II.19. Bottom layer Control Circuit PCB fabrication mask.

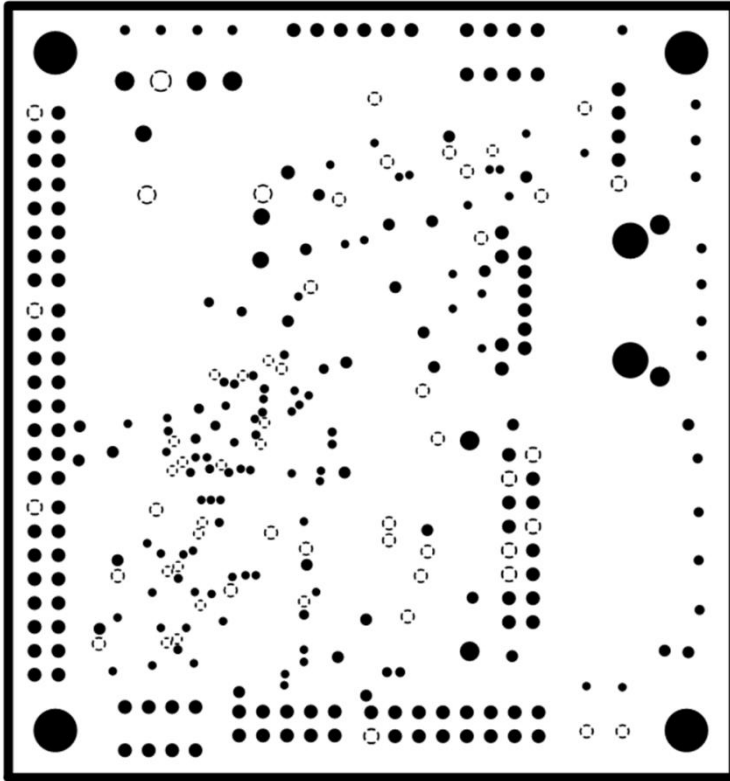


Figure II.20. Power (+5V) internal plane of the Control Circuit PCB fabrication mask (negative view).

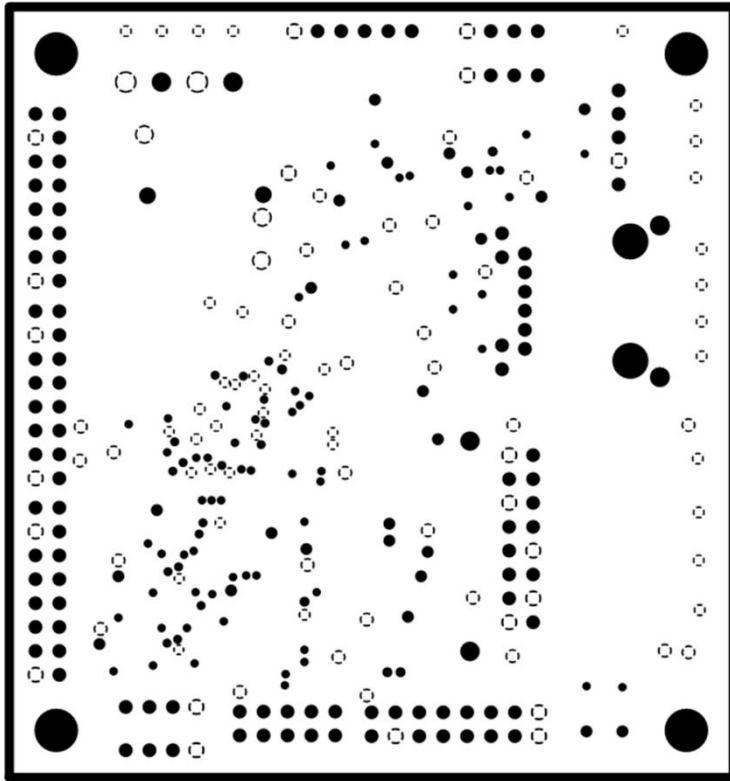


Figure II.21. Ground internal plane of the Control Circuit PCB fabrication mask (negative view).



Figure II.22. Top view of the assembled control and communication circuit.

## II.2. HFF-QCM sensors and Flow Cell

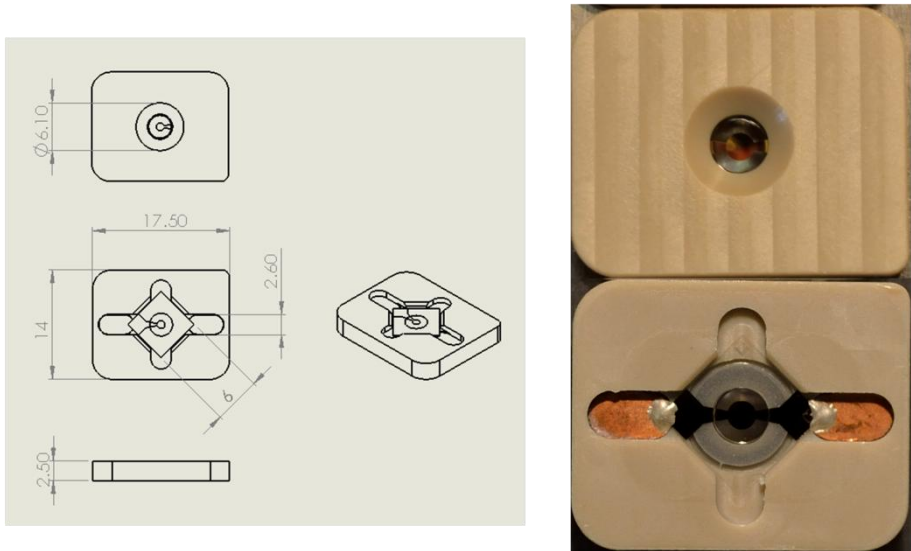


Figure II.23. HFF-QCM sensor chip dimensions (left) and manufactured sensor's top and bottom view (right). Sensors were based on square shaped, 6 mm x 6 mm, AT-cut, inverted mesa crystals (Xeco, Inc.). The inverted mesa etched area (2.62 mm diameter) thickness was 33  $\mu\text{m}$ , for 50 MHz crystals, and 17  $\mu\text{m}$  for 100 MHz crystals. Electrode active surface ranged from 0.196 to 3.142  $\text{mm}^2$  (for 0.5 to 2.0 mm electrode diameter). Sensors were permanently assembled to a polyether ether ketone (PEEK) with a conical aperture exposing the mesa area of one of the sides of the resonator. Bonding of the sensor to the support was done by an adhesive epoxy. Copper contact extensions were assembled on the PEEK support and electrical contact to the crystal electrodes was done using conductive epoxy paste.

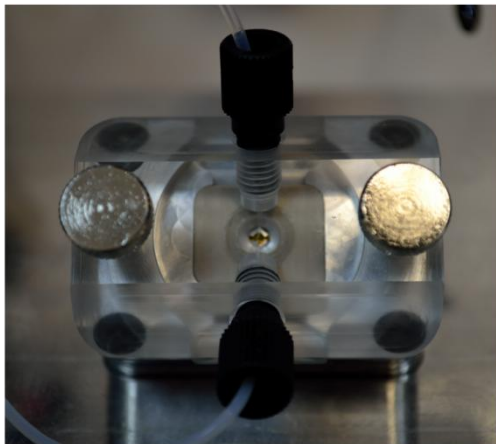
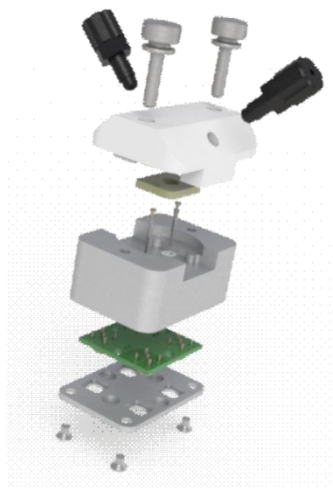


Figure II.24. Exploded view of the 3D flow cell assembly (left) and implemented flow cell during an experiment with fluidic fittings connected (right). The upper part of the cell was made of polymethyl methacrylate (PMMA) with o-rings made of polydimethylsyloxane (PDMS) or nitrile. The o-rings sealed over the peek support and confined the flow over the exposed side of the resonator. Flow volume over the exposed area of the sensor was  $2.75 \mu\text{l}$ . The electrical contact to the sensor chip was done by spring contact probes. The spring probes were soldered to the cell pcb. On this pcb are located the passive components network which perform the sensor's type dependant phase shifting and attenuation, as explained in previous sections. The lower part of the cell was manufactured of aluminum, which provided good thermal conductivity (for rapid temperature stabilization and minimal thermal gradients) and electrical conductivity (for proper grounding and shielding).

### II.3. Flow Injection Analysis System

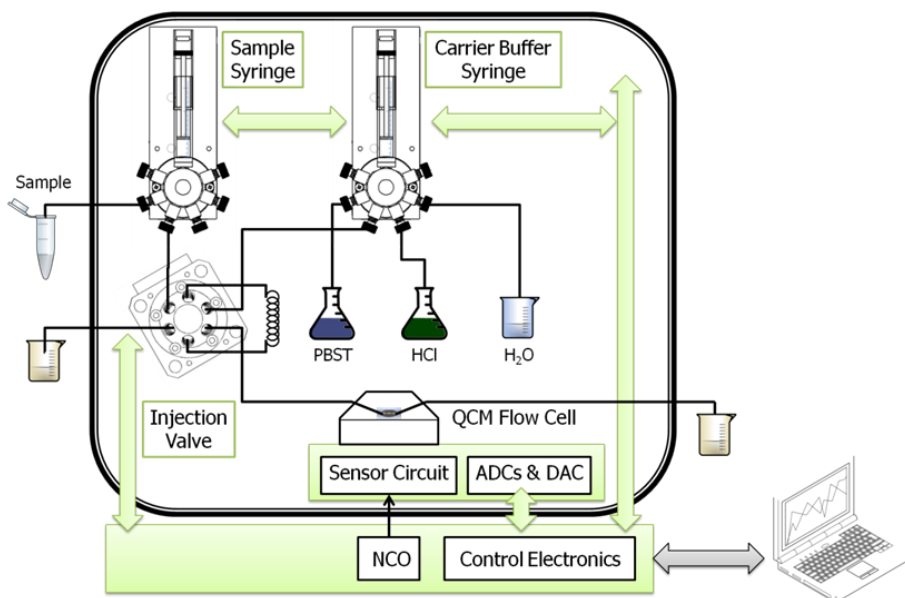


Figure II.25 Block diagram of the flow injection analysis system designed. A syringe pump with an integrated distribution valve, models PSD/4 and HVCX 6-5 (Hamilton Company), are used to select the appropriate buffer and to inject it through the entire flow system. A two-position injection valve, Cheminert Model 62 (VICI AG International), is used to inject the sample stored in the loop into the system. Although the system was designed for manual sample loading, the syringe pump of a different channel can be used to perform the sample loading. The syringe pumps are controlled via a Controller Area Network (CAN) interface and the injection valve position is controlled via relay switching. Two different electronic circuit boards, acting as interface bridges between the fluidic elements and the I2C control bus, were used. The flow system elements and the temperature sensitive sensor circuits were placed inside a thermostatic chamber. An air-to air peltier based thermoelectric assembly and a programmable controller (AA-040-12V and PR-59, Laird Technologies), were selected as the thermal management solution for the system. All the elements were controlled by the PC software application.

---

## II.4. Instrument's enclosure. AWS A10 RP

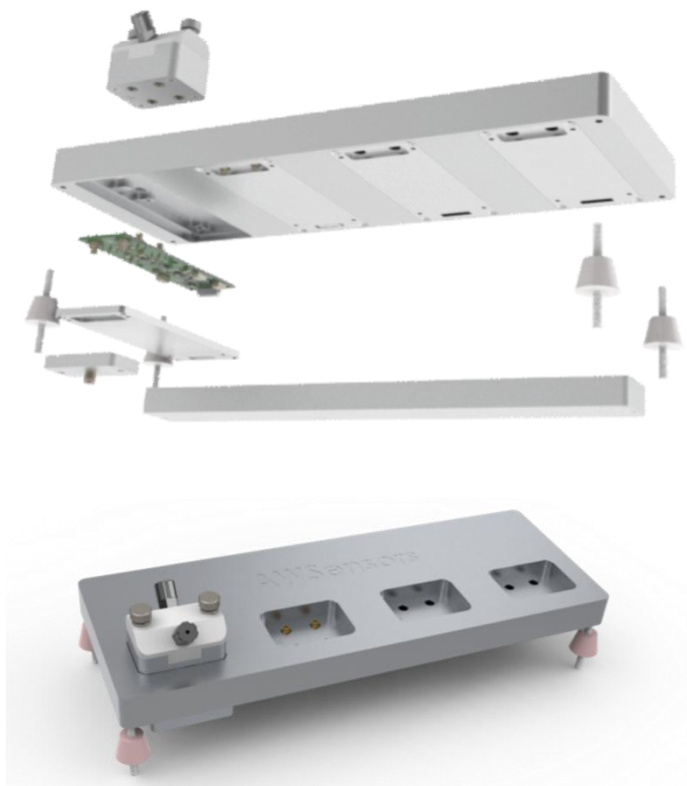


Figure II.26. 3D exploded (top) and assembled (bottom) views of the characterization system. The quadrature modules, sensor circuits and bus adapter circuit were assembled in a custom-made CNC mechanized aluminum module, placed inside the thermostatic chamber.



Figure II.27. Picture of the AWS A10 Research Platform (Awsensors S.L).



## References

---

- Abracon Corporation, 2011. AOCJY3 Series OVEN CONTROLLED CRYSTAL OSCILLATOR.
- Analog Devices, 2009. AD7864, 4-Channel, Simultaneous Sampling, High Speed, 12-Bit ADC.
- Analog Devices, 2008. AD9959, 4-Channel, 500 MSPS DDS with 10-Bit DACs.
- Analog Devices, 2006. AD8307, Low Cost, DC to 500 MHz, 92 dB Logarithmic Amplifier.
- Analog Devices, 2003. AD835, 250 MHz, Voltage Output, 4-Quadrant Multiplier.
- Analog Devices, 2002. AD8302, LF–2.7 GHz RF/IF Gain and Phase Detector.
- Andle, J.C., Vetelino, J.F., 1994. Acoustic wave biosensors. *Sensors Actuators A Phys.* 44, 167–176. doi:10.1016/0924-4247(94)00801-9

- 
- Arnau, A., 2008. A Review of Interface Electronic Systems for AT-cut Quartz Crystal Microbalance Applications in Liquids. *Sensors* 8, 370–411. doi:10.3390/s8010370
- Arnau, A., Ferrari, V., Soares, D., Perrot, H., 2008. Interface Electronic Systems for AT-Cut QCM Sensors: A comprehensive review, in: *Piezoelectric Transducers and Applications*. Springer Berlin Heidelberg, Berlin, Heidelberg, pp. 117–186. doi:10.1007/978-3-540-77508-9\_5
- Arnau, A., Jimenez, Y., Fernández, R., Torres, R., Otero, M., Calvo, E.J., 2006. Viscoelastic Characterization of Electrochemically Prepared Conducting Polymer Films by Impedance Analysis at Quartz Crystal. *J. Electrochem. Soc.* 153, C455. doi:10.1149/1.2195893
- Arnau, A., Jimenez, Y., Sogorb, T., 2001. An extended Butterworth Van Dyke model for quartz crystal microbalance applications in viscoelastic fluid media. *IEEE Trans. Ultrason. Ferroelectr. Freq. Control* 48, 1367–1382. doi:10.1109/58.949746
- Arnau, A., Jiménez, Y., Sogorb, T., 2000. Thickness-shear mode quartz crystal resonators in viscoelastic fluid media. *J. Appl. Phys.* 88, 4498. doi:10.1063/1.1309122
- Arnau, A., Sogorb, T., Jiménez, Y., 2002. Circuit for continuous motional series resonant frequency and motional resistance monitoring of quartz crystal resonators by parallel capacitance compensation. *Rev. Sci. Instrum.* 73, 2724. doi:10.1063/1.1484254
- Auge, J., Hauptmann, P., Eichelbaum, F., Rösler, S., 1994. Quartz crystal microbalance sensor in liquids. *Sensors Actuators B Chem.* 19, 518–522. doi:10.1016/0925-4005(93)00983-6
- Ballantine, D.S., Jr., White, R.M., Martin, S.J., Ricco, A.J., Zellers, E.T., Frye,

- 
- G.C., Wohltjen, H., 1996. *Acoustic Wave Sensors: Theory, Design, & Physico-Chemical Applications*. Academic Press.
- Barnes, C., 1991. Development of quartz crystal oscillators for under-liquid sensing. *Sensors Actuators A Phys.* 29, 59–69. doi:10.1016/0924-4247(91)80032-K
- Ben-Dov, I., Willner, I., Zisman, E., 1997. Piezoelectric Immunosensors for Urine Specimens of *Chlamydia trachomatis* Employing Quartz Crystal Microbalance Microgravimetric Analyses. *Anal. Chem.* 69, 3506–3512. doi:10.1021/ac970216s
- Cady, W.G., 1964. *Piezoelectricity: an introduction to the theory and applications of electromechanical phenomena in crystals*, *Piezoelectricity: An Introduction to the Theory and Applications of Electromechanical Phenomena in Crystals*. Dover Publications.
- Calosso, C.E., Gruson, Y., Rubiola, E., 2012. Phase noise and amplitude noise in DDS, in: 2012 IEEE International Frequency Control Symposium Proceedings. IEEE, pp. 1–6. doi:10.1109/FCS.2012.6243619
- Calvo, E.J., Etchenique, R., Bartlett, P.N., Singhal, K., Santamaria, C., 1997. Quartz crystal impedance studies at 10 MHz of viscoelastic liquids and films. *Faraday Discuss.* 107, 141–157. doi:10.1039/a703551i
- C-MAC MicroTechnology, 2005. CFPT9000 SMD Temperature Compensated Crystal Oscillator.
- Ferrari, V., Lucklum, R., 2008. Overview of Acoustic-Wave Microsensors, in: *Piezoelectric Transducers and Applications*. Springer Berlin Heidelberg, Berlin, Heidelberg, pp. 39–62. doi:10.1007/978-3-540-77508-9\_2
- Ferrari, V., Marioli, D., Taroni, A., 2003. ACC oscillator for in-liquid quartz microbalance sensors, in: *Proceedings of IEEE Sensors 2003 (IEEE Cat.*

---

No.03CH37498). IEEE, pp. 849–854.  
doi:10.1109/ICSENS.2003.1279063

Ferrari, V., Marioli, D., Taroni, A., 2001. Improving the accuracy and operating range of quartz microbalance sensors by a purposely designed oscillator circuit. *IEEE Trans. Instrum. Meas.* 50, 1119–1122. doi:10.1109/19.963169

Francis, L.A., 2006. Thin film acoustic waveguides and resonators for gravimetric sensing applications in liquid. Université catholique de Louvain.

Fu, Y.Q., Luo, J.K., Du, X.Y., Flewitt, A.J., Li, Y., Markx, G.H., Walton, A.J., Milne, W.I., 2010. Recent developments on ZnO films for acoustic wave based bio-sensing and microfluidic applications: a review. *Sensors Actuators B Chem.* 143, 606–619. doi:10.1016/j.snb.2009.10.010

Fung, Y.S., Wong, Y.Y., 2001. Self-Assembled Monolayers as the Coating in a Quartz Piezoelectric Crystal Immunosensor To Detect Salmonella in Aqueous Solution. *Anal. Chem.* 73, 5302–5309. doi:10.1021/ac010655y

Furtado, L.M., Su, H., Thompson, M., Mack, D.P., Hayward, G.L., 1999. Interactions of HIV-1 TAR RNA with Tat-Derived Peptides Discriminated by On-Line Acoustic Wave Detector. *Anal. Chem.* 71, 1167–1175. doi:10.1021/ac980880o

Gabl, R., Feucht, H.-D., Zeininger, H., Eckstein, G., Schreiter, M., Primig, R., Pitzer, D., Wersing, W., 2004. First results on label-free detection of DNA and protein molecules using a novel integrated sensor technology based on gravimetric detection principles. *Biosens. Bioelectron.* 19, 615–620. doi:10.1016/S0956-5663(03)00259-8

Gabl, R., Green, E., Schreiter, M., Feucht, H.D., Zeininger, H., Primig, R., Pitzer, D., Eckstein, G., Wersing, W., 2003. Novel integrated FBAR

- 
- sensors: a universal technology platform for bio- and gas-detection, in: Proceedings of IEEE Sensors 2003. IEEE, pp. 1184–1188. doi:10.1109/ICSENS.2003.1279132
- Gabrielli, C., Perrot, H., Rose, D., Rubin, A., Toqué, J.P., Pham, M.C., Piro, B., 2007. New frequency/voltage converters for ac-electrogravimetric measurements based on fast quartz crystal microbalance. *Rev. Sci. Instrum.* 78, 074103. doi:10.1063/1.2751093
- Gronewold, T.M.A., 2007. Surface acoustic wave sensors in the bioanalytical field: Recent trends and challenges. *Anal. Chim. Acta* 603, 119–128. doi:10.1016/j.aca.2007.09.056
- Hengerer, A., Kösslinger, C., Decker, J., Hauck, S., Queitsch, I., Wolf, H., Dübel, S., 1999. Determination of phage antibody affinities to antigen by a microbalance sensor system. *Biotechniques* 26, 956–60, 962, 964. doi:5119998
- Hewlett-Packard Company, 1997. *Fundamentals of the Electronic Counters*.
- Höök, F., Ray, A., Nordén, B., Kasemo, B., 2001. Characterization of PNA and DNA Immobilization and Subsequent Hybridization with DNA Using Acoustic-Shear-Wave Attenuation Measurements. *Langmuir* 17, 8305–8312. doi:10.1021/la0107704
- Janshoff, A., Galla, H.-J., Steinem, C., 2000. Piezoelectric Mass-Sensing Devices as Biosensors - An Alternative to Optical Biosensors?
- Jiménez, Y., Fernández, R., Torres, R., Arnau, a, 2006. A Contribution To Solve the Problem of Crystal Microbalance Applications. *IEEE Trans. Ultrason. Ferroelectr. Freq. Control* 53, 1057–1072.
- Jiménez, Y., Otero, M., Arnau, A., 2008. QCM Data Analysis and Interpretation, in: *Piezoelectric Transducers and Applications*. Springer

---

Berlin Heidelberg, Berlin, Heidelberg, pp. 331–398. doi:10.1007/978-3-540-77508-9\_14

Johannsmann, D., Gruner, J., Wesser, J., Mathauer, K., Wegner, G., Knoll, W., 1992. Viscoelastic Properties Of Thin-Films Probed With A Quartz Crystal Resonator. *Makromol. ChemieMacromolecular Symp.* 46, 247–251.

Johansson, S., 2005. New frequency counting principle improves resolution, in: *Proceedings of the 2005 IEEE International Frequency Control Symposium and Exposition, 2005.* IEEE, pp. 628–635. doi:10.1109/FREQ.2005.1574007

Johnson, H., Graham, M., 1993. *High Speed Digital Design: A Handbook of Black Magic.* Prentice Hall.

Kalantar-Zadeh, K., Wlodarski, W., Chen, Y.Y., Fry, B.N., Galatsis, K., 2003. Novel Love mode surface acoustic wave based immunosensors. *Sensors Actuators B Chem.* 91, 143–147. doi:10.1016/S0925-4005(03)00079-0

Kanazawa, K.K., Gordon II, J.G., 1985. The oscillation frequency of a quartz resonator in contact with liquid. *Anal. Chim. Acta* 175, 99–105. doi:10.1016/S0003-2670(00)82721-X

Kankare, J., 2002. Sauerbrey Equation of Quartz Crystal Microbalance in Liquid Medium. *Langmuir* 18, 7092–7094. doi:10.1021/la025911w

Kankare, J., Loikas, K., Salomäki, M., 2006. Method for Measuring the Losses and Loading of a Quartz Crystal Microbalance. *Anal. Chem.* 78, 1875–1882. doi:10.1021/ac051908g

Kurosawa, S., Kitajima, H., Ogawa, Y., Muratsugu, M., Nemoto, E., Kamo, N., 1993. Resonant frequency of a piezoelectric quartz crystal in contact with solutions. *Anal. Chim. Acta* 274, 209–217. doi:10.1016/0003-

---

2670(93)80467-Y

- KVG Quartz Crystal Technology GmbH, 2007. O-3000AT Series Datasheet.
- Lakin, K.M., 2005. Thin film resonator technology. *IEEE Trans. Ultrason. Ferroelectr. Freq. Control* 52, 707–716. doi:10.1109/TUFFFC.2005.1503959
- Länge, K., Rapp, B.E., Rapp, M., 2008. Surface acoustic wave biosensors: a review. *Anal. Bioanal. Chem.* 391, 1509–19. doi:10.1007/s00216-008-1911-5
- Lin, Z., Yip, C.M., Joseph, I.S.S., Ward, M.D., 1993. Operation of an ultrasensitive 30-MHz quartz crystal microbalance in liquids. *Anal. Chem.* 65, 1546–1551. doi:10.1021/ac00059a011
- Lucklum, R., Hauptmann, P., 1997. Determination of polymer shear modulus with quartz crystal resonators. *Faraday Discuss.* 107, 123–140. doi:10.1039/a703127k
- Lucklum, R., Soares, D., Kanazawa, K., 2008. Models for Resonant Sensors, in: *Piezoelectric Transducers and Applications*. Springer Berlin Heidelberg, Berlin, Heidelberg, pp. 63–96. doi:10.1007/978-3-540-77508-9\_3
- March, C., García, J. V., Sánchez, Á., Arnau, A., Jiménez, Y., García, P., Manclús, J.J., Montoya, Á., 2015. High-frequency phase shift measurement greatly enhances the sensitivity of QCM immunosensors. *Biosens. Bioelectron.* 65, 1–8. doi:10.1016/j.bios.2014.10.001
- March, C., Manclús, J.J., Jiménez, Y., Arnau, A., Montoya, A., 2009. A piezoelectric immunosensor for the determination of pesticide residues and metabolites in fruit juices. *Talanta* 78, 827–33. doi:10.1016/j.talanta.2008.12.058
- Martin, S.J., Granstaff, V.E., Frye, G.C., 1991. Characterization of a quartz

- 
- crystal microbalance with simultaneous mass and liquid loading. *Anal. Chem.* 63, 2272–2281. doi:10.1021/ac00020a015
- Maxim Integrated, 2007. MAX038 High-Frequency Waveform Generator.
- Maxim Integrated, 2002. MAX9601, Dual ECL and Dual/Quad PECL, 500ps, Ultra-High-Speed Comparators.
- Moll, N., Pascal, E., Dinh, D.H., Pillot, J.-P., Bennetau, B., Rebière, D., Moynet, D., Mas, Y., Mossalayi, D., Pistré, J., Déjous, C., 2007. A Love wave immunosensor for whole *E. coli* bacteria detection using an innovative two-step immobilisation approach. *Biosens. Bioelectron.* 22, 2145–2150. doi:10.1016/j.bios.2006.09.032
- Montagut, Y., Garcia, J., Jimenez, Y., March, C., Montoya, A., Arnau, A., 2011a. QCM Technology in Biosensors, in: Serra, P.A. (Ed.), *Biosensors - Emerging Materials and Applications*. InTech. doi:10.5772/17991
- Montagut, Y., García, J. V., Jiménez, Y., March, C., Montoya, Á., Arnau, A., 2011b. Validation of a Phase-Mass Characterization Concept and Interface for Acoustic Biosensors. *Sensors (Basel)*. 11, 4702–4720. doi:10.3390/s110504702
- Montrose, M.I., 1998. *Emc & the Printed Circuit Board: Design, Theory, & Layout Made Simple*, 1st Editio. ed. Wiley-IEEE Press.
- Niedermayer, A.O., Reichel, E.K., Jakoby, B., 2009. Yet another precision impedance analyzer (YAPIA)—Readout electronics for resonating sensors. *Sensors Actuators A Phys.* 156, 245–250. doi:10.1016/j.sna.2009.04.020
- Nirschl, M., Blüher, A., Erler, C., Katzschner, B., Vikholm-Lundin, I., Auer, S., Vörös, J., Pompe, W., Schreiter, M., Mertig, M., 2009. Film bulk acoustic resonators for DNA and protein detection and investigation of in vitro

- 
- bacterial S-layer formation. *Sensors Actuators A Phys.* 156, 180–184. doi:10.1016/j.sna.2009.02.021
- Noel, M.A.M., Topart, P.A., 1994. High-frequency impedance analysis of quartz crystal microbalances. 1. General considerations. *Anal. Chem.* 66, 484–491. doi:10.1021/ac00076a011
- Ogi, H., Nagai, H., Fukunishi, Y., Hirao, M., Nishiyama, M., 2009. 170 MHz electrodeless quartz crystal microbalance for highly sensitive biosensors, 2009 IEEE International Ultrasonics Symposium. IEEE. doi:10.1109/ULTSYM.2009.5442069
- Rabus, D., Friedt, J.M., Ballandras, S., Martin, G., Carry, E., Blondeau-Patissier, V., 2013. High-sensitivity open-loop electronics for gravimetric acoustic-wave-based sensors. *IEEE Trans. Ultrason. Ferroelectr. Freq. Control* 60, 1219–1226. doi:10.1109/TUFFC.2013.2685
- Rabus, D., Martin, G., Carry, E., Ballandras, S., 2012. Eight channel embedded electronic open loop interrogation for multi sensor measurement, in: 2012 European Frequency and Time Forum. IEEE, pp. 436–442. doi:10.1109/EFTF.2012.6502420
- Reed, C.E., Kanazawa, K.K., Kaufman, J.H., 1990. Physical description of a viscoelastically loaded AT-cut quartz resonator. *J. Appl. Phys.* 68, 1993. doi:10.1063/1.346548
- Richert, L., Lavalle, P., Vautier, D., Senger, B., Stoltz, J.-F., Schaaf, P., Voegel, J.-C., Picart, C., 2002. Cell Interactions with Polyelectrolyte Multilayer Films. *Biomacromolecules* 3, 1170–1178. doi:10.1021/bm0255490
- Rocha-Gaso, M.-I., García, J.-V., García, P., March-Iborra, C., Jiménez, Y., Francis, L.-A., Montoya, Á., Arnau, A., 2014. Love Wave Immunosensor for the Detection of Carbaryl Pesticide. *Sensors* 14, 16434–16453. doi:10.3390/s140916434

- 
- Rocha-Gaso, M.-I., March-Iborra, C., Montoya-Baides, A., Arnau-Vives, A., 2009. Surface generated acoustic wave biosensors for the detection of pathogens: a review. *Sensors (Basel)*. 9, 5740–69. doi:10.3390/s90705740
- Rodahl, M., Höök, F., Kasemo, B., 1996. QCM Operation in Liquids: An Explanation of Measured Variations in Frequency and Q Factor with Liquid Conductivity. *Anal. Chem.* 68, 2219–27. doi:10.1021/ac951203m
- Rodahl, M., Kasemo, B., 1996a. A simple setup to simultaneously measure the resonant frequency and the absolute dissipation factor of a quartz crystal microbalance. *Rev. Sci. Instrum.* 67, 3238. doi:10.1063/1.1147494
- Rodahl, M., Kasemo, B., 1996b. Frequency and dissipation-factor responses to localized liquid deposits on a QCM electrode. *Sensors Actuators B Chem.* 37, 111–116. doi:10.1016/S0925-4005(97)80077-9
- Rubiola, E., 2010. *Phase Noise and Frequency Stability in Oscillators*, 1st ed. Cambridge University Press.
- Sauerbrey, G., 1959. Verwendung von Schwingquarzen zur Wägung dünner Schichten und zur Mikrowägung. *Zeitschrift für Phys.* 155, 206–222. doi:10.1007/BF01337937
- Schröder, J., Borngräber, R., Lucklum, R., Hauptmann, P., 2001. Network analysis based interface electronics for quartz crystal microbalance. *Rev. Sci. Instrum.* 72, 2750. doi:10.1063/1.1370560
- Sogorb, T., 2003. Caracterización y desarrollo de un dispositivo electrónico para la monitorización continua de la frecuencia de resonancia serie y resistencia dinámica de una microbalanza de cristal de cuarzo como sensor de procesos superficiales en medios fluidos. Universitat Politècnica de València.
- Stobiecka, M., Cieśla, J.M., Janowska, B., Tudek, B., Radecka, H., 2007.

- 
- Piezoelectric Sensor for Determination of Genetically Modified Soybean Roundup Ready (R) in Samples not Amplified by PCR. *Sensors* 7, 1462–1479. doi:10.3390/s7081462
- Texas Instruments, 2002. LMH6702 1.7-GHz Ultra-Low Distortion Wideband Op Amp.
- Torres, R., García, J. V, Arnau, A., Perrot, H., Kim, L.T.T., Gabrielli, C., 2008. Improved frequency/voltage converters for fast quartz crystal microbalance applications. *Rev. Sci. Instrum.* 79, 045113. doi:10.1063/1.2908430
- Vale, C., Rosenbaum, J., Horwitz, S., Krishnaswamy, S., Moore, R., 1990. FBAR filters at GHz frequencies, in: 44th Annual Symposium on Frequency Control. IEEE, pp. 332–336. doi:10.1109/FREQ.1990.177515
- Voinova, M.V., Jonson, M., Kasemo, B., 2002. “Missing mass” effect in biosensor’s QCM applications. *Biosens. Bioelectron.* 17, 835–841. doi:10.1016/S0956-5663(02)00050-7
- Weber, J., Albers, W.M., Tuppurainen, J., Link, M., Gabl, R., Wersing, W., Schreiter, M., 2006. Shear mode FBARs as highly sensitive liquid biosensors. *Sensors Actuators A Phys.* 128, 84–88. doi:10.1016/j.sna.2006.01.005
- Wessendorf, K.O., 1993. The Lever oscillator for use in high resistance resonator applications, in: 1993 IEEE International Frequency Control Symposium. IEEE, pp. 711–717. doi:10.1109/FREQ.1993.367466
- Wingqvist, G., Bjurström, J., Liljeholm, L., Yantchev, V., Katardjiev, I., 2007. Shear mode AlN thin film electro-acoustic resonant sensor operation in viscous media. *Sensors Actuators B Chem.* 123, 466–473. doi:10.1016/j.snb.2006.09.028

- 
- Wingqvist, G., Yantchev, V., Katardjiev, I., 2008. Mass sensitivity of multilayer thin film resonant BAW sensors. *Sensors Actuators A Phys.* 148, 88–95. doi:10.1016/j.sna.2008.07.023
- Yang, M., Thompson, M., 1993. Acoustic network analysis and equivalent circuit simulation of the thickness-shear mode acoustic wave sensor in the liquid phase. *Anal. Chim. Acta* 282, 505–515. doi:10.1016/0003-2670(93)80114-Z
- Yang, M., Thompson, M., Duncan-Hewitt, W.C., 1993. Interfacial properties and the response of the thickness-shear-mode acoustic wave sensor in liquids. *Langmuir* 9, 802–811. doi:10.1021/la00027a033
- Zhang, Z., Vetelino, J.F., 2001. Bulk acoustic wave sensors for sensing measurand-induced electrical property changes in solutions. *IEEE Trans. Ultrason. Ferroelectr. Freq. Control* 48, 773–778. doi:10.1109/58.920710
- Zhou, X., Liu, L., Hu, M., Wang, L., Hu, J., 2002. Detection of hepatitis B virus by piezoelectric biosensor. *J. Pharm. Biomed. Anal.* 27, 341–345. doi:10.1016/S0731-7085(01)00538-6

## Context of research

---

This thesis has been developed in the Center of Research and Innovation in Bioengineering (Centro de Investigación e Innovación en Bioingeniería - Ci2B) of the Universitat Politècnica de València (UPV). A current research line of this Center includes modeling of piezoelectric resonators, design of electronic interfaces for these devices and their applications. Since 2002 the following research projects related with the work presented in this Thesis have been developed:

- 1) Desarrollo de Inmunosensores Piezoeléctricos para la Detección de Plaguicidas N-Metil-Carbamatos y Organofosforados en Alimentos y Bacterias Lácticas en Cerveza (Reference : AGL2002-01181). (2002-2005)
- 2) Desarrollo de un Inmunosensor Piezoeléctrico Multi-residuo para la Detección de Residuos de Plaguicidas en Alimentos y Aguas. Ministerio de Ciencia y Tecnología (Reference : AGL2006-12147/ALI). (2006-2009).
- 3) Inmunosensor Piezoeléctrico de Alta Frecuencia para la Detección de Bisfenol A y Ftalatos en Alimentos Envasados (Reference : AGL2009-13511/ALI). (2009-2010).

- 
- 4) Validación de la tecnología QCM de Alta Resolución en Aplicaciones Bioquímicas (Reference : PAID/2011/061). (2011-2012).
  - 5) Demostrador Tecnológico Basado en Transductores Acústicos para Aplicaciones de Prevención y Diagnóstico en Salud (DETECTA) (Reference : IPT-2011-1082-900000). (2011 –2012).
  - 6) Diseño de una plataforma basada en matrices de sensores de cuarzo de alta resolución para HTS (High-Throughput Screening) de residuos en mieles (Reference : AGL2013-48646-R). (2014/31-2016).

After more than 15 years working with microgravimetric techniques, the research group in which this Thesis has been developed has achieved very important progresses in electronic characterization systems for piezoelectric resonators. In project AGL2002-01181 a 9 MHz traditional QCM sensor was used for the detection of Carbaryl pesticide in fruit juices. In this project an interface system based on a PLL with a manual control of the parallel capacitance compensation was developed. The LOD achieved for that mentioned pesticide was 11 ug/L (March et al., 2009). These obtained results were not good enough to accomplish with the European regulatory levels established for the detection of residues in food or drinking water. For that reason, one of the main challenges in the research activity of the group has been the improvement of the LOD when working with acoustic devices. The ability for multianalyte detection, which is a mandatory requirement for High-Throughput Screening applications, has been another imperative challenge.

The LOD improvement was dealt with in AGL2006-12147/ALI and AGL2009-13511/ALI projects. This improvement involves increasing the device sensitivity and reducing the electronic system noise and other disturbances introduced by the fluidic system or by changes in temperature, among others. The sensitivity improvement was addressed by using HFF-QCM sensors, then the fragility of these devices when handled was revealed. This hindrance launched two parallel research lines in the group: 1) the search of a more robust and sensitive acoustic device and 2) the way to improve HFF-QCM sensors handling. For the first line, Love Wave sensors were selected as

firm candidates; for the second line the possibility of using clamping frames with HFF-QCM devices was explored. From this moment, two parallel Thesis were started-up in the group, the first Thesis dealt with the LOD improvement by using LW sensors and the second (which is the one here presented) by using framed HFFQCM devices. Very encouraging results, which improve one order of magnitude the LODs obtained with optical techniques (such as Surface Plasmon Resonance), have been obtained (March et al., 2015; Rocha-Gaso et al., 2014).

Regarding the reduction of the characterization system noise, a new electronic interface approach, based on the measurement of sensor phase shifts while the sensor is interrogated at a fixed frequency, was developed. This new concept was developed in projects PAID/2011/061 y IPT-2011-1082-900000, and has lead to the patent «*Método y Dispositivo de Nanogravimetría en Medios Fluidos Basado en Resonadores Piezoeléctricos*» (P200901503), which has been extended to Spain, Colombia, USA and China. This new approach overcame the instability problems detected with high frequency oscillators. Moreover, its fast operation and low cost makes easier the simultaneous characterization of several sensors, making possible a multi-array implementation. Multianalyte detection challenge has been dealt with in project AGL2013-48646-R, currently under development. To face with this challenge, the ability to miniaturization of quartz resonators is used. This capability makes it possible to integrate multiple sensors in an array configuration, giving rise to what is known as Monolithic Multichannel Quartz Crystal Microbalance (MQCM), consisting of several microbalances on a single quartz substrate. This is a promising new technology, because miniaturization of the resonator implies further advantages such as reduced cost, reduced consumption of samples and reagents, and reduced assay time trial.



## Publications

---

### International Journal Articles

March, C., **García, J. V.**, Sánchez, Á., Arnau, A., Jiménez, Y., García, P., Manclús, J.J., Montoya, Á., 2015. High-frequency phase shift measurement greatly enhances the sensitivity of QCM immunosensors. *Biosens. Bioelectron.* 65, 1–8. doi:10.1016/j.bios.2014.10.001

**García, J.V.**, Rocha, M.I., March, C., García, P., Francis, L.A., Montoya, A., Arnau, A., Jimenez, Y., 2014. Love Mode Surface Acoustic Wave and High Fundamental Frequency Quartz Crystal Microbalance Immunosensors for the Detection of Carbaryl Pesticide. *Procedia Eng.* 87, 759–762. doi:10.1016/j.proeng.2014.11.649

Rocha-Gaso M-I, **García J-V**, García P, March-Iborra C, Jiménez Y, Francis L-A, et al. Love Wave Immunosensor for the Detection of Carbaryl Pesticide. *Sensors.* 2014;14: 16434–16453. doi:10.3390/s140916434

Montagut, Y.J., **García, J. V.**, Jiménez, Y., March, C., Montoya, A., Arnau, A., 2011. Frequency-shift vs phase-shift characterization of in-liquid quartz crystal microbalance applications. *Rev. Sci. Instrum.* 82, 064702. doi:10.1063/1.3598340

Montagut, Y., **García, J. V.**, Jiménez, Y., March, C., Montoya, Á., Arnau, A., 2011. Validation of a Phase-Mass Characterization Concept and Interface for Acoustic Biosensors. *Sensors (Basel).* 11, 4702–4720. doi:10.3390/s110504702

---

Arnau, A., Montagut, Y., **García, J.V.**, Jiménez, Y., 2009. A different point of view on the sensitivity of quartz crystal microbalance sensors. *Meas. Sci. Technol.* 20, 124004. doi:10.1088/0957-0233/20/12/124004

Arnau, A., **García, J. V.**, Jimenez, Y., Ferrari, V., Ferrari, M., 2008. Improved electronic interfaces for AT-cut quartz crystal microbalance sensors under variable damping and parallel capacitance conditions. *Rev. Sci. Instrum.* 79, 075110. doi:10.1063/1.2960571

Torres, R., **García, J. V.**, Arnau, A., Perrot, H., Kim, L.T.T., Gabrielli, C., 2008. Improved frequency/voltage converters for fast quartz crystal microbalance applications. *Rev. Sci. Instrum.* 79, 045113. doi:10.1063/1.2908430

Torres, R., Arnau, A., Perrot, H., **García, J.**, & Gabrielli, C. (2006). Analogue–digital phase-locked loop for alternating current quartz electrogravimetry. *Electronics Letters*, 42(22), 1272. doi:10.1049/el:20062269

## Meetings and Conferences

March, C., **García, J.V.**, Fernández, R., Jiménez, Y., Arnau, A., Montoya, A., 2014. Further Sensitivity enhancement of HFF-QCM immunosensors for pesticides. 4th International Conference on Bio–Sensing Technology

**García, J.V.**, Rocha, M.I., March, C., García, P., Francis, L.A., Montoya, A., Arnau, A., Jimenez, Y., 2014. Love Mode Surface Acoustic Wave and High Fundamental Frequency Quartz Crystal Microbalance Immunosenors for the Detection of Carbaryl Pesticide. *Eurosenors*

Rocha-Gaso, M.I., **García, J.V.**, March-Iborra, C., Jiménez, Y., Francis, L.A., Montoya, A., 2013. Love wave saw immunosensor for detection of carbaryl pesticide. 3rd International Conference on Bio–Sensing Technology.

Montoya, A., Manclús, J.J., Arnau, A., Jimenez, Y., **García-Narbón, J.V.**, March, C., 2013. Advanced, high sensitivity QCM piezoelectric immunosensors for pesticide analysis, based on the measurement of phase changes at high fundamental frequency (HFF) 8th Symposium del Mediterranean Group of Pesticide Research (MGPR).

Montoya, A., **García-Narbón, J.V.**, Sánchez, A., Arnau, A., Jiménez, Y., March, C., 2012. Un nuevo concepto de Imunosensor Piezoeléctrico (QCM) para plaguicidas, basado en la detección de cambios de fase a alta frecuencia (A new concept of piezoelectric immunosensor (QCM) for pesticides, based on detection of phase shifts at high frequency). 8th Ibero-American Congress on Sensors (Ibersensor 2012)

Rocha-Gaso, M.I., March, C., **García, J.**, Francis L.A., Jiménez, Y., Arnau, A., Montoya, A., El Fissi, L., 2012. User-friendly love wave flow cell for biosensors. *Biosensors 2012*

---

**J.V. García**, C. March, A. Sánchez, Y. Montagut, A. Montoya, A. Arnau, A., 2012. High-sensitivity piezoelectric immunosensor for pesticide analysis. *Biosensors 2012*

Montagut, Y., **García, J.V.**, Jimenez, Y., March, C., Montoya, A., Arnau, A., 2011. A new QCM Sensor Characterization Technique Based on the Phase/Mass Sensitivity Concept. 5th Joint Conference of the 65th IEEE International Frequency Control Symposium/25th European Frequency and Time Forum.

Montoya Baidés, A., Fernández Arteaga, J., Ocampo González, A., **García Narbón, J.V.**, Montagut Ferrizola, Y., March Iborra, C., 2010. Inmunosensor piezoeléctrico para el análisis de plaguicidas. (Piezoelectric immunosensor for pesticide analysis). XXIX Congreso Latinoamericano de Química – CLAQ 2010.

Montoya Baidés, A., Fernández Arteaga, J., Ocampo González, A., **García Narbón, J.V.**, Montagut Ferrizola, Y., March Iborra, C., 2009. Desarrollo de inmunosensores piezoeléctricos para el análisis de plaguicidas y sus metabolitos. (Development of immunosensors for pesticide analysis and its metabolites). Congreso Iberoamericano de Biotecnología y Biodiversidad.

Montagut Ferrizola, Y., **García Narbón, J.V.**, Rocha-Gaso, M.I. Arnau Vives, A., 2009. Interfaz para la microbalanza de cuarzo (QCM) basada en osciladores que permite la aplicación de biosensores. (Interface for quartz crystal microbalance based on oscillators that allows the application of biosensors). XXVII Congreso anual de la Sociedad Española de Ingeniería Biomédica (Caseib 2009)

Arnau, A., **García, J.V.**, Jimenez, Y., Ferrari, V., Ferrari, M., 2007. Advanced electronic interfaces for the monitoring of at-cut quartz crystal resonators used as acoustic sensors in fluid media. ICA 2007. 19th International Congress on Acoustics.

Arnau, A., **García, J.V.**, Jimenez, Y., Ferrari, V., Ferrari, M., 2007. Improved Electronic Interfaces for Heavy Loaded AT Cut Quartz Crystal Microbalance Sensors. Frequency Control Symposium, Joint with the 21st European Frequency and Time Forum. IEEE International. pp. 357-362

## Book Chapters

Montagut, Y., **García Narbón, J.**, Jiménez, Y., March, C., Montoya A., Arnau, A., 2011. Biosensors - Emerging Materials and Applications. InTech (Ed.) 978-953-307-328-6

## Patents

Arnau Vives, A., García Molla, P., **García Narbón, J.V.**, Jiménez Jiménez, Y., Montagut Ferrizola, Y., Reig Fabado, A. Método y dispositivo de nanogravimetría en medios fluidos basado en resonadores piezoeléctricos. (Method and device for nanogravimetry in fluid media using piezoelectric resonators). Application number:

---

P200901503. Priority country: Spain Priority date: 23-06-2009 Organization: Universidad Politécnica de Valencia Countries where it is applicable: European Union; United States; Japan; Australia; South Korea Companies: Advanced Wave Sensors S.L.



